EXPERIMENTAL AND COMPUTATIONAL STUDIES ON EXIT-HOLE-FREE FRICTION STIR SPOT WELDING PROCESSES

A thesis submitted in partial fulfilment of the requirements for the degree of

DOCTOR OF PHILOSOPHY

by

Nitish Bhardwaj
(Roll number: 176103008)

DEPARTMENT OF MECHANICAL ENGINEERING
INDIAN INSTITUTE OF TECHNOLOGY GUWAHATI
GUWAHATI – 781039
INDIA
SEPTEMBER 2023

DECLARATION

I declare that,

a. The work contained in this thesis is original and has been done by me under the guidance of my supervisors.
b. The work has not been submitted to any other institute for any degree or diploma.
c. I have followed the guidelines provided by the institute in preparing the thesis.
d. I have confirmed to the norms and guidelines given in the ethical code of conduct of the institute.
e. Whenever I used material (data, theoretical analysis, figure and text) from other sources I have given due credit to them by citing them in the text of the thesis and giving their details in reference.

Signature of student

(Nitish Bhardwaj)

Department of Mechanical Engineering,
Indian Institute of Technology Guwahati,
Guwahati – 781039, INDIA

CERTIFICATE

It is certified that the work contained in the thesis entitled "Experimental and Computational Studies on Exit-Hole-Free Friction Stir Spot Welding Processes" is submitted by Mr. Nitish Bhardwaj to the Indian Institute of Technology Guwahati for the award of the degree of Doctor of Philosophy has been carried out under our supervision in the Department of Mechanical Engineering, Indian Institute of Technology Guwahati. This work has not been submitted elsewhere for the award of any other degree or diploma.

Dr. R. Ganesh Narayanan
Professor
Department of Mechanical Engineering,
Indian Institute of Technology Guwahati,
Guwahati-781039, India

Dr. Uday Shanker Dixit
Professor
Department of Mechanical Engineering,
Indian Institute of Technology Guwahati,
Guwahati-781039, India

Date: 25/09/2023

Dedicated to the Almighty, whose creation we are perceiving, whose consciousness we are experiencing.

Dedicated to my father, Shri Deben Bordoloi and my mother, Shrimati Dipali Bordoloi, who with their efforts, have allowed me the freedom to tread my own journey.

Dedicated to all my Gurus, who have shaped the eyes I see the world through.

Acknowledgements

It is with heartfelt appreciation that I express my deepest gratitude to the Almighty for His benevolent presence. I would like to extend my sincere thanks to my esteemed institution, IIT Guwahati, for providing me with a conducive environment to nurture my intellectual growth. The nurturing atmosphere, state-of-the-art facilities, and scholarly community at IIT Guwahati have been instrumental in shaping my research path and fostering my academic pursuits.

My heartfelt gratitude goes to my supervisors, Prof. Uday Shanker Dixit and Prof. R. Ganesh Narayanan. Their guidance, mentorship, and support have been invaluable throughout my research journey. Prof. Dixit's profound insights and Prof. Narayanan's astute observations have not only shaped my work but also enriched my understanding of the subject. I extend my sincere appreciation to the members of the doctoral committee, namely Prof. Swarup Bag (Chairman), Prof. Pankaj Biswas, and Prof. Sajal K. Deb, for their scholarly inputs, invaluable suggestions, and critical evaluations. Their expertise and constructive feedback have significantly enhanced the quality of my research work, and I am truly grateful for their mentorship.

I would like to express my heartfelt thanks to the staff members of the workshop, including N.K. Das, Mrinal Sarma, Dilip Chetry, Sanjib Sarma, Chandra Kanta Boro, Minesh Medhi, Bijay Kr Choudhury, Dhaneshwar Khaklary, Upen Gohain, Dulumoni Das, Gautam Gogoi, Gwmchar Baro, Gokul Das, Mukut Medhi, Chandan Banikya, and Sontosh Gogoi. I am grateful to the Central Instruments Facility (CIF) at IIT Guwahati for providing access to their sophisticated instruments, which were crucial for the successful completion of my research work. I would like to extend my heartfelt thanks to Mrs. Pallabita Chowdhury for her guidance and counseling during moments of both academic and personal challenges. I would also like to express my gratitude to my senior colleagues, Dr. Arvind Singh, Dr. Pritam Rana, Dr. Saibal Barik, Dr. Tinu Saju, Dr. Polash P. Dutta, Dr. Rajkumar Sufen, Dr. Amit Raj, Dr. Vikash Kumar, Saptarshi Dutta, and Sujit Das, for their invaluable insights and introduction to the world of research. Their experiences and guidance were instrumental in shaping the early stages of my Ph.D. journey. To my fellow lab mates, Sukanta Das, Rishabh Saxena, Priyabrat Nath, Kaustabh Chatterjee, Bappa Das, Bhanu and Vivekananda Halder, I extend my heartfelt thanks. Their camaraderie, intellectual discussions, and constant support have made this research journey a truly enriching experience. I would like to express my gratitude to my friends Nilkamal Mahanta, Nilavjyoti Sharma, Biswajit Barman, Pranjyoti Saikia, Abhilasha Bora, Larionette Mawlong, Niharika Keot, Halim Hussain, Faladrum Sharma, and Dhiraj Bombarde for their support and encouragement throughout. I also thank my friends, Nishant Das, Susmita Das, Kasturi Goswami, Geetartha Das, Abhishek Borah, Ritam Sharma, Saurav Kalita, Rohan Barooah and Animesh Bordoloi, for words of encouragement, interests and support during this journey.

Woven intricately into the fabric of my journey, alongside the pursuit of knowledge, I am forever grateful for the support of my beloved family. I take the opportunity to thank my grandfather and grandmother, Late Jogeshwar Bordoloi and Late Konika Bordoloi, who taught me how to write my first letters. To my father, Deben Bordoloi, his steadfast belief in my abilities, sage guidance, and selfless sacrifices have laid the foundation of my aspirations. My mother, Dipali Bordoloi, her nurturing embrace, boundless affection, and faith in my dreams have been my constant inspiration. My wife, Pratyashi Bordoloi, her unwavering presence, love, and understanding have been the elixir of my motivation and perseverance. To my sister, Queen Bhardwaj, and brother-in-law, Tapan Deka, I am grateful for their support and for shouldering responsibilities when I needed it the most. To my dear nephew Harshiv, your very arrival into this world has brought a renewed sense of motivation and joy. To my father-in-law, Parashmoni Bordoloi, mother-in-law, Santwana Bordoloi, and sister-in-law, Prapti Bordoloi, thank you for believing in me and being an integral part of this journey. Together, as a family, we have shared the joys and challenges of this doctoral odyssey, and I am forever thankful for your constant belief in my potential.

Nitish Bhardwaj

IIT Guwahati

Abstract

Pursuing sustainable and technologically advanced welding techniques has led to extensive research in developing environmentally friendly and defect-free methods for industrial applications. Friction stir welding (FSW) and its variant friction stir spot welding (FSSW) have emerged as promising solid-state welding processes that generate effective joints through frictional heat without the drawbacks of arc flash, spatter, harmful gases, and pollution. This study focuses on enhancing the understanding of FSW and FSSW by investigating friction and heat generation at the contacting surfaces and developing techniques to address the issue of exit-hole formation. Literature survey revealed that there are methods to solve exit-hole defects; however, while some methods had insufficient penetration depth, others involved complicated tools and multi-step operations for a single joint.

Investigations into heat generation during FSSW of aluminium alloy sheets using an H13 tool revealed that lubrication reduces the coefficient of friction, resulting in lower torque (44–55% reduction) and plunge force (12–24% reduction) requirements. This led to successful welding with reduced energy input without compromising joint strength, as confirmed by peel and lap shear tests. The study emphasizes the prominent role of plastic deformation along with friction in heat generation. An inverse approach was proposed to determine and model friction at different interfaces during FSSW. It is assumed that the frictional behaviour at the pin-workpieces interface is sticking in nature and follows the constant shear model of friction. This aspect is analysed by carrying out finite element (FE) simulations in DEFORM-3D on a shoulder-less pin and validating it through in-house experiments. A hybrid friction model (combination of Coulomb's and constant shear models) is used on the shoulder-workpieces interface. The friction parameters are adjusted through an optimization approach by minimizing the error between experiments and simulation. In a typical case, the pin-workpiece interface's friction factor (m) was 1.05. Friction at the shoulder-work interface was best represented by a hybrid model, with $m = 0.77$ for the high-pressure region and $\mu = 0.29$ for the low-pressure region, where μ is the Coulomb's coefficient of friction.

To remove the exit-hole, a technique of refilling the exit-hole using waste aluminium chips is discussed. The exit-hole left after FSSW of two AA6082 sheets is filled with waste aluminium chips, and a tool is used to stir over it. This leads to an exit-hole-free joint. The refilled joints were compared with those produced by conventional FSSW using a tool with pin and pin-less tool. Refilling the exit-hole with waste chips delivered 16% and 84% higher load bearing capacity during T-peel test as compared to conventional FSSW with a tool having pin and a pin-less tool. Furthermore, a novel method of FSSW using consumable pin is proposed to produce exit-hole-free joints. To understand the influence of quality of consumable pin, two AA6061-T6 sheets were welded using three different consumable pin materials, viz. AA6061-T6, mild steel (MS) and oil hardened non-shrinking die steel (OHNS). The

joint strength of the welds evaluated by lap shear test revealed that FSSW using AA6061-T6, MS and OHNS consumable pins resulted in 40, 36.6 and 37.6% higher joint strengths, respectively, as compared to conventional FSSW with pinless tool. The joint strength using consumable pins was comparable to conventional FSSW with hard pin, however, with the added advantage of an exit-hole-free joint. The study also revealed that AA6061-T6 consumable pin performed better than MS and OHNS consumable pins. The cross sections of the joints were also compared in terms of microstructure and microhardness. To understand the physics of the process, FE simulations were carried out in DEFORM-3D, which revealed that the consumable pin contributed to the stirring of the workpiece material, similar to a conventional hard pin. Based on the study, a mechanism of joint formation for FSSW using consumable pin has been proposed. The consumable pin stirs the workpiece material as it rotates and penetrates into the workpiece while simultaneously getting deformed. Under a high downward plunge forge at elevated temperature, bonding of the two sheets occurs and the consumable pin gets assimilated in the workpiece material, producing an exit-hole-free FSSW joint.

The impact of rotational speed on joint quality in FSSW using consumable pins was evaluated. A 1.7 times increase in joint strength was observed at 900 RPM compared to 360 RPM, with a continuous increase in joint strength up to 900 RPM followed by a decline. Additionally, the effect of plunge rate on joint quality was investigated. Varying the plunge rate showed a 4% increase in lap shear strength at 15 mm/min compared to 6 mm/min, while there was an 8.5% decrease in energy requirement. However, at 35 mm/min, there was a 25% decrease in joint strength. Microstructure and microhardness analysis, along with simulation results, explained the observed trends. FE simulations accurately predicted temperature distribution, force, torque, energy requirements, and material flow at different process parameters, aiding in the understanding of joint strength variations. The Cockcroft-Latham damage model provided closer predictions to experimental data compared to the Freudenthal damage model when lap shear test simulations were performed. The FE model developed was able to predict lap shear strength for welding at a given process parameter. The proposed adhesive bonding of the consumable pin to the tool shoulder demonstrated comparable lap shear strength (within 5% variation) and improved production efficiency, eliminating the need for additional machining steps. Moreover, the application of lubricants in conjunction with adhesive-bonded consumable pin in FSSW offers improved production efficiency while maintaining satisfactory joint strength. The integration of lubrication reduces energy requirements for weld formation (35–42%) and ensures the production of strong joints.

Overall, this comprehensive study contributes to the understanding of FSSW and its various aspects, including friction, heat generation, exit-hole elimination, rotational speed, plunge rate, and the integration of lubricants and adhesive-bonded consumable pin. The findings provide valuable insights for the development and optimization of FSSW techniques for industrial application.

Table of Contents

List of Figures

List of Tables

Nomenclature

List of symbols

α	coefficient of thermal expansion
$\dot{\gamma}$	slip rate
δ_{ij}	Kronecker's delta
ε	strain
$\dot{\bar{\varepsilon}}$	strain rate
ε^{p}	plastic strain
${}_{t}\Delta\varepsilon_{ij}^{L}$	incremental logarithmic strain
η	inelastic heat fraction (Taylor and Quinney coefficient)
η_{Q}	heat transfer efficiency
μ	Coulomb's coefficient of friction
v	Poisson's ratio
ρ	density
σ	true stress
σ_{b}	Stefan–Boltzmann constant
σ_{y}	yield stress of a material
σ_{ij}	Cauchy's stress tensor
σ'_{ij}	Cauchy's stress tensor's deviatoric component
ω	angular velocity
C_{f}	critical damage value
C_{v}	heat capacity
D	damage value
E	Young's modulus of elasticity
F_{n}	plunge force at nth step
${}_{t}\Delta F$	polar decomposition
G	modulus of rigidity
H	scalar hardening function
h	enthalpy
K	strength coefficient
k	conductivity

M_n	torque at nth step
m	friction factor
n	hardening exponent
Q_{eff}	activation energy for precipitate dissolution
$\dot{q}_p$	heat generation rate due to plastic deformation
$\dot{q}_f$	heat generation rate due to friction
R	gas constant
T	temperature
Δt	sampling time difference
${}_t\Delta U$	incremental right stretch tensor derived from the incremental deformation gradient tensor
${}_t\Delta u$	tensor caused by incremental displacement
${}_t\Delta u_{i,j}$	derivative of the incremental displacement with respect to position ${}^t x$
V	speed of heat source
v_{mat}	velocity of the material under the tool
v_{tool}	position dependent tangential velocity of the tool
χ_n	plunge depth at nth step

List of Abbreviations

AAFSW	Arc Assisted Friction Stir Welding
ALE	Arbitrary Lagrangian-Eulerian
AMC	Aluminium Matrix Composites
AS	Advancing Side
ASTM	American Society for Testing and Materials
AWS	American Welding Society
BM	Base Material
BTFSW	Bobbin Tool Friction Stir Welding
CA	Cellular Automata
CAFE	Cellular Automata Finite Element
CEL	Coupled Eulerian-Lagrangian
DFSW	Double Sided Friction Stir Welding
EAFSW	Electrically Assisted Friction Stir Welding
EBW	Electron Beam Welding
EDS	Energy Dispersive Spectroscopy

ESW	Electroslag Welding
FBJ	Friction Bit Joining
FCAW	Flux-Cored Arc Welding
FE	Finite Element
FESEM	Field Emission Scanning Electron Microscope
FFSW	Filling Friction Stir Welding
FSAM	Friction Stir Additive Manufacturing
FSP	Friction Stir Processing
FSS	Friction Stir Scribe
FSSW	Friction Stir Spot Welding
FSW	Friction Stir Welding
FTPW	Friction Taper Plug Welding
GMAW	Gas Metal Arc Welding
GTAFSW	Gas Torch Assisted Friction Stir Welding
GTAW	Gas Tungsten Arc Welding
HAZ	Heat Affected Zone
HDPE	HDPE High Density Polyethylene
HGSFSW	Hot Gas Stream Assisted Friction Stir Welding
hp	Horsepower
IAFSW	Induction Assisted Friction Stir Welding
IMC	Intermetallic Compound
JCPDS	Joint Committee on Powder Diffraction Standards
JLR	Joint-Line Remnant
KB	Kissing Bonds
LAFSW	Laser Assisted Friction Stir Welding
LBW	Laser Beam Welding
LFW	Linear Friction Welding
MES	Mitsui Engineering and Shipbuilding
MIG	Metal Inert Gas
MS	Mild Steel
MWCNT	Multi-Walled Carbon Nano-Tube
N-KFSW	Non-Keyhole Friction Stir Welding
OFW	Orbital Friction Welding
OHNS	Oil Hardened Non-Shrinking Die Steel
PAFSW	Plasma Assisted Friction Stir Welding
PAW	Plasma Arc Welding

PcBN	Polycrystalline Cubic Boron Nitride
RAFSSW	Rotating Anvil Friction Stir Spot Welding
RDRFSW	Reverse Dual Rotation Friction Stir Welding
RFSSW	Refill Friction Stir Spot Welding
RPM	Revolutions Per Minute
RS	And Retreating Side
RW	Resistance Welding
SMAW	Shielded Metal Arc Welding
SSFSW	Stationary Shoulder Friction Stir Welding
SSW	Stir Spot Welding
SZ	Stir Zone
TIG	Tungsten Inert Gas
TMAZ	Thermo-Mechanically Affected Zone
TWI	The Welding Institute
UAFSW	Ultrasonic Assisted Friction Stir Welding
USW	Ultrasonic Welding
UTM	Universal Testing Machine
XRD	X-Ray Diffraction

Chapter 1

Background and Scope

1.1 Introduction to Welding

Welding is a critical process in the manufacturing and construction industries that involves joining two or more materials, usually metals, by heating them and allowing them to cool and solidify. The origins of welding can be traced back to ancient times when early humans discovered that they could heat and fuse metals together to create tools and weapons. However, the modern welding process as an industrial process began with the advent of electric arc welding in the late 19th century. This process involved using an electric arc to produce heat and melt metals, which were then fused together as they cooled. The electric arc welding process was first introduced by Nikolai Benardos and Auguste de Meritens in 1881. Benardos was awarded the patent for carbon electrode processes in 1887 and bare metallic electrode processes in 1889. It quickly became popular in the shipbuilding and construction industries.

Over the years, welding technology continued to improve and evolve, with new welding techniques and equipment being developed to meet the growing demands of industry. Today, welding is used in a wide range of applications, from manufacturing automobiles and aircraft to constructing bridges and buildings. There are various types of welding techniques that have been developed over the years, each with its unique set of advantages and applications. Some of the most common welding techniques include gas metal arc welding (GMAW), shielded metal arc welding (SMAW), gas tungsten arc welding (GTAW) and flux-cored arc welding (FCAW). Other than electric arc welding, there are laser beam welding (LBW), plasma arc welding (PAW), electroslag welding (ESW), electron beam welding (EBW), friction stir welding (FSW), ultrasonic welding (USW), thermit welding (TW) and resistance welding (RW). These welding techniques utilize the heat generated from sources other than electric arc. For example, TW, also known as exothermic welding, is a process that uses heat generated by a chemical reaction to fuse two metal surfaces together. This process was first developed in the late 19th century and is still widely used today in railway construction, pipeline welding, and electrical grounding applications. Gas welding uses a gas flame to melt and fuse metal surfaces together. The most common types of gas welding are oxy-fuel welding and air-acetylene welding. This welding technique was first developed in the early 1900s and has since become a popular technique for welding thin metal sheets, pipes, and tubing. Friction welding is a solid-state welding process that involves the rubbing together of two metal surfaces until they reach a plastic state, and they are forged together to create a strong bond. Friction welding is a popular welding technique in the aerospace, automotive, and construction industries due to its speed, efficiency, and high-quality welds (Kumar et al., 2018).

One of the key advantages of welding is its ability to produce strong, durable joints that can withstand high stress and load. This makes it an essential process in the construction and manufacturing industries. There is ongoing research into developing new welding techniques and materials that can improve the efficiency and effectiveness of the welding process, as well as reduce its environmental impact. In recent years, the concern for the environmental impact of welding and other industrial have risen. This has led to increased research into sustainable and green welding techniques that minimize waste and energy consumption. Some of the emerging green welding techniques include FSW, Laser Welding, EBW and the integration of robotics and automation into the welding process (ASM International, 2003; Cao and Liu, 2017). These techniques have shown promise in reducing the environmental impact of welding while still meeting the demands of industry. FSW, for example, has shown great promise in reducing the environmental impact of welding by reducing the amount of energy required to create welds (Kumar et al., 2018).

1.2 Green Welding

Traditional welding processes often result in environmental challenges due to the release of harmful gases, excessive energy consumption, and generation of hazardous waste. As such, the concept of green welding has emerged, which causes less harm to the environment. Green welding encompasses a range of techniques that aim to minimize the environmental impact. These include reducing energy consumption, minimizing waste generation, and utilizing sustainable materials. Green welding approaches typically involve the adoption of energy-efficient approaches, advanced equipment, innovative process designs, and eco-friendly consumables. Green welding techniques are particularly beneficial in industries that prioritizes sustainability and must adhere to strict environmental norms, such as automotive manufacturing, aerospace, and construction. These techniques enable the production of environment-friendly and efficient products, contributing to a greener future. As industries strive for greener practices, the adoption of green welding techniques is likely to increase, leading to a more sustainable future. Sustainability refers to the judicious use of resources to meet our present needs without compromising the needs of the future generation. It translates to higher efficiencies in energy consumption, resource utilization, lower pollution and long-term ecological benefits with balanced economic, social, and environmental considerations to create a harmonious and lasting system.

Some welding techniques considered as Green Welding are:

1. Laser Welding: Laser welding is an energy-efficient technique that utilizes a high-intensity laser beam to join materials. It offers precise control, minimal heat-affected zones, and reduced distortion compared to conventional welding methods.

2. EBW: It employs a high-velocity electron beam to generate heat and join materials. This technique provides high-quality welds with minimal distortion, and precise control over the welding process.
3. FSW: It is a solid-state welding process that joins materials by using frictional heat generated by a rotating tool. This technique offers advantages such as low energy consumption, absence of filler material, and the ability to join dissimilar materials effectively (Mishra and Ma, 2005).

1.3 Conventional Fusion Welding versus Solid State Welding

Two commonly used welding techniques are fusion welding and solid-state welding. They differ significantly in terms of their mechanisms and applications. This section explores the differences between conventional fusion welding and solid-state welding by highlighting their unique features and advantages.

Conventional fusion welding encompasses various techniques such as arc welding, gas welding, plasma welding and laser welding. These methods involve the application of heat to melt the parent materials, followed by the addition of a filler material, if required. The molten material solidifies upon cooling, resulting in a bond between the joined parts. During conventional fusion welding, a heat source, such as an electric arc or laser beam, is utilized to raise the temperature of the parent materials above their melting points. This causes localized melting, enabling the fusion of the adjoining surfaces. The filler material, if used, is introduced in the molten state to reinforce the joint and promote better mechanical properties. Conventional fusion welding offers several advantages in mechanical engineering applications. It allows the joining of dissimilar materials, such as metals and alloys, facilitating the construction of complex structures. Additionally, the use of filler material provides enhanced strength and durability to the joint. This method is widely adopted in industries like automotive, aerospace, and construction due to its versatility and established techniques.

In contrast to conventional fusion welding, solid state welding techniques achieve bonding without reaching the melting point of the parent materials. These methods exploit mechanical pressure and temperature to create a molecular bond between the components. Solid state welding includes friction welding, ultrasonic welding, diffusion welding, and explosive welding, among others. These techniques rely on interatomic diffusion and plastic deformation to generate atomic bonding between the surfaces. By applying pressure and heat below the melting point, solid state welding enables the formation of a strong, metallurgical bond. Solid state welding techniques offer distinct advantages in mechanical engineering applications. Since no melting occurs, the process avoids problems associated with solidification, thermal distortion and residual stresses. Solid state welding is particularly suitable for dissimilar materials, as it minimizes the formation of brittle

intermetallic compounds. Moreover, this technique preserves the original microstructure of the materials, resulting in improved mechanical properties and corrosion resistance.

1.4 Friction Stir Welding and Friction Stir Spot Welding

FSW has been considered as one of the most significant developments in joining process in the last two decades. It is a solid-state welding technique that is also considered as a green welding process. In this welding technique, a rotating tool is brought in contact with the workpiece, which results in heat generation due to friction and plastic deformation. The heat plasticizes the workpiece material. The stirring action and axial pressure applied by the tool results in bond formation in the workpiece. Friction stir spot welding (FSSW) is a variant of FSW where welding is performed at one spot only. Multiple spot joints are made to join materials with large dimensions. FSW possesses the benefits of solid-state welding while being more energy efficient and environment friendly. As such, it was introduced into all major industries and holds high potential to become the leading welding process in future commercial applications. An in-depth introduction to FSW and its working principle is provided in Chapter 2. Owing to the numerous benefits of FSW over fusion welding, both in terms of joint quality and environmental aspects, FSW as the green welding technology has the scope of a wider and more flexible applications in both large scale and small-scale industries in the future. Some present applications of FSW and FSSW in different industries are discussed in the following section.

1.5 Commercial Applications of FSW and FSSW

Due to its advantageous economic and environmental implications, FSW has gained substantial traction in a wide range of industrial applications. The application of FSW in industries has resulted in notable benefits in performance, cost reduction as well as weight reduction of welded components.

1.5.1 Automobile Industry

Automobile industry has been concentrating on the increased use of aluminium in the last decade owing to its light-weight and high strength-to-weight ratio. It reduces weight of the vehicles without compromising passenger safety. The increased use of aluminium in automobile industry has been successful due to capability of FSW to produce sound welds with similar as well as dissimilar aluminium alloys. Front portion of engine, alloyed wheel rims, fuel tankers, bodies of heavy-duty vehicles and tailored blanks are some of automobile parts where FSW has been employed. In 1998, TWI suggested the use of FSW in joining aluminium tailored blanks for use in car door panels. It was subsequently used for mass production of automotive components and dissimilar aluminium welding with steel automotive parts. Honda successfully employed FSW for Al-Steel dissimilar welding in its vehicle suspension system in mass-production. (Honda, 2012). Press formed steel

halves were joined to die cast aluminium in lap configuration in the front sub-frame of Honda Accord that helped support the engine and suspension parts. A 50% saving in electricity consumption and reduction of 25% in total body weight was reported by Honda as compared to conventional steel sub-frame (Honda, 2012). Honda was also first to apply FSW and FSSW to join aluminium and steel in application to door panels of mass production vehicles (Honda, 2013). Tower Automotive reported an increase of mechanical strength by two times and a 40% weight reduction due to use of FSW as compared to GMAW (ESAB, 2012). Mazda MX-5 vehicle's trunk lid was joined using FSSW where aluminium alloy sheets were welded to galvanized steel brackets. Mazda Motor Corporation claimed weight reduction, lower production cost and energy efficiency due to use of FSSW. Ford reported 30% increase in joint strength along with dimensional accuracy using FSW as compared to automated GMAW (Kallee, 2010).

1.5.2 Aerospace Industry

FSW is used in the aerospace industry for fabrication of various parts and components such as wings, fuel tanks and stringers of aircrafts owing to the high strength and lightweight nature of the welds. It also finds application in repairing of faulty welds. The components and structures used in aerospace undergo different loading conditions and thus require different properties in a single component making use of dissimilar materials inevitable. The ability of FSW to produce sound dissimilar material welds becomes helpful. Boeing, Lockheed Martin and Air Bus uses fuel tanks that are made of AA2219 welded using FSW which have resulted in significant reduction in welding cost as compared to previously used tungsten inert gas (TIG) welding (Polt, 2004). Boeing claimed a cost saving of 60% in fabrication of their Delta II and Delta IV space launch vehicle by the use of FSW. Orion spacecraft was built by NASA's Michoud Assembly Facility implementing FSW for welding of bulkhead and nosecone of the spacecraft (NASA, 2001). The bonding of core stage's rings, barrel segments and domes of space launch system (SLS) are also achieved using FSW at NASA. The welding of the fuel tank of space launch vehicles Falcon 9 by SpaceX is regarded as the largest fully FS-welded aluminium-lithium alloy structure in the world (SpaceX, 2013). Eclipse Aviation Corporation of New Mexico eliminated the use of 7000 rivets and other fasteners in their Eclipse 500 commercial aircraft by use of FSSW that helped lower assembly time and cost (ESAB, 2012). It was also claimed that FSW improved fatigue life and strength compared to conventional fastening techniques. The industries have continued the use of FSW to minimize aircraft weight and improve mechanical properties.

1.5.3 Shipbuilding and Marine Industries

The shipbuilding industry uses FSW mainly for applications of welding dissimilar aluminium alloy welding. 5xxx and 6xxx dissimilar aluminium welding is extensively used in shipbuilding industries. FSW finds application in welding of various parts like panels for decks, bulkheads, sides,

and floors, boat internal surface, aluminium hulls, superstructures, helicopter landing platforms and ship body structures. Hollow aluminium extruded panels were welded by Sapa in 1996 for application in fishing boats. Marine Aluminum in 1996 employed FSW to weld large number of panels that were used in the cruise ship 'The World' in Haugesund. 'Super Liner Ogasawara', a freight and passenger ship was built by the Mitsui Engineering and Shipbuilding (MES) with vast application of FSW (Khan et al., 2017a). In 2004, for the building of 55 m long Inshore Patrol Vessels, the naval architect of New Zealand and Australia specified FSW to be used in significant portions of their welding requirements (Delany, 2007). Donovan Group commercially used FSW in mid-2005 for building Inshore Patrol Vessels in Whangarie. Apart from these applications, FSW is also widely used for producing honeycomb and seawater resistant panels in Japanese industries. FSW has also been finding wide commercial applications in cruise ship's wide aluminium panels and in offshore oil platforms. Kawasaki Heavy Industries successfully welded AA5083 plates with a maximum thickness of up to 50 mm having excellent seawater corrosion resistance for shipbuilding purposes (Kawasaki, 2002).

1.5.4 Railway Industry

The advances in FSW and the improvements in performance of weldments have led to widespread use of FSW in railway industry. Sapa has been commercially utilizing FSW for welding train side walls and train floor panels since 2001 in their Munich suburban trains. The previously used technique of mechanized metal inert gas (MIG) was replaced by FSW to weld aluminium plates up to thickness of 23 mm and welding with lighter weight and lesser cost was achieved (Hydroextrusions, 2018). Large panels of aluminium extrusion are being increasingly used in fabricating modern railway carriages. The technology has seen large commercial utilization especially in Japan by Hitachi (Hitachi, 2018). Low distortion of welded parts was beneficial in eliminating the cost of straightening of arc welded aluminium sheets of thin thickness. Another manufacturer Nippon Sharyo used FSW to fabricate floor panels in the Shinkansen, which are popularly known as bullet trains. Nippon Light Metals also utilized FSW in subway rolling stock in Tokyo (Nikkeikin, 2018). Another Japanese company Kawasaki Heavy Industries used FSW to attach stringers to roof panels (Kawasaki, 2018). Aluminium car body shells were also produced by them utilizing the low distortion property of FSWed thin sheets.

1.5.5 Other Industries

Apart from extensive use of FSW in automobile, aerospace and railway industries, it also finds applications in other industries including construction and electrical industries. FSW is used to produce facade panels made from aluminium, copper and titanium, window frames, pipe fabrications, building of large structures such as aluminium bridges, reactors for power plants. However, the portability of FSW is a limiting factor in widespread use of FSW in construction

industry. In the electrical industry, FSW is being employed for welding of electric motor housings, electrical connectors and encapsulation of electronic products. Much more research is needed at the same time to increase the reach of FSW in these applications and falls under potential applications of FSW.

1.6 Scope of the Thesis

FSW has been adopted in commercial use before fully understanding the physics involved. Defects produced during FSW have not been addressed satisfactorily, especially the exit-hole defect that remains in the weld after the tool pin is retracted out of the workpiece. The exit-hole defect is a significant problem as it hampers the strength, aesthetic value and corrosion resistance of products welded by FSW. This is particularly problematic in case of FSSW. These prompt extensive research efforts aimed at enhancing the efficiency of the FSSW process and resolving the inherent defect of exit-hole. The present thesis discusses a study on the friction at the interface of the FSW tool and workpiece. Lowering of friction by application of lubricants and thereby reducing energy requirement for welding is discussed. An inverse methodology to determine friction at the tool-workpiece interface is proposed for improving modeling and simulation. The aim of the present thesis is to develop a process to produce exit-hole-free welds using FSSW. Two strategies, namely refilling exit-hole using waste chips and FSSW using consumable pin are discussed. The effect of consumable pin material and process parameters, viz. rotational speed and plunge rate, on joint quality, assessed using lap shear test, microhardness and microstructure analysis along with fractography are discussed. The thesis also focusses on developing an understanding of the FSSW process in relation to material flow, heat generation, and friction involved in the interacting surfaces through experiments and finite element (FE) simulation. Two fracture models, Cockcroft-Latham and Freudenthal models, are implemented on the joints to study their efficacy in failure prediction of the FSSWed joints. Finally, the thesis proposes a production strategy to improve the production efficiency of the process for industrial application.

1.7 Organization of the Thesis

The present work is organized in the form of nine chapters. Chapter 1 introduces the broad area of research i.e. welding and presents a background to the study area of the thesis. It outlines the motivation for the study, highlights the significance of the research area and discusses the organization of the thesis. In Chapter 2, the latest research efforts on enhancing the horizon of FSW are reviewed. The chapter discusses the existing literature, identifies research gaps, and presents the objectives of the present thesis. Chapter 3 focuses on a preliminary study conducted on FSSW with an exit-hole. The chapter investigates the effect of lubrication on energy requirement, heat generation and joint properties during FSSW. Additionally, it presents an inverse approach for determining friction in FSSW. Chapter 4 investigates the feasibility and effectiveness of using

waste chips for refilling the exit-hole in FSSW. Chapter 5 discusses the technique of Exit-Hole-Free FSSW using a consumable pin. The quality of consumable pin is studied in this chapter after establishing the feasibility of the process. Chapter 6 and Chapter 7 present experimental and numerical investigations focused on studying the effect of rotational speed and plunge rate, respectively, on exit-hole-free FSSW with a consumable pin. The implementation of damage models to the welded joints to predict failure is also discussed in this chapter. In Chapter 8, the final design of a tool with an adhesive-bonded consumable pin for exit-hole-free FSSW is presented. Additionally, the application of lubricant to improve production efficiency is discussed. The chapter focuses on enhancing the welding process through tool design and lubrication techniques. Finally, Chapter 9 summarizes the key findings of the thesis and provides concluding remarks. It discusses the contributions of the research and highlights potential future directions for further exploration in the field. The chapters are followed by References, which lists the sources cited throughout the thesis.

Chapter 2

Literature Review

2.1 FSW Process

The growing energy demands, and environmental concerns have resulted in an unprecedented stress on sustainability. Manufacturing industries are spending a large amount of money to develop sustainable (economical, energy-efficient and environmentally friendly) processes. FSW technology is one such sustainable manufacturing processes that has established itself as an appropriate alternative to several traditional welding processes. FSW is a solid-state welding process, developed mainly for joining difficult-to-weld materials. A solid-state welding process exploits plastic deformation to form metallurgical bond without the use of a filler material. Temperature developed in the process is lower than the melting point of the joined materials (Messler, 1999); hence, there is low distortion and good dimensional stability of the joined product. It is a suitable alternative to fusion welding process that are susceptible to hot cracking, poor solidification and embrittlement (Zimmer et al., 2009). Apart from these key advantages, FSW is a highly energy efficient process as it uses only a fraction of energy needed for fusion welding. There is no requirement of filler material during welding resulting in cost-reduction. The absence of arc flash, spatter and harmful fumes provides a safer working environment for the workers. Overall, FSW is an appealing sustainable welding alternative, finding wide applications in many industries including automotive, railway, aerospace and maritime.

2.1.1 History

With the exception of cold welding, in which the joining takes place by the application of large amount of pressure, all welding processes require heat to melt or enhance coalescence between the materials to be joined. Possible heat sources are electric arc, flame, resistance heating and friction. Friction welding was patented as far back as 1891 (Bevington, 1891), in which the spinning of one axisymmetric part relative to other axisymmetric part generated frictional heat to join the parts together. It is a solid-state welding processes where joining is achieved without melting the base materials. Friction Welding can be classified as rotary, linear and orbital friction welding. Rotary friction welding is the oldest amongst friction welding methods. In this process, a rotating part is pressed against a stationary part to produce frictional heat between the contacting surfaces. The heat-softened parts are forged together to achieve the weld-joint. It has two types (i) direct drive, with a continuous drive and (ii) inertia drive, which uses kinetic energy stored in a flywheel. Direct drive has been in use since 1950s, while inertia drive came into usage in 1960s (Maalekian, 2007). Linear friction welding (LFW) was first patented in 1929, however, it achieved widespread usage in 1960s (Bhamji et al., 2011). LFW uses reciprocating motion, of small linear displacement,

between two bodies pressed against each other to produce frictional heat. Orbital friction welding (OFW) is a combination of rotary and linear friction welding. In this technique, the center of one component is moved in a 2D curve relative to the other component. OFW has been in commercial use since 1970s. However, these processes were limited by the geometries of the workpiece. In order to cope with this, friction generated by a rotating shoulder over the workpiece was utilized to produce the heat and plastic strains on the workpieces to form a joint, which came to be known as FSW.

FSW was first patented by W.M. Thomas from The Welding Institute (TWI) in Cambridge, U.K. (Thomas et al., 1991). The process was introduced for the butt welding of high strength aluminium alloys that were hard to weld. However, soon the process started to be used for T-joints and lap joints for materials ranging from copper, magnesium and its alloys to high melting point materials like steel and titanium (Khan et al., 2017a).

Instances of commercial utilization of FSW can be found from mid-1990s. Marine Aluminium, a Norwegian company, used FSW to weld heat exchangers in 1995. The same company in 1996 used FSW for shipbuilding. Since then FSW has been finding wide applications in shipbuilding industry as well as aerospace industry. In 1998, Boeing company from United States used FSW to produce seams in a fuel tank (Khan et al, 2017a). FSW has also been finding wide acceptance in the automobile industry. In 2000, automotive components were produced using FSW by SAPA. The same year saw use of FSW in making housings for laser system and motor housings by General Tools (United States) and Hydro Aluminium (Norway). By 2001, companies were using FSW extensively for manufacturing train bodies across the world like Alstom from Germany, Hydro Aluminium from Norway, Hitachi from Japan. Automotive parts manufacturers like Showa (Japan), Tower Automotive (USA), Honda Motor Company (Japan) have been utilizing FSW for welding since 2001 and the trend continues. The lightweight nature of weld produced by FSW is advantageous in space applications as evident from its use in space shuttle external tank welds used by Lockheed Martin (USA) in 2004. The use of FSW in commercial shipbuilding continues with companies like Advanced Joining Technology (USA) and Friction Stir Link (USA) using the technology since 2003 (Amini et al., 2014). More advanced researches have been constantly taking place in this field and industrial application of FSW has been increasing in the last decade. A detailed discussion on FSW process has been presented in the next subsection.

2.1.2 Technology of FSW

In a typical butt joint welding, the two contacting surfaces of the base material are brought in contact with each other and clamped using strong fixtures to restrict their movement during plunging of a rotating FSW tool. Large axial force is applied by a non-consumable rotating tool during plunging as it is brought in contact with the joint line. The tool with specially designed shoulder and the pin

is inserted into the abutting edges of the sheets and kept rotating for a few seconds to plasticize the workpiece material. The tool is then traversed in the direction of the weld with the shoulder enclosing the plasticized material. A base plate is used between the workpiece and the anvil to avoid sticking during welding. Due to large plastic strains and high temperature, the material undergoes dynamic recrystallization during the process and produces equiaxed grains (Chang et al., 2011; Jata et al., 2000; Liu et al., 1997; Rhodes et al., 1997), thus improving the mechanical properties of the joint. In a comparative study by Taban and Kaluc (2007) of MIG, TIG and FSW welds of AA5086-H32, FSW welds were found to be the strongest both in bending and tensile tests. FSW welded joints also show higher fatigue Strength (Ericsson and Sandström, 2003).

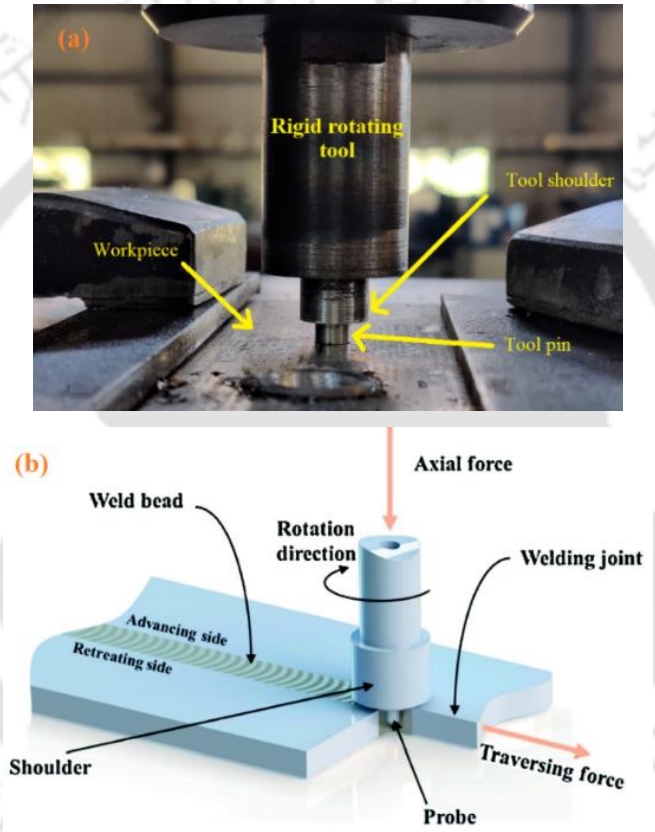

Figure 2.1 FSW process experiment and schematics: (a) tool resting on the workpiece (b) a schematic (With permission from Eslami et al., 2015; Copyright Elsevier)

Figure 2.1 shows schematic of FSW process. The two sides about the weld centerline can be distinguished as the advancing side (AS) and retreating side (RS), which show difference in their microstructure as well as properties (Mahoney et al., 2001). In the advancing side, the tool tangential velocity due to rotation and traverse velocity are in the same direction. On the other hand, the tangential and traverse velocities are in the opposite direction in the retreating side. Advancing side shows higher temperature as compared to the retreating side due to relatively higher velocity between tool and workpiece (Chao et al., 2003; Kwon et al., 2004; Sato et al., 2002). As a result of higher temperature, the grain size is found to be larger in the advancing side.

Understanding of material flow in FSW is crucial for controlling weld quality and minimization of defects. Material flow in FSW is complex and many researchers tried to visualize the material flow using different techniques like tracer technique (Colligan, 1999; Reynolds, 2000; Kumar et al., 2018), plasticine with dissimilar colours (Liechty and Webb, 2007) and high-speed camera to observe periodic material deposition (Gratecap et al., 2012). In addition, a few computational models tried to explain the material flow using finite element analysis approach (Colegrove and Shercliff, 2004; Tongne et al., 2017). Colligan (1999) and Reynolds (2000) studied material flow using embedded small steel balls as tracers and proposed that material is extruded around the pin and deposited at the back of the tool. At the same time, extrusion around the pin and stirring action near the shoulder at the top of the weld created a secondary vortex of material moving vertically and in circular motion within the pin diameter. Kumar et al. (2018) evaluated strain rates in FSW using particle image velocimetry and glass tracers in a transparent visco-plastic material. FSW microstructure and metal flow features were compared with that of aluminium extrusion and forging by Arbegast (2003). Arbegast suggested that FSW process produces five distinct metalworking zones: (i) preheat zone which is the heated material ahead of the pin, (ii) initial deformation zone, where stress exceeds the critical flow stress of the material and it starts to flow, (iii) extrusion zone, adjacent to the pin where the material flows around the pin from front of the pin to the rear, (iv) forging zone where the shoulder applies large axial forging force on the material extruded around the pin and (v) cool down zone where the material cools under forced or passive cooling conditions as shown in Figure 2.2. A similar model was given by Reynolds (2000), who explained FSW as an in-situ extrusion process where the cold base material outside the weld-zone acts as an 'extrusion chamber', i.e., the boundary of the extrusion zone where magnitude of temperature and stress are insufficient to cause material to flow.

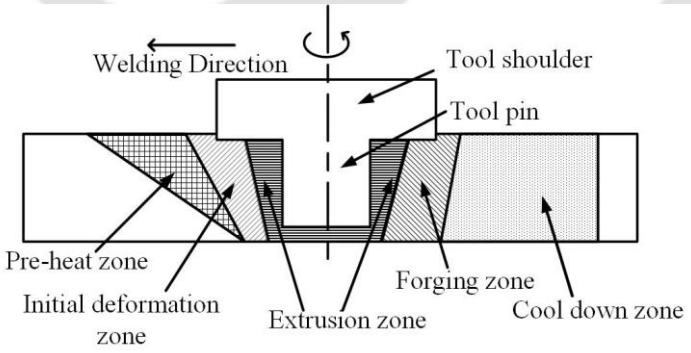

Figure 2.2 Different metalworking zones in FSW

Different weld zones can be observed in the joint produced with FSW showing distinct microstructure and mechanical properties. The first comprehensive classification of weld zones according to microstructure was given by Thomas et al. (1999). The classification was focused on aluminium alloys; however, it is applicable to other materials as well. Stirring zone (SZ) is the zone where stirring of materials takes place. It is also known as nugget zone and undergoes dynamic

recrystallization with equiaxed and refined grain size as compared to base material. Thermo-mechanically affected zone (TMAZ) is observed after the SZ as we move away from the weld center. This region is affected by both thermal cycle and deformation. Microstructure changes in the TMAZ are mainly due to dynamic recovery. Temperature and strain experienced by this region are insufficient for recrystallization resulting in elongated, narrow and relatively coarse grains than those observed in the SZ. Heat affected zone (HAZ) is the region found between base material and TMAZ, affected by thermal cycle only and does not undergo deformation. HAZ experiences grain coarsening due to the effect of heat. Base material (BM) is the undeformed region adjacent to the HAZ, far away from joint.

ISO standards for FSW of aluminium is given as ISO 25239, titled 'Friction stir welding — Aluminium'. It consists of five sections on vocabulary, design of joints, qualification of weld operators, specifications and qualifications of welding procedures, quality and inspection requirements. AWS-D17.3/D17.3M:2016 titled 'Specification for friction stir welding of aluminum alloys for aerospace applications' suggests welding specifications for aerospace applications, which can also be regarded relevant for all FSW users. Apart from the ISO and AWS standards, there are certifying agencies like Lloyds Register, DNV, Germanischer Lloyd etc., that give specifications for welding procedures.

2.1.3 FSW Process Parameters

The main process parameters that effect the joint formation in FSW are tool rotational speed, traverse speed, tool plunge depth, tool tilt angle and tool offset. These are briefly described.

2.1.3.1 Rotational and Traverse Speeds

The temperature of the stirring zone increases with increase in rotational speed of the tool. However, monotonic increase in frictional heat with increase in rotation is not observed since coefficient of friction changes as well at high rotational speeds. A lower rotational speed generates insufficient heat resulting in inadequate plasticization of material, which adversely affects the joint quality. On the other hand, higher rotational speed may generate more heat. This causes undesirable grain growth, dissolutions or coarsening of strengthening precipitates and minimization of dislocation density; all these phenomena degrade the joint strength.

With increase in tool traverse speed, heat input to the weld region is decreased resulting in a decrease in the peak temperature in the SZ. This result in lower material flow and increases the requirement of torque as well as force for traversing the tool ahead. Higher torque and longitudinal force requirements lead to lowering of tool life.

2.1.3.2 Tool Tilt Angle

It is the inclination of the tool axis from the normal to the workpiece surface like in orbital forging. The tool tilt increases the localized pressure for the same amount of plunging force. A typical tool tilt angle is 3º. However, for high welding speeds, tool tilt angle of 1º is preferred (Hovanski et al., 2015; Arici and Selale, 2007). Higher tool tilt resulted in greater weld flash and reduced thickness of the weld nugget.

2.1.3.3 Plunge Depth

Plunge depth is defined as the depth of lowest point of shoulder below the surface of welded plate. It plays an important role in controlling the depth of the stirred zone, heat generation and amount of forging force applied during welding. A higher plunge depth results in thinning of the joint area, which is not desirable. An optimized plunge depth must be used in order to produce quality welds to avoid associated defects of overheating or under-heating.

2.1.3.4 Tool Pin Offset

A shift of tool axis on either side of the joint line is regarded as tool pin offset. The distribution of heat generated on AS or RS is governed by the tool offset given. It also affects the mixing of dissimilar materials during FSW.

2.1.4 Defects in FSW

The amount of heat input during FSW plays a vital role in determining whether sound weld will be formed or defects will appear in the weld. Due to high heat input, defects like nugget collapse, surface galling and excess weld flash are observed. On the other hand, if the heat input is low, defects like kissing bonds (KB), tunneling defect, joint-line remnant (JLR) and hook defect appear in the weld.

Apart from extrusion of material around the pin, there is a simultaneous upward movement of material during FSW (Chen and Nakata, 2008; Muthukumaran and Mukherjee, 2008). This upward movement of material causes hook defect mostly in overlapping joints. When the lower sheet material is pulled up into the upper sheet, at the interface hook defect is generally observed. It is observed prominently at the TMAZ towards the AS. The hook height increases with increase in rotational speed since higher rotation speed leads to higher vertical movement of material. This is especially true in case of threaded pin. Hook height decreases with increase in weld traverse speed.

Tunneling defect is caused due to low heat input (Kim et al., 2006). Low heat input hampers material movement, which causes higher flow stress. There is deficient movement of material around the tool and a tunnel is left behind the pin due to lack of material consolidation as the tool

moves forward. It is an internal defect formed below the surface and usually not visible on the surface.

KB defect is formed because of inefficient plastic deformation due to low heat input and insufficient stirring action where the interfaces are just touching each other with no metallurgical bond between them. Oxide layer on the interface if not properly cleaned before welding may also result in KB (Oosterkamp et al., 2004).

Incomplete root penetration may be observed as a result of insufficient tool plunge, inadequate length of pin or inappropriate tool design. An unstirred region remains unconsolidated at the joint root. Uneven faces of the abutting plates, local variation in plate thickness may also result in incomplete root penetration. Some of the defects along with their causes and location of defect are listed in Table 2.1.

Table 2.1 Types of defects in FSW, their location and causes

	Defect	**Location of the defect**	**Causes**
1	Hook defect	TMAZ	• High rotation speed • Low weld traverse speed • Improper tool design • Tool tilt being inadequate
2	Kissing bond	SZ, interface of upper and lower sheet	• Low heat input • Insufficient stirring of material • Oxide layer at interface
3	Tunnelling defect	Under the weld surface, on AS near SZ-TMAZ interface	• Low heat input • High weld traverse speed with low rotational speed • Low plunge depth • Inappropriate pin offset
4	Void	On or below the weld surface on the AS of the weld	• Incorrect forging pressure • Welding speed too high
5	Incomplete root penetration	Below the pin/ SZ at the interface of the faying surfaces	• Improper tool design • Insufficient plunge depth • Local variation in thickness of plate
6	Joint line remnant	At remnant of original faying surfaces in SZ, At weld root	• Poor joint alignment • Inappropriate pin offset • Non-removal of oxide layer on the surfaces

2.2 Variants of FSW Process

In order to improve the weld quality, remove defects and better economics of the process, several variants of FSW have come up. A brief introduction to variants of FSW process is provided in the following subsections.

2.2.1 Stationary Shoulder FSW (SSFSW)

In conventional FSW, there is a shoulder affected zone and a pin affected zone resulting in different mechanical properties in these two zones. TWI developed a stationary shoulder FSW (SSFSW), where the pin rotates inside a non-rotating shoulder and slides over the workpiece. The primary contribution to frictional heat is by the rotating pin that softens, deforms and stirs the material. The shoulder only provides the axial forging force and prevents stirred material from moving out of the weld zone. This leads to uniform temperature distribution in the through-thickness direction, as well as improved hardness distribution and microstructural homogeneity (Li and Liu, 2014; Ji et al., 2014; Maltin et al., 2014; Ji et al., 2016). Figure 2.3 shows a schematic of the SSFSW.

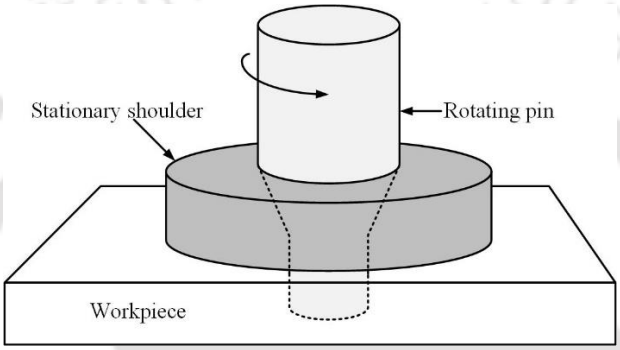

Figure 2.3 Schematic diagram of SSFSW

Overall improvement in mechanical properties of the weld and microstructural homogeneity are key features of SSFSW. The joint region can be distinguished as SZ, TMAZ, HAZ and BM. The SZ is bowl-shaped or drum-shaped and shows maximum width at mid-thickness as shown in Figure 2.4. The SZ shows a homogeneous distribution of equiaxed, refined and recrystallized grains in the through-thickness direction. SSFSW has immense scope in welding aluminium alloys and titanium alloys; however, it is not well suited for welding Fe or Ni alloys (Maltin et al., 2014).

Figure 2.4 Optical macrographs of SSFSWed Al 7075-T651 (With permission from Li et al., 2015. Copyright Elsevier)

2.2.2 Reverse Dual Rotation FSW (RDRFSW)

Overheating of the workpiece is a major problem in FSW due to large gradient in tangential speed between center of the tool and the periphery of the shoulder (Li and Liu, 2014). The problem is solved by allowing the pin to rotate at higher angular speed than the shoulder. The shoulder is usually made to rotate in an opposite direction to that of the pin. This reduces part of the torque

exerted by the tool on the workpiece, which helps in reducing clamping requirements. The process is called reverse dual rotation FSW (RDRFSW) (Figure 2.5) (Shi et al., 2014; Shi et al., 2015a). One major benefit of the process is reducing asymmetry in the temperature distribution between the AS and RS, thereby helping to obtain uniform mechanical properties (Shi et al., 2015b).

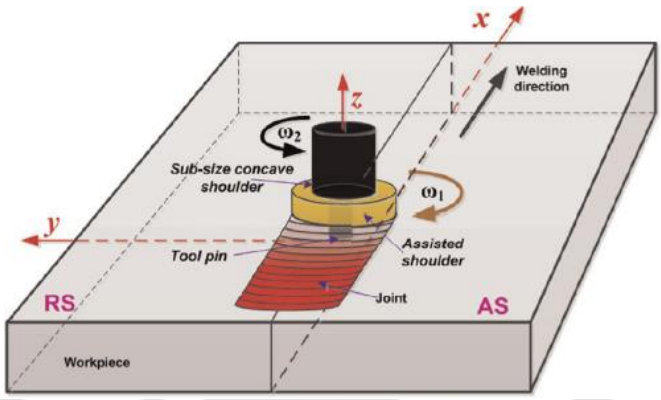

Figure 2.5 Schematic of RDRFSW. (With permission from Shi et al., 2015a. Copyright Elsevier)

2.2.3 Bobbin Tool FSW (BTFSW)

Bobbin tool FSW (BTFSW) or self-reacting FSW is a variant of FSW that consists of a bobbin tool with two shoulders, one above the workpiece and another below it. A pin passing through the entire thickness of the workpiece connects the two shoulders. The bottom shoulder removes the need of a separate base plate and provides the reaction to the axial force of the top shoulder such that the reacting forces are contained within the tool itself (Hilgert et al., 2011; Threadgill, 2010; Chaudhary and Bhavsar, 2016). Figure 2.6 shows the process and the specially designed bobbin tools used for the process. BTFSW starts by driving the tool into the workpiece from one of the edges or from a predrilled through-hole into the workpiece.

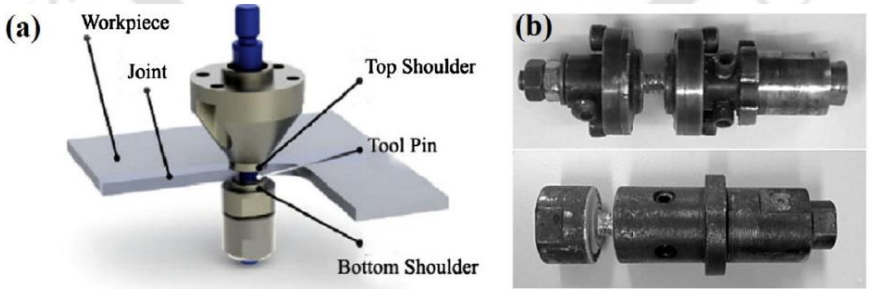

Figure 2.6 BTFSW process: (a) welding setup (With permission from Li et al., 2014b. Copyright Elsevier) (b) bobbin tools used (With permission from Sued et al., 2014. Copyright Elsevier)

2.2.4 Friction Stir Spot Welding (FSSW)

FSSW is basically conventional FSW without the tool traverse, i.e., the weld is made by the rotating tool at one spot only. It is extensively used as an alternative to riveting to help save weight. Sumitomo Light Metal Industries Ltd., Kawasaki Heavy Industries Ltd., Mazda, and Norsk Hydro

were among the first to adopt FSSW for spot welding (Pan et al., 2004; Gerlich et al., 2007). There are a few variants of FSSW to eliminate exit-hole left after retracting the pin and/or to increase bonding length. Some of these variants are summarized here.

2.2.4.1 Refill FSSW

This process was developed to eliminate the exit-hole left after FSSW. The process consists of three components: (i) a stationery clamp in the form of a ring, (ii) a rotating shoulder and (iii) a traversing pin (Pan et al., 2004; Schilling and dos Santos, 2004; Kumagai and Tanaka, 2001). Figure 2.7 shows the various steps involved in the welding process. First, the stationary clamping ring holds the overlapping workpiece, and the rotating shoulder along with the pin is plunged into the workpiece. The material expelled by the pin is confined by the shoulder. A dwell time is given after which the pin starts to retract, and the shoulder is moved downwards pushing the expelled material to fill the gap left after retracting the pin.

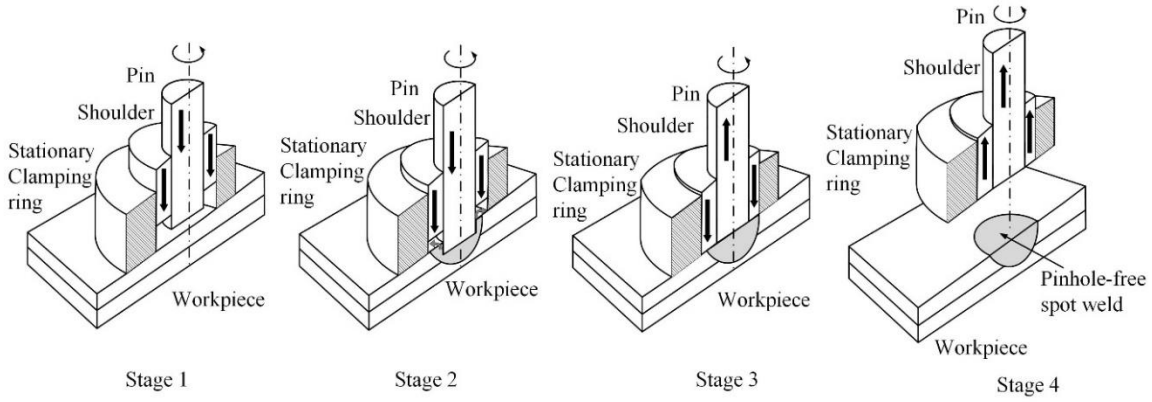

Figure 2.7 Schematic of refill FSSW process

2.2.4.2 Rotating Anvil FSSW (RAFSSW) and Double-sided FSSW:

Rotating anvil FSSW and double sided FSSW are both pin-less tool variants of FSSW to eliminate the problem of the exit-hole. RAFSSW is a one-sided FSSW process in which the rotating shoulder applies massive forging force on the workpiece supported by a stationary anvil. The sheet thickness that can be welded is, however, limited to 1 mm only. Double-sided FSSW is an improved variant of RAFSSW, which uses two flat shoulders on top as well as bottom of the workpiece (Figure 2.8). The bottom shoulder is called the rotating anvil in this case.

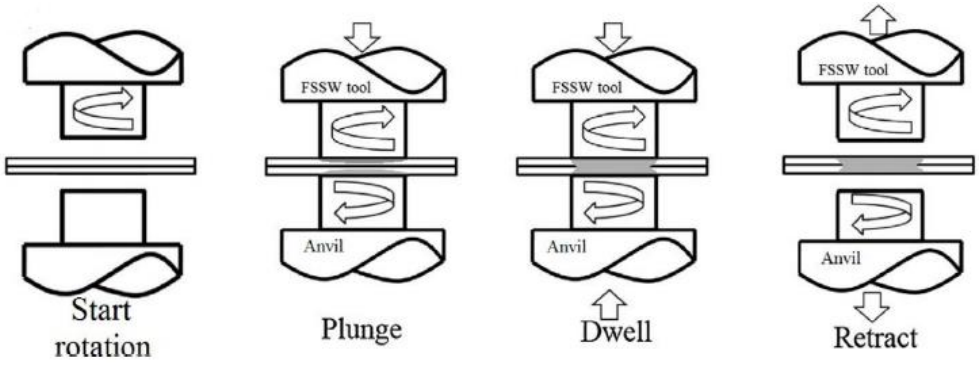

Figure 2.8 Schematic diagram of double sided FSSW (With permission from Padhy et al., 2018. Copyright Elsevier)

2.2.4.3 Short Traverse FSSW Processes:

In order to achieve larger joint area, the tool is traversed by a certain distance after FSSW, which results in higher strength. These processes can be classified as short traverse FSSW. They are usually of two types as shown in Figure 2.9. In stitch FSSW, the tool undergoes a short traverse to enhance the size of weld nugget. Figure 2.9a illustrates three sequential linear motions of the rotating tool. During motion 1, the tool plunges into the workpiece. During motion 2, tool traverses in the plane of workpiece and reaches a new spot. After a dwell of few seconds at the new spot, it retracts during motion 3. In the swing FSSW, the tool swings by a small angle about an axis perpendicular to the tool axis after a spot weld is created; this results in a short traverse of the tool by about 5 mm in the plane of the workpiece. These two processes are conveniently accomplished with the help of a robot. Due to elongated weld nugget, the strengths of stitch and swing FSSW are found to be higher than the strength of conventional FSSW welds (Tweedy et al., 2008; Buffa et al., 2008; Hunt et al., 2006; Okamoto et al., 2005; Padhy et al., 2018).

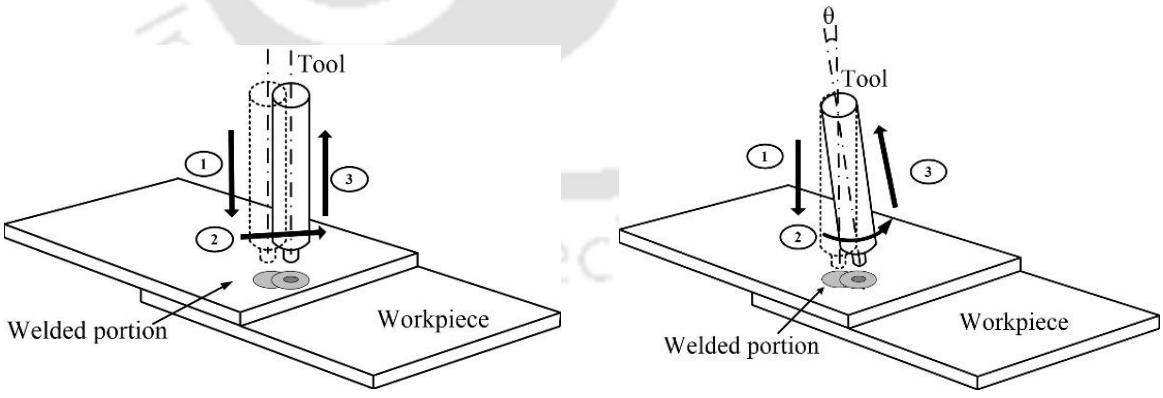

(a) (b)

Figure 2.9 Short traverse FSSW processes: (a) stitch (b) swing FSSW

2.2.5 Friction Stir Scribe (FSS)

When joining dissimilar materials with melting points of the materials differing by more than 20% and densities differing by more than 10%, conventional FSW process leads to unstable joining

(Padhy et al., 2018). There is a chance of the low melting point material flowing away from the bonding area. To overcome this problem, friction stir scribe welding has been developed that uses a specially designed tool for welding dissimilar materials in lap joint configuration. The tool is designed such that the tip of the pin has an added scribe cutter at an offset position from the axis of the tool (Justman, 2013; Upadhyay et al., 2017). Figure 2.10 shows the tool with scribe cutter and its use in the process.

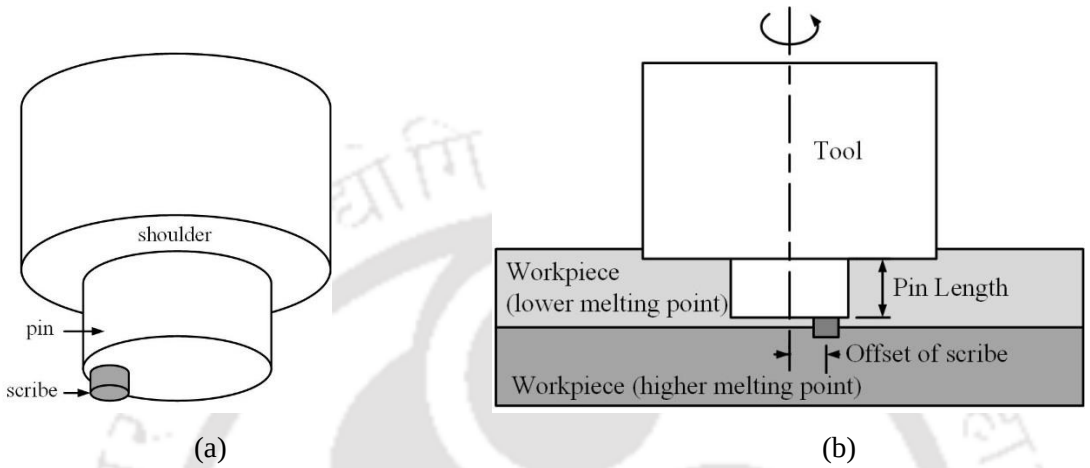

Figure 2.10 FSS process: (a) tool with scribe cutter (b) schematic of the process

During the welding process, the softer material is overlaid on the harder material and the rotating tool is plunged in the workpiece in such a way that the pin completely penetrates the upper sheet (material with low melting point) and the scribe cutter is inside the lower sheet (material with high melting point) by 0.1–1.0 mm depth. At the bottom sheet, the scribe cutter forms a special interlocking feature. The interlocking feature is filled by the plastic material extruded by the scribe from the top sheet (Hovanski et al., 2015), producing joints with higher lap shear strength.

2.2.6 Auxiliary Energy Assisted FSW Processes

For the plasticization of workpiece material ahead of the FSW tool, auxiliary sources of energy are also used to provide heat along with frictional energy. The use of auxiliary sources of energy helps in expanding the applicability of FSW to all types of materials, widening its commercial exploitation. There a number of auxiliary energy assisted process as listed in Table 2.2. These are electrically assisted FSW (Liu and Wu, 2016; Santos et al.,2014; Ferrando, 2012), induction assisted FSW (Oeystein,1999; Sinclair, 2010), laser assisted FSW (Palm, 2004; Kohn et al., 2002), arc assisted FSW (Joo, 2013; Kou and Cao, 2006), plasma assisted FSW (Yaduwanshi et al., 2014), hot gas stream assisted FSW (Lotfi and Nourouzi, 2014), gas torch assisted FSW (Choi et al., 2011), and ultrasonic assisted FSW (Siddiq and Sayed, 2012).

All the auxiliary energy assisted FSW techniques primarily aid in softening of the material during welding and hence reducing the mechanical forces on the tool and aiding material flow. This improves tool life and its performance leading to lower manufacturing costs. The welding speed

can also be seen to increase in all processes leading to productivity that is more efficient. Alvarez et al. (2014) observed an increase in welding speed from 100 to 200 mm/min due to application of IAFSW. A 30% reduction in plunge force and 35% reduction in welding force were also observed due to material softening. Thus, it can be seen that the use of auxiliary sources of energy can be beneficial in many aspects including increasing productivity and efficiency of the FSW process as well as improving tool life by reducing mechanical forces on the tool and its consequent wear. However, these studies are in their initial stages and require more research to develop into fully implemented commercial processes.

Table 2.2 Auxiliary energy assisted FSW processes

Type of auxiliary energy assisted FSW	References	Remarks
Electrically assisted FSW (EAFSW)	Liu et al., 2015; Santos et al.,2015; Ferrando, 2012	Softening takes place due to Joule heating as well as electro-plastic effect. The process needs an electrically conductive tool and/or workpiece. The technology is still in infancy.
Induction assisted FSW (IAFSW)	Oeystein,1999; Sinclair, 2010	It is a non-contact method of preheating that utilizes eddy currents induced by varying magnetic field for heating. Depth of heating can be controlled by frequency of supply current. It is effective with ferrous tool. Thermoplastic materials have been welded.
Laser assisted FSW (LAFSW)	Palm, 2004; Kohn et al., 2002	It is a non-contact type preheating by laser sources such as Nd:YAG fiber optical, diode or CO_2. Localized heating has better control on HAZ, but the process is not suitable for reflective workpieces. Equipment cost is also high.
Arc assisted FSW (AAFSW)	Joo, 2013; Kou and Cao, 2006	Mainly used in welding of dissimilar materials with a tungsten inert gas (TIG) arc offset towards the high melting point material to compensate for mismatch of melting points. It lacks precision, but equipment cost is low.
Plasma assisted FSW (PAFSW)	Yaduwanshi et al., 2014	The process is simple, economical and precise, but not as precise as LAFSW.

Hot gas stream assisted FSW (HGSFSW)	Lotfi and Nourouzi, 2014	It is preheating system that uses hot gas stream (e.g., nitrogen stream) ahead of the tool. Economic and energy audit of the process needs to be carried out to find out the efficacy.
Gas torch assisted FSW (GTAFSW)	Choi et al., 2011	A gas torch is used behind the FSW tool for welding high-carbon steel workpiece. This results in slower cooling rate after the welding and less martensite structures in the weld zone.
Ultrasonic assisted FSW (UAFSW)	Siddiq and Sayed, 2012	High frequency vibrations cause material softening without significant heating; it also needs less energy compared to thermal softening. Voids and tunnel defects are also suppressed by use of ultrasonic vibrations.

2.3 Material, Geometry and Life of FSW Tool

FSW tool is a critical component determining the formation of a successful joint. The heat generated during the FSW process is due to friction between the tool and the workpiece. A significant amount of axial force is applied by the tool on the workpiece. As such, the tool experiences severe stress and high temperatures, especially during welding of high strength alloys. The commercial application of FSW of titanium alloys, high strength steel and other hard alloys is limited by tool wear and short tool life. The tool material and design play a crucial role in determining its life and effective usage period.

2.3.1 Tool Material

The most commonly used FSW tools are made of high-speed steel used for welding of softer materials such as aluminium alloys, magnesium alloys or aluminium matrix composites (AMC) (Prado et al., 2003; Fernandez and Murr, 2004; Rajakumar et al., 2011). Some specially developed tool materials are discussed here.

2.3.1.1 Polycrystalline Cubic Boron Nitride (PcBN) Tools

For welding of high strength alloys such as steel and titanium, PcBN tools are preferred owing to its high temperature stability and high hardness and strength at elevated temperatures (Sato et al., 2009; Park et al., 2009). These tools also have low coefficient of friction that helps in producing smooth surface during welding. However, PcBN have low fracture toughness and are susceptible to breakage during initial plunging stage itself. It is reported to have maximum welding depth of 10 mm for steel and titanium alloys (Sorensen and Nelson, 2007). These tools are also costly to manufacture, which limits their commercial usage.

2.3.1.2 Tungsten based Tools

Tungsten has high strength at elevated temperature, which makes it suitable for use in FSW tools. However, it is brittle at ambient temperature owing to its low toughness resulting it high wear rate during welding of steel and titanium alloys. FSW tools were made using tungsten-rhenium alloys with 25% wt. Re with improved tool life (Khan et al., 2007). Weinberger et al. (2009) welded martensitic precipitation hardened steels using tungsten-rhenium alloy tool and produced good quality welds. The use of W-25% wt. Re alloys for FSW tool was recommended by Gan et al. (2007) since PcBN tools are brittle and boron from PcBN has a probability of getting dissolved into workpiece to produce undesirable phases. However, Re is an expensive material and limits the widespread use of tungsten-rhenium alloy tools. Tungsten carbide tools are a feasible alternative. WC has a hardness of ~1650 HV and its toughness of is also excellent. It is also insensitive to sudden temperature and load fluctuations during welding (Meran et al., 2007). The radial wear of pin was found to be significant as compared to shoulder wear and longitudinal pin wear. The radial pin wear initiated at the shoulder and increased down the length of the pin (Liu et al., 2005).

2.3.1.3 Other Tool Materials

Si_3N_4 is a great cutting tool and its low coefficient of thermal expansion, high hardness and high thermal conductivity makes it appropriate for FSW tool; it results in O and N contamination leading to formation of finer martensite. It also causes Si and N contamination of workpiece (Ohashi et al., 2009). This problem can be solved by coating Si_3N_4 tool with diamond or TiC, which improves its wear resistance. The use of Molybdenum based alloy tool has also been reported by Lienert et al. (2003) for welding AISI 1018 mild steel.

2.3.2 Tool Geometry

Tool geometry can affect the heat generation rate, torque, traverse force and the thermo-mechanical environment experienced by the tool. Apart from the traverse and rotational motion of the tool, flow of plasticized material in the workpiece is also affected by the tool geometry. It mostly constitutes the shoulder diameter, shoulder surface angle, profile in the shoulder surface and pin geometry.

2.3.2.1 Shoulder Diameter

The shoulder generates most of the heat and largely establishes the material flow field by gripping on the plasticized material. Heat is generated by both sliding and sticking friction whereas material flow takes place only due to sticking. Arora et al. (2011a) proposed an analytical model to determine the optimal shoulder diameter for minimizing the torque. The mechanical behaviour of FSW sheets like forming limit and springback can be modified to the betterment by controlling the shoulder diameter, along with other parameters like rotation speed, traverse speed and plunge depth (Ramulu et al., 2012; Ramulu et al., 2013; Katre et al., 2015).

2.3.2.2 Shoulder Surface

The shoulder surface plays an important role in determining FSW joint quality. Hirasawa et al. (2010) studied the effect of concave, convex and flat tool on joint quality. It was found that concave shoulder along with a triangular pin resulted in the highest strength spot welds. Microstructure and failure modes of the weld were also found to be significantly affected by the shoulder surface angle of the FSW tool (Lin et al., 2008). Cederqvist et al. (2009) studied the effect of different shoulder surfaces on weld quality, temperature generated and flash produced. The study was conducted on concave, convex and flat shoulder tool with and without scrolls/grooves on the shoulder face. It was found that minimum flash was produced by convex scrolled shoulder with no defects and good process stability. On the other hand, a concave shoulder tool resulted in medium flash with surface defects.

2.3.2.3 Pin Geometry

Numerous studies have pointed out that tool pin shape influences the plasticized material flow and the weld quality. Kumar and Kailas (2008) suggested that the shoulder of the tool caused the bulk material stirring while the pin facilitated the layer-by-layer movement of material around it. Different pin geometries are used to aid material flow in the workpiece, influence axial forces and produce welds with minimum defects. Figure 2.11 shows some of the different geometries of pin being used in FSW tool.

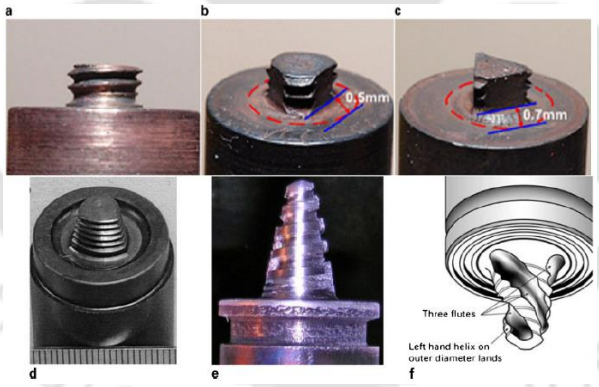

Figure 2.11 Pin geometries used in FSW tool: (a) cylindrical threaded; (b) three flat threaded (c) triangular (d) trivex (e) threaded conical (f) schematic of a triflute (With permission from Rai et al., 2011. Copyright Taylor & Francis)

Hirasawa et al. (2010) mentioned that a triangular or 'trifluted' pin causes higher material flow than that of a cylindrical pin. Threaded tools are being used to improve material flow around the tool. Zhao et al. (2005) used both plain and threaded columnar taper pins and observed that minimum defects were produced by tapered pin profile with screw thread during welding of AA2014. Colegrove and Shercliff (2004) studied the material flow using a triangular tool with convex surfaces called trivex tool. Comparisons were made with triflute tool, which revealed that triflute tool showed increase in the downward force due to its strong drilling action. On the other

hand, Buffa et al. (2006b) suggested increasing the pin angle to increase peak temperature during welding. A study by Ravi et al. (2018) revealed that square pin with flat shoulder is a good choice for FSSW of double-layered sandwich sheets made of Al6082-T6 and HDPE.

2.3.3 Tool Life

Tool life is an important aspect of any process that influences its commercial application. A longer tool life with minimal cost are preferred attributes of a commercially viable tool. Tool wear during FSW plays a significant role in determining the tool life as well as quality of weld produced during welding. Sparse studies conducted on FSW tool life indicate the significant role of diffusion and abrasion in causing the wear. Reaction of the tool with ambient oxygen in the atmosphere results in tool erosion. Thus, reactivity of the tool plays an important role in determining the tool life. The material flow during FSW is hampered by reduction in pin length or erosion of tool profile, which in turn increases welding defects (Bist et al., 2016).

Fernandez and Murr (2004) asserted that tool wear increased with rotation speed, whereas it decreased with increase in welding speed. Prado et al. (2003) showed that increase in tool rotation speed increases the tool wear that reaches maximum at around 1000 revolutions per minute. Further increase in rotational speed decreased the tool wear due to the increase in fluid like behaviour and turbulent material flow. It was also observed that tool wear is significant at the beginning of the welding that continues to decrease as the welding progresses and the tool attains a self-optimized shape, after which tool wear rate reduces. Thus, if the self-optimized shape is used as the initial pin shape the tool life could be increased. Prado et al. (2003) further argues against the need to used threaded pin, since the threaded pins continued to produce good quality welds even after the threads were eroded by tool wear.

It is observed that the tool failure mostly occurs at the pin; it suffers more wear and deformation as compared to the shoulder. The reasons for this are as follows:

(i) The pin is completely immersed in the workpiece and faces more resistance to its motion during welding.

(ii) Since maximum heat is generated at the shoulder-workpiece interface, resistance experienced by the shoulder is much less as compared to the pin.

(iii) The load bearing capabilities of the pin is much lower than the shoulder due to the high stresses from combination of bending and torsional stresses in the slender pin.

Gan et al. (2007) suggested use of harder, wear resistant material such as PcBN or WC for pin and relatively softer material for the shoulder of the tool. Although there has been significant

research in the development of cost effective and reusable tools following empirical approach, scientific procedures for tool design need to be developed.

2.4 FSW of Dissimilar Materials

The welding of dissimilar materials by fusion welding has always been a challenging task due to their chemical and metallurgical incompatibilities. As such during fusion welding of dissimilar materials, the weld region is significantly different from the base material. FSW has been effectively used for welding dissimilar materials by many industries (Luijendijk, 2000; Kasai et al., 2015; Cavaliere et al., 2009; DebRoy and Bhadeshia, 2010).

Material flow in dissimilar material is mainly of two types— (1) a vortex-like material flow where two materials are intermingled and (2) a flow with sharp interface between two materials, as shown in Figure 2.12. The vortex-like flow can be observed as fine intercalated lamellar microstructure with bands of the two dissimilar materials resulting in mechanical interlocking that improves joint properties. Vortex-like flow occurs when the two dissimilar metals possess similar flow stresses at the welding temperature (Fu et al., 2015). Vortex-like flow is also promoted by an increase in heat input (Song et al., 2014; Xue et al., 2011a, b; Derazkola et al., 2015). The second type of flow, i.e., sharp interface type, can be observed when melting points of two dissimilar materials differ considerably or an insufficient amount of heat is generated. It is characterized by lower joint strength. Sharp interfaces were observed by Lan et al. (2016) and Tanaka et al. (2015) in the welding of Al and steel. Wu et al. (2015) observed zigzag pattern at the interface in welding of Ti and Al. However, if sufficient amount of heat is generated by using high rotational speed and low traverse speed of the tool, materials with large difference in melting points can undergo vortex type material flow (Silva et al., 2011). The transition of one flow type to other also depends on the orientation of the plates to be joined. Fu et al. (2015) observed that placing Al on the AS, produced sharp interface flow, while placing Al on RS resulted in a vortex like flow at same process parameters.

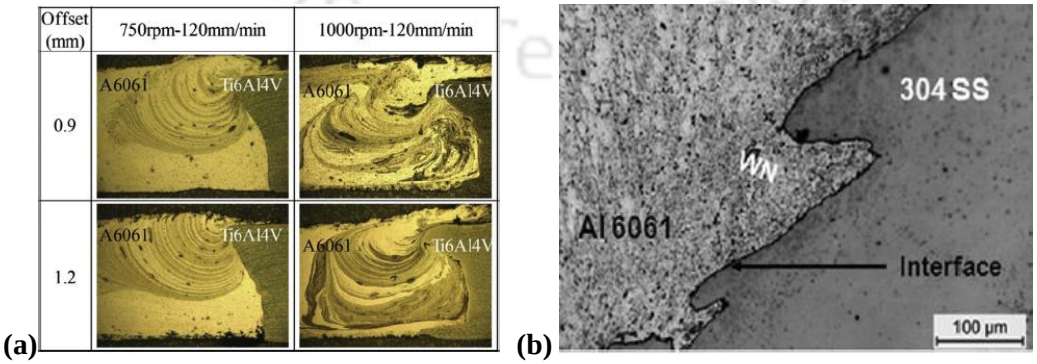

Figure 2.12 Flow in dissimilar metal welding: (a) vortex-like (With permission from Song et al., 2014. Copyright Elsevier) (b) sharp interface flow in Al-Steel joint (With permission from Ghosh et al., 2014. Copyright Springer Nature)

A few salient research efforts on dissimilar material welding using FSW have been described in Table 2.3. It summarizes the research effort of the following researchers: Simar and Avettand, 2017; Tanaka et al., 2009; Wu et al., 2015; Li et al., 2014; Kar et al., 2019; Firouzdor et al., 2010; Mofid et al., 2012; Zhao et al., 2015; Kasai et al., 2015; Aonuma et al., 2010; Galvao et al., 2011; Esmaeili et al., 2011; Tan et al., 2013; Park et al., 2010; Aval et al., 2011; Palanivel et al., 2013; Elangovan and Balasubramanian, 2007; Khan et al., 2017; Bahemmat et al., 2012; Silva et al., 2011; Guo et al., 2014; Gerard and Ehrstrom, 2004; Amancio-Filho et al., 2008; Cole et al., 2014. A notable work is by Li et al. (2014b). They designed a new butt weld configuration to weld Al and Ti as shown in Figure 2.13. The joint was designed such that the top surface of the Al sheet was 0.2 mm higher than the Ti sheet with tool offset towards the Al side. Plunge depth was given such that when the shoulder barely touches the Ti sheet, there is excess shoulder plunge on the Al side. This helped avoiding tool attrition and improved tool life. The design resulted in a weld joint with more than 92% tensile strength of the base Al alloy.

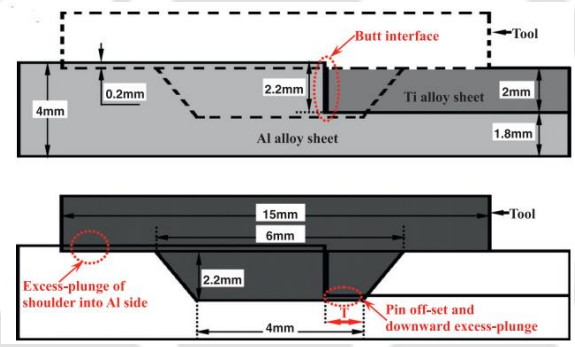

Figure 2.13 Modified butt weld configuration developed by Li et al., 2014a for Al-Ti FSW (With permission from Li et al., 2014. Copyright Elsevier)

Table 2.3 Dissimilar materials welded using FSW and their salient features

Type of dissimilar welding	Salient features
Al to steel	• A tool offset of 0.2 to 1.3 mm given towards the Al side produced better joints (Simar and Avettand, 2017). • Al should be placed on the RS to facilitate harder steel from AS to be dragged inside softer Al. • Based on the thickness of IMC (intermetallic compound) layer formed, Tanaka et al. (2009) suggested that the tensile strength was inversely proportional to heat input.
Al to Ti	• A tool offset of 0.6 to 0.9 mm towards the Al side was observed to produce good welds (Wu et al., 2015; Li et al., 2014). • Ti is placed on the AS. • In case of lap welding Ti is chosen as the lower sheet. • Critical IMCs formation in the weld can be minimized by using an interlayer material (E.g. Zn) at the interface of Al and Ti (Kar et al., 2019) thereby improving joint strength.
Al to Mg	• Mg on AS produced vortex like flow, while Mg on RS produced sharp interface; which in turn governed the tensile strength of the welds (Firouzdor et al., 2010).

	• Mofid et al. (2012) and Zhao et al. (2015) studied Al to Mg welding using underwater FSW and found that the process produced finer microstructure with lesser IMC formation.
Mg alloy to steel	• Kasai et al. (2015) observed increase in joint strength with increase in Al content in the Mg alloy. • Steel and pure Mg welding is not much widely studied since they form an immiscible system due to lack of reactivity.
Mg to Ti	• FSW of Mg to Ti have been studied in a few research works but mainly focused on the effect of alloying elements in Mg alloy. • Increase in percentage of Ca in AM60 alloy improved the weld strength (Aonuma et al., 2010).
Al to Cu	• Tool offset is given slightly towards Cu side (Galvao et al., 2011). • A low traverse speed of tool below 200 mm min^{-1} is suggested (Esmaeili et al., 2011; Tan et al., 2013)
5xxx to 6xxx aluminium alloys	• AA5086 with higher flow stress should be placed on the AS where more heat is generated (Park et al., 2010). • Aval et al. (2011) and Palanivel et al. (2013) observed tunnel defects at low rotational speed. High rotational speed results in turbulent flow of material in the SZ leading to defects and more flash generation (Elangovan and Balasubramanian, 2007). Thus, optimization is important. • 5xxx is more corrosion resistant and thus used in outer parts of ships, automobiles; while 6xxx gives better finish and used in inside parts (Khan et al., 2017).
2xxx to 7xxx aluminium alloys	• Highest peak temperature was observed on the AA2024-T4 side since it was placed on the AS side and more plastic work was done by the tool on it (Bahemmat et al., 2012). • Material flow type changed from sharp interface at 800 RPM to vortex type at 2000 RPM (Silva et al., 2011)
6xxx to 7xxx aluminium alloys	• Material mixing was found to be better when AA6061 was positioned on AS since harder AA7075 is difficult to move from the AS to RS due to its higher flow stress. (Guo et al., 2014). • However, most researchers suggest positioning the higher strength materials at AS for improved joint strength (Gerard and Ehrstrom, 2004; Amancio-Filho et al., 2008; Cole et al., 2014). • When tool offset was given towards AA7075, lower heat is generated on the softer AA6061 resulting in less coarsening of precipitates in HAZ of the softer material, improving joint strength. Thus, tool offset towards AA7075 is preferred (Cole et al., 2014)

2.5 Modelling of FSW Process

FSW involves combination of several physical phenomena like frictional heat due to tool-work surface interaction, heat due to large plastic deformation, dynamic microstructural evolution and material stirring (He et al., 2014). Multiple process parameters influence the quality of weld produced. The fine-tuning of these parameters helps in producing defect-free welds by controlling the heat input during welding. Modelling and simulation of the FSW process helps to choose the best process parameters without undergoing extensive experimental trials, making the FSW process economical and less time-consuming. Moreover, modelling of the process using various numerical methods and computational tools helps in understanding the process and improving it. Analysis and visualization of material flow, stress and strain evolution, residual stresses after welding and

temperature field in the cross-section during welding can be obtained easily by modelling (Neto and Neto, 2013). Modelling does not have the physical limitations of experimental observation; thus, it can be effective in the understanding of the effect of process parameters during welding. There has been a drastic improvement in the modelling of multiphysics problems, including FSW, in the recent years. However, the studies are limited and there is a requirement of further studies in the modelling of FSW process, especially for reducing simulation time. This section presents a literature review of different approaches taken for modelling of FSW and its future scope.

2.5.1 Basic Governing Equations of the Process

As discussed earlier, modelling is an important aspect of analysis of a process in order to gain understanding as well as for optimization of the process. Process modelling and optimization helps reduce expensive and time-consuming experiments. Two aspects should be modelled in FSW— plastic deformation and heat transfer. This subsection discusses both the aspects.

2.5.2 Modelling of Plastic Deformation

When a body undergoes plastic deformation, it retains the deformed configuration after removal of load and cannot go back to its original form. It is generally observed that for small deformation, a material behaves elastically at the initial stage and with further deformation, the material behaves plastically. A yield criterion is set to determine the end of elastic behavior and onset of plastic behavior. For continued further plastic deformation after (initial) yield point, additional stress is required suggesting that the yield condition keeps on changing with plastic deformation. This is known as strain hardening. A criterion for subsequent yielding is required for modelling the hardening behavior. Mathematically, yield criterion, in the form of a scalar function, is represented as

$$f(\sigma_{ij}) = 0, \tag{2.1}$$

where f is a yield function and σ_{ij} are Cauchy stress tensor components. Two commonly used yield criteria for representing material behavior in the context of FSW are von Mises and Tresca yield criteria (Dixit and Dixit, 2008). In solving plastic deformation problems, two strain hardenings laws are widely used— isotropic hardening and kinematic hardening. Figure 2.14 shows schematics of isotropic, kinematic and a combination of both, combined hardening. Detailed explanation of the hardening models can be found in Dixit and Dixit (2008).

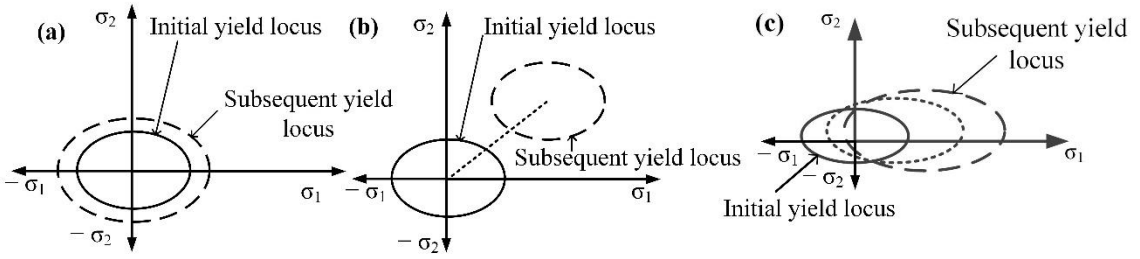

Figure 2.14 Hardening laws: (a) isotropic hardening (b) kinematic hardening (c) combined hardening

Two different approaches are taken when formulating the governing equations of a mathematical model for evaluating stresses, strains, displacement or other parameters. One is the Lagrangian approach, in which the region of analysis keeps changing continuously; the other is the Eulerian approach where analysis is performed in a fixed region of space. Eulerian formulation assumes a fixed space known as the control volume, where the entire analysis takes place. It is assumed that the deforming material flows through the control volume behaving like a non-Newtonian fluid. This approach is also referred to as flow formulation to imply the flowing nature of the deformed material. It is essential to compute the material boundary at each time increment, since material and element boundaries in Eulerian approach do not correspond to each other. Processes like rolling, wire drawing and extrusion that involve flow of material continuously through a control volume can be modelled using the Eulerian approach (Dixit and Dixit, 2008). The mesh in Eulerian approach never changes; therefore, there is no problem of excessive mesh distortion in processes with high plastic strains (Xu et al. 2001). However, this approach is not much suitable for modelling free boundary surfaces. The elemental and boundary nodes may not coincide and can be used only if the surface boundaries that are deformed are known (Priyadarshini et al., 2012). An impression of the tool shape needs to be created on the workpiece in order to implement this formulation in FSW because plunging stage cannot be modelled using Eulerian formulation. Eulerian formulation is not suitable for unsteady problems as well. Due to these disadvantages and difficulty in tracking surfaces and boundary conditions, a purely Eulerian approach for modelling FSW is rarely used.

In Lagrangian formulation the analysis is performed on a set of particles, which keep moving with the deformed material. The path of the particle is traced from the original configuration to the material's new deformed state. The primary variable in Lagrangian configuration can be incremental displacement as the deformation takes place incrementally with respect to time. This approach is generally used for processes like forging, deep drawing, or processes involving interaction of solid boundaries (Dixit and Dixit, 2008; Hossfeld and Roos, 2013). It is also easier to use boundary conditions in this approach. In this approach the material and element boundary coincide with each other (Lorrain et al., 2009). However, with large deformation, there is distortion and tangling of mesh leading to difficulty in convergence. Although Lagrangian approach requires

complex remeshing, its ability to model heat from friction at the contacting surface of tool and workpiece, material deformation in the workpiece and material flow makes it a suitable and widely used approach for modelling FSW process (Jain et al., 2018; Neto and Neto, 2013). The reference for the current deformed state can be set as the reference frame at $t = 0$ or the deformed configuration from previous state; the former is known as total Lagrangian formulation and the latter is known as the updated Lagrangian formulation (Dixit and Shufen, 2020). In the updated Lagrangian formulation, it is assumed that the deformations are finite. It is also assumed that solution at time t (previous state) is known for evaluation of unknown variables for the state at $t + \Delta t$. The following are the governing equations (Dixit and Dixit, 2008):

1. Incremental strain-displacement relations:

$$ {}_t\Delta\varepsilon_{ij}^{L} = \begin{cases} \ln({}_t\Delta\lambda_i) & \text{if } i = j \\ 0 & \text{if } i \neq j \end{cases}, \tag{2.2} $$

$$ {}_t\Delta U_{ij}^{2} = ({}_t\Delta F)_{ik}^{T}({}_t\Delta F)_{kj}, \tag{2.3} $$

$$ {}_t\Delta F_{ij} = \delta_{ij} + {}_t\Delta u_{i,j}, \tag{2.4} $$

where ${}_t\Delta\varepsilon_{ij}^{L}$ denotes incremental logarithmic strain, tensor caused by incremental displacement ${}_t\Delta u$ and ${}_t\Delta u_{i,j}$ represents the derivative of the incremental displacement with respect to position ${}^t x$. The incremental right stretch tensor ${}_t\Delta U$ is derived from the incremental deformation gradient tensor ${}_t\Delta F$ by its polar decomposition. The eigenvalues for the tensor ${}_t\Delta U$ are given by ${}_t\Delta\lambda_i$. The measure of finite deformation as well as rotation $\boldsymbol{F}$ is expressed as

$$ F_{ij} = \frac{\partial x_i}{\partial (x_0)_j} = x_{i,j}, \tag{2.5} $$

where $\boldsymbol{x_0}$ is the position vector at initial configuration. All the time-dependent variables are denoted with the subscript t.

2. Different stress-strain relations:

All materials follow different constitutive relations before and after yielding. The governing equations for most of the metals are given as

a. post yielding:

$$ {}_t\Delta\sigma_{ij} = \int_t^{t+\Delta t} {}^tC_{ijkl}^{EP}\,\mathrm{d}\left({}_t\Delta\varepsilon_{kl}^{L}\right) - \int_t^{t+\Delta t} {}^tC_{ijkl}^{EP}\,\alpha\delta_{kl}\,\mathrm{d}\left({}_t\Delta T\right), \tag{2.6} $$

where ${}^tC_{ijkl}^{EP}$ is a fourth-order tensor given by (Hsu, 2012)

$$ {}^tC_{ijkl}^{EP} = \frac{\left(\dfrac{2\nu}{1-2\nu}\right)G\delta_{kl}\delta_{ij} + 2G\delta_{ik}\delta_{jl} - \dfrac{9G^2}{2}\,{}^ts'_{ij}\,{}^ts'_{kl}}{\left({}^tH' + 3G\right){}^t\sigma_{eq}^2}, \tag{2.7} $$

and ${}^ts'_{ij}$ given by

$$ {}^ts'_{ij} = \begin{cases} {}^t\sigma'_{ij} & \text{for isotropic hardening} \\ {}^t\sigma'_{ij} - {}^t\alpha'_{ij} & \text{for kinematic hardening} \end{cases}, \tag{2.8} $$

and

$$ {}^t\sigma_{eq} = H\left({}^t\varepsilon_{eq}^{p}\right). \tag{2.9} $$

Further, ν is the Poisson's ratio, G is the modulus of rigidity, α is the coefficient of thermal expansion, ${}_t\Delta T$ is temperature rise at time t with respect to ambience.

b. Before yielding and after unloading:

$$ {}_t\Delta\sigma_{ij} = \int_t^{t+\Delta t} {}^tC_{ijkl}^{E}\,\mathrm{d}\left({}_t\Delta\varepsilon_{kl}^{L}\right) - \int_t^{t+\Delta t} {}^tC_{ijkl}^{E}\,\alpha\delta_{kl}\,\mathrm{d}\left({}_t\Delta T\right), \tag{2.10} $$

where

$$ {}^tC_{ijkl}^{E} = \left(\frac{2\nu}{1-2\nu}\right)G\delta_{kl}\delta_{ij} + 2G\delta_{ik}\delta_{jl}. \tag{2.11} $$

3. Updating scheme:

It is important to use the stress tensors in objective form to nullify the effect of rigid body rotation. The tensors are made objective by making them invariant with change in reference frame. In case of finite deformation in an updated Lagrangian formulation, the procedure to convert the stress tensor into objective is given as

$$ {}^{t+\Delta t}\sigma = \left({}_t\Delta R\right)\left({}^t\sigma\right)\left({}_t\Delta R\right)^{\mathrm{T}} + {}_t\Delta\sigma, \tag{2.12} $$

where ${}_t\Delta R$ represents a finite incremental form of rotation tensor.

4. Equilibrium equations:

$$\frac{\partial^{t+\Delta t}\sigma_{ij}}{\partial^{t+\Delta t}x_j} = 0, \tag{2.13}$$

where ${}^{t+\Delta t}\sigma_{ij}$ and ${}^{t+\Delta t}x_j$ are stress tensor components and position vectors, respectively, at updated time.

Both Eulerian and Lagrangian approaches have their own advantages and disadvantages. There have been efforts to combine the advantages of the two formulations in a single approach. Arbitrary Lagrangian-Eulerian (ALE) is one such formulation that takes advantage of the two formulations in the same part mesh. As seen in Figure 2.15, in case of Lagrangian formulation the mesh gets distorted after deformation. In case of Eulerian approach, material moves through the mesh as the workpiece gets deformed while the mesh stays fixed in its position. In case of ALE, the mesh adjusts according to the deformed body such that uniformity of mesh is maintained while deformation of the body takes place. ALE consists of two phases – Lagrangian phase and Eulerian phase, connected by some convective terms. In ALE, instead of material configuration, motion is described by the reference configuration as in Lagrangian formulation, and spatial configuration as in Eulerian formulation. The mesh and material movements are identical in Lagrangian phase, while in the Eulerian phase, the mesh undergoes an arbitrary motion independent of material motion while keeping the mesh undistorted. The approach involves analyzing each time step by Lagrangian phase until convergence, followed by application of Eulerian phase to keep mesh configuration undistorted. All the dependent variables (stress, strain etc.) are convected through the Eulerian phase since there is relative displacement between material and mesh.

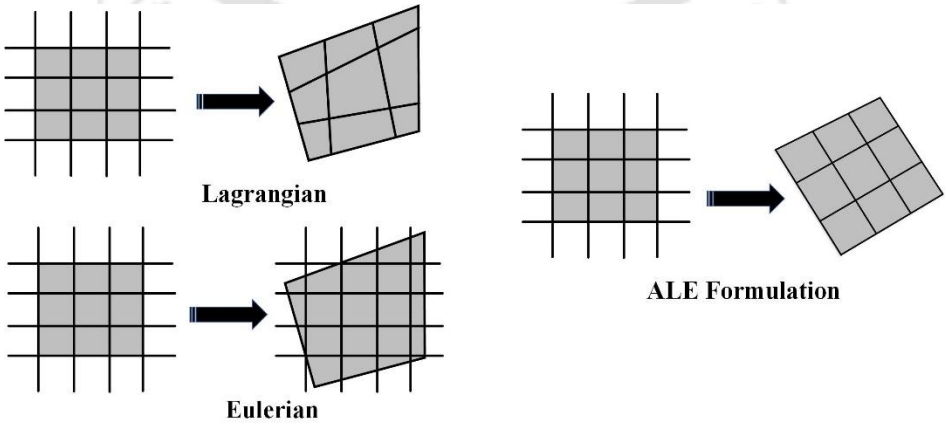

Figure 2.15 Graphical representation of Lagrangian, Eulerian and ALE formulations (shaded portion is material)

There are three domains in ALE formulation: material Ω_0, spatial Ω and reference or ALE domain $\hat{\Omega}$. The transformation equations mapping the domain are (Khoei et al., 2003)

$$\boldsymbol{x} = \boldsymbol{x}(\boldsymbol{X}, t), \quad \boldsymbol{x} = \boldsymbol{x}(\boldsymbol{\chi}, t), \tag{2.14}$$

which give spatial position of material point $\boldsymbol{X}$ and grid point $\boldsymbol{\chi}$, respectively. The relative motion between the mesh and material defined as convective velocity is

$$\boldsymbol{c} = \boldsymbol{v} - \hat{\boldsymbol{v}}, \tag{2.15}$$

where $\hat{\boldsymbol{v}}$ is the mesh velocity and $\boldsymbol{v}$ is the material velocity. Similarly, acceleration $\boldsymbol{a}$ is

$$\boldsymbol{a} = \left.\frac{\partial \boldsymbol{v}}{\partial t}\right|_{x} = \left.\frac{\partial \boldsymbol{v}}{\partial t}\right|_{\chi} + (\nabla \boldsymbol{v})\boldsymbol{c} \equiv \left.\frac{\partial \boldsymbol{v}}{\partial t}\right|_{\chi} + (\boldsymbol{c} \bullet \nabla)\boldsymbol{v}, \tag{2.16}$$

where $\left.\frac{\partial v}{\partial t}\right|_{\chi}$ is called the local acceleration and $(\nabla \boldsymbol{v})\boldsymbol{c}$ is called the convective acceleration; $\nabla \boldsymbol{v}$ is the spatial gradient of velocity. Using $\boldsymbol{a}$ from Eq. (2.16) and substituting in momentum equation in Lagrangian formulation gives

$$\sigma_{ji,j} + \rho b_i = \rho a_i \equiv \rho \left.\frac{\partial v_i}{\partial t}\right|_{\chi} + \rho c_j v_{i,j}, \tag{2.17}$$

where $\boldsymbol{b}$ is the body force per unit mass, $\boldsymbol{\sigma}$ is the Cauchy stress and ρ is the density. Assuming that loads are applied slowly and inertia forces are much smaller, acceleration can be omitted which results in the equilibrium equation expressed as

$$\sigma_{ji,j} + \rho b_i = 0. \tag{2.18}$$

Equation (2.18) is common for Lagrangian, Eulerian and ALE formulations as there are no convective terms in the equation.

The material rate of stress in nonlinear solid mechanics is dependent on current state of stress and deformation history. A convective term is added for the relation between material and reference rate of stresses as

$$\left.\frac{\partial \boldsymbol{\sigma}}{\partial t}\right|_{x} = \left.\frac{\partial \boldsymbol{\sigma}}{\partial t}\right|_{\chi} + (\boldsymbol{c} \bullet \nabla)\boldsymbol{\sigma}. \tag{2.19}$$

This approach helps to reduce element distortion in parts undergoing large deformations (Lorrain et al., 2009). Some amount of mesh distortion still occurs in the tool which can be solved by using adaptive remeshing tools (Grujicic et al., 2010). ALE has been used to model temperature

distribution, material flow and residual stresses in friction stir welded joints (Buffa et al., 2009; Trimble et al., 2012).

Another approach that takes advantage of the combination of strengths of Eulerian and Lagrangian approaches is the coupled Eulerian-Lagrangian (CEL) formulation. In CEL approach, the body undergoing large deformation is meshed exclusively with Eulerian element and the stiffer body is meshed exclusively using Lagrangian elements. In case of FSW, the tool is meshed using Lagrangian elements while the workpiece is meshed using Eulerian elements. The kinematic constraint for Eulerian calculation is implemented by using the velocity of the Lagrangian boundary. On the other hand, surface forces on the Lagrangian domain is calculated using stresses within the Eulerian cell (Benson, 1992, 1997; Brown et al., 2002). In addition to the advantages of ALE, CEL approach can simulate void formation and defects in FSW (Al-Badour et al., 2013). However, this approach is not widely used since it requires very powerful computational facility (Malik et al., 2014). For more details on the CEL approach, the article by Skrzat (2012) may be referred. A comparison of the formulations is summarized briefly in Table 2.4.

Table 2.4 Salient points of formulations for modelling FSW

Formulation	Salient points
Eulerian approach	• Assumes fixed control volume for analysis • Capable of simulating material flow • Material and element boundaries do not correspond to each other
Lagrangian approach	• Position of particle under analysis keeps changing with deformation • Can simulate material flow, heat developed due to friction and material deformation • In case of severe deformation, frequent complex remeshing is required
ALE approach	• Combines advantages of Eulerian and Lagrangian approaches • Mesh adjusts according to the deformed body such that uniformity of mesh is maintained • Element distortion is reduced for parts undergoing severe plastic deformation
CEL approach	• Tool is formulated using Lagrangian approach, while the work piece is formulated using Eulerian approach • Combines advantages of Lagrangian and Eulerian formulations. No problem of mesh distortion • High computation cost

2.5.3 Thermal Modelling

The thermal history of a welding process determines the thermal stresses and microstructure, which leads to determination of the strength, hardness, fatigue behavior and elongation of the joined product. As such, modeling of heat source is an important aspect and the basics of modelling conduction in moving heat source is briefly described in this section. A detailed section on thermal modelling of FSW process is provided later.

The convective diffusion equation is

$$\frac{\partial \rho u}{\partial t} + \frac{\partial \rho h V}{\partial x} = \nabla \cdot (k \nabla T) + \dot{q}, \tag{2.20}$$

where ρ represents density, k is the conductivity, u is the internal energy, h is the enthalpy, $\dot{q}$ is volumetric heat source, V is the speed of heat source and T is the temperature. The tool is considered stationary. The velocity of the moving workpiece is in x direction, y lies on the plane of workpiece top surface perpendicular to x, and z is perpendicular to the workpiece top surface (Figure 2.16).

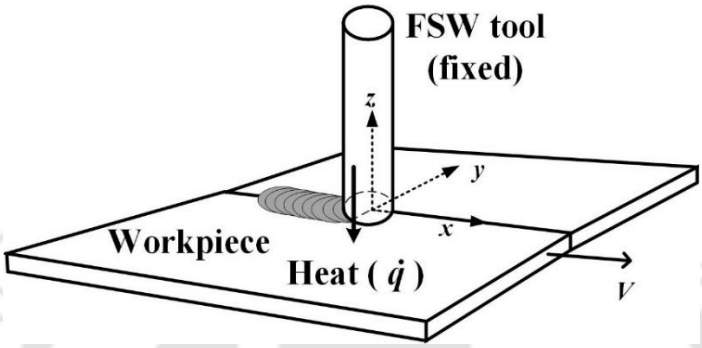

Figure 2.16 Reference frame for heat transfer during welding

If $V = 0$, and $du = C_v dT$, Eq. (2.20) becomes

$$C_v \frac{\partial \rho T}{\partial t} = \nabla \cdot (k \nabla T) + \dot{q}, \tag{2.21}$$

where C_v is the heat capacity. Using the continuity equation, the steady state equation for constant velocity V can be expressed as (Cengel and Boles, 2007)

$$\frac{\partial \rho}{\partial t} + \frac{\partial \rho V}{\partial x} = 0. \tag{2.22}$$

Further considering $du = dh = C_v dT$, as there is no significant volumetric expansion, Eq. (2.21) becomes (Van Elsen et al., 2007)

$$\rho C_v(T) V \frac{\partial T}{\partial x} = \nabla \cdot \{k(T) \nabla T\} + \dot{q}\,. \tag{2.23}$$

The temperature distribution due to a moving point heat source was given by Carslaw and Jaeger (1959) as

$$T = T_0 + \frac{P_L}{4\pi k R} \exp\{-V(R + x)/2\kappa\}, \tag{2.24}$$

where T_0 represents ambient temperature, P_L applied power, R distance from the source of heat where $\left(R^2 = x^2 + y^2 + z^2\right)$ and κ is the thermal diffusivity. The axis x is considered to be along the heat source velocity, y is on the plane of workpiece top surface and perpendicular to x, and z is

also perpendicular to x along the thickness. However, in case of FSW, the equation has to be modified to account for the heat source being non-uniform.

2.5.4 Analytical Modelling of FSW

Analytical modelling of FSW includes mathematical expressions that help in understanding the process better by arriving at relationship between different parameters (tool dimensions, process parameters etc.) and related outputs (heat generated, torque produced etc.) involved during welding. Since FSW is a complex multiphysics problem with transient nature, there has been very few analytical studies on the process. The analytical modelling of FSW has been limited to its thermal aspect only, dealing mainly with heat generation during welding and corresponding temperature distribution. Modelling of material flow, mechanical properties, defects and residual stresses have been undertaken using numerical approach which will be discussed in the next section. Some significant works on analytical modelling of FSW are discussed in this section.

Frigaard et al. (1998) was among the first to describe an analytical approach for calculating the heat generated during FSW. The heat generated was expressed as a function of axial load and torque required. The torque applicable on the tool during rotation is given by

$$M = \int_0^R \mu P 2\pi r^2 \mathrm{d}r = \frac{2}{3}\mu\pi P R^3, \tag{2.25}$$

where M is the torque required, P is the axial pressure assumed to be constant, μ is the Coulomb's coefficient of friction between the FSW tool and workpiece and R denotes tool radius. A differential ring-shaped area of width dr on the circular tool is considered at a distance r from the centre of the tool. It is assumed that all the shear work is converted into heat. The average rate of heat generation per unit area is given by

$$q_0 = \int_0^R \omega \mu P 2\pi r^2 \mathrm{d}r, \tag{2.26}$$

where ω is the angular velocity in rad/s. If the tool rotates at N revolutions per second (rps), then $\omega = 2\pi N$ and

$$q_0 = \int_0^R 4\pi^2 \mu P N r^2 \mathrm{d}r = \frac{4}{3}\pi^2 \mu P N R^3, \tag{2.27}$$

Frigaard et al. (1998) considered the tool to be a flat shoulder pinless tool, thus ignored the contribution from the pin in heat generation. Schmidt et al. (2003) considered the contributions in heat generation from different parts of tool separately. The schematic diagram of the FSW tool with its different parts is shown in Figure 2.17a. The tool has a shoulder radius of R_{sh}, pin radius of R_{pin}, pin height of H_{pin} and cone angle of α. The cone angle is the angle made by the concave shoulder surface with the horizontal.

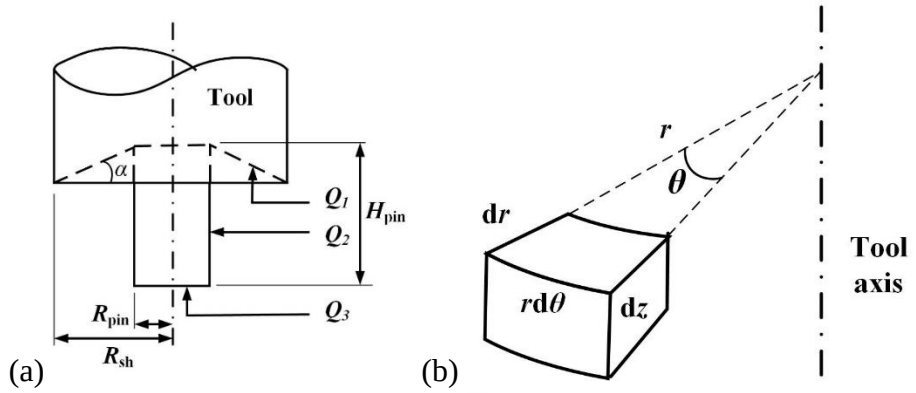

Figure 2.17 Diagram of an FSW tool (a) with contributions to heat generation by different parts of the tool (b) infinitesimal element on the tool (Drawn based on explanations of Schmidt et al., 2003)

The total heat produced by the tool is the summation of contributions of the shoulder portion Q_1, pin side Q_2, pin bottom Q_3 as

$$Q_{total} = Q_1 + Q_2 + Q_3. \tag{2.28}$$

The mechanical power input is converted into heat generated at the tool as per the following relation:

$$\mathrm{d}Q = \omega r \tau_{contact} \mathrm{d}A, \tag{2.29}$$

where r is the radius at which a differential area dA exists with contact shear stress of $\tau_{contact}$. The differential area is calculated for each portion by considering an element of height dz, width dr in the radial direction subtending an angle θ at the centre and of length $r\mathrm{d}\theta$ in the circumferential direction. (Figure 2.17b). Using Eq. (2.29), dQ is integrated over the entire surfaces to arrive at the different heat contributions expressed as

$$Q_1 = \int_0^{2\pi}\int_{R_{pin}}^{R_{sh}} \omega \tau_{contact} r^2 (1+\tan\alpha)\mathrm{d}r\mathrm{d}\theta = \frac{2}{3}\pi\tau_{contact}\omega\left({R_{sh}}^3 - {R_{pin}}^3\right)(1+\tan\alpha), \tag{2.30}$$

$$Q_2 = \int_0^{2\pi}\int_0^{H_{pin}} \omega \tau_{contact} {R_{pin}}^2 \mathrm{d}z\mathrm{d}\theta = 2\pi\tau_{contact}\omega {R_{pin}}^2 H_{pin}, \tag{2.31}$$

$$Q_3 = \int_0^{2\pi}\int_0^{R_{pin}} \omega \tau_{contact} r^2 \mathrm{d}r\mathrm{d}\theta = \frac{2}{3}\pi\tau_{contact}\omega {R_{pin}}^3. \tag{2.32}$$

From Eq. (2.28)

$$Q_{total} = \frac{2}{3}\pi\tau_{contact}\omega\left\{\left({R_{sh}}^3 - {R_{pin}}^3\right)(1+\tan\alpha) + {R_{pin}}^3 + 3{R_{pin}}^2 H_{pin}\right\}. \tag{2.33}$$

For a flat shoulder tool (α = 0), which simplifies Eq. (2.33) to arrive at

$$Q_{total} = \frac{2}{3}\pi\tau_{contact}\omega\left(R_{sh}{}^{3} + 3R_{pin}{}^{2}H_{pin}\right). \quad \textbf{(2.34)}$$

However, while considering the force and torque on the inclined shoulder surface, Schmidt et al. (2003) split up the contributions from projected vertical and horizontal areas of the inclined area. Perhaps a more accurate approach would have been to consider the area of the inclined plane for force and torque calculations. This aspect needs more investigation. Depending on the surface interaction condition, $\tau_{contact}$ varies as follows:

(a) *Sticking condition*

By using von Mises criterion,

$$\tau_{contact} = \tau_{yield} = \frac{\sigma_{yield}}{\sqrt{3}}. \quad \textbf{(2.35)}$$

From Eq. (2.33)

$$Q_{total} = \frac{2}{3}\pi\frac{\sigma_{yield}}{\sqrt{3}}\omega\left\{\left(R_{sh}{}^{3} - R_{pin}{}^{3}\right)\left(1+\tan\alpha\right) + R_{pin}{}^{3} + 3R_{pin}{}^{2}H_{pin}\right\}. \quad \textbf{(2.36)}$$

(b) *Sliding condition*

$$\tau_{contact} = \tau_{friction} = \mu p, \quad \textbf{(2.37)}$$

where p denotes the axial contact pressure. From Eq. (2.33) using Eq. (2.37)

$$Q_{total} = \frac{2}{3}\pi\mu p\omega\left\{\left(R_{sh}{}^{3} - R_{pin}{}^{3}\right)\left(1+\tan\alpha\right) + R_{pin}{}^{3} + 3R_{pin}{}^{2}H_{pin}\right\}. \quad \textbf{(2.38)}$$

Considering a flat tool (α = 0) and $p = \frac{F}{A_{projected}}$, where $A_{projected} = \pi R_{sh}{}^{2}$ is the projected area where pressure is applicable; Eq. (2.38) can be further simplified as

$$Q_{total} = \frac{2}{3}\mu F\omega\left(R_{sh} + 3\frac{R_{pin}{}^{2}H_{pin}}{R_{sh}{}^{2}}\right). \quad \textbf{(2.39)}$$

Equation (2.39) is similar to Eq.(2.27) obtained by Frigaard et al. (1998). However, it shows a directly proportional relationship between Q and F, which is experimentally found to be not true in case of FSW. Thus, sliding friction model alone does not give the true nature of the problem.

(c) *Partial sticking/sliding condition*

In this condition, the interaction may not be purely sticking or sliding. A variable δ is defined as

$$\delta = \frac{v_{mat}}{v_{tool}} = 1 - \frac{\dot{\gamma}}{v_{tool}}, \tag{2.40}$$

$$\dot{\gamma} = v_{tool} - v_{mat}, \tag{2.41}$$

where $\dot{\gamma}$ is the slip rate, v_{mat} is the velocity of the material under the tool, v_{tool} is the position dependent tangential velocity of the tool. $\delta = 1$ implies sticking condition and $\delta = 0$ implies sliding condition. $0 < \delta < 1$ implies partial sticking/sliding condition. Combining Eq. (2.36) and Eq. (2.38) we get

$$\begin{aligned} Q_{total} &= \delta Q_{total,sticking} + (1-\delta) Q_{total,sliding} \\ &= \frac{2}{3}\pi\left(\delta\tau_{yield} + (1-\delta)\mu p\right)\omega\left\{\left(R_{sh}{}^{3} - R_{pin}{}^{3}\right)(1+\tan\alpha) + R_{pin}{}^{3} + 3R_{pin}{}^{2}H_{pin}\right\}. \end{aligned} \tag{2.42}$$

Mijajlovic et al. (2012) proposed heat transfer efficiency η_Q as opposed to 100% conversion efficiency considered by Schmidt et al. (2004) and gave heat generation as

$$Q_{generated} = \eta_Q P, \tag{2.43}$$

where P is the mechanical power and $Q_{generated}$ is the heat generated by the tool the typical value of η_Q varies from 0.6 to 1. A median value of 0.865 for the complete weld cycle and 0.9 for the welding stage was obtained during the study.

Based on Schmidt et al. (2003) work, Salimi et al. (2016) developed a mathematical relation to calculate the temperature distribution in the weld zone. Heat flux generated beneath the shoulder q_1, pin side q_2 and pin bottom surface q_3 were given as

$$q_1 = \omega r \tau_c, \tag{2.44}$$

$$q_2 = \omega R_{pin} \tau_c, \tag{2.45}$$

$$q_3 = \omega r \tau_c, \tag{2.46}$$

where τ_c represents equivalent shear stress, which depends on the contact condition. The temperature field is described by heat conduction equation. Although Salimi et al. (2016) nicely described the heat conduction phenomenon but their expressions for rate of heat generation per unit volume denoted by the function $g(x, y, z, t)$ were mathematically not correct. Here, the correct expressions are provided using Dirac delta function. Dirac delta function converts heat flux into

heat per unit volume. Assuming that there are four heat flux sources, the function g is split into four parts, i.e.,

$$g(x,y,z,t) = g_1(x,y,z,t) + g_2(x,y,z,t) + g_3(x,y,z,t) + g_4(x,y,z,t). \quad \textbf{(2.47)}$$

Thus, FSW tool is considered to be a three dimensional non-uniform moving heat source that supplies has three heat sources; the rate of heat generation by i^{th} sources is $g_i(x, y, z, t)$. Expressions for rate of heat supplied due to rubbing of the shoulder on the top surface of the plates is given as

$$g_1(x,y,z,t) = \begin{cases} \omega r \tau_c \delta(z-h) & \left(\bar{x}(t) - \sqrt{R_{sh}^2 - (y-\bar{y}(t))^2}\right) < x < \left(\bar{x}(t) + \sqrt{R_{sh}^2 - (y-\bar{y}(t))^2}\right), \\ & \left(\bar{y}(t) - R_{sh}\right) < y < \left(\bar{y}(t) + R_{sh}\right); \\ 0 & \text{otherwise,} \end{cases} \quad \textbf{(2.48)}$$

where $\delta(\cdot)$ is the delta function of Dirac, and centres of tool are denoted by $\bar{x}(t)$ and $\bar{y}(t)$. However, expression given by Eq. (2.48) gives non-zero heat in the shoulder area where there is pin and consequently no heat generation. To nullify it, negative heat generation is taken at that portion. Thus,

$$g_2(x,y,z,t) = \begin{cases} \omega r \tau_c \delta(z-h) & \left(\bar{x}(t) - \sqrt{R_{pin}^2 - (y-\bar{y}(t))^2}\right) < x < \left(\bar{x}(t) + \sqrt{R_{pin}^2 - (y-\bar{y}(t))^2}\right), \\ & \left(\bar{y}(t) - R_{pin}\right) < y < \left(\bar{y}(t) + R_{pin}\right); \\ 0 & \text{otherwise.} \end{cases} \quad \textbf{(2.49)}$$

To take into account the heat due to rubbing of pin bottom surface, the expression $g_3(x, y, z, t)$ is given as

$$g_3(x,y,z,t) = \begin{cases} \omega r \tau_c \delta\left(z-h+H_{pin}\right) & \left(\bar{x}(t) - \sqrt{R_{pin}^2 - (y-\bar{y}(t))^2}\right) < x < \left(\bar{x}(t) + \sqrt{R_{pin}^2 - (y-\bar{y}(t))^2}\right), \\ & \left(\bar{y}(t) - R_{pin}\right) < y < \left(\bar{y}(t) + R_{pin}\right); \\ 0 & \text{otherwise,} \end{cases} \quad \textbf{(2.50)}$$

where H_{pin} is the pin length. Finally, heat generation from cylindrical surface of the pin is accounted for by the following expression:

$$g_4(x,y,z,t) = \begin{cases} \omega r \tau_c \ \delta\left(\sqrt{\left(x-\bar{x}(t)\right)^2+\left(y-\bar{y}(t)\right)^2}-R_{pin}\right) & \left(h-H_{pin}\right)<z<h, \\ 0 & \text{otherwise.} \end{cases} \quad \textbf{(2.51)}$$

These expressions are for zero plunge depth, i.e., the shoulder just touches the top surface of the plates. If there is some plunge depth, the aforesaid expressions will get modified slightly. With x_0 and y_0 as the initiation points and *v* as the welding speed

$$\bar{x}(t) = x_0 + vt, \quad \textbf{(2.52)}$$

$$\bar{y}(t) = y_0 . \quad \textbf{(2.53)}$$

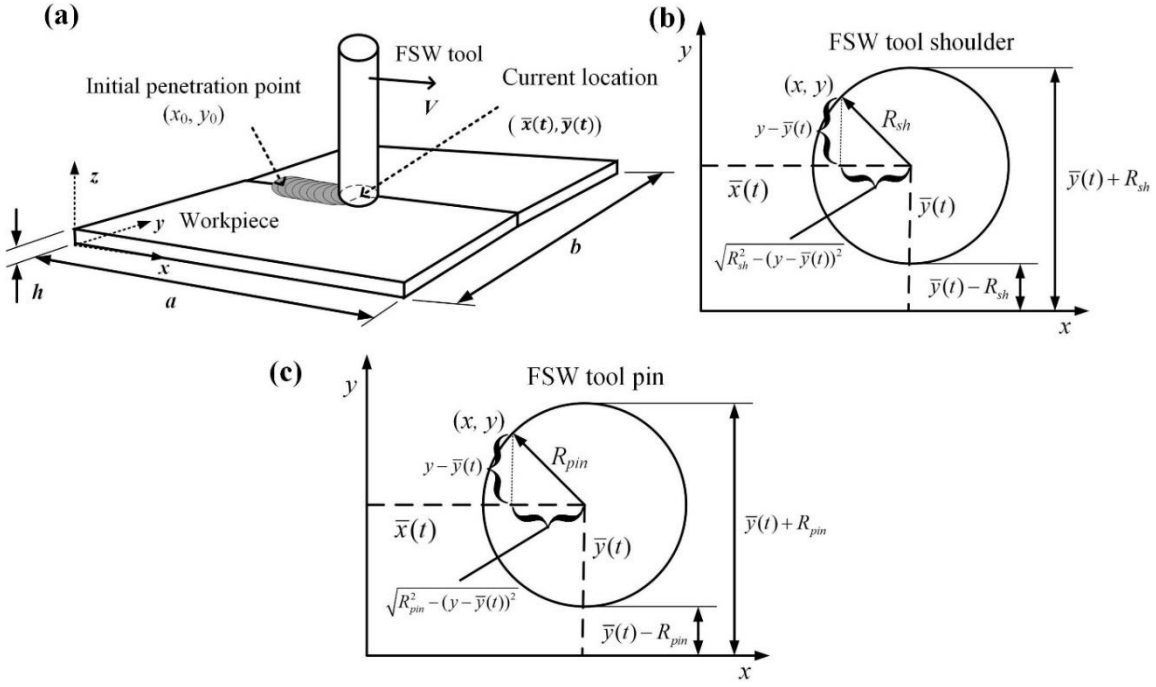

Figure 2.18 Coordinate system used by Salimi et al. (2016) for describing 3D heat flux during FSW: (a) initial position and current position of tool, workpiece dimensions (b) FSW tool shoulder (c) FSW tool pin

The boundary conditions used to solve the heat conduction equation are:

$$T_i = T(x,y,z,0) = 25\ ^\circ\text{C}, \quad \textbf{(2.54)}$$

$$\frac{\partial T(a,y,z,t)}{\partial x} = \frac{\partial T(0,y,z,t)}{\partial x} = 0, \quad \textbf{(2.55)}$$

$$\frac{\partial T(x,b,z,t)}{\partial y} = \frac{\partial T(x,0,z,t)}{\partial y} = 0, \quad \textbf{(2.56)}$$

$$k\frac{\partial T(x,y,h,t)}{\partial z} = h_1\left[T_1 - T(x,y,h,t)\right], \quad \textbf{(2.57)}$$

$$k\frac{\partial T(x,y,0,t)}{\partial z} = -h_0\left[T_0 - T(x,y,0,t)\right], \quad \textbf{(2.58)}$$

where h_0 is the coefficient of convective heat transfer for heat interaction of the workpiece and the backing plate considering equivalent amount of heat transfer through conduction, T_1 is the ambient temperature, T_0 is the workpiece temperature on the surface and h_1 is the heat transfer coefficient. On the other hand, T_i is the initial temperature. The length of the workpiece is considered as a, the width is considered as b and the thickness as h (Figure 2.18). For the complete solution, the work of Salimi et al. (2016) may be referred.

2.5.5 Numerical Modelling

Numerical modelling of the FSW process is carried out to improve the understanding of the technology. Numerical simulations help in capturing the complex nature of the process by including different aspects like thermal aspects, thermo-mechanical aspects, contact conditions and material behavior in a single problem. The computational models are especially helpful in visualizing material flow, temperature distribution, stress and strain evolution during the FSW process. Most of the numerical approaches use finite element method (FEM) for modelling. Different commercially available codes are used nowadays for numerical simulation which are based on FEM. A brief introduction to FEM is given in the next section followed by its implementation into FSW modelling for thermal, material flow and mechanical properties analysis. An introduction to cellular automata finite element (CAFE) is also given, which is gaining popularity for predicting microstructure evolution during FSW.

2.5.5.1 Basics of Finite Element Modelling

A method used to numerically solve differential as well as integral equations by discretizing a body into small finite elements is referred to as FEM. The method is useful for numerically solving both ordinary and partial differential equations. The solution is arrived at by assuming a piecewise continuous function and obtaining parameters of the function such that error in the solution reduces. It can be applied to solve physical problems when the governing equations of the physical

phenomenon are available. The steps involved in FEM are: (i) pre-processing that involves mesh generation (ii) obtaining the assembled system of equations, for which the elemental matrices and vectors are to be evaluated (iii) determining the boundary conditions and applying them (iv) the system of equations is solved (v) post processing. Finite difference approximation is taken for solving time-dependent problems by treating the derivative with time (Dixit, 2009).

In FEM, the continuum body is discretized into subdivisions called finite elements that are connected to each other via joints called nodes/nodal points. The field variables (e.g., displacement, temperature, stress etc.) are approximated using a simple function (approximating function or interpolation models). The approximating functions are defined using the nodal field variables. A polynomial form is considered for the solution or interpolation model. The new unknowns in the field equations for the whole continuum, will be values of the field variables at the nodes. After solving the set of finite element equations, the nodal field variables will be known which will lead to approximation of the field variables in the whole continuum. Since, a complicated physical problem is converted to a simpler problem, only an approximate solution is obtained. However, the approximate solution can be refined and improved by reducing the error by using more computational efforts. The method is explained with a following simple example.

A linear differential equation can be represented as

$$L\boldsymbol{u} + \boldsymbol{q} = 0, \tag{2.59}$$

where $\boldsymbol{u}$ is the vector of primary variables of the problem as a function of the coordinates, $\boldsymbol{q}$ is the vector of known functions and L represents a differential operator. The differential equation is subjected to natural and essential boundary conditions. The conditions that are sufficient for completely solving a differential equation are called essential boundary conditions. However, the natural boundary conditions contain higher order derivatives and cannot solve the differential equation completely. For example, considering the differential equation

$$\frac{\mathrm{d}^2}{\mathrm{d}x^2}\left(EI\frac{d^2\Omega}{dx^2}\right) - q = 0. \tag{2.60}$$

The differential equation can be completely solved by specifying Ω and $\mathrm{d}\Omega/\mathrm{d}x$ at either both ends or $\mathrm{d}^2\Omega/\mathrm{d}x^2$ and/or $\mathrm{d}^3\Omega/\mathrm{d}x^3$ as boundary conditions. However, out of the four boundary conditions, two must be as follows:

i. Ω is specified at both ends.
ii. Ω is specified at one end and $\mathrm{d}\Omega/\mathrm{d}x$ at the other end.

Here Ω and $\mathrm{d}\Omega/\mathrm{d}x$ constitute essential boundary conditions and $\mathrm{d}^2\Omega/\mathrm{d}x^2$ and/or $\mathrm{d}^3\Omega/\mathrm{d}x^3$ constitute natural boundary conditions.

The variables in FEM are generally approximated using Galerkin formulation and Ritz formulation. In case of Galerkin formulation, the approximation of the primary variable is by using a continuous function inside the element. A residue is obtained depending on the approximating function when primary variable $\boldsymbol{u^e}$ is substituted in Eq. (2.59), i.e.,

$$Lu^e + q = R. \tag{2.61}$$

The residue should be zero everywhere, however, it is difficult to approximate the true value. Therefore, the weighted residual is made equal to zero, i.e.,

$$\int_D wRdA = 0, \tag{2.62}$$

where $\boldsymbol{w}$ is the weight function. In order to weaken the requirement on the differentiability of the approximating function, Eq. (2.62) is integrated by parts to redistribute the order of derivative in $\boldsymbol{w}$ and $\boldsymbol{R}$. The weight function is of the same form as the approximating function in Galerkin method, which is usually some algebraic function. The unknown coefficients of the function are replaced by unknown nodal degrees of freedom as

$$u^e = [N]\{u^{ne}\}, \tag{2.63}$$

where$\{\boldsymbol{u^{ne}}\}$ represents nodal degrees of freedom and [*N*] represent the shape functions matrix.

In Ritz formulation, using calculus of variation, the differential equation Eq. (2.59) is converted in its integral form. Equation (2.63) is substituted in the integral equation and it is partially differentiated with respect to $\{\boldsymbol{u^{ne}}\}$ in order to extremize the form.

Assembly of the elemental equations is performed in the next step. The equations of each element are written in global form and added to each similar equation of all the elements i.e. all equation number 1 of each element is added to obtain the first equation, and so on. After the boundary conditions are applied, the equations are solved by suitable solver. It is followed by post-processing (Dixit, 2009).

Different commercial software applications are available for solving FEM problems in engineering like ABAQUS, ANSYS, DEFORM-3D etc. The software applications perform the FE analysis in three steps: (1) Pre-processing: The geometry of the parts, loads applicable, material properties and boundary conditions are specified in this step. Finite element mesh is generated by an in-built automatic mesh generation module where the type, size and remeshing criteria are specified. (2) Numerical analysis: The stiffness matrices (element characteristics) and load vectors are generated and assembled to generate the system of equations. The specified boundary conditions are implemented and the nodal field variables (e.g., displacement) are obtained by solving the equations to compute the element resultants (e.g., stress and strains). (3) Post-processing: The solutions are displayed either in tabular form or graphically. It is extremely important to verify the

results obtained from FE analysis from the software applications by comparing the results with known solutions.

2.5.5.2 Thermal Modelling

Thermal model governs the mechanical and microstructure models. Understanding of the heat generation is vital to understanding the process and its related phenomena. Material flow, which depends on flow stress, thus is depended on the thermal cycle during welding. One of the first thermal models given by Chao and Qi (1998). It was a three-dimensional heat transfer model that assumed sliding friction only to generate a constant heat flux with Coulomb's law for friction. Pressure was assumed to be constant. However, the study only used heat generated by the tool shoulder. Frigaard et al. (1998) improved the model by incorporating heat generated at the interfaces of FSW tool shoulder-workpiece and the pin-workpiece. Smith et al. (2000) and Bendzsak et al. (2000) used finite difference method for heat transfer modelling as well as material flow in FSW assuming workpiece material to be a non-Newtonian fluid. Gould and Feng (1998) developed a model using the Rosenthal equation for heat transfer during FSW. Russell and Shercliff (1999) also used the Rosenthal equation to incorporate heat input as a point source or line source. Khandkar et al. (2001, 2003) proposed a torque-based heat input model. The modified steady state energy conservation equation used by Nandan et al. (2006) is expressed as

$$\rho C_p \frac{\partial (u_i T)}{\partial x_i} = -\rho C_p U_1 \frac{\partial T}{\partial x_1} + \frac{\partial}{\partial x_i}\left(k \frac{\partial T}{\partial x_i} \right) + Q_i + Q_b , \qquad \textbf{(2.64)}$$

where u_i is the velocity of plastic flow, U_1 is the tool velocity, Q_i is the heat generation rate per unit volume due to frictional heat and Q_b is the heat generation rate per unit volume contributed by plastic deformation.

The contact conditions play a crucial role in thermal modeling of FSW process. However, there are only a few dedicated researches on friction in FSW. A sliding friction model using Coulomb's law was used by Chao and Qi (1998) to model the contact condition by a trial and error technique to obtain close match between experimental and computed temperatures. A constant Coulomb's coefficient of friction (μ = 0.4) was used by Frigaard et al. (1998). The Coulomb's friction law is widely used, which gives frictional shear stress τ as

$$\tau = \mu p , \qquad \textbf{(2.65)}$$

where p represents axial contact pressure and μ represents coefficient of friction. Schmidt et al. (2003) defined a term contact state variable, which is the ratio of velocity of workpiece material to velocity of its contact point on the tool. Based on the contact state variable, the contact condition at

the interface may be (i) sliding, (ii) sticking or (iii) combination of both sticking and sliding. Another widely used friction model is the constant shear (Tresca) friction model given as

$$\tau = mk, \tag{2.66}$$

where $k = \frac{\sigma_y}{\sqrt{3}}$ with σ_y is the yield stress of a material following von Mises yield criteria and m is the friction factor. Apart from these two laws, Norton law of friction is also used by few researchers (Guerdoux et al., 2004; Guerdoux and Fourment, 2005; Feulvarch, 2005). It is expressed as

$$\tau = -\mu K \left|V\right|^{q-1} V, \tag{2.67}$$

where K is the consistency and V is the differential velocity (Lorrain et al., 2009).

Heat dissipation can occur by three ways: (a) heat dissipated into the tool (b) heat dissipated to the backing plate (c) heat loss to the atmosphere. Loss of heat to the tool is very insignificant, which can be estimated by considering temperatures at two points on the tool axis (Schmidt and Hattel, 2005). A convective heat transfer coefficient is assigned to account for equivalent heat transfer through conduction during experiment. The heat dissipation Q_{wt} to tool is given as

$$Q_{wt} = K_{wt} \frac{\partial T}{\partial z} = h_t \left(T - T_t\right), \tag{2.68}$$

where K_{wt} and h_t are the conductance and convective heat transfer coefficient, T_t is the tool temperature and T is the workpiece temperature. The heat dissipation from the top surface to the environment consists of both convective and radiation losses expressed as

$$Q_{wa} = \sigma_b \varepsilon_b \left(T^4 - T_a^4\right) + h_b \left(T - T_a\right), \tag{2.69}$$

where Q_{wa} is heat loss through top surface to surrounding, σ_b is the Stefan–Boltzmann constant, h_b is the heat transfer coefficient at the top surface, T_a is the ambient temperature and ε_b is the emissivity. The heat loss at the workpiece bottom surface and the backing plate Q_{wb} is modelled by considering a suitable convective heat transfer coefficient with equivalent conductive heat transfer during experiment. The heat dissipation to backing plate is expressed as

$$Q_{wb} = K_{wb} \frac{\partial T}{\partial z} = h_b \left(T - T_b\right), \tag{2.70}$$

where K_{wb} and h_b are the conductance and convective heat transfer coefficient for the heat interaction of workpiece and the backing plate and T_b is the temperature of the backing plate.

2.5.5.3 Material Flow Modelling

In order to obtain high structural efficiency of the welds and for optimal tool design, it is necessary to understand the material flow. Computational fluid dynamics (CFD) using commercial software Fluent was employed by Colegrove and Shercliff (2004) to model the material flow in FSW. They developed a 'slip' model where the local shear stresses govern the interface conditions. It was

assumed that the shear stress experienced by the workpiece is different for different tool materials. The surface shear stress was assigned maximum limiting value. Two different boundary conditions were used: (a) Stick condition, where the shear stress was lower than the limiting shear stress and (b) Slip condition, where for stick condition to exist, the shear stress necessary was more than the limiting shear stress; however, the applied shear stress was limited to the maximum shear stress value, thus resulting in slipping at the interface. A three-dimensional thermo-mechanical FE model was developed by Jain et al. (2018) to predict the material flow and forces in FSW. The model used Lagrangian formulation with a built-in feature of DEFORM-3D called point tracking tool to analyze the velocity and material flow (Figure 2.19).

Sellars-Tegart law is also used to model steady state flow stress. Sellars-Tegart law (Sellars and Tegart, 1972) considers the material to be incompressible viscous non-Newtonian fluid. It puts forward a relation between temperature T and rate of deformation $\dot{\varepsilon}$ by using the Zener-Hollomon parameter as

$$Z = \dot{\varepsilon} \exp\left(\frac{Q}{RT}\right) = A\left(\sinh \alpha\sigma\right)^n, \tag{2.71}$$

where R is the gas constant, Q is the activation energy, α, A and n are material parameters (Neto and Neto, 2013). Some researchers used CEL to developed three-dimensional model for predicting voids (Al-Badour et al., 2013). CEL was used by Tongne et al. (2017) to study the formation of alternate bands of light and dark rings during FSW. The study also analyzed defects in FSW with particular interest in correlation of kissing bonds with banded structures.

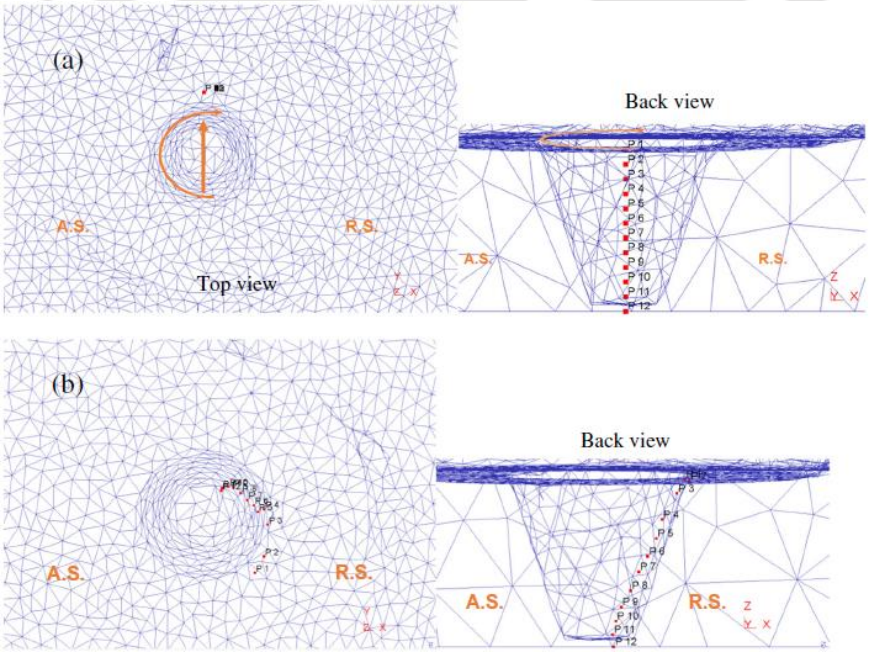

Figure 2.19 Use of point tracker tool to visualize material flow in DEFORM-3D (with permission from Jain et al., 2018. Copyright Springer Nature)

2.5.5.4 Cellular Automata Modeling of FSW

A cellular automata (CA) model uses an algorithm to represent discrete spatial and/or temporal evolution of a complex system by application of deterministic/probabilistic transformation rules to the lattice locations (Qian and Guo, 2004). Cellular automata (CA) models are generally used to relate the initial microstructure to evolving microstructure during materials processing techniques such as rolling, extrusion, welding, casting solidification etc. It is a collection of 'coloured' cells on a grid of specified shape that evolves through a number of discrete time steps according to a set of rules based on the states of neighboring cells. The rules are applied iteratively for as many time steps as required. Figure 2.20 shows a schematic of the working of CA with a set of simple rules as an example. Often, CA is combined with FEM to provide robust simulation methodology called the cellular automata finite element (CAFE) method. In this method, CA cells containing properties of micro features (like dislocation density, initial grain size) are connected to the integration point of elements that are once again related to macro, micro outputs (like stress, strain etc.).

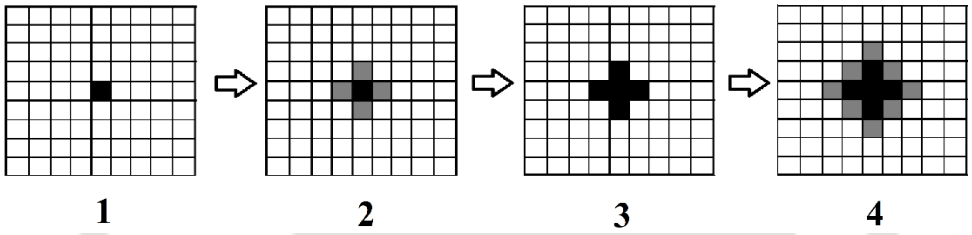

Figure 2.20 Schematic of working principle of Cellular Automation with four iterations; assuming the simple rules: (i) every white cell adjacent to a black cell turns grey (ii) all grey cells adjacent to black cells turn black

For several years, the applications of CAFE models include modeling mixed microstructures (Das, 2010), evolution of microstructure during rolling (Zheng et al., 2008), effect of microstructure on Nb microalloyed rolled sheet properties (Wu et al., 2005) and similar studies. Specifically, in materials processing, the notable works are from Gandin and Rappaz (1994), Davies (1995), Lan et al. (2004), Shterenlikht and Howard (2006), Madej et al. (2009).

In recent times, CA/CAFE models are applied to FSW for understanding the significance of process parameters on the microstructures in the weld zone. It also helps in designing and optimizing the FSW process and selection of tools to minimize FSW defects, and for reducing experimental time and associated costs. For the first time, Saluja et al. (2012) used ABAQUS to develop a CAFE model to predict the size of grains during FSW of AA6061-T6 thin sheets. In this attempt, the stirring of materials that takes place physically in real world during FSW is not simulated. Instead, the strain, heat flux, and strain-rate developed during the process are calculated using existing analytical equations, which are subsequently provided as inputs to FE and CA cells via user sub-routine. To predict the final size of the grains, a group of CA cells with initial grain size that are distributed following Gaussian distribution are created in three-dimensional fashion. The final grain size (D_{CA}) during FSW has been obtained using the transition rule,

$$D_{CA} = C\varepsilon^{x}\dot{\varepsilon}^{y}d^{z}\exp\left(\frac{-Q}{RT}\right), \quad \textbf{(2.72)}$$

where ε, $\dot{\varepsilon}$, T are strain, rate of deformation and temperature during FSW, Q is continuous recrystallization activation energy, d is the initial grain size, and R is gas constant. x, y, z are material constants evaluated by error minimization. Later, the tensile behavior of FSW sheet has been predicted by considering the flow stress evolution at element level and at CA cell level.

The CAFE model has been utilized to develop an artificial neural network (ANN) model for predicting the yield strength and grain size during FSW (Patel et al., 2012). CAFE model generated yield strength and grain size as a function of FSW parameters, and the outputs are trained by neural network. Valvi et al. (2016) extended the CA model to predict the dislocation density (ρ) in the FS zone from grain size (D_{CA}) by using (i) $\rho = \left(\frac{k}{\alpha E b}\right)^{2} D_{CA}^{-1}$, where k is a constant, b is the burgers vector, E denotes the elastic modulus and (ii) fourth order polynomial equation relating it with D_{CA}. To predict the flow stress evolution during tensile deformation of FSW sheets, four different methods were also designed using the CAFE model. Tool selection with various pin profiles for single- and double-side FSW of sheets was done by Rajpoot et al. (2018) using the CAFE method. In this method, grain size is used as output and optimized for different pin profiles to select the appropriate one; however, actually the pin profile used was a different one. The influence of single-side FSW and double-side FSW on grain size distribution was also analyzed with predictions from CAFE model.

There have been several other researches to predict the evolution of microstructure during FSW and other FS variants of various sheet grades. For instance, Shojaeefard et al. (2014) optimized the mechanical properties and grain size of FS welds made of AA1100 using Taguchi method, and the microstructure model was built using CA model in DEFORM (a commercial FEM package) environment. They predicted the dislocation density using modified Laasraoui–Jonas (LJ) model in combination with CA model to optimize rotational speed, transverse speed and tilt angle during FSW. LJ model is a dislocation density model used to predict flow stresses and evolution of dislocation densities during a hot working process. The effect of grain boundary migration on dislocation density is also considered in the modified LJ model. The dislocation density given by the modified LJ method is expressed as (Xiao, 2013)

$$\mathrm{d}\rho_i = \left(h - r\rho_i\right)\mathrm{d}\varepsilon - \rho_i \mathrm{d}V, \quad \textbf{(2.73)}$$

where ρ_i represents the dislocation density for the ith grain; dV denotes volume swept by the boundaries; ε is the strain; average strain hardening denoted by a parameter h and recovery

coefficient *r*. Akbari et al. (2016) established a FE model in combination with CA, LJ and Kocks − Mecking (KM) models to predict the microstructure evolution (such as nucleation and grain growth) during dynamic recrystallization of FSW of AZ91 in DEFORM environment. Besides evaluating the microstructures, the model predicted macro outputs such as strain, temperature as a function of sheet thickness and rotation and traverse speeds. Asadi et al. (2015, 2016) made similar attempts. The microstructure evolution by DRX (dynamic recrystallization) in the friction stir blind riveting process (Samanta et al., 2018), prediction of microstructure during friction stir extrusion process (Behnagh et al., 2019), CA model development for FSW of Titanium alloy (Song et al., 2014) are other notable contributions.

2.5.6 Challenges in Modelling FSSW

One of the major challenges in numerical simulation of FSW is the computational time. FSW simulation is a complex multiphysics problem and are computationally very expensive. As the computation capabilities of modern computers have increased, the simulation time has reduced drastically. However, there is a need to further reduce the simulation time, which will make it more suitable for repetitive simulations with minor variation in process parameters. Although there have been many numerical studies on FSW, there are a very few researches on analytical studies. Most analytical works have extended the work of Schmidt et al. (2003) along with the assumptions taken by them, thus, inheriting their limitations at the same time. The tool-workpiece interface contact condition is a vital aspect of modelling process and needs specific studies on the friction conditions. The different friction models available are not capable of predicting mechanical responses (torque or plunge force etc.) accurately when used alone. Hybrid friction models incorporating more than one friction model may be used for better agreement with experimental results.

2.6 Research Efforts on Enhancing the Horizon of FSW

In the recent past, researchers and practicing engineers started exploring newer applications of FSW including FSW of polymeric materials. A glimpse of these ongoing applications is provided in this section. Titanium is one of preferred materials for space applications due to its high strength to weight ratio and high corrosion resistance (Shtrikman, 2015; Brassington et al., 2017). Tools have been developed for Ti welding with water cooling system and argon gas delivery for shielding in order to improve weld quality (Russell et al., 2007). Liu et al. (2018) presented a comprehensive overview of developments in FSW of steel, tool design, material flow and properties of joint produced. FSW of polymers is another important area. Eslami et al. (2017) presented a state-of-the-art review of research and advances that have taken place in the field of FSW of polymers. Rana et al. (2018, 2019a, 2019b) performed FSSW of sandwich sheets with AA5052-H32/HDPE/AA5052-H32 at varying rotational speed, plunge depth, and plunge speed. All the parameters show

significant effect on joint formation and static strength. Dissimilar polymers welding, polymer-metal welding and composites welding are a few examples of new welding materials that are currently being researched using FSW.

Gao et al. (2015) welded high density polyethylene (HDPE) and acrylonitrile butadiene styrene (ABS) using submerged FSW (SFSW). In order to reduce defects such as pores and cracks, they added different amounts of multi-walled carbon nano-tubes (MWCNTs) at the interface of the joint. The tensile and hardness tests showed increase in tensile strength and elongation by addition of MWCNTs to the joint; however, hardness of the joint decreased. Another possible future application FSW could be in the welding of Meteoric materials for space applications. Materials derived from meteors are being contemplated to be used for space applications by many space agencies at present. Attempts to weld iron meteorite were made using electron beam welding. However, the fast cooling due to presence of phosphorous, sulphur and carbon resulted in extensive cracking. Thus, FSW was proposed as a viable, innovative alterative welding technique (Elmer et al., 2014).

Additive manufacturing is a rapidly evolving manufacturing technology in which layer-by-layer addition of metallic material results in a three-dimensional structure. Friction stir additive manufacturing (FSAM) is a solid-state additive manufacturing method in which the sheets or plates are lap joined one above another using FSP. There are several key benefits of FSAM as compared to additive manufacturing based on fusion welding and ultrasonic (Palanivel et al., 2015a), and few demerits as well. In this method, the final thickness of the joint is controlled by the sheet thickness and numbers of sheets. Palanivel et al. (2015a) attempted FSAM of WE43 Magnesium alloy and strength as high as 400 MPa with about 17% ductility have been achieved with four layers of sheets, each of 1.7 mm thickness. However, cracking due to residual stresses developed from excessive thermal gradient are also observed. FSAM has been extended for AA5083 sheets as well (Palanivel et al., 2015b). Yuqing et al. (2016) attempted FSAM of nine layers of 5 mm thick plates of AA7075 and demonstrated the improvement in overall strength of the joint. TWI has attempted to make metallic structures made of Ti-6Al-4V using SSFSW (Russell et al., 2008). Dilip et al. (2012) fabricated a cylinder with 19 mm diameter and 78 mm height using friction welding, and later used friction deposition to deposit one material (rod of AISI 304) to another (rod of Mild steel). Excellent microstructures and tensile properties of stainless-steel joint show its capability in modifying microstructures. A Ni–Cr–Mo superalloy was deposited onto Ni–Cr–Fe alloy plate using gas tungsten arc process and subsequently FSPed. Such additive FSP along with suitable heat treatment resulted in considerable surface hardness improvement as suggested by Rodelas and Lippold (2013). In a recent development on additive FS deposition, a hollow shoulder, through which the depositing material in the form of solid rod or powder are fed, is used to construct layers through

intense stirring (Hang et al., 2018). More details on FSAM can be seen in a review by Padhy et al. (2018).

2.7 Exit-hole and Strategies to Resolve

Improper process parameters, tool design, joint configuration etc. may lead to formation of defects like cavity, kissing bonds, groove etc. which significantly deteriorate the mechanical performance of the joint. Apart from these defects, the exit-hole which remains in the weld adversely affects the joint quality. It is formed at the weld bead after retracting the non-consumable pin of the tool when welding operation is completed. The presence of the exit-hole results in reduction of both lap shear strength and cross-tension strength as a result of smaller bonding area compared to rest of the weld (Huang et al., 2011). It also leads to stress concentration as well as increase in susceptibility to corrosion. The exit-hole acts as a cavity for corrosive substances to get accumulated. The accumulation of chlorides on the surface may result in breaking of the protective passive oxide layer and lead to pitting corrosion. Corrosive liquid (for example salt water) may fill the exit-hole and with passage of time become more acidic in nature, as seen in crevice corrosion in aluminium and aluminium alloys, leading to corrosion (Corral et al., 2000). Thus, the exit-hole left after the FSW process is one of the major problems. It is especially problematic in case of FSSW or in case of welding circular cylindrical work-piece where use of runoff plate is not possible. The need to solve the exit hole problem arises due to several critical factors:

(i) Structural Integrity: The exit hole is often identified as the weakest point in the FSW joint, potentially compromising the overall structural integrity of the weld. Addressing this issue is crucial to ensure the welded components can withstand operational loads without failure (Ghavimi et al., 2020; Wang et al., 2022).

(ii) Prevention of Premature Fracture: Exit holes can contribute to premature fracture in the welded material. Solving the exit hole problem becomes essential to prevent unexpected failures and enhance the longevity of the weld (Wang et al., 2022).

(iii) Enhanced Reliability: FSW is a widely used welding technique known for its advantages, but the presence of exit holes can undermine its reliability. By addressing and solving the exit hole problem, the overall reliability of FSW joints is improved (Deng et al., 2023).

(iv) Minimizing Residual Stresses: Exit holes are associated with residual stresses that can affect the mechanical properties of the material. Solving this problem helps minimize the impact of residual stresses and contributes to better weld quality (Wang et al., 2022).

There have been recent studies on tool geometry and other aspects of the welding process in order to remove the exit-hole. These studies recognize the exit-hole as a critical aspect that requires

remediation, highlighting the importance of addressing exit-hole-related concerns. Some strategies are discussed.

Tozaki et al. (2010) developed a new tool without pin with a scroll groove on its shoulder for effective FSW. The spiral shaped groove in the tool shoulder helped in more effective stirring of the metal and aided in increasing penetration depth to a certain extent. Tool rotation (3000 RPM) and plunge depth of shoulder were found to be important process parameters. However, for a 2 mm thick Al alloy plate, the plunge depth used to achieve sufficient stirring was 0.7 to 0.9 mm, which is very high. This results in excessive thinning of the weld area which is adversely effects mechanical properties of the weld. Aota and Ikeuchi (2009) had also attempted to use FSSW process without probe but sufficient depth of SZ was not achieved. They had used a pin-less tool which was used to weld low carbon steel plates with 0.5 mm thickness in lap configuration. Lin et al. (2008) studied the difference in microstructure and fracture modes of welds made by flat tool versus concave tool. Badarinarayan et al. (2009) also studied the effect of tool geometry, probe profile and probe length on static strength and suggested that for proper penetration depth of the SZ, pin is a necessary component of the tool and cannot be avoided.

Allen and Arbegast (2005) and Uematsu et al. (2008) used a double acting tools for FSSW process consisting of outer shoulder and inner probe. The tool consisted of three parts: a clamp ring, shoulder and inner pin which could have independent motion with respect to each other with the help of separate actuating systems (Figure 2.21). The shoulder and the pin rotated in the same direction and at same speed which were held in place by the outer stationary clamp ring. The clamp ring is used to press the upper and lower plates together and both shoulder and pin are plunged to just touch the surface of the workpiece. After the workpiece is sufficiently heated and plasticization of the material begins, the pin is plunged further while the shoulder is retracted resulting in forming a reservoir to capture the material displaced by the plunging pin. Next, the pin is retracted and simultaneously the rotating shoulder is plunged to extrude the material that was pushed into the reservoir back into the weld zone. Assuming there is no material loss, the method was able to successfully eliminate the exit-hole but system was very complicated.

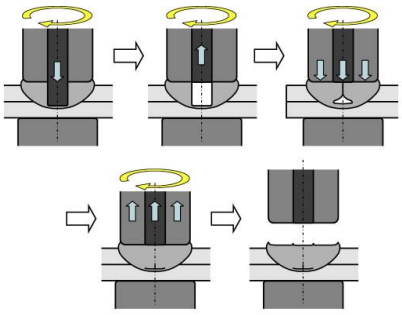

Figure 2.21 Schematic of the double acting tool refilling FSSW (With permission from Uematsu et al. 2008 Copyright Elsevier)

A new technique of self-refilling FSW (SRFSW) to repair keyhole was introduced by (Zhou et al.,2012). In this study welding of 316L stainless steel was performed where keyhole was filled by combined effect of plastic deformation and flow of material around the key hole. A series of tools were designed with changed pin diameter and lengths and used step by step. Figure 2.22 shows the schematics of the process. A spiral groove was also employed in the shoulder for better stirring. The SRFSW was carried out in 8 steps, each step involving the use of a new tool with different geometry. After each subsequent step, the pin length was kept reducing while the pin diameter was increased. The conicity of the pin was kept at 30º for the first 6 steps and on the 7th step 80º pin conicity was used. The last 8th step used a flat shoulder tool to finally arrive at exit-hole free joint. Due to friction and plasticization, the surrounding keyhole material was heated and squeezed into the keyhole. The grains in the refilled zone were found to be significantly refined by the tool. It was also found that the refilled joint fractured at the base metal side during tensile test. The relative tensile strength and elongation of the refilled zone were found to be 112% and 82% of the base metal respectively. Mehta et al. (2020) used a similar approach to remove exit hole produced in dissimilar FSSW of Al and Mg alloys as well as Al and Cu alloy (Mehta et al., 2021). Two different tools, with increasing pin diameter but decreasing pin lengths, were used consecutively after conventional FSSW to remove the exit hole.

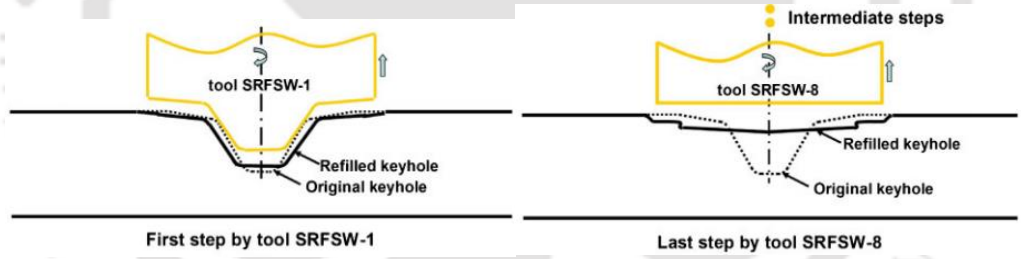

Figure 2.22 Schematics of the SRFSW process (With permission from Zhou et al., 2012. Copyright Elsevier)

Huang et al. (2011, 2012) came up with a new technique of filling FSW (FFSW) where a semi-consumable tool was used. A non-consumable shoulder with a consumable joining bit is used in this process (Figure 2.23). It is a repair technique to fill the keyhole left after the welding process. It consisted of a three-step process where in step 1, spot welding was performed with an exit-hole remained after the process. Step 2 involved use of the consumable joining bit inserted into the exit-hole while being rotated by the non-consumable shoulder and plunged downwards. FSP was performed as the step 3 to produce a smooth surface. The operation with the consumable joining bit consists of 3 stages *viz.* friction stage, stirring stage and joining stage. At the first stage the bit contacts the walls of the exit-hole and rubs against its inner surface to produce frictional heat. It also self-cleanses the bonding surfaces. The second stirring stage is where the bit is plunged into the exit-hole until the non-consumable alloy steel shoulder touches the workpiece. The material of the bit and the exit-hole is softened and stirred due to the friction produced at the interface of the

bit and the exit-hole. It is followed by the joining stage, where due to the heat the bit and the exit-hole joins together and the bit is cut off thereby becoming the filler material. It was found that FFSW produced joints with higher tensile strength and elongation as compared to that produced by FSP without filler material and TIG welding. Relative tensile strength and relative elongation was found to be 84.3% and 98.9% of base weld without exit-hole. Behmand et al. (2015) investigated different geometries of the consumable pin as used by Huang et al. (2011). It was found that the pins that were not conical did not produce sound welds. The geometry of the pin is important in order to have correct contact at the pin-exit-hole interface for sufficient frictional heat as well as stirring to take place.

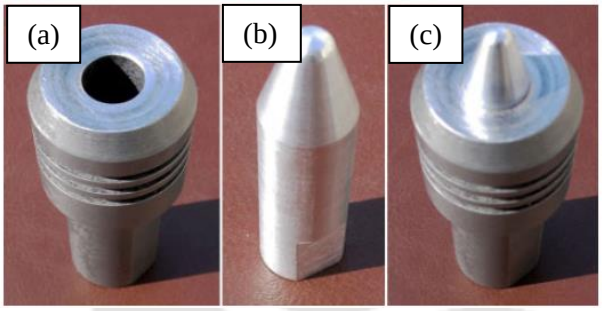

Figure 2.23 Components of FFSW (a) Alloy steel shoulder (b) Joining bit (c) Joining bit combined with tool (With permission from Huang et al., 2011. Copyright Elsevier)

It is relevant here to mention the friction taper plug welding (FTPW), developed by TWI in 1990, where a through tapered hole is drilled into a plate. A tapered plug with similar included angle is friction welded to the matching surface of the hole in few seconds by forcing the rotating plug against the drilled hole. A lot of subsequent research has been performed on use of plug. Dunkerton et al. (1991) had filed a patent on repairing defective metal workpiece by FSW with metal plug. Another patent on Friction plug extrusion for solid phase welding thick plates was filed by Thomas and Temple-Smith (1997). Unfried et al. (2010) worked on microstructural evaluation of friction taper plug welding of C-Mn steel. This process also finds application in repair of space shuttle external tank as described by Hartley (2002). Friction bit joining (FBJ) is another process that relies on consumable joining bit. In this type of joining the lap shear strength was found to be better than self-piercing rivets. The process is capable of joining soft and very hard material combination. Huang et al. (2009), Miles et al. (2009) and Miles et al. (2010) have worked on FBJ. The FBJ can be considered to have two steps: cutting step and joining step. During cutting step the bit cuts through the top layer of the two sheets to be joined at a relatively lower rotation of 300-800 RPM. The rotation speed of the bit is increased (1000–1600 RPM) after cutting through the top sheet to generate more heat and facilitate bonding of the bit and the sheets. At the lower RPM, the cutting edge is maintained by the bit, but as the rotation speed increases, the frictional heat softens the bit material smoothing the cutting edge as it bonds with the sheets. At the end of the joining,

spindle of welding machine is stopped rapidly and then restarted to separate the joining bit from the weld.

Zhang et al. (2014) proposed a new technique of filling friction stir weld keyhole using pin free tool and T shaped fillet bit (Figure 2.24). The use of the T shaped filler bit had the following advantages over conventional filler bit:

- Enhanced friction at the side interface (increasing the moment arm)
- Preheat the filler bit and side interface by friction between larger T cap and shoulder end.
- Avoiding excessive thinning of base plate.

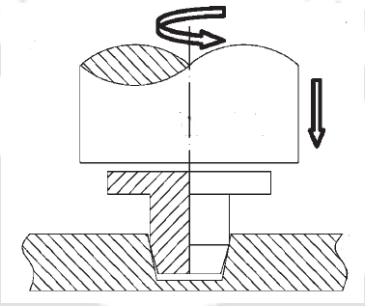

Figure 2.24 T shaped filler bit used for FFSW (With permission from Zhang et al., 2014. Copyright Elsevier)

Double sided FSW (DFSW) is another method for achieving higher penetration depth of stirring. It uses an upper tool as well as a lower tool, with variations in tool rotation direction or geometry or arrangement. Its advantages were discussed by Chen et al. (2013). Also Chen et al. (2017) worked on optimization of mechanical properties of fine grained magnesium alloy joint by asymmetrical double sided FSW. Goebel et al. (2017) worked on semi-stationary shoulder bobbin tool for FSW process of AA2198-T851. BT-FSW consists of two rotating shoulders connected by a probe. There is no requirement of an anvil. The process can be experimented with to produce exit-hole free spot welds if the use of probe can be avoided.

Reimann et al. (2017) discussed microstructure and mechanical properties of keyhole repair welds in AA7075-T651 using refill FSW. The same author had first used the RFSSW process in 2016 (Reimann et al.,2016) where a retractable pin is employed to achieve an exit-hole free spot weld. It consists of a plug, probe/pin, sleeve and clamping rings. First sleeve moves down and simultaneously probe retracts upwards, hence the material flows in the gap. Next the sleeve retracts and the probe is pushed down. Finally, whole tool retracts leaving the plug and surrounding workpiece joined (Figure 2.25).

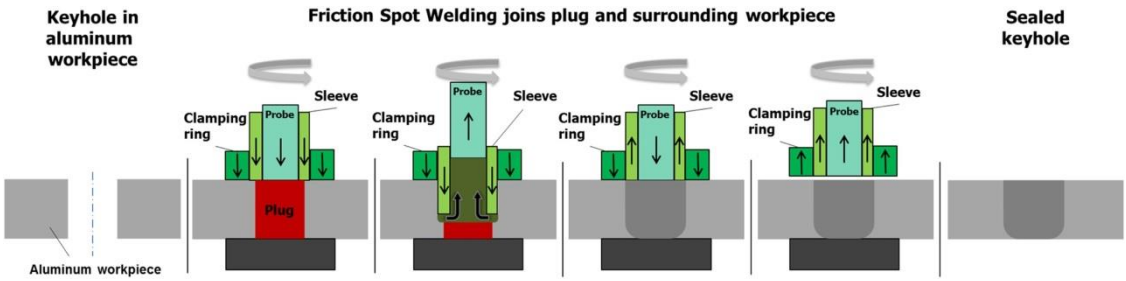

Figure 2.25 Schematic of RFSSW for refilling exit-hole (With permission from Reimann et al., 2016. Copyright Elsevier)

Dong et al. (2019) investigated the joining time and thickness of intermetallic compounds (IMC) formed during refill FSSW of dissimilar Al/Mg alloys. It was found that as the thickness of intermetallic compound layer increased, the failure load of the joint decreased. The thickness of IMC layer in Al/Mg refill FSSW was dependent on the amount of liquid eutectic phase formed during welding (Chai et al., 2019). Some studies have also been performed to understand the material flow during the refill FSSW process. Whereas Shen et al. (2020) studied the material flow experimentally by observing cross-sections of the welds made using a grooved tool, Kubit et al. (2018) used finite element simulation for the study. Although there is good intermixing of material of the two sheets, hook defects were observed by Zhang et al. (2021) during refill FSSW of AZ91D magnesium alloy. Gong et al. (2022) extended the concept to refill FSSW by traversing the tool along the weld line and termed the process as non-keyhole FSW (N-KFSW).

2.7.1 Parametric Studies of FSSW and Exit-hole-free FSSW

In order to have proper control over the process and optimise the weld quality, studies on the effect of process parameters on FSSW joints have been performed for both conventional FSSW and exit-hole-free FSSW. The rotational speed of the tool is one of the key parameters affecting joint quality as it primarily determines the amount of heat input into the weld zone due to the rubbing action of the tool and workpiece surfaces and subsequent plastic deformation of the workpiece material (Arora et al., 2010). A few notable researches on the effect of tool rotational speed are discussed. It is observed in literature that an increase in tool rotational speed results in increase in temperature of the SZ. However, with increase in temperature, the coefficient of friction at the interface also changes resulting in variation of frictional heat input; thus, a monotonic relation of temperature and rotational speed is not observed. It is important to assess the relationship between rotational speed and heat input as an insufficient heat input at lower rotational speed results in inadequate plasticization, whereas, higher heat input at higher rotational speeds causes dissolution, undesirable grain coarsening and lowering dislocation density, leading to decrease in joint strength. It is recommended to keep the rotational speed moderately low; enough to cause plasticization of the workpiece while maintaining SZ properties closer to the BM (Hao et al., 2013; Jambhale et al., 2015; Merzoug et al., 2010). During FSW of AA6061, Elangovan et al. (2008) found that tensile

properties increased up to 1200 RPM and decreased with further increase in rotational speed. Zhang et al. (2011) observed highest tensile and shear strengths of FSSW joints at a lower rotational speed of 1541 RPM (RPM range 1541−2256). The SZ hardness remained same as that of BM at this rotational speed. A similar trend in tensile strength with respect to rotational speed is observed in case of FSSW of aluminium alloy using pinless tools by Suryanarayanan and Sridhar (2020) , where the tensile strength increased up to 1000 RPM and reduced with further increase in rotational speed. A lower rotational speeds is also recommended in case of refill FSSW to ensure good material flow and high tensile shear force Lage et al., 2019; Ferreira et al., 2020). Tier et al. (2013) found that the joint strength decreased with increase in rotational speed from 900 to 1900 RPM during RFSSW due to unwanted grain growth. Ahmed et al. (2022) used modified RFSSW to produce pinhole free joints and studied the effect of rotational speed on the joint quality, in the range of 400 to 1000 RPM. Tensile strength increased up to 600 RPM and decreased with increase in rotational speed. Similar to conventional FSSW, rotational speed was found to contribute maximum in determining nugget width and joint strength in RFSSW (de Castro et al., 2018).

The plunge rate of the FSSW tool is also an important process parameters, which influences the plastic deformation, heat input and overall joint quality (Suryanarayanan and Sridhar, 2021; Çam et al., 2022). Su et al. (2006) reported that temperature produced at the pin's tip decreases with an increase in plunge rate from 0.1 to 10 mm/s for FSSW of AA6061-T6. As the plunge rate increases, the width of the SZ decreases, negatively impacting joint strength. An increase in plunge rate reduces the heat input as it reduces the thermal cycle duration (Suryanarayanan and Sridhar, 2020). Additionally, a lower plunge rate improves material mixing and heat input into the weld, leading to an increase in weld strength. Aziz et al. (2018) conducted an experimental and numerical study of FSW of AA2219-T87 and found that a lower plunge rate leads to higher friction and plastic dissipation energy because it allows more time to stir the workpiece material, generating more heat energy. The torque and axial force during welding increases as the plunge rate increases. It is recommended to use a lower plunge rate to keep the axial forces low, however, too low axial force can result in insufficient plastic deformation and heat input leading to defects. Therefore, a balance must be maintained to achieve optimal weld quality (Khosa et al., 2010; Sathyaseelan et al., 2022). Ramya et al. (2022) showed that during FSSW of AA7075 to mild steel the tensile strength and hardness increased between plunge rates 2 and 4 mm/min and decreased after that. In a study by Zhang et al. (2014) on FFSSW, it was found that high plunge rates resulted in rough joint surfaces and a greater likelihood of T-filler offset from the centre. An optimum plunge rate of 6 mm/min was suggested. Zhou et al. (2018) in RFSSW found that joint strength initially increases, then decreases as plunge rate increases. However, other studies have suggested that higher plunge rates can lead to the formation of equiaxed grains in the TMAZ with highest joint strength obtained at a plunge rate of 30 mm/min (Sezhian et al., 2021). While Karthikeyan and Balasubramanian (2010)

found that plunge rate has a significant impact on joint strength, Baskoro et al. (2020) suggested that plunge rate has minimal effect on tensile shear strength, but can influence the hardening and softening of the workpiece material. As such, there are opposing reports on the impact of plunge rate on joint quality. Additionally, there is limited research on plunge rate as compared to other process parameters.

2.8 Gaps in the Literature

From study of the published literature, research gap was found with possibilities of further examination. The gap found in literature are summarised as follows:

Although there have been many approaches to producing exit-hole-free FSSW joints, no process has been able to fully accomplish the needs for commercial application. In some cases, the stirring depth was found to be insufficient for thicker sheets (Tozaki et al., 2010); some processes were repair techniques only (Reimann et al., 2017; Zhou et al., 2012; Mehta et al., 2020; Huang et al., 2012), while in others, the tool used was too complex (Allen and Arbegast, 2005; Uematsu et al., 2008; Reimann et al., 2016). On the other hand, some techniques consisted of multiple steps to produce a single exit-hole-free joint, which is not commercially viable due to limitations of production speed (Zhou et al., 2012; Mehta et al., 2020; Huang et al., 2012). There is a need to address the issue of exit-hole in FSSW in an industrially viable manner. Consequently, a method to refill exit-hole by waste chips and a method of producing exit-hole-free FSSW joints using consumable pin are proposed in the present thesis, which requires detailed study on feasibility and joint quality.

There is limited literature available on the effect of process parameters on exit-hole-free FSSW processes. With the introduction of new techniques to produce exit-hole-free FSSW joints in the present thesis, a study on the effect of process parameters on joint quality becomes important. Tool rotational speed and plunge rate are important process parameters determining joint quality and requires in depth study.

A friction model to encompass the friction properties at pin-workpiece, tool-workpiece interfaces during different stages of the FSSW process was not found in literature. In most studies in literature, a constant value of friction is used for all interacting surfaces for all stages of FSSW. The heat generation during pin plunging, shoulder plunging and dwelling are different due to variation of friction properties at the interfaces during these stages, which requires a study on the same. Moreover, scant literatures are available on heat generation during FSSW emphasising the role of both friction and plastic deformation. A study on understanding the heat generation can help reduce the energy requirement for welding.

Literature on an FE model simulating the FSSW process considering both thermal and mechanical aspects, to predict temperature generation, material flow and deformation behaviour along with quantitative assessment of joint quality is very minimum. An FE model that can simulate the welding process and further mechanical testing for evaluating joint strength would save time and expenses of doing experimental trials for different process parameters. Moreover, literature on FE model simulating exit-hole-free FSSW using RFSSW, FFSW or SRFSW is very minimum. There is a requirement to study the material flow, temperature generation and deformation behaviour during the proposed exit-hole-free FSSW technique using consumable pin for better understanding of the process.

2.9 Objectives of the Present Thesis

From the literature survey and identification of the research gap, the following objectives are decided for the thesis.

- **To study the effect of lubrication in FSSW processes**

  The first objective of the thesis is to conduct a preliminary study on how heat generation and joint strength change with changes in friction during FSSW. Different lubrication conditions were used, resulting in friction change between the tool and workpiece. The joint strength and energy required for welding are experimentally evaluated to assess the role of friction and plastic deformation in joint formation during FSSW. This understanding is important to realize the underlying physics involved in the FSSW process.

- **To develop a procedure for estimating friction in FSSW**

  There is scant literature available on friction during FSSW. As such, the second objective is to develop an inverse estimation method for friction during FSSW. As part of the preliminary study to understand the FSSW process, a temperature-dependent friction model is proposed by minimizing the error between experimental and simulation torque and plunge force during various stages of FSSW. The friction model and understanding developed are further used for FSSW simulation in the thesis.

- **To study the feasibility of refilling the exit-hole using waste chips**

  The third objective is to investigate the feasibility of producing exit-hole-free FSSW joints using waste chips. The study involved filling the exit-hole with waste aluminium chips and stirring over it to produce the final welds. The joint quality is compared to welds produced using conventional FSSW processes. The process parameters were optimized for achieving the highest joint quality using Evolutionary optimization.

- **To develop an exit-hole-free FSSW process using a consumable pin**

  The fourth objective is to investigate the feasibility of producing exit-hole-free FSSW joints using consumable pins. A novel method is proposed, where a consumable pin is used instead of a hard pin. The joint strength is compared to conventional FSSW using static mechanical tests. A FE simulation is also presented to investigate the temperature generated, material flow, deformation behaviour and overall joint formation mechanism for FSSW using consumable pin. Three consumable pin materials, namely AA6061-T6, mild steel (MS) and oil-hardened non-shrinking die steel (OHNS) with varying strengths, are investigated to determine the best pin material.

  The effect of rotational speed and plunge rate of the tool on joint quality for FSSW using consumable pin are discussed. The joint strength and energy required for welding are determined and analyzed at different rotational speeds and plunge rates to assess the effect of these process parameters. The trend in joint strength is explained with the help of microstructure and microhardness analysis, fractography, torque, plunge force and temperature evolution. A FE simulation of the FSSW process and lap shear test using FEM package DEFORM-3D is presented. The model helped understand the deformation behaviour of the consumable pin, which governed the penetration depth, material stirring and overall joint strength. It was also used to predict shear load at any process parameter within the experimental range. Two damage models, namely Cockcroft-Latham and Freudenthal damage models, were implemented to the joints to predict the failure.

  Finally, a technique of using adhesive-bonded consumable pin along with application of lubricants to improve process efficiency is introduced. To improve the efficiency and to reduce additional machining step, it is proposed to join the consumable pin to tool shoulder using adhesive, and the same has been successfully demonstrated at lab scale delivering comparable lap shear strength as compared to joints using conventional FSSW joints. A reduction in energy requirement for welding due to application of lubricants is also demonstrated. A production cycle scheme is suggested for industrial application, where tools with adhesive-bonded consumable pins are reused in batches.

The research plan of the thesis is represented in the form of a flow chart in Figure 2.26.

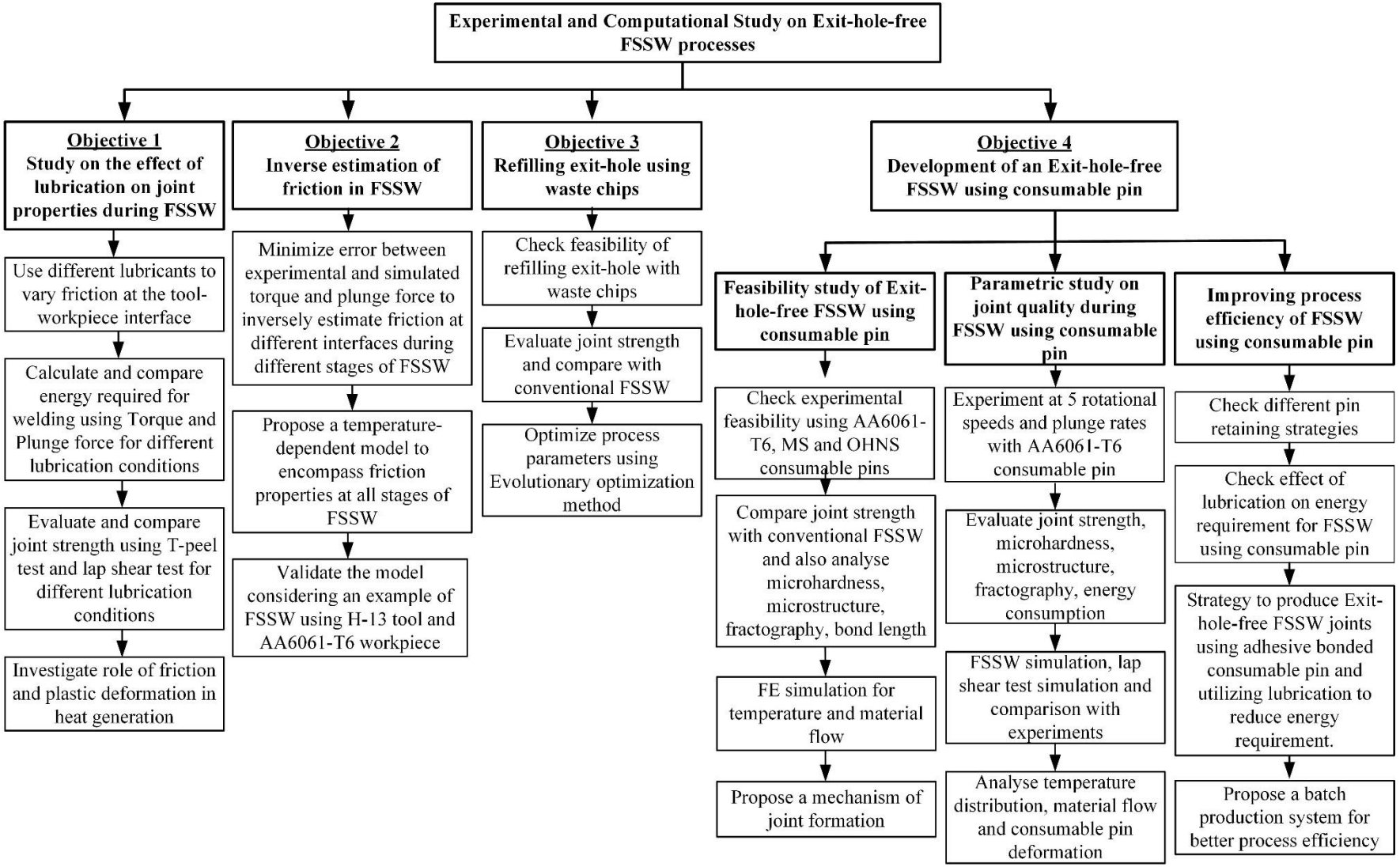

Figure 2.26 Flow chart of research plan

Chapter 3

An Experimental and Computational Study on Conventional FSSW

3.1 Introduction

Heat generated during welding is an important aspect to understand a particular welding process. In FSSW, friction and plastic deformation are the sources of heat generation. However, literature predominantly reports the role of friction only. To understand the heat generation in FSSW better, this chapter studies the effect of reducing friction by application of lubrication and therby emphasising the significant role of plastic deformation in heat generation and welding. Additionally, an inverse method to determine friction during FSSW during various stages of welding is also presented in this chapter.

3.2 Effect of Lubrication on Energy Requirement and Joint Properties during FSSW of AA5052-H32 Aluminium Alloy

Studies on heat generated and temperature distribution during FSW are important aspects to understand the underlying physics and to effectively control the process for improving weld quality. The heat during FSW is generated with the help of a non-consumable rotating tool that is inserted into the joint region of the workpiece. Studies show that the material around the pin is extruded which imply severe plastic deformation and associated heat generation (Reynolds, 2000; Arbegast, 2003). At present, it is accepted that friction between the tool and the workpiece as well as plastic deformation are the sources of energy during FSW (Su et al., 2006; Arora et al., 2009; Awang and Mucino, 2010). Khandkar et al. (2003) proposed a torque-based heat input model which encompassed heat produced due to friction and plastic deformation. Su et al. (2006) carried out a comprehensive study on the energy utilization during FSSW and observed that only a small percentage (4%) of the total heat generated is used for SZ formation. Rest of the heat is dissipated into the clamping setup, tool assembly, sheet, anvil and the atmosphere. It was also found that about 70% of the energy was contributed by the pin during FSSW. Another variant of the FSW, stationary shoulder FSW (SSFSW), utilizes a non-rotating shoulder and a rotating pin, where major contributor in the weld formation is the rotating pin around which material undergoes severe plastic deformation (Maltin et al., 2014; Li et al., 2015).

In this section, a study on the effect of lubrication between the tool shoulder and the workpiece, thereby lowering friction, has been presented and the significant role of plastic deformation in heat generation during welding has been emphasised. An understanding of the heat

generation during FSSW is achieved through this study. The section also suggests stir spot welding (SSW) as the name for the FSSW process that reduces the bias towards friction as the more important factor for heat generation during welding.

3.2.1 Experimental Details

FSSW was performed to study the effect of lubrication on plunge force and torque requirement during welding. Two AA5052-H32 sheets with 1 mm thickness were taken in overlap configuration and welded using an FSW machine as shown in Figure 3.1a. The as received material properties are given in Table 3.1. Four different lubrication conditions namely (i) unlubricated (ii) solid lubricant (iii) liquid lubricant and (iv) coated lubricant (MoS_2) were used, to check the effect of lowering friction between the tool and the workpiece (Table 3.2). The solid lubricant used was chisel paste acquired from Cauldron Petrotech India Pvt. Ltd. The operating temperature of the lubricant was from room temperature up to 700 ℃. The liquid lubricant used was ST Forge Star E (from ST Kool) which is a graphite free water miscible hot forging die lubricant. The working temperature range of the lubricant was 40 ℃ to 450 ℃. The lubricant was mixed with water in the ratio of 1:1 and continuously poured on the tool-workpiece interface during welding process. For the coated lubricant, MoS_2 bonded coating spray (from Release-On) was used. The optimum coating thickness of the lubricant given by the manufacturer was 7–15 µm for effective performance. The operating temperature range for the coated lubricant was 100 ℃ to 450 ℃. An FSW tool with shoulder diameter of 12 mm with pin diameter of 6 mm and pin length of 1.2 mm was used (Figure 3.2a). For all the welds a plunge depth of 0.2 mm, dwell time of 10 s and rotational speeds of 440 revolutions per minute (RPM) and 600 RPM were used. A constant plunge speed of 2 mm/min was used during plunging. In the unlubricated condition, welding was done as conventional FSSW process without lubricant. In case of solid lubricant, the tool and the workpiece were covered with a thick layer of chisel paste during FSSW. In the third condition, the liquid lubricant was continuously poured on the interface of the tool and the workpiece during FSSW. The fourth condition involved spraying both the tool and the workpiece surfaces with MoS_2 coating of lubricant which was allowed to cure for 5 minute after which welding was performed. Although the lubricant was intended to reduce friction between all contacting surfaces of the tool and the workpiece, it was observed that during plunging, the lubricant around the pin was scraped off as the pin went inside the workpiece. It can be effectively assumed that the lubricants reduced the friction between the shoulder surface and the workpiece. Integrated sensors were used to record the torque and plunge force during welding via a strain data logger MP31C09. The joint strength was checked by peel test and lap shear test as per AWS B4.0-2007 standards and were tested in a universal testing machine at room temperature with uniform cross-head speed of 1 mm/min (Figure 3.1b). The schematic diagram of samples with dimensions for peel test and lap shear tests are shown in Figure 3.2b and Figure 3.2c respectively. The maximum load carrying capacity of the welds was recorded.

Figure 3.1 Experimental details: (a) FSW machine with integrated force and torque sensors, (b) peel test samples tested in UTM at room temperature

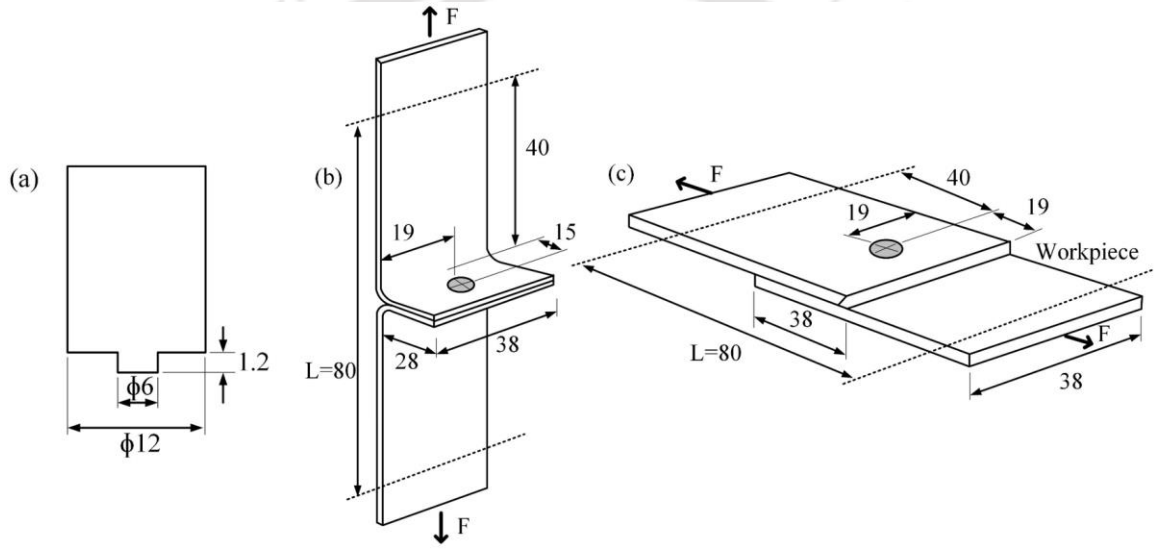

Figure 3.2 Schematic diagrams: (a) FSW tool with dimensions (b) peel test sample (b) lap shear test sample (all dimensions are in mm; L is the gripping length; F is the force applied by UTM)

Table 3.1 Tensile properties of AA5052-H32

Property	**Value**
Ultimate tensile stress	228 MPa
0.2% offset yield stress	193 MPa
Total elongation	12%
Strain hardening exponent	0.1
Strength coefficient	320 MPa
Plastic strain ratio	0.8

Table 3.2 Lubricants used for FSSW

Operating condition	Details of Lubricant used
Unlubricated	No lubricant.
Solid lubricant	Chisel paste (from Cauldron Petrotech India Pvt. Ltd.) Operating temperature up to 700 ℃.
Liquid lubricant	ST Forge Star E (from ST Kool): graphite free water miscible hot forging die lubricant. Working temperature range of 40 ℃ to 450 ℃
Lubricant coating	MoS_2 Bonded coating spray (from Release-On). 7-15 µm coating thickness for optimum performance. Operating temperature range of 100 ℃ to 450 ℃.

3.2.2 Numerical Modelling

A numerical analysis of the process was done using DEFORM-3D using Lagrangian implicit code and adaptive remeshing with sparse solver and direct iteration method. The model used was a fully coupled temperature-displacement analysis which calculated both temperature and displacement simultaneously at each node. Sheet and tool dimensions were kept as that of experiments. Tetrahedral meshing was done in both tool and sheet with minimum global element size of 2 mm and local minimum element size of 0.3 mm at the tool workpiece interface for better accuracy. Figure 3.3 shows the DEFROM-3D model with global and local meshing.

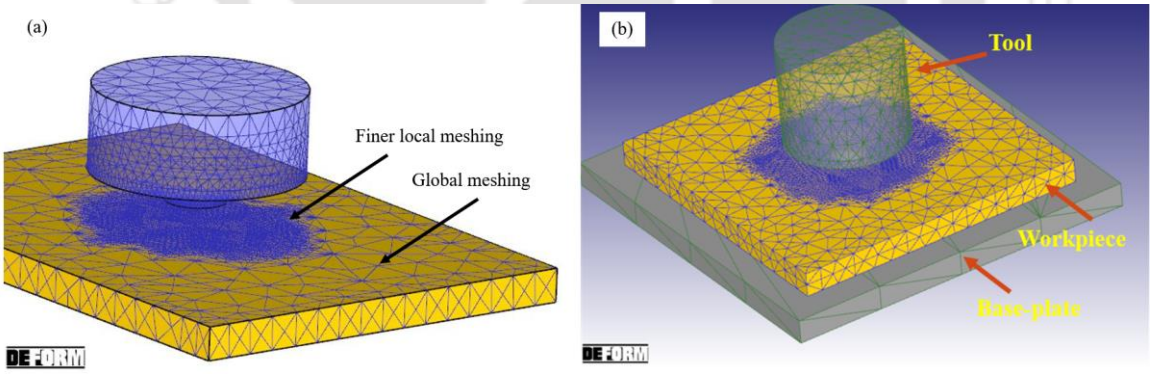

Figure 3.3 DEFORM-3D simulation: (a) local and global meshing (b) tool, workpiece and baseplate

Mesh sensitivity analysis was carried out to arrive at the optimal mesh size. Initial mesh size of 2 mm was used globally which was reduced to 1.5, 1 and 0.5 mm locally at the tool-workpiece interface at the consequent steps. Further reduction in mesh size was carried out by reducing in steps of 0.1 mm. After a local element size of 0.3 mm, there was no significant change in the simulation results with further reduction in mesh size. Thus, 0.3 mm was chosen as the optimal mesh size for the simulation. The boundary conditions used were: (i) bottom surface of the

sheet at zero velocity in *z*-direction (vertical), (ii) tool free to rotate about *z*-axis and translate in *z*-direction, (iii) convective heat transfer coefficient between sheet and environment is 20 W/m^2 (Jain et al., 2017), (iv) heat transfer coefficient between bottom surface of sheet and backing plate is 200 W/m^2°C (Asadi et al., 2011). Material was modelled as visco-plastic material with flow stress $\bar{\sigma}$ as a function of strain ε, strain rate $\dot{\bar{\varepsilon}}$ and temperature T. Heat generation $\dot{q}$ during welding comprises contributions from frictional heat $\dot{q}_f$ and plastic deformation $\dot{q}_p$.

$$\dot{q}_p = \eta \bar{\sigma} \dot{\varepsilon} \ , \tag{3.1}$$

where η is the inelastic heat fraction (Taylor and Quinney coefficient) which is taken as 0.9. The temperature distribution is governed by Fourier heat conduction equation

$$k\nabla^2 T + \dot{q} = \rho c_p \frac{\partial T}{\partial t} \ , \tag{3.2}$$

where ρ is the density, c_p heat capacity per unit mass and k the thermal conductivity. For the unlubricated condition sticking friction has been assumed with m = 1 at the contacting surfaces as

$$\bar{\tau} = m\tau_{\max} \ , \tag{3.3}$$

where $\bar{\tau}$ is the frictional shear stress, m is the friction factor and $\tau_{\max}$ is the shear yield strength.

Finite element simulation was performed for m = 1 for the unlubricated condition and the torque obtained from simulations was found to be close match with the experimentally obtained torque. Further the plunge force obtained from simulation was also compared with the experimental results to validate the assumption of friction factor as m = 1 for the unlubricated condition. For analysis of the lubricated condition, the pin surface was assigned local sticking friction with m = 1 since during experiment the lubricant was scrapped off the surface of the pin and it acted as an unlubricated surface. The value of m was varied locally for the shoulder surface in FE simulation, while keeping m = 1 for the pin surface constant, in order to match the experimentally found torque for the lubricated conditions. The value of m starting from 1 was decreased in steps of 0.1 for the shoulder-workpiece interface. With the decrease in m, there was a consequent decrease in torque obtained from the FE simulations. Close match with experimental torque values for coated lubricant and solid lubricant was found for m = 0.5 and m = 0.4 respectively. Further decrease in m resulted in increase of deviation from experimental results. Thus, m values were refined in the range of 0.4–0.5 by giving a deviation of ±0.05. Close match was obtained with m = 0.45 for liquid lubrication condition. Thus, for the three lubrication conditions i.e. liquid, solid and coated conditions the value of m was found to be 0.45, 0.4 and 0.5 respectively which gave close match between simulation and experimentally found torque values. Further, the plunge forces obtained from simulations for m = 0.45, m = 0.4 and m = 0.5 were compared with their corresponding experimental plunge forces which gave satisfactory agreement.

3.2.3 Results and Discussion

The experimental results revealed that the plunge force and torque during FSSW with lubricant (all three types) was lower than that of unlubricated condition. The plunge force and torque obtained during welding was used to calculate the energy applied during the welding using the following equation:

$$Q_{applied} = \sum_{n=1}^{n=N} F_n (x_n - x_{n-1}) + \sum_{n=1}^{n=N} M_n \omega_n \Delta t \ , \qquad \textbf{(3.4)}$$

where x_n is plunge depth at step (n), ω the angular velocity, n step number, N the final step and Δt is the sampling time. F_n and M_n are plunge force and torque, respectively (Su et al., 2006).

Figure 3.4a shows that the plunge force for FSSW in lubricated cases is lower than that in unlubricated condition. Significant decrease in torque was also observed due to application of lubricant (Figure 3.4b). Table 3.3 summarizes the average plunge force and torque (during t = 0 to t = 94 s) for the different lubrication conditions. It is seen that there is a reduction of 48.7%, 54.9% and 44.7% in torque due to use of liquid, solid and coated lubricants, respectively. A reduction of 24.44%, 25.67% and 12.22% is observed for the plunge force by use of liquid, solid and coated lubricants, respectively. By using Eq. 3.4 the energy required for the welding with different lubrication conditions was calculated. It was found that 5.18 kJ of energy was required to produce the weld in case of unlubricated condition. The calculated values of energy requirement for liquid, solid and unlubricated conditions were 1.93 kJ, 1.82 kJ and 2.19 kJ respectively. There was a reduction of 63%, 65% and 57% in energy from unlubricated condition by use of liquid, solid and coated lubricants, respectively (Table 3.3). The use of lubricants reduced the friction at the contacting surfaces and resulted in the reduction in plunge force, torque and consequently the energy requirement for weld formation.

Table 3.3 Plunge force, torque and energy for different lubrication conditions during FSSW

Lubrication condition	Avg. Torque (N·m)	Avg. Plunge Force (N)	% difference in Torque from unlubricated condition	% difference in Force from unlubricated condition	Energy (kJ)
Unlubricated	10.14	409.5	-	-	5.182
Liquid	5.28	309.1	48.7	24.4	1.934
Solid	4.57	304	54.9	25.7	1.827
Coating	5.61	359	44.7	12.2	2.193

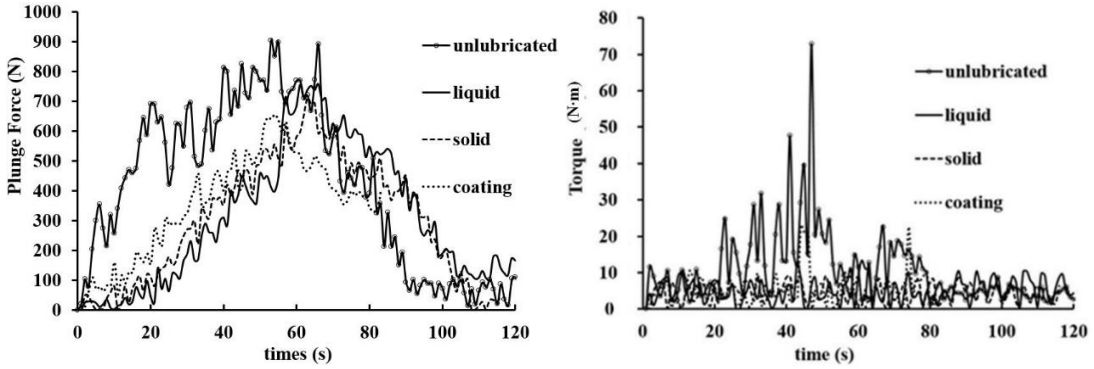

(a) (b)

Figure 3.4 Experimental plots for different lubrication conditions: (a) plunge force vs time (b) torque vs time

The decrease in torque and plunge force imply the reduction in friction between the contacting surfaces. However, there was no significant decrease in weld joint strength as observed from the peel test and lap shear test data for the joints as shown in Table 3.4. For the unlubricated case, maximum load bearing capacity in peel test was achieved for 440 RPM which was 587 N. For the solid, coated and liquid lubrication conditions the maximum load bearing capacity was found to be 576 N, 593 N and 601 N respectively at 440 RPM. For all the cases, it was found that higher load bearing capacity was observed for 440 RPM as compared to 600 RPM. A similar observation was made in case of lap shear tests as well where higher load bearing capacity was observed for 440 RPM. Maximum load bearing capacity in case of lap shear tests for unlubricated, solid, coated and liquid lubrication conditions were found to be 1056 N, 1065 N, 1074 N and 1077 N respectively. It can be observed that there was no significant difference in the maximum load bearing capacity for unlubricated and lubricated conditions for both peel test and lap shear tests. Although friction was higher in case of the unlubricated condition, it did not result in significant change in joint strength. It can be inferred form the above observation that plastic deformation plays a more vital role in joint formation in case of FSSW as compared to friction.

Table 3.4 Peel test and lap shear test results for various lubrication conditions

Lubrication condition	Rotational speed (RPM)	Maximum load bearing capacity in Peel Test (N)		Maximum load bearing capacity in Lap Shear Test (N)	
		Trial 1	Trial 2	Trial 1	Trial 2
Unlubricated	440	587	581	1056	1049
	600	551	565	1047	1040
Solid	440	573	576	1065	1058
	600	568	563	1051	1055
Coating	440	593	582	1071	1074
	600	559	544	1065	1059
Liquid	440	588	601	1075	1077
	600	576	575	1061	1057

Figure 3.5 shows the temperature contour at the cross-section of the weld obtained from FE simulations. It can be seen that even though there is a decrease in temperature adjacent to the shoulder in lubricated condition, the maximum temperature generated around the pin (564 ℃) remained the same for both lubricated and unlubricated conditions. It is known that material around the pin gets extruded around it and undergoes severe plastic deformation. This plastic deformation around the pin contributes significantly to heat generation at the vicinity of the pin. This phenomenon was captured well by the FE simulations which reveal that the reduction of friction between the shoulder and the workpiece had very little effect on the maximum temperature developed in the weld zone. The maximum temperature in the weld zone was governed by the plastic deformation of workpiece material. Although the maximum temperature generated was found to be same, the size of the HAZ was less in case of lubricated conditions which may be beneficial for joint quality explaining a slight improvement in joint strength during peel test and lap shear test. The aforesaid observations suggest that plastic deformation plays a more important role in heat generation. The predicted force and torque evolutions agreed well with experimental data for unlubricated as well as lubricated conditions. Figure 3.6 shows comparison between experimental and simulation data for unlubricated condition. It can be observed that by matching the simulation torque values with experimental torque values and arriving at friction factor value as m = 1, the plunge force values for simulation and experiments showed good agreement. With an application of similar approach, it was found that for solid, liquid and coated lubrication conditions, at the shoulder-workpiece interface m = 0.4, 0.45 and 0.5, respectively, gave the closest match between experimental and simulation results. The comparison between experimental and simulation results for solid, liquid and coated lubrication conditions are shown in Figure 3.7, Figure 3.8 and Figure 3.9, respectively. Also, the results have been compiled in Table 3.5.

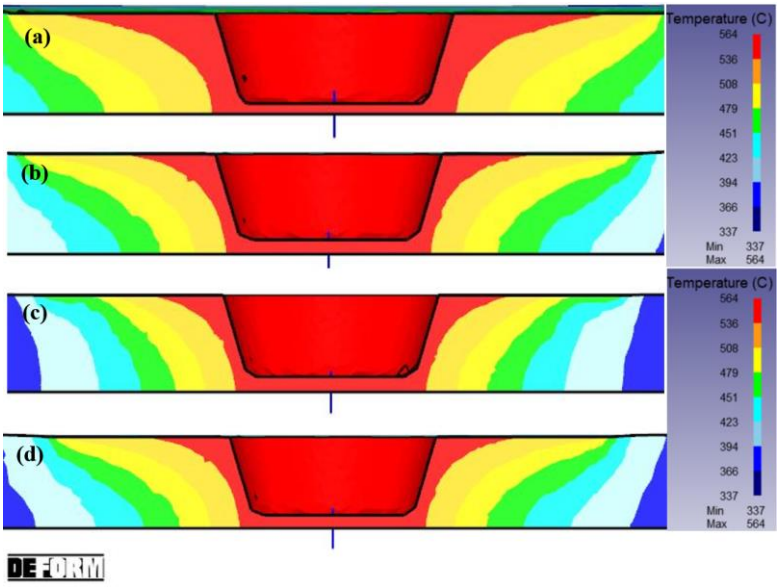

Figure 3.5 Temperature contour simulation of cross-section of the joint in (a) unlubricated condition (b) solid lubricant (c) liquid lubricant and (d) coated lubricant

Table 3.5 Comparison between simulation and experimental torque and plunge force

Lubrication condition	Experimental Torque (N·m)	Simulated Torque (N·m)	% error in Torque	Experimental Plunge Force (N)	Simulated Plunge Force (N)	% error in Force
Unlubricated	10.14	10.3	1.5%	409.5	427	4.2%
Liquid	5.28	5.4	2.2%	309.1	319	3.2%
Solid	4.57	4.8	5%	304	327	7.5%
Coating	5.61	5.8	3.4%	359	324	9.7%

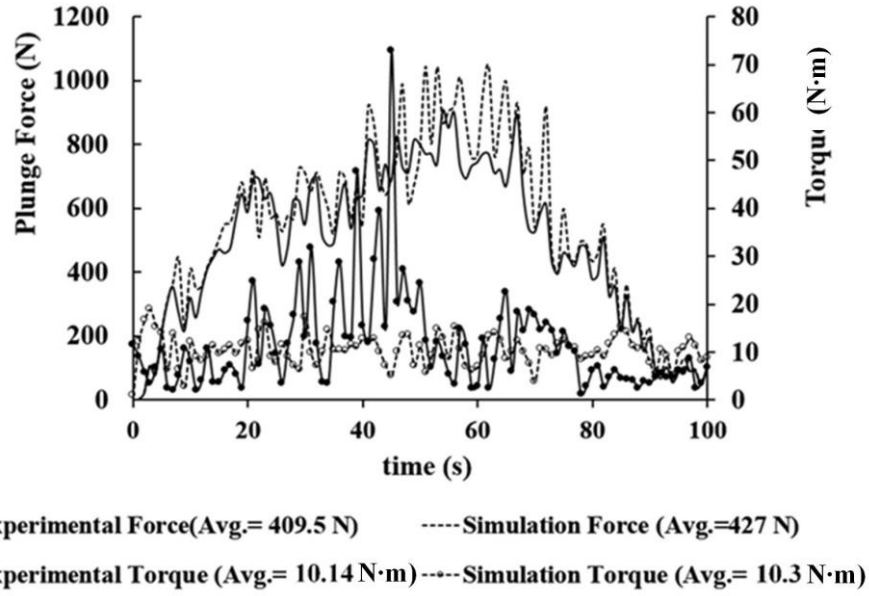

Figure 3.6 Plunge force and torque vs time plots for simulation and experiment (unlubricated condition, *m* = 1)

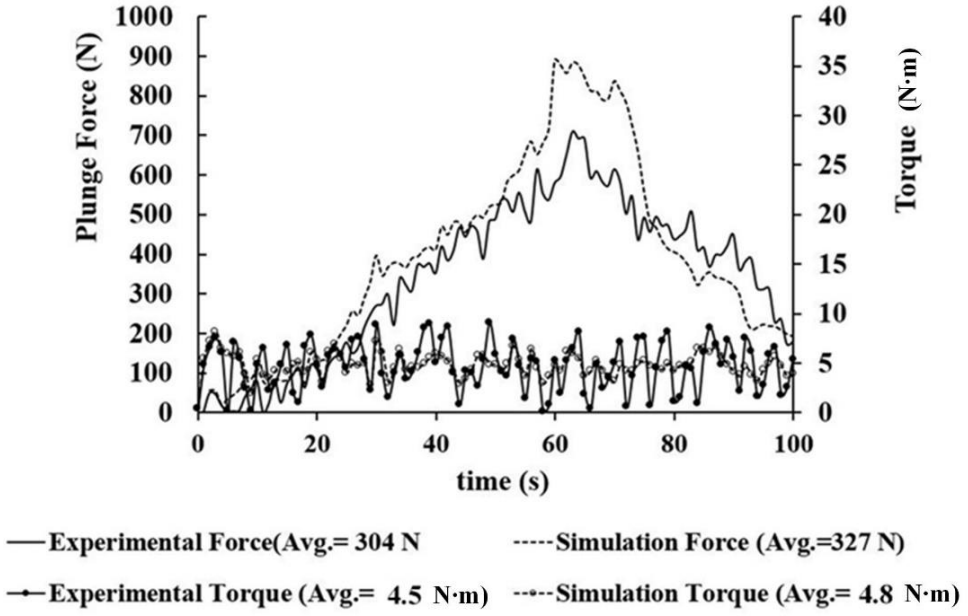

Figure 3.7 Plunge force and torque vs time plots for simulation and experiment (solid lubricant, *m* = 0.4)

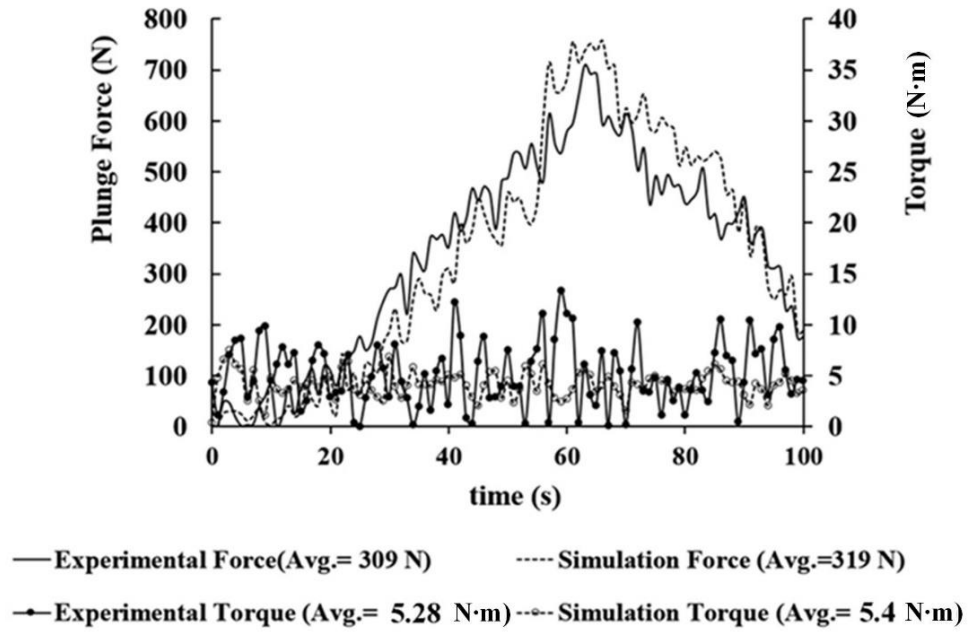

Figure 3.8 Plunge force and torque vs time plots for simulation and experiment (liquid lubricant, *m* = 0.45)

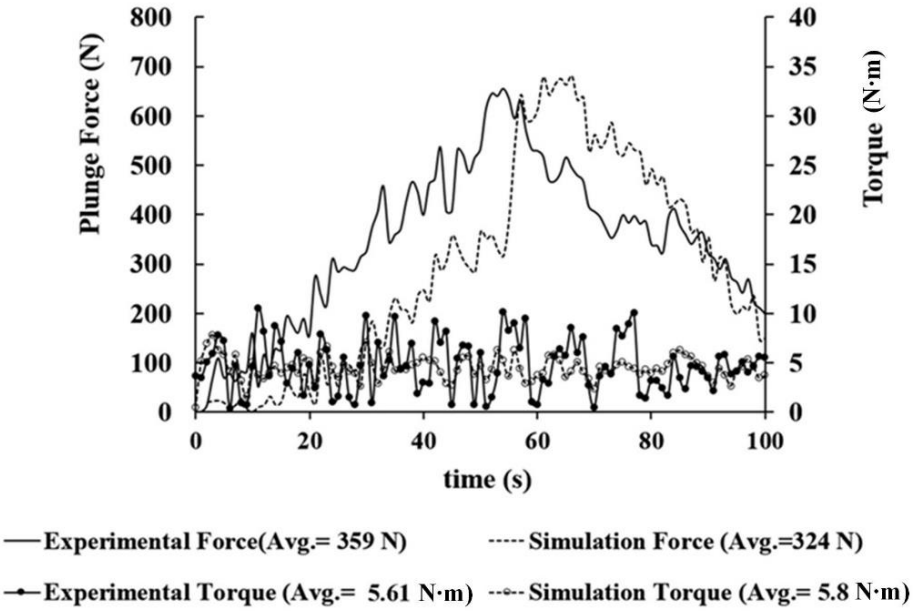

Figure 3.9 Plunge force and torque vs time plots for simulation and experiment (coated lubricant, m = 0.5)

3.3 An Inverse Approach Towards Determination of Friction in FSSW

The sources of heat in FSW are the plastic deformation and friction at the tool-workpiece interface. Although friction has a major influence on the quality of welds, there are only a few researches dedicated to the analysis of friction in FSW. Chao and Qi (1998) developed a 3D heat transfer model assuming only sliding friction that generated a constant heat flux. Friction was estimated using Coulomb's law and constant pressure was assumed at the tool interface. Frigaard et al. (2001) used a constant Coulomb's coefficient of friction of 0.4 but reduced it when the maximum temperature reached a threshold value. Schmidt et al. (2003) proposed that the friction at the interface did not follow Coulomb's law alone, since it is based on friction between two rigid contacting bodies. The workpiece, which gets much softer than the tool as the temperature increases, cannot be considered as a rigid body. It was suggested that sliding, sticking or partial sticking/sliding conditions prevail depending on a contact state variable. An inexpensive method for experimental determination of the coefficient of friction was presented by Kumar et al. (2009), who used a load cell to determine the torque and axial force during welding. The coefficient of friction was determined as

$$\mu = \frac{3T}{2R_p P}, \tag{3.5}$$

where T is the torque generated by the rotating pin, R_p is the pin radius and P is the axial force. However, the model considered only sliding friction at the interface and μ varied in the range of 0.12 to 1.4. This section proposes a simple inverse method to determine the friction parameters at the tool-workpiece interface during FSSW by minimizing the error between computed and experimental torques produced during welding. The method has been illustrated by FSSW of AA6061-T6 using H13 tool. Inversely determined friction parameters were used to estimate the temperature during the process and torque for FSSW process with a tool of different size.

3.3.1 Methodology

A methodology is proposed for the determination of friction parameters at tool-workpiece interface during different stages of FSSW using an inverse method. It is assumed that Coulomb's friction law is valid only at low pressure; at high pressure friction force becomes independent of pressure. The material in the vicinity of the pin is extruded around it; hence, only sticking friction is considered at the pin-workpiece interface. It is modelled with a constant shear friction model. On the shoulder-workpiece interface, a hybrid friction model is assumed which incorporates both Coulomb's and constant shear (Tresca) models.

All the frictional parameters are obtained by minimizing the error between computed and experimental torques. It was noted that torque during FSSW is very much sensitive to friction. Plunge force is not very sensitive to friction. The proposed methodology first estimates the friction factor at the pin-work interface by measuring the torque when the pin has been plunged in the workpiece but the shoulder does not touch the surface of the workpiece. Subsequently, Coulomb's coefficient of friction as well as friction factor of hybrid friction model are determined for the contact between shoulder and workpiece.

3.3.1.1 Determination of Friction Factor at Pin-Work Interface

For determining the friction at the pin-work interface, the torque is recorded during stirring with pin plunged into the workpiece before the shoulder touches the top surface of the workpiece. This eliminates the effect of shoulder-work friction and considers only pin-work friction. It is assumed that the friction at the pin-work interface is sticking friction following the constant shear friction law (Tresca model) given by

$$\tau = mk \ , \tag{3.6}$$

where τ is the frictional contact stress, m is the friction factor and k is given as

$$k = \frac{\sigma_{yt}}{\sqrt{3}} , \tag{3.7}$$

where σ_{yt} is the tensile yield strength of the workpiece. The workpiece material is assumed to follow von Mises yield criterion with temperature-dependent yield strength, which makes the frictional contact stress temperature-dependent as well. The following steps are executed:

Step 1: The experimental torque, T_e, is determined.

Step 2: FEM simulation of the pin plunging with rotation is carried out by using two initial guess values of friction factor, m_1 and m_2. Simulated torque, T_s, is recorded in each case. The percentage error between computed and experimental torques is defined as

$$e = \frac{T_e - T_s}{T_e} \times 100\% . \quad \textbf{(3.8)}$$

Step 3: The error is minimized using the secant method (Rao, 2019) with friction factor m as a decision variable. Secant method fits a straight line between friction factor and error based on the torque values at m_1 and m_2. The fitted straight line locates the value of friction factor, m_o, at which error becomes zero. Simulation is performed at that value of the friction factor and error between computed and experimental torque is recorded. If the absolute value of the error is more than a prescribed value, then either m_1 or m_2 is replaced by m_o and the procedure is repeated with new guess values of m_1 and m_2. It is a good practice to have m_1 and m_2 in such a manner that they provide the errors of the opposite signs. This ensures that zero error point will be obtained by interpolation and not by extrapolation. The iterations are carried out till e is less than the prescribed value. Final value of m_o is taken as the friction factor at pin-work interface.

3.3.1.2 Determination of Friction Parameters at Shoulder-Work Interface

After determining the friction factor at pin-work interface, the friction parameters of the shoulder-workpiece interface are adjusted to minimize the error in the torque when the pin as well as the shoulder are plunged in the workpiece. When the Coulomb's friction model alone is used in the entire region of shoulder plunge, a good match between computed and experimental torque in the low plunge depth region is achieved by adjusting the coefficient of friction μ; however, torque is overestimated in the high plunge depth region. On the other hand, when constant shear friction model alone is used in the entire region, the high plunge depth region showed a good match between computed and experimental torque by adjusting the friction factor m; however, torque is overestimated in the low plunge depth region. The use of a single model is unable to reduce the error simultaneously for both low and high shoulder plunge depth regions. Hence, the shoulder plunge stage is divided into two parts: low plunge depth region and high plunge depth region. The estimation of friction parameters is done separately for the two regions. In low plunge depth region, Coulomb's friction was used and μ was inversely estimated by minimizing the error between

computed and experimental torque using secant method. In the high plunge depth region, constant shear friction model was used where *m* was inversely estimated by minimizing the error between computed and experimental torque using secant method. Integrating the two models into one, a hybrid model (Figure 3.10) is developed for the entire shoulder-work interface. The model considers Coulomb's model in the low-pressure region and constant shear friction (Tresca) model in the high-pressure region. This type of model was first used by Orowan (1943) for the analysis of rolling process.

It can be seen (Figure 3.10) that in the hybrid model the frictional contact stress τ, at a particular temperature, keeps increasing with increase in axial pressure p up to a maximum value of $\tau = mk$, after which it becomes constant. The value of k is temperature-dependent. Therefore, the maximum limiting value of frictional contact stress at a particular point also becomes temperature-dependent. The implementation of hybrid friction model in FEM is done as shown in Figure 3.11.

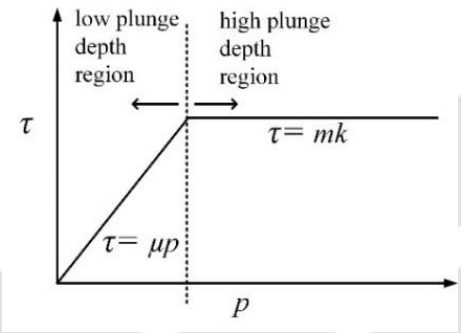

Figure 3.10 Hybrid friction model at a particular temperature

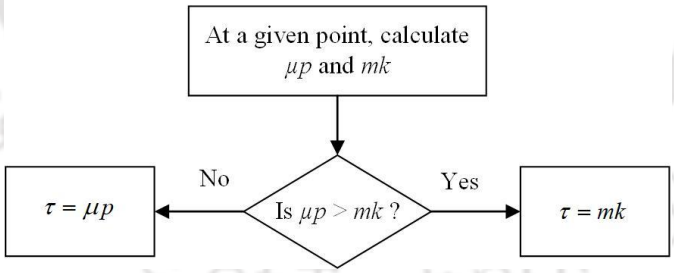

Figure 3.11 Working of the hybrid model during FEM simulations

3.3.1.3 Confirmation of Friction Parameters Based on The Results During Dwelling

The dwelling stage is accompanied by a large increase in temperature and softening of the workpiece material. As such the friction condition at the interface during dwelling is mostly sticking. However, at times, a sticking zone may change to sliding zone and vice versa due to the influence of temperature. When the temperature is high, there is a tendency to have sticking friction with reduced friction force. Reduced friction force reduces the temperature that again results in the hardening of the material with subsequent increase in forces and thereby temperatures. Force and temperature data depict this fluctuation around some average values. The proposed friction model

automatically captures this phenomenon as it is a temperature-dependent model. Experimental torque at dwelling stage is compared with the simulated torque. A low error serves as an indication of efficacy of the model.

3.3.2 An Example

The application of the proposed methodology is described with an example. The experimental and simulation details are described along with the inverse methodology to determine the friction condition at the different interfaces. The different contact surfaces are pin-workpiece interface and shoulder-workpiece interface.

3.3.2.1 Experimental Details

FSSW of AA6061-T6 sheets in lap configuration was performed using a tool of H13 grade steel. A vertical milling machine modified for FSW (model RMV-1800 from Royal Machine Tools) with 20 horsepower motor was used for the experiments. The sheets were of 150×150×1.5 mm size. The tool was a flat shoulder tool with a cylindrical pin. The shoulder diameter was 12 mm, pin diameter 6 mm and pin length was 1.5 mm. For the determination of friction factor in the pin region, experimental torque was considered only during pin plunging when the shoulder was not in contact with the workpiece. A constant rotational speed of 540 revolutions per minute (RPM) was used for all the experiments. The plunge rate was also fixed at 20 mm/min and a total plunge depth (pin + shoulder plunge) of 1.7 mm was given in all cases. A dwell time of 5 s was given for each case. The timeline of the process for the different stages is shown in Figure 3.12. Integrated sensors were used to record the torque and plunge force during welding via a strain data logger MP31C09. MP31C09 is a microprocessor-based system designed to receive the input signals from strain gauges, process it and display the torque and plunge force data on a digital display unit. The data is then sent to a computer via USB and stored. The experimental setup is shown in Figure 3.13. The experimental torque versus time and axial pressure versus time are shown in Figure 3.14 and Figure 3.15, respectively. The sudden rise in torque at 4.5 s corresponds to the shoulder touching the workpiece. A sudden decrease in axial pressure is also observed when the shoulder touches the workpiece.

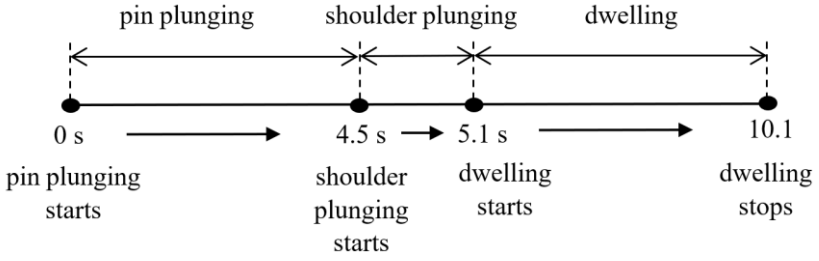

Figure 3.12 Timeline of the FSSW process

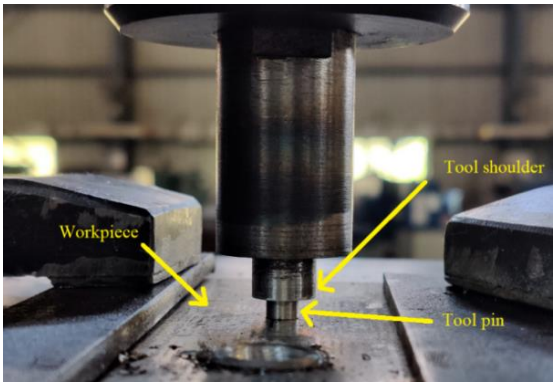

Figure 3.13 Experimental setup for FSSW

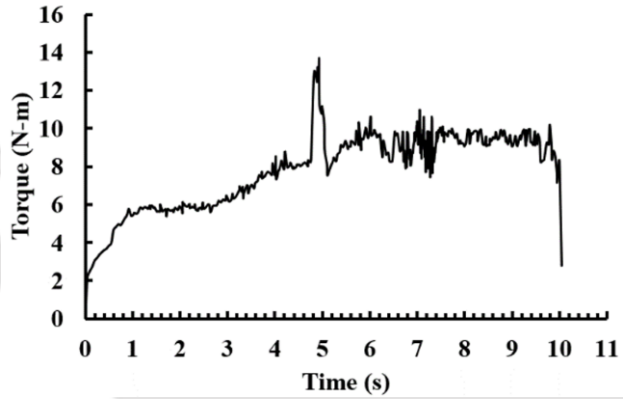

Figure 3.14 Variation of torque with time during experiment

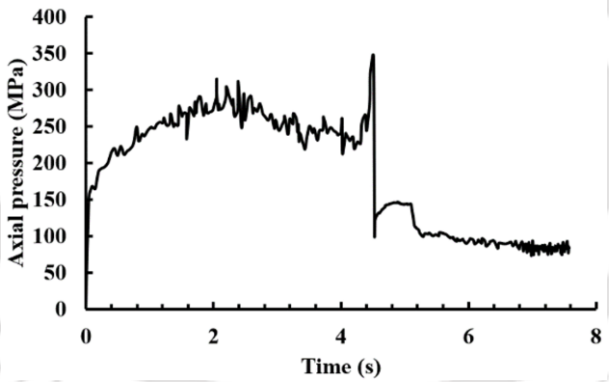

Figure 3.15 Variation of axial pressure with time during experiment

3.3.2.2 Simulation Details

Finite element simulation of the FSSW process was performed using the commercial software DEFORM-3D. Lagrangian implicit code with adaptive remeshing and sparse solver with direct iteration was used for the solution. The model used was a fully coupled temperature-displacement model capable of calculating both temperature and displacement simultaneously at each node. The dimensions of the sheet and tool were kept as that of experiments. Tetrahedral mesh with a minimum global element size of 2 mm and local minimum element size of 0.3 mm at the tool-workpiece interface was used for obtaining a good accuracy in a reasonable simulation time. The boundary conditions used were as follows:

- bottom surface of the sheet assigned zero velocity in *z*-direction (vertical),
- tool free to rotate about *z*-axis and translate in *z*-direction,
- convective heat transfer coefficient between sheet and environment as 20 W/(m^2.K) (Jain et al., 2017),
- heat transfer coefficient between bottom surface of sheet and backing plate as 200 W/(m^2.K) (Asadi et al., 2011).

The workpiece material was modelled as visco-plastic with flow stress as a function of strain, strain rate and temperature. The material was considered rate dependent with isotropic hardening and followed von Mises yield criteria. The elastic deformation of the material was neglected for faster convergence. The assumption to neglect elastic deformation can be considered valid since the effective strain during FSW is in the range of 6−80 which is much higher than elastic strain of 0.002 used in offset method to calculate yield point (Jain et al., 2016). True plastic stress-strain data from DEFORM-3D database were used as material properties input for the workpiece during welding. Hollomon flow stress model, given by $\sigma = k\varepsilon^n$ is used for extrapolation of the material properties to larger strain values, where k is the strength coefficient and n is the strain hardening exponent. Here k = 415 MPa and n = 0.1 is used, i.e. $\sigma = 415 \times \varepsilon^{0.1}$. The material properties at strain rate of 0.001 s^{-1} and 10 s^{-1} were given as input from DEFORM-3D database. Using the data at the two strain rates, material properties at other strain rates were either interpolated or extrapolated. The tool was modelled as a rigid body since the tool material used was much harder than the workpiece material. The material constants used for the simulation for the tool and workpiece are given in Table 3.6. The tool was given displacement in the *z*-direction for plunging into the workpiece according to the plunge rate used in experiments. The determination of the friction parameters is described in the following section.

Table 3.6 Tool and workpiece material properties

Properties	**Tool steel H13**	**AA6061**
Young's modulus (N/mm^2)	210000	68947
Thermal conductivity (W/(m.K))	24.5	180.2
Heat capacity (N/mm^2.K)	2.78	2.43
Coefficient of thermal expansion (μm/(mm.K))	11.7	22
Poisson's ratio	0.3	0.3

3.3.2.3 Determination of Friction Parameters

The application of the inverse method is described as follows. The pin-work interface was modelled to follow sticking friction. Average experimental torque in the pin plunging region was considered for the analysis. The error between computed and experimental torque is minimized using secant method. After two iterations, *e* was 2.1% which was within acceptable limits. The corresponding

value of friction factor was m = 1.05. The friction property at the pin-workpiece interface was fixed as m = 1.05. The iterations are compiled in tabulated form in Table 3.7. The frictional shear stress was more than the shear strength of the materials, which might be due to the welding of asperities at the contact. This was further supported by the observation of workpiece material that remained stuck around the pin after welding was completed.

Table 3.7 Comparison of experimental and computed torques for different m

Friction factor (m)	Experimental torque (T_e) in N·m	Computed torque (T_s) in N·m	% error (e)
1	6.12	5.4	11.8
1.1	6.12	6.6	−7.8
1.06	6.12	6.27	−2.45
1.05	6.12	6.25	−2.1

For estimating the frictional parameters at the shoulder-pin region, the shoulder plunge region was divided into low plunge depth region and high plunge depth region as shown in Figure 3.18. The shoulder touches the workpiece at 4.5 s and plunging continues up to 5.1 s during which the shoulder is plunged by 0.2 mm. Plunge depth up to 0.1 mm is considered low plunge depth and the remaining plunge depth is considered as high plunge depth. The pin surface was assigned constant local sticking friction with m = 1.05. The friction property at the shoulder-workpiece was varied locally in order to match the experimentally found torque with minimum error. The tabulated iterations to arrive at minimum error for the low plunge depth region and high plunge depth region following the proposed methodology are presented in Table 3.8 and Table 3.9, respectively.

Table 3.8 Comparison of experimental and computed torques for different μ during plunging at low plunge depth

Coefficient of friction (μ)	Experimental torque (T_e) in N·m	Computed torque (T_s) in N·m	% error (e)
0.4	8.14	9.8	−20.4
0.25	8.14	7.87	3.3
0.27	8.14	7.89	3.1
0.29	8.14	7.97	2

Table 3.9 Comparison of experimental and computed torques for different m during plunging at high plunge depth

Friction factor (m)	Experimental torque (T_e) in N·m	Computed torque (T_s) in N·m	% error (e)
1	11.34	12.76	−12.6
0.5	11.34	9.6	15.1
0.77	11.34	11.61	2.4

The coefficient of friction μ = 0.29 is accepted in the low plunge depth region and m = 0.77 is accepted in the high plunge depth region and these values are integrated as one single hybrid model at the shoulder-workpiece interface. The hybrid friction model with the mentioned coefficient of friction and friction factor was able to predict the torque during the entire shoulder plunging process with an error < 3%, which was considered acceptable.

Table 3.10 shows the comparison of experimental and computed torque using the hybrid model for the dwelling stage. The hybrid model was able to predict the torque during the dwelling stage as well with an error < 3%. A plot for experimental and computed torque versus time for all the stages of welding *viz.* pin plunging, shoulder plunging and dwelling by the implementation of the final friction model is shown in Figure 3.16. The final friction model (Figure 3.17) can be summarized as

- m = 1.05 in the pin-workpiece interface.
- A hybrid model with μ = 0.29 and m = 0.77 for the shoulder-workpiece interface.

Table 3.10 Comparison of experimental and computed torques for the hybrid model during dwelling

Friction parameters	**Experimental torque (T_e) in N·m**	**Computed torque (T_s) in N·m**	**% error (e)**
μ = 0.29, m = 0.77 (at shoulder-work) and 1.05 (at pin-work)	9.32	9.56	–2.6

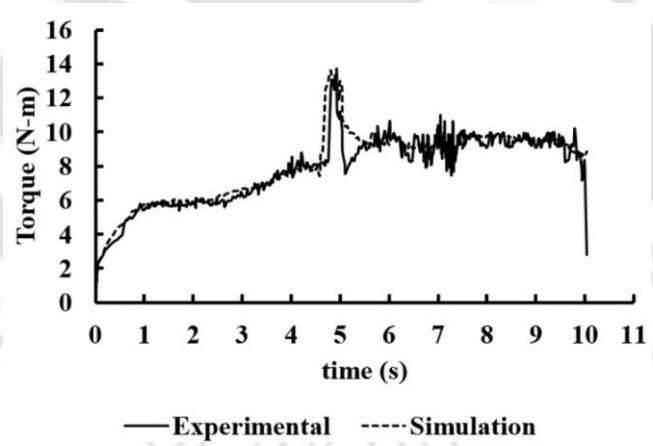

Figure 3.16 Variation of experimental and computed torque with time

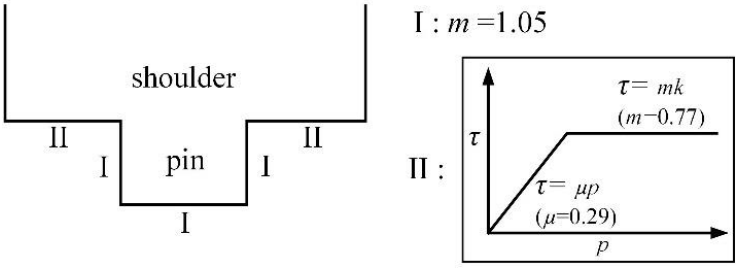

Figure 3.17 Diagrammatic representation of the final friction model

3.3.3 Results and Discussion

A methodology was successfully developed to determine the friction parameters at different interfaces of tool and workpiece during FSSW. The validation of the proposed model in the illustrated example was performed by two methods. The first method involved measuring the experimental temperature and comparing it with simulation temperature using the determined friction model in the example. The second method involved testing the friction model for welding with different tool dimensions but the same tool-workpiece material combination. The methods are described in detail in the following subsections.

3.3.3.1 Validation of Temperature

The temperature of two points (P1 at 5 mm and P2 at 15 mm from the shoulder edge on the top surface of the workpiece as shown in Figure 3.18) was measured experimentally using K-type thermocouple and found to closely match with simulated temperature using the friction parameters found from the three-test method for the illustrated example. All other experimental conditions were kept identical to the previous test.

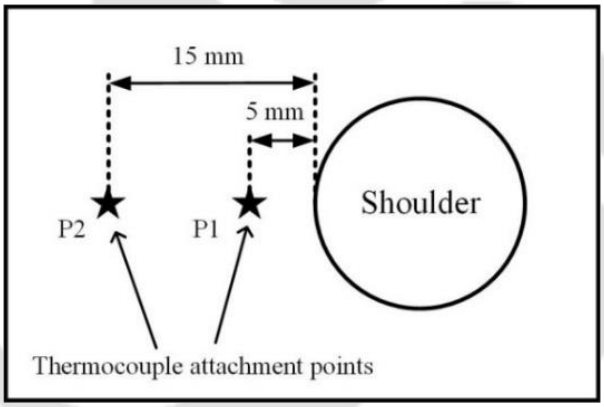

Figure 3.18 Placement of thermocouples on the top surface of workpiece

The results show that the friction model was able to simulate the temperature versus time at both points P1 and P2 (Figure 3.19) with an acceptable error of less than 10% compared to that of experimental results. A comparison of experimental and computed maximum temperature at P1 and P2 during the three stages is also shown in Figure 3.20. Since the model was able to predict the temperature at two points with an error < 10%, it is assumed that the temperature was predicted to the same accuracy at the rest of the region as well. The computed temperature contour in the weld region at the onset of dwelling is shown in Figure 3.21. The reason for lesser prediction accuracy for point P2 compared to P1 may be due to extra heat dissipation through the clamping setup, which was closer to P2, during experiments.

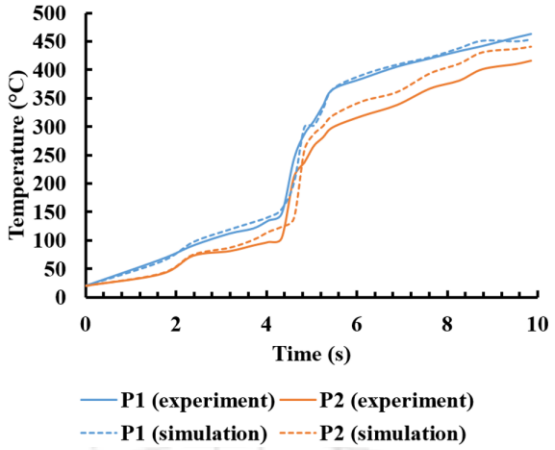

Figure 3.19 Variation of temperature with time for points P1 and P2

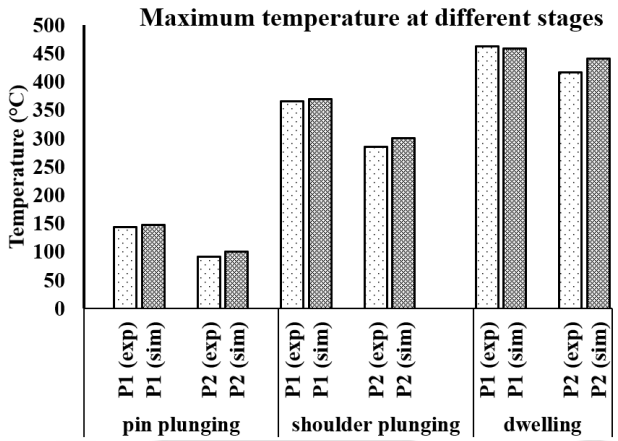

Figure 3.20 Difference between experimental and simulated maximum temperature

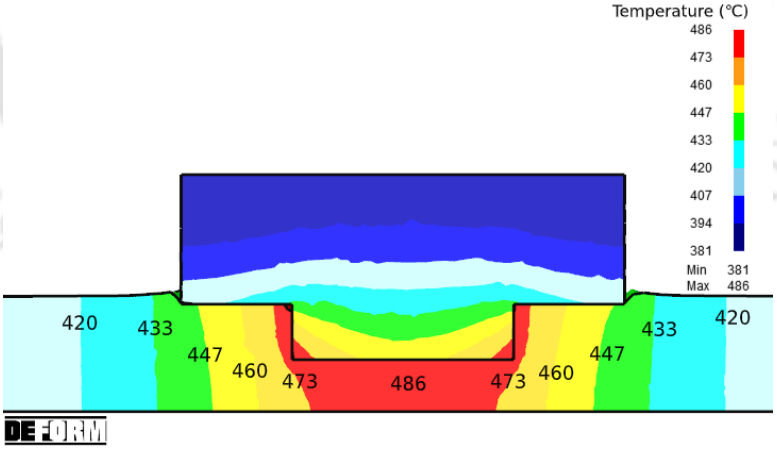

Figure 3.21 Simulated temperature contour at the onset of dwelling

3.3.3.2 Validation for a Tool-Workpiece of Different Dimensions

The validity of the friction model from the illustrated example was checked for a tool and workpiece of different dimension from the example. However, the interacting materials were kept the same, *i.e.* workpiece of AA6061-T6 and tool of H13 grade steel. The tool was a flat shoulder tool with a cylindrical pin having a 20 mm shoulder diameter, a 6 mm pin diameter and a pin length of 3 mm. The sheets used were 2 mm thick in lap configuration. The rest of the process parameters were kept

the same as that in the illustrated example. Using the friction parameters determined from the example, the torque and plunge force for the FSSW were simulated and compared with the experimental results as shown in Fig 3.22 and Figure 3.23, respectively. Computed torque was found to match with an error < 5%. On the other hand, an error < 10% was observed for the computed plunge force with respect to the experimental result.

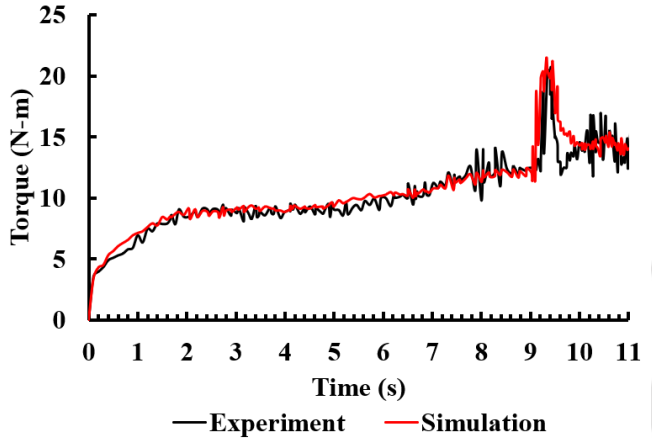

Figure 3.22 Variation of experimental and computed torque with time

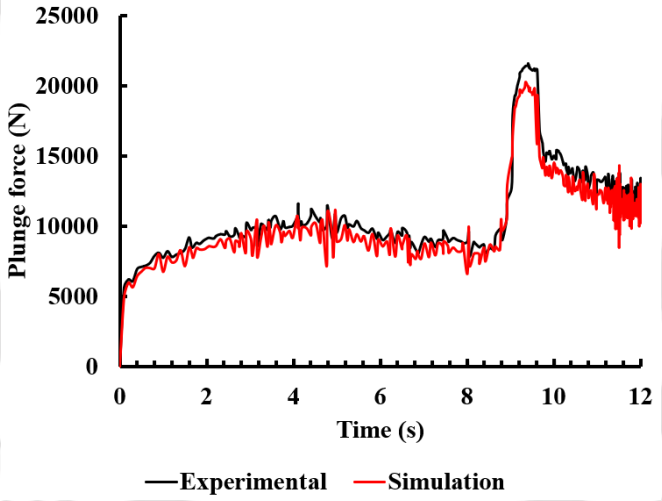

Figure 3.23 Variation of experimental and computed plunge force with time

3.4 Conclusion

The preliminary studies on FSSW were important in developing a better understanding of the process, which is used in subsequent chapters. The first part of the chapter reveals that the use of lubricant in FSSW process leads to decrease in torque and plunge force due to reduction in friction between tool shoulder and workpiece. This consequently results in lesser energy requirement for weld formation. More than 50% reduction in energy requirement was observed due to use of lubricants with insignificant change in joint strength. It can be thus concluded that plastic deformation plays a more important role in joint formation in FSSW as compared to friction. FSSW could be called as stir spot welding (SSW) to emphasis the predominant role of plastic deformation

in welding. The finite element simulation results on plunge force and torque evaluation agree well with experimental data for the lubricated as well as unlubricated conditions by adjusting the friction factor, *m*. Finite element simulation also provided temperature distribution, which indicates that size of HAZ can be reduced with proper lubrication.

In the second part of the chapter, an inverse method was proposed in order to predict the friction parameters during FSSW. The friction model has three parameters: (i) friction factor at pin-work interface (ii) Coulomb's coefficient of friction at low pressure region of shoulder-work interface and (iii) friction factor at high pressure region of shoulder-work interface. The determined friction parameters were compiled in the form of a friction model. The developed model is temperature-dependent due to the involvement of the yield strength of the workpiece.

In a typical case study of FSSW of AA6061-T6 sheets using H13 grade steel, the friction factor (*m*) on the pin-workpiece interface was found to be 1.05. Friction at the shoulder-work interface was best represented by a hybrid model, with $m = 0.77$ for the high-pressure region and $\mu = 0.29$ for the low-pressure region, where μ is the Coulomb's coefficient of friction. The estimated friction parameters could predict the temperature accurately. They could also predict the torque and plunge force for a tool of different size.

Chapter 4

Refilling of Exit-hole in FSSW using Waste Chips

4.1 Introduction

In order to solve the exit-hole problem in FSW, runoff plates could be used, but it becomes particularly challenging in case of circumferential welds or FSSW due to geometrical and metallurgical limitations. In this chapter, a novel technique of refilling exit-hole with waste chips has been introduced that does not require a complex mechanism to operate. The use of waste chips to fill the exit-hole also adds to the sustainable nature of the FSW process. Further, the process parameters used in this method were optimized using evolutionary optimization.

4.2 Experimental Details

In this study on refilling exit-hole in FSSW using waste aluminium chips, spot welding and T-peel tests were performed as part of experiments. The joint quality was evaluated by the results of the T-peel test. The following sections describe the processes in detail.

4.2.1 Welding

Two aluminium alloy AA6082 sheets of 1.5 mm thickness each were welded using FSSW and subsequently the exit-hole was refilled by waste aluminium chips. The waste chips were derived from chips produced during turning of commercially available pure aluminium rod. The chips produced by turning have been termed ‘waste chips’ since it does not find any usage and often discarded as scrap or recycled by re-melting which requires additional expenditure of energy. The base material properties found from tensile test are as given in Table 4.1. A vertical milling machine was used to perform FSSW. The welding operation involved two steps. In Step-1, the two overlapping sheets were clamped and FSSW was performed using a tool with pin having shoulder diameter of 12 mm, pin diameter of 6.5 mm and pin length of 1.2 mm. The rotational speed and the plunge depth were varied for the study. However, after this step, an exit-hole of about 6.5 mm diameter remained in the weld spot. Step-2 involved refilling of the exit-hole with waste aluminium chips. The amount of chip was derived from calculation of volume of exit-hole and density of aluminium. A 20% more than calculated mass of chip was taken as a safety measure in order to compensate for waste in the form of flash and other losses. An amount of 0.12 g of chips was compacted into ball shaped structures as shown in Figure 4.1. The chips were then inserted into the exit-hole. Subsequently a flat tool of diameter 14.4 mm was taken and stirred over the chip filled exit-hole with the same rotational speed and axis of rotation as that in Step-1. Different plunge depths during refilling were also used for the study. In all cases, a dwell time of 15 seconds was used. Thus, three variable process parameters viz. rotational speed, plunge depth during welding

(Step-1), plunge depth during refilling (Step-2) were considered for the study. During welding the plunge depth is considered as the sum of plunge depth of the pin and the shoulder of the tool for convenience of calculation during optimization.

Figure 4.1 Chips compacted into ball shaped structure

4.2.2 T-peel Test

In order to compare the quality of the welded joints T-peel test was conducted to find out the maximum load carrying capacity of each joint. Samples were prepared according to AWS B4.0-2007 standards as shown in Figure 4.2a. In order to keep the weld spot unaffected during sample preparation, the weld spot was fixed in a vice. The extended parts which were to be used for clamping were then bent to form the T shaped sample for the test as shown in Figure 4.2b. The samples were securely clamped, and test was performed as shown in Figure 4.3 in a universal testing machine at room temperature. The test gave a plot of the load *vs* extension graph, where the extension is the opening of the root of the T as shown in Figure 4.3. The extensions at maximum load and at failure were recorded during the test.

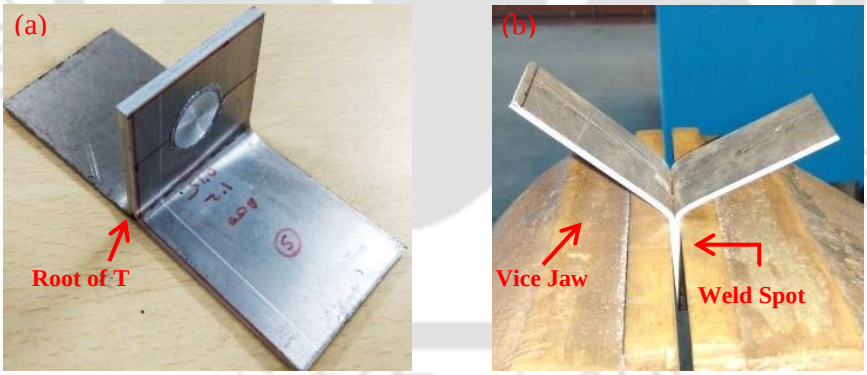

Figure 4.2 Sample preparation: (a) T-shaped sample prepared for T-peel test (b) sample preparation for T-peel test

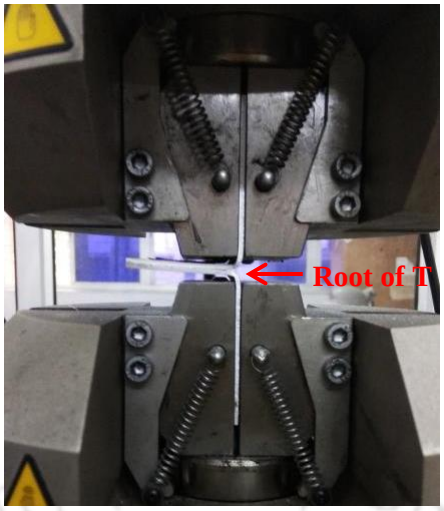

Figure 4.3. T-peel test perfomed in a universal testing machine

Table 4.1 Tensile properties of AA6082

Property	Value
Ultimate Tensile Stress	350 MPa
Breaking Stress	294 MPa
0.2% offset Yield Stress	314 MPa
Uniform Elongation	10%
Total Elongation	15%
Strain Hardening Exponent	0.1
Strength Coefficient	485 MPa
Plastic Strain Ratio	0.7

4.3 Evolutionary Optimization

To arrive at the best combination of process parameters for the welding process, Evolutionary Optimization technique, given by G.E.P. Box, was used. In this optimization technique (Rao, 2010), for an N dimensional case, 2^N+1 points are evaluated to find the best functional value or output. Starting from an initially assumed best point, $\bar{x}$, a hypercube is created around that point with 2^N corner points where functional value is evaluated. The size of the hypercube is given by Δ, known as reduction parameter. It denotes the length of each dimension of the hypercube, fixed according to precision required. A variation of $\pm\Delta/2$ is given to the best point, $\bar{x}$, to form the hypercube around it. The best functional value or output is found from the 2^N+1 points and the point which gives the best output value is chosen as the next $\bar{x}$. The process is repeated by choosing that point as the next best point. However, if no improvement is found, the size of the hypercube is reduced by reducing Δ only and repeating the process.

4.4 Results and Discussion

The results of refilling the exit-hole are discussed in the following subsections. The T-peel tests results were used to employ evolutionary optimization. Three samples for each set of process parameters were tested and the mean value was taken as the final joint strength. The standard deviations of the joint strengths lie in the range of 0.02−0.09. The detailed optimization process by using the T-peel test results in successive iterations is described.

4.4.1 Refilled Exit-Hole

The exit-hole left after the Step-1 was successfully refilled in Step-2 for all the cases. The stirring operation on filled waste chips was able to effectively refill the exit-hole to give a surface with no depression mark as shown in Figure 4.4 (a and b). Apart from aesthetic appearance of the weld spot, the refilled joint also showed better load bearing capacity. A comparison of maximum load bearing capacity in T-peel test of (a) conventional FSSW joint made using a tool having pin, (b) FSSW joint with refilled exit-hole using waste chips and (c) FSSW using pin-less flat shoulder tool is given in Table 4.2. For conventional FSSW, rotational speed of 440 revolutions per minute (RPM) and plunge depth of 1.32 mm was used as in Step-1. For refilled FSSW, rotational speed of 440 RPM, plunge depth of 1.32 mm during welding and 0.18 mm plunge depth during refilling process was used. For FSSW with pin-less tool, 440 RPM was used as the rotational speed and 0.18 mm was used as the plunge depth during welding.

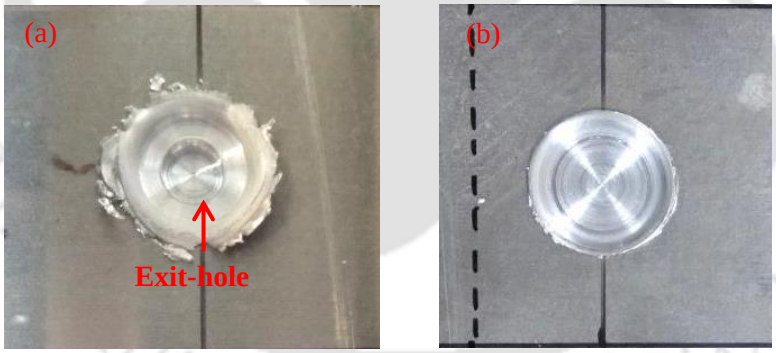

Figure 4.4. Top view of (a) FSSW joint after Step-1 with exit-hole (b) refilled FSSW joint after Step-2

Table 4.2 Maximum load bearing capacity of different welded joints

Samples	Maximum Load (N)
(a) FSSW joint with a tool having pin	838
(b) Refilled FSSW joint	972
(c) FSSW using pin-less tool	528

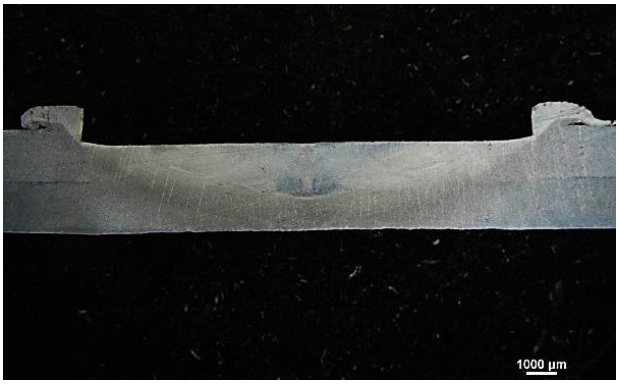

Figure 4.5. Cross-section of refilled FSSW joint using waste aluminium chips

It can be seen from the results that refilling the exit-hole with waste chips delivered 16% higher load bearing capacity as compared to conventional FSSW with a tool having pin. The reason can be attributed to increase in bonded area from that of the joint with exit-hole as well as reduction in stress concentration. The absence of exit-hole would also result in lesser susceptibility to corrosion since there is no depression on the surface for accumulation of corrosive substances. The exit-hole acts as a cavity for corrosive substances to get accumulated. The accumulation of chlorides on the surface may result in breaking of the protective passive oxide layer and lead to pitting corrosion. Corrosive liquid (for example salt water) may fill the exit-hole and with passage of time become more acidic in nature, as seen in crevice corrosion in aluminium and aluminium alloys, leading to corrosion (Oguzie, 2007). The refilling of the exit-hole eliminates the possibility of accumulation of corrosive substances on the surface of the product. On the other hand, an increase of 84% load bearing capacity was observed as compared to joint made by a pin-less flat shoulder tool. The lack of sufficient penetration depth of stirring zone in case of pin-less flat shoulder tool resulted in a significantly lower maximum load bearing capacity for the joint. Thus, it can be inferred that the tool pin plays an important role in stirring of the material and in order to refill the exit-hole left after welding, use of waste aluminium chips is an effective solution. The cross-section of the filled FSSW joint using waste aluminium chips is shown in Figure 4.5 that shows an effective refilling of the exit-hole and a seamless joint between the two plates. Here the stirred zone as well as refilled exit-hole area can be visualized along with effective joining between the two plates.

4.4.2 Optimization of Process Parameters

For this study, as starting point, initial best point, $\bar{x}$ was assumed to have process parameters of 600 RPM as rotational speed, plunge depth during welding of 1.2 mm and plunge depth during refilling of 0.15 mm (Sample S_0) which is tabulated in Table 4.3. The hypercube of 8 corner points was created around $\bar{x}$ by giving ±10% variation to each of the three process parameters at $\bar{x}$. However, due to machine constraints, rotational speed of 440 RPM was used for 10% lower value of 600 RPM and 815 RPM was used for 10% higher value of 600 RPM. Also, the plunge depth was constrained by the least count of 0.03 mm. The new set of 8 combinations is listed as shown in

Table 4.4. The corresponding T-peel test results are also mentioned. The mathematically obtained combination of process parameters for $S_{1.3}$, $S_{1.4}$, $S_{1.7}$ and $S_{1.8}$ gave combinations where the shoulder of the tool did not come in contact with the base material. For conventional FSSW process to fabricate a successful spot joint, the shoulder of the tool must be in contact with the base material. Thus, the four points were discarded from actual experimentation and no tests were performed. For nomenclature of the samples, in the subscript of S, the digit on left hand side of the decimal denotes the iteration number, while the digit on right hand side of the decimal denotes the sample number in that iteration.

From the results of T-peel test and taking maximum load bearing capacity as the deciding criteria, sample $S_{1.1}$ showed the highest load bearing capacity among all the points. Hence, the next best point, $\bar{x}$ is chosen as the parameters corresponding to $S_{1.1}$ and the process was repeated. To form the hypercube, the next set of combination was obtained by giving ±10% variations to the process parameters of sample $S_{1.1}$. The combinations and the T-peel test results are tabulated in Table 4.5.

Table 4.3 Initially assumed best point and load carrying capacity in T-peel test

Sample	Rotational Speed (RPM)	Plunge during welding (mm) Step-1	Plunge during refilling (mm) Step-2	T-peel Test Results		
				Maximum Load (N)	Extension at maximum load (mm)	Extension at failure (mm)
S_0	600	1.20	0.15	883	4.21	10.56

Table 4.4 Load carrying capacity for combination of parameters with ±10% variations from parameters of sample S_0

Sample	Rotational Speed (RPM)	Plunge during welding (mm) Step-1	Plunge during refilling (mm) Step-2	T-peel Test Results		
				Maximum Load (N)	Extension at maximum load (mm)	Extension at failure (mm)
$S_{1.1}$	440	1.32	0.18	972	4.99	13.80
$S_{1.2}$		1.32	0.12	678	3.51	8.55
$S_{1.3}$		1.08	0.18	-	-	-
$S_{1.4}$		1.08	0.12	-	-	-
$S_{1.5}$	815	1.32	0.18	684	3.40	7.82
$S_{1.6}$		1.32	0.12	782	7.74	13.84
$S_{1.7}$		1.08	0.18	-	-	-
$S_{1.8}$		1.08	0.12	-	-	-

Table 4.5 Load carrying capacity for combination of parameters with ±10% variations from parameters of sample $S_{1.1}$

Sample	Rotational Speed (RPM)	Plunge during welding (mm) Step-1	Plunge during refilling (mm) Step-2	T-peel Test Results		
				Maximum Load (N)	Extension at maximum load (mm)	Extension at failure (mm)
$S_{2.1}$	325	1.44	0.21	834	5.93	13.93
$S_{2.2}$		1.44	0.15	512	3.22	10.11
$S_{2.3}$		1.20	0.21	794	6.64	12.35
$S_{2.4}$		1.20	0.15	549	5.54	5.62
$S_{2.5}$	600	1.44	0.21	664	7.13	13.96
$S_{2.6}$		1.44	0.15	789	8.49	15.64
$S_{2.7}$		1.20	0.21	972	9.02	18.17
$S_{2.8}$		1.20	0.15	964	8.23	15.07

It can be observed from Table 4.5 that there was no improvement in the maximum load bearing capacity for any of the new combinations with ±10% variation from sample $S_{1.1}$. For the next iteration the point $\bar{x}$ remained the same, however, the variation given to form the new hypercube was reduced to ±5% in order to refine the results. Since the rotational speed variation was limited by machine constraints and the plunge depth during refilling was constrained by the least count of 0.03 mm of the machine; only the plunge depth during welding was given a ±5% variation. Table 4.6 shows the combination as well as the T-peel test results. It can be observed that there was no improvement in maximum load bearing capacity with ±5% variation given to $\bar{x}$. Therefore $\bar{x}$ remained the same and to further refine the results, variation of ±2.5% was given as tabulated in Table 4.7. No improvement in result was observed even with ±2.5% variation and the least count constraint for variation of plunge depth during welding was also reached. Hence the point $S_{1.1}$, with parameters of 440 RPM, 1.32mm plunge depth during welding, 0.18 mm plunge depth during refilling, was regarded as the optimized combination of the process parameters with the maximum load bearing capacity of 972 N and failure occurring at an extension of 13.80 mm. However, if the deciding criterion for optimization was chosen as extension at the maximum load or extension at failure, the resultant combination of parameters with optimized output would be different from this analysis. Depending on the required property, the deciding criteria for optimization can be chosen.

Table 4.6 Load carrying capacity for combination of parameters with ±5% variations from parameters of sample $S_{1.1}$

Sample	Rotational Speed (RPM)	Plunge during welding (mm) Step-1	Plunge during refilling (mm) Step-2	T-peel Test Results		
				Maximum Load (N)	Extension at maximum load (mm)	Extension at failure (mm)
$S_{3.1}$	440	1.26	0.18	937	8.49	11.66
$S_{3.2}$		1.38	0.18	862	4.96	10.28

Table 4.7 Load carrying capacity for combination of parameters with ±2.5% variations from parameters of sample $S_{1.1}$

Sample	Rotational Speed (RPM)	Plunge during welding (mm) Step-1	Plunge during refilling (mm) Step-2	T-peel Test Results		
				Maximum Load (N)	Extension at maximum load (mm)	Extension at failure (mm)
$S_{4.1}$	440	1.29	0.18	956	8.94	25.43
$S_{4.2}$		1.35	0.18	824	5.64	12.87

4.5 Conclusion

In this study, a novel method introduced to refill the exit-hole in FSSW using waste aluminium chips showed higher load bearing capacity as compared to both conventional FSSW using a tool having pin as well as FSSW using pin-less tool. The method of refilling imparts both aesthetic value as well as lesser susceptibility to corrosion in the weld spot formed. A seamless bonding of the two plates was also observed in the cross-section of the weld spot with no trace of the exit-hole. Thus, refilling exit-hole with aluminium chips can be regarded as an effective method of elimination of the exit-hole in FSSW. Difference in joint strength between FSSW joint with hole and waste chip refilled samples is 16 %. The evolutionary optimization method revealed that rotational speed of 440 RPM, plunge depth during welding of 1.32 mm and plunge depth during refilling of 0.18 mm gave the best results with 972 N maximum load bearing capacity. A higher plunge depth resulted in thinning of the bonded reason while a lower plunge depth results in insufficient penetration of stirred zone. Thus, optimization of the process parameters gave the best combination for this process to get the most favourable output. However, due to the unknown origin of the waste chips and its material properties, there is possible uncertainties in the joint characteristics. Further study can be performed to remove these uncertainties.

Chapter 5

Exit-Hole-Free FSSW of Aluminium Alloy Sheets using a Consumable Pin

5.1 Introduction

It is discussed in literature review that for proper penetration depth of the SZ, pin is a necessary component of the tool and cannot be avoided. Allen and Arbegast (2005) and Uematsu et al. (2008) used a tool consisting of three parts: a clamp ring, shoulder and inner pin which could have independent motion with respect to each other with the help of separate actuating systems. A similar tool was used by Reimann et al. (2016) and the process was named refill FSSW. Zhou et al. (2012) introduced self-refilling FSW (SRFSW) which was carried out in 8 steps, each step involving the use of a new tool with different geometry. Huang et al. (2012) reported a new technique called filling FSW (FFSW), where a semi-consumable tool was used. The process was a repair technique to fill the exit hole left after the welding process.

The currently available approaches to produce exit-hole-free FSSW joints have not been able to fully accomplish the needs for commercial application. In some cases, the stirring depth was found to be insufficient for thicker sheets (Tozaki et al., 2010); some processes were repair techniques only (Reimann et al., 2017; Zhou et al., 2012; Mehta et al., 2020; Huang et al., 2012), while in others, the tool used was too complex (Allen and Arbegast, 2005; Uematsu et al., 2008; Reimann et al., 2016). On the other hand, some techniques consisted of multiple steps in order to produce a single exit-hole-free joint, which is not commercially viable due to limitations of production speed (Zhou et al., 2012; Mehta et al., 2020; Mehta et al., 2021; Huang et al., 2012). This chapter involves a novel technique to produce exit-hole-free joints using consumable pin. Unlike some techniques found in literature, which use complex tools, this study uses a simple tool that is cost-effective. This technique avoids the use of multi-step process to repair the exit hole and produces exit-hole-free welds in a single step, which is both fast and cost-efficient. The influence of consumable pin quality is also studied by using three different consumable pin materials, *viz.* AA6061-T6, mild steel (MS) and oil hardened non-shrinking die steel (OHNS) with varying strengths. The joint quality for the different welds produced is studied using lap shear test, microstructure study and microhardness study. The understanding of the physics of the problem involving material flow as well as temperature distribution is also carried out using FEM simulations in DEFORM-3D.

5.2 Experimental Details

The experimental details and the characterization of the materials used for producing the joints are described in this section. The joint quality evaluation techniques that were used are also described.

5.2.1 FSSW with Consumable Pin and Joint Characterization

Two AA6061-T6 sheets of 1.5 mm thickness each were taken in lap configuration. The dimensions of the sheets were 150 mm ×150 mm ×1.5 mm. A hard (H13 grade steel) flat shoulder tool of shoulder diameter 12 mm was used for welding. A vertical milling machine modified for FSW (model RMV-1800 from Royal Machine Tools) with a 20 hp motor was used for the experiments. The FSW machine had integrated sensors (strain-gage-based) to record the torque and plunge force during welding. A constant rotational speed of 557 revolutions per minute (RPM) was used for all the experiments. The plunge rate was fixed at 20 mm/min and a dwell time of 10 s was given for all cases. In the present study, the consumable pin was placed on the upper sheet. The flat shoulder non-consumable hard tool was rested on top of the consumable pin with sufficient axial force to keep the setup intact (Figure 5.1). The tool was then rotated, which led to the subsequent rotation of the consumable pin. The tool was slowly plunged downwards until the shoulder touched the surface of the workpiece. After dwelling for 10 s, the tool was retracted back, giving an exit-hole-free joint. In order to improve control over the placement of the pin, a small circular indent of the same diameter as the pin was created on the upper sheet to place the consumable pin. The indent was created using the hard pin FSSW tool.

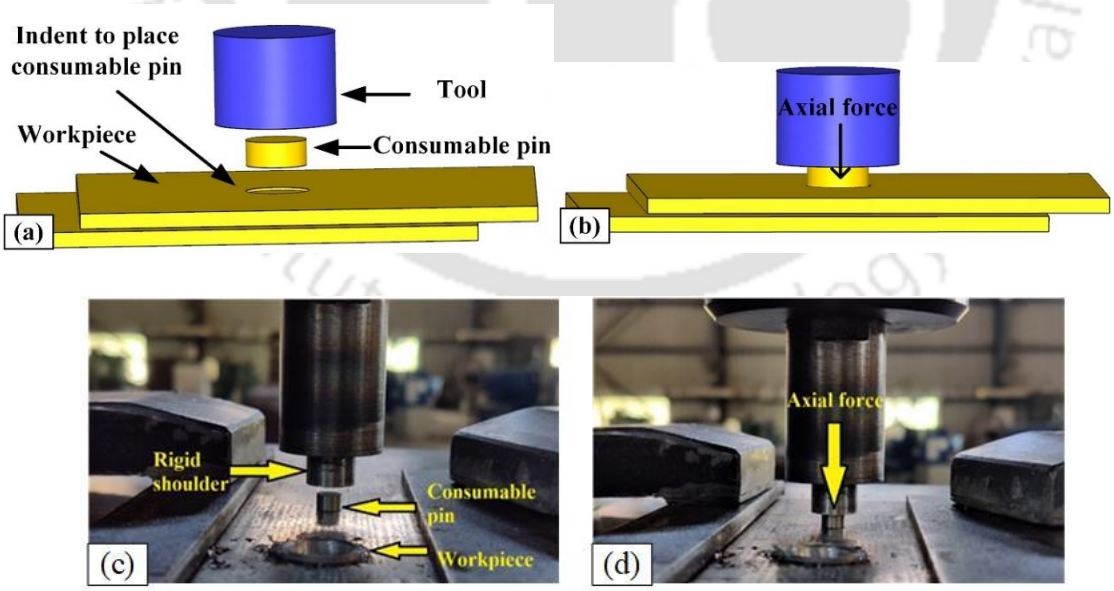

Figure 5.1 FSSW using consumable pin: (a) schematic diagram of the components for welding (b) schematic diagram of consumable pin on the upper sheet (c) experimental set up with consumable pin placed on the upper sheet (d) application of axial force by the flat shoulder to keep the setup intact

The consumable pin taken was of diameter 6 mm and length 2.5 mm. Three different pin materials were considered for the study, *viz.* AA6061-T6, mild steel (MS) and oil hardened non-shrinking die steel (OHNS). Along with AA6061-T6, which is the same as the sheet material, the performance of MS and OHNS consumable pins was studied as their mechanical properties are closer to that of conventionally used hard pins. The joint properties of the welds using the three consumable pin materials were compared with welds made with conventional FSSW with a pinless flat shoulder tool of diameter 12 mm and a tool with hard pin having shoulder diameter of 12 mm, pin diameter of 6 mm and pin length of 1.5 mm. The joint strengths were evaluated by lap shear tests using AWS B4.0-2007 standards in a universal testing machine at room temperature with a uniform cross-head speed of 1 mm/min. The schematic of the lap shear sample is shown in Figure 5.2. Alignment shims were used during lap shear test, as shown in Figure 5.2d, to reduce eccentricity of the load path, which results in out-of-plane bending moments. The alignment shims ensure pure shear mode of loading by keeping bending load to a minimum (Lancaster, 1999). Microstructure of the cross-section of the joints was also analysed using an optical microscope (Carl Zeiss- Axiotech). The microhardness profile of the cross-section of the joints was studied and correlated with the microstructure and temperature history during welding. In order to record the temperature generated during welding, two K-type thermocouples were attached at 5 mm and 15 mm distance from the tool shoulder edge on the top surface of the workpiece. Although it is possible to place thermocouples just below the tool shoulder in thorough holes drilled in the workpiece, it was avoided in order to reduce its effects on material flow during welding. Temperature was recorded at a minimal distance away from the shoulder to keep the joint region unaffected with reasonable accuracy. Temperature in the weld region was further predicted using FE simulation and validated by experimentally recorded temperatures. For understanding the deformation behaviour of the consumable pin, the welding process was stopped at two intermediate positions of 1/3rd plunge depth and 2/3rd plunge depth. The cross-sections of joints at the intermediate positions of the pin plunge were also observed under the microscope.

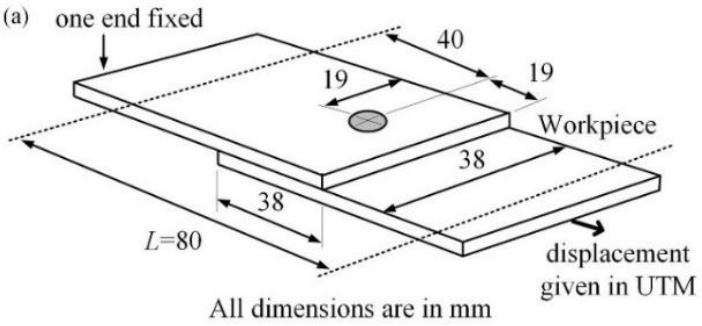

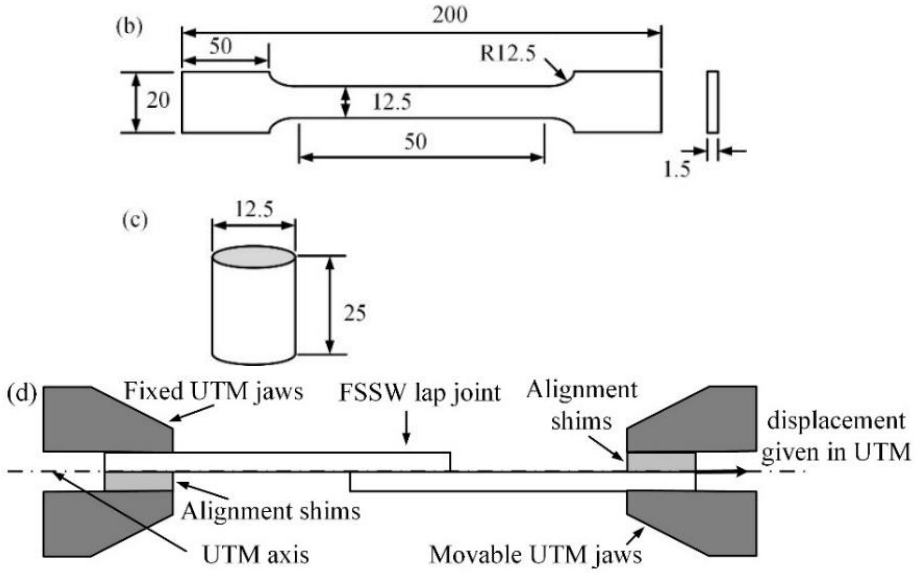

Figure 5.2 Schematic diagrams of (a) lap shear test sample (*L* is the gripping length) (b) tensile test sample (c) compression test sample (all dimensions are in mm) (d) side view of lap shear test with alignment shims to minimize bending load

The microhardness at the cross-section of the joint was recorded at thirteen equidistant positions on two lines, Line A and Line B, at a distance of 1 mm and 2.7 mm below the top surface of the workpiece, respectively (Figure 5.3). The distance between each position on Line A and B was 1 mm. The samples were sectioned in the middle of the weld and polished to mirror finish before evaluating the microhardness. The microhardness test was performed in a Vicker microhardness tester by OmniTech (model: MVH-11). A force of 200 g was applied for 10 s for AA6061-T6 pin and 500 g force for 10 s was used for cases with pin made of MS and OHNS to produce the indent. Three measurements were taken at each position on lines A and B. One reading was taken on the line, one above and another below the line, to ensure the indentations do not overlap. The average of the three readings was taken as the final microhardness at that position.

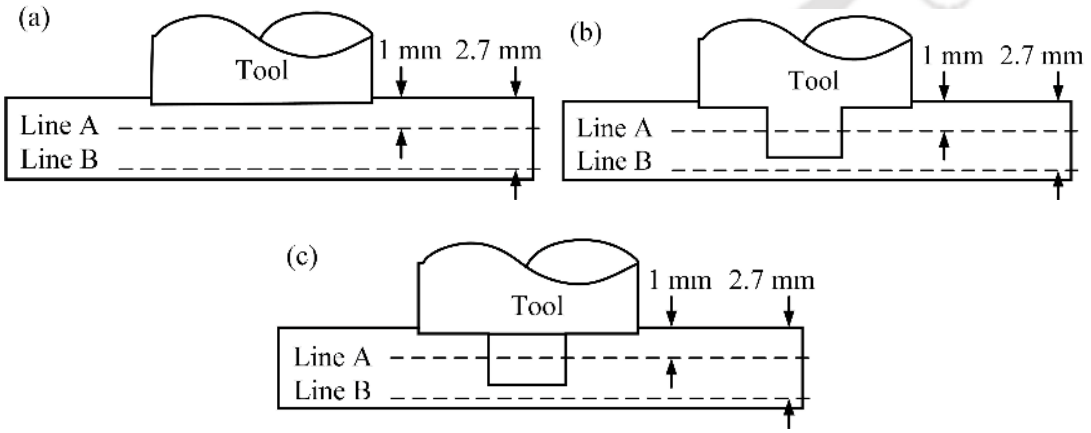

Figure 5.3 Schematic diagram of the cross section of the joint with position of the FSW tool shown as dotted line: (a) flat shoulder pinless tool (b) tool with pin (c) consumable pin

The joints were sectioned perpendicular to the top surface of the sheet through the centre of the weld spot using electrical discharge machining to cause minimum influence due to heat and plastic deformation during cutting operation. The sectioned welds were mounted on an epoxy resin mount for ease of handling the samples. The cross-sections were polished using silicon carbide emery papers of five different grit size: 400, 600, 900, 1000 and 2000 successively, until a smooth surface was arrived. Further polishing was done using a velvet cloth with a commercial abrasive paste to obtain a mirror finish. The abrasive paste usually used for polishing aluminium surfaces is Silvo paste and for harder MS or OHNS, alumina powder solution in water is used. If alumina powder solution is used with aluminium surface, it deposits an alumina layer and also causes micro-scratches on the surface. On the other hand, Silvo paste is ineffective in removal of finer scratches from the harder MS and OHNS surfaces. Therefore, the MS and OHNS parts were polished to mirror finish first with alumina powder, which caused some scratches on the aluminium alloy part. The scratches on AA6061-T6 were removed in the subsequent stage by polishing with Silvo paste, which did not affect the MS and OHNS part during polishing. Thus, polishing of both materials in the same component was achieved.

In order to observe the macrostructure and microstructure of the sections, different etchants were tried. Initially, standard etchant used for aluminium alloys, Keller's reagent with composition 1 mL HF, 1.5 mL HCl, 2.5 mL HNO_3 and 95 mL H_2O, was tried where sample was dipped for 50−60 s; however, only macrostructure could be observed with little details on microstructure. Another trial was made with Poulton's reagent with 12 mL HCl, 6 mL HNO_3, 1 mL HF (48% concentration), 1 mL H_2O. The modified form of this agent with added 10 mL HNO_3 and 16 mL H_2CrO_4 (chromic acid) solution (3g H_2CrO_4 in 10 mL H_2O) to the standard solution was used for better results. The samples were dipped in the solution for 5 s and immediately washed under running water for 10 s. The process was repeated three times. It was observed that in order to observe the grain boundaries of AA6061-T6 alloy under optical microscope, the modified Poulton's reagent delivered the best result. Fractography of the fractured surface during lap shear test was also carried out using field emission scanning electron microscope (FESEM – Zeiss, Model: Sigma 300).

5.2.2 Material Properties

The chemical composition of the base material and the three consumable pins is shown in Table 5.1. The chemical composition of the materials was evaluated using wet methods (IS-504-2002 for AA6061-T6 and IS-228-1997 for MS and OHNS). In the wet method, the sample is decomposed with reagents such as acids and dissolved in a solvent, where the targeted elements are identified and quantified. The chemical composition of the sheets and the AA6061-T6 consumable pin was the same. The base material properties at room temperature are shown in Table 5.2. The properties of the base material were evaluated at four different temperatures *viz.* room temperature, 100 °C,

200 °C and 400 °C, using universal testing machine for a tensile sample with 50 mm gauge length, 12.5 mm width and 1.5 mm thickness (modified ASTM E8/E8M standards). The plastic stress-strain curves for the base material at four different temperatures are shown in Figure 5.4. These properties were given as input for base material in simulation of the FSSW process. From the true stress-strain curve, strength coefficient and strain hardening exponent were evaluated by curve fitting using Hollomon expression given by $\sigma = k\varepsilon^n$, where *k* is the strength coefficient and *n* is the strain hardening exponent. Similarly, compressive properties were evaluated for the three consumable pin materials at room temperature, 100 °C, 200 °C and 400 °C, using compression test samples of 24 mm length and 12 mm diameter (ASTM E9 standards). The true plastic stress-strain data derived from experiments were used as material properties input for simulation of the behaviour of the consumable pin during welding (Figure 5.5). The software used for simulation, DEFORM-3D, assumes linear relation between stress and strain up to the yield point using database and beyond that, uses true stress vs plastic strain data, given as input from experiments. Hollomon flow stress model is used for extrapolation of the material properties to larger strain values.

Table 5.1 Chemical composition of pin and sheet materials

%	C	Mn	Si	S	P	Cr	Cu	Mg	Zn	Fe	Al
AA6061-T6	Nil	0.09	0.46	Nil	Nil	Nil	0.10	0.40	0.06	0.30	balance
MS	0.25	0.65	0.26	0.018	0.022	Nil	Nil	Nil	Nil	balance	Nil
OHNS	1.02	0.58	0.24	0.018	0.016	1.10	Nil	Nil	Nil	balance	Nil

Table 5.2 Tensile properties of AA6061-T6 at room temperature (RT), 100 °C, 200 °C and 400 °C

Property	**Value**			
	RT	**100°C**	**200°C**	**400°C**
Ultimate Tensile Stress (MPa)	330	285	251	190
0.2% offset Yield Stress (MPa)	276	242	220	156
Total Elongation (%)	12	13	13.5	16
Strain Hardening Exponent	0.1	0.1	0.1	0.1
Strength Coefficient (MPa)	415	378	300	205

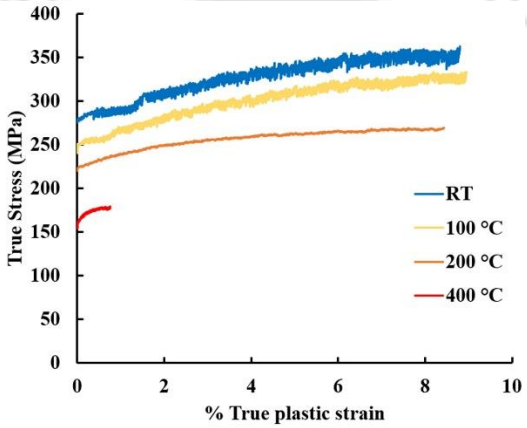

Figure 5.4 True plastic stress-strain curve for AA6061-T6 sheets up to necking at room temperature (RT), 100 °C, 200 °C and 400 °C

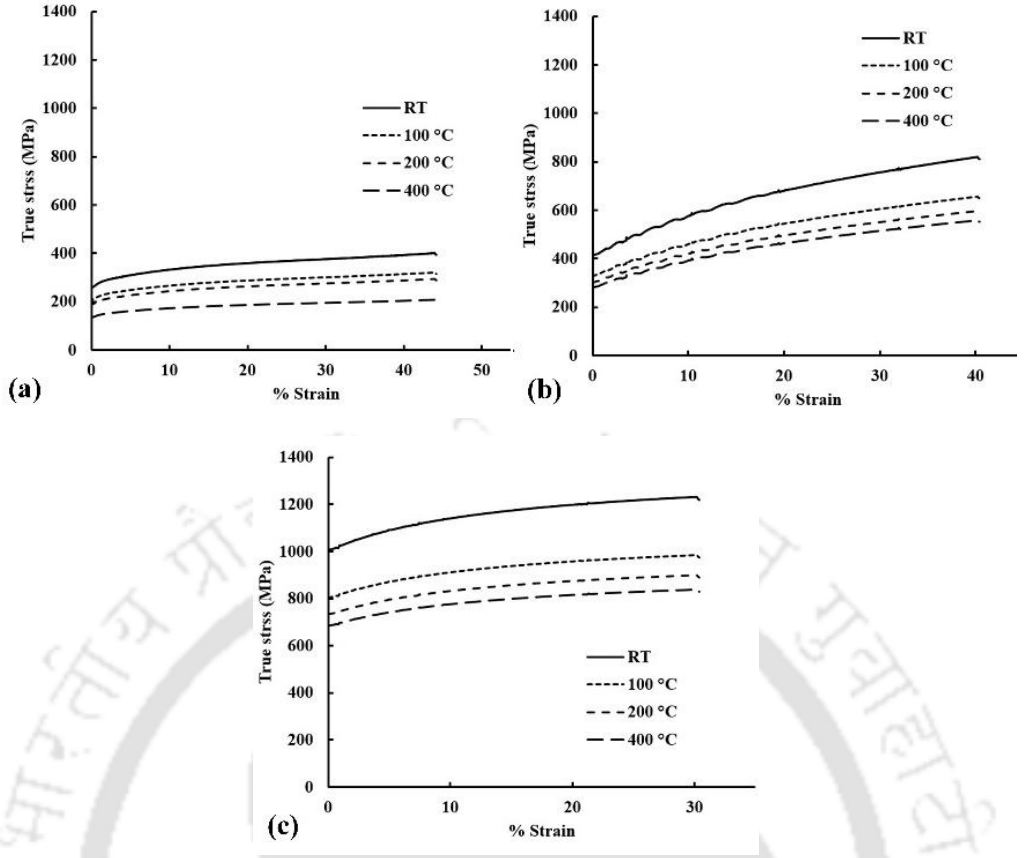

Figure 5.5 True plastic stress-strain curves of consumable materials during compression test for (a) AA6061-T6 (b) MS (c) OHNS at room temperature (RT), 100 °C, 200 °C and 400 °C

5.3 Finite Element Simulation Details

Finite element (FE) modelling of the process was carried out using commercial software DEFORM-3D (version 11.2). A fully coupled temperature-displacement model was developed using a Lagrangian implicit code with adaptive remeshing, which calculated both temperature and displacement simultaneously at each node. The solver used was sparse solver with direct iteration method. Dimensions of tool were kept as that of experiments. However, in order to reduce simulation time, a single circular sheet of 30 mm diameter and 3 mm thickness was used instead of two overlapping 1.5 mm sheets of 150 mm ×150 mm dimensions. A similar approximation was used by Buffa et al. (2006), where two overlapping sheets were considered as a continuum and modelled as one single sheet with the total thickness of the two sheets to reduce contact instabilities and simulation time. This continuum-based model is widely used by researchers in simulation of FSW/FSSW process for studying thermal, mechanical and material flow behaviour during welding (Trimble et al., 2012; Gao et al., 2013; Pashazadeh, 2014; Asadi et al., 2016). Tetrahedral mesh was used with minimum global element size of 2 mm and local minimum element size of 0.3 mm at the tool-workpiece interface for better accuracy and reasonable simulation time.

As discussed in Section 5.2.2, the experimentally obtained load-displacement data for each material were converted into true stress-strain data and used as material input for simulation. The

material properties of the workpiece were derived from tensile testing at four different temperatures. However, since the consumable pin undergoes compressive loading, material properties for the three consumable pin materials were derived from compression tests of the materials at four different temperatures (Figure 5.5). The true stress-strain data were fitted in Hollomon equation in order to find the strength coefficient (k) and strain hardening exponent (n). Subsequently, Hollomon flow stress model was used to extrapolate the material properties for larger strain values. The thermal properties of the materials used in simulation are provided in Table 5.3.

Table 5.3 Thermal properties of materials used in simulation

Material	Thermal conductivity (W/m•K)	Volumetric heat capacity ($\times 10^6$ J/m^3•K)	Coefficient of thermal expansion ($\times 10^{-6}$/°C)
AA6061-T6	180.2	2.43	22
MS	51.7	3.81	12
OHNS	51.7	3.81	12

Mesh sensitivity analysis was carried out for simulation of AA6061-T6 consumable pin FSSW. Initially, global mesh size was fixed at 2 mm and at the contact positions (Jain et al., 2016), mesh size was reduced locally to 1.5, 1 and 0.5 mm at consequent steps. Further, the local mesh size was reduced in steps of 0.1. It was found that there was no significant difference in results with the reduction of mesh beyond 0.3 mm (Table 5.4). The mesh sensitivity analysis provided 0.3 mm as the optimum local mesh element size, which was used for all other simulations. The element size of the consumable pin was considered as 0.3 mm throughout the whole component. The following boundary conditions were used: (i) bottom face of the sheet was assigned zero velocity in z-direction, (ii) tool was allowed to translate and rotate about the z-axis, (iii) the convective heat transfer coefficient between the workpiece and the surrounding environment was given as 20 W/m^2°C (Jain et al., 2017). The bottom face of the workpiece and the backing plate was assumed to have a heat transfer coefficient of 200 W/m^2°C at the interface. The heat transfer coefficient at the pin-workpiece, tool-workpiece and tool-pin interface is considered as 1100 W/m^2°C (Asadi et al., 2011). Figure 5.6 shows the different thermal boundary conditions used in the simulation.

Table 5.4 Mesh sensitivity analysis

Local mesh size (mm)	Average torque (N·m)	% error from experimental torque
2	9.80	18%
1.5	9.64	16%
1	9.72	17%
0.5	9.22	11%
0.4	9.03	8.7%
0.3	8.80	6%
0.2	8.79	5.9%
0.1	8.78	5.7%

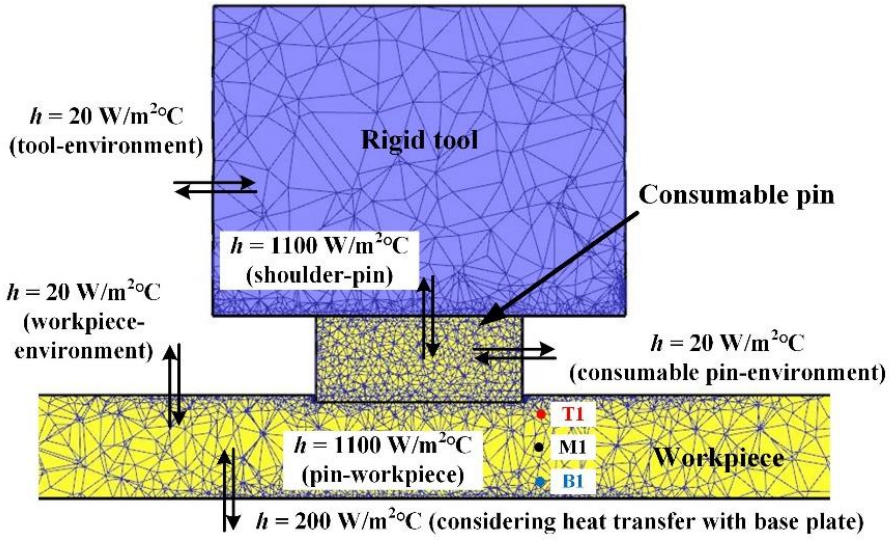

Figure 5.6 Different thermal boundary conditions used in simulation

The heat generated $\dot{q}$ during welding was the sum of frictional heat $\dot{q}_f$ and heat due plastic deformation $\dot{q}_p$.

$$\dot{q} = \dot{q}_f + \dot{q}_p \tag{4.1}$$

The temperature distribution is governed by Fourier heat conduction equation

$$k_t \nabla^2 T + \dot{q} = \rho c_p \frac{\partial T}{\partial t} \tag{4.2}$$

where ρ is the density, c_p the heat capacity per unit mass and k_t is the thermal conductivity. One of the most important parameters for simulation was the contact properties at the different contacting surfaces. Unlike conventional FSSW, where the contact properties for only the tool and workpiece interaction needs to be provided, FSSW with consumable pin requires additional contact properties for tool-consumable pin, consumable pin-workpiece and tool-workpiece interfaces. The contact properties used were derived from Chapter 3, where the contact properties at the different interfaces were determined using an inverse approach by reducing error between experimental and simulation torque during welding. As depicted in Figure 5.7, three interfaces namely, pin-workpiece, tool-workpiece and pin-tool exist. The pin-workpiece and pin-tool interface are modelled by constant shear friction (Tresca) model, given as $\tau = mk$, where *k* is the temperature-dependent yield stress of the material. Friction factor, *m* = 1 at the pin-workpiece and pin-tool interface and hybrid model with coefficient of friction, μ = 0.29 and *m* = 0.77 at the tool-workpiece interface was used in the present simulation. For the pin-tool interface *m* = 1 was used, since it was assumed that completely sticking friction exists between the pin and the tool. The assumption was taken since, the pin-shoulder interface was intentionally made rough using sandpaper of grit size 100 during experiments, to reduce slip between the pin and the shoulder. An inverse analysis of

friction factor at the pin-tool interface would result in a more accurate value of *m*. However, the main objective of the study is to emphasize the capability of consumable pin FSSW to produce joints without exit hole with comparable strength to that of conventional FSSW. Therefore, a simplified model with $m = 1$ was used at pin-tool interface for all consumable pins. In the hybrid model used at the shoulder-workpiece interface, frictional stress τ increased with increase in plunge pressure p as $\tau = \mu p$ up to limiting value of $\tau = mk$ (as discussed in Chapter 3). A maximum time increment of 0.05 s was used for each step, which the software automatically decreased whenever a lower time increment was required for convergence. The approach was used for all the different consumable pin materials.

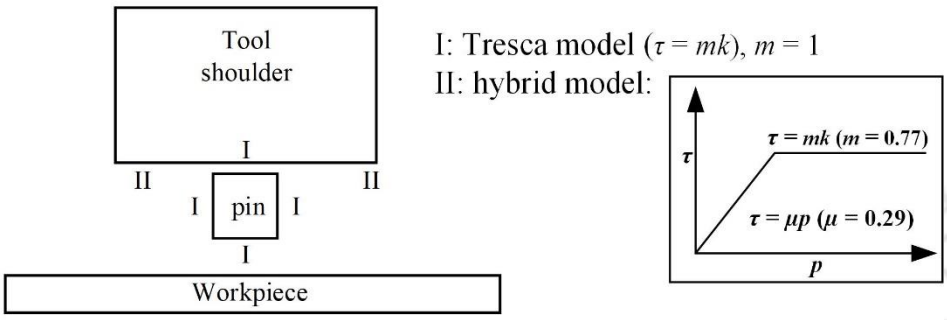

Figure 5.7 Friction model used at different interfaces denoted by condition I at pin-tool and pin-workpiece interface, condition II at tool-workpiece interface

5.4 Results and Discussion

In order to determine the joint strength, lap shear test was performed. Along with joint strength the quality was also assessed by determining the microhardness at the cross-section of the joint. The microstructure of the different zones produced during welding, namely SZ, TMAZ, HAZ and BM was also observed. Simulation of the welding process was performed to develop better understanding of the process by analysing the torque and plunge force produced during welding as well as temperature evolution during the joining process. A qualitative idea of material flow during welding was also determined, using that a mechanism of joint formation using consumable pin was proposed. The results have been discussed as follows.

5.4.1 Joint Strength

The joint strength of the welds was determined using lap shear test. The joint strength was determined for the three consumable pin materials *viz.* AA6061-T6, MS and OHNS. The strength of the joints was also compared to joints made with conventional FSSW with flat shoulder pinless tool and a tool with hard pin. Table 5.5 shows the lap shear test results for the different joints.

Table 5.5 Comparison of maximum load (failure load) during lap shear test in initial experiment

Process	Maximum load (kN)			Standard deviation
	Sample 1	Sample 2	Sample 3	
Conventional FSSW with flat shoulder tool	1.87	1.82	1.88	0.032
Conventional FSSW with tool having a hard pin	2.84	2.79	2.76	0.04
Consumable pin FSSW (material = AA6061-T6)	2.57	2.64	1.94	0.38
Consumable pin FSSW (material = MS)	2.39	2.14	2.51	0.19
Consumable pin FSSW (material = OHNS)	2.36	2.62	2.63	0.15

In case of the welds using consumable pin, the repeatability of the results was not achieved initially with standard deviation of three trials each as 0.38, 0.19 and 0.15, for AA6061-T6, MS and OHNS consumable pins, respectively. The reason for this could be the dependence of the behaviour of the consumable pin on its placement on the workpiece as well as on the alignment of the axis of the consumable pin and the tool, thus resulting in difference in joint properties. Since in the initial experiment, the consumable pin was only rested on the upper sheet with downward force from the tool, the position of the consumable pin was not controllable. In order to solve this, a small circular indent of 6 mm diameter was made on the upper sheet and the consumable pin was placed on the indent. This restricted the consumable pin from slipping away from its position and helped in maintaining the alignment of the pin and tool axis during welding. The repeatability of the results could thus be achieved as shown in Table 5.6, with the standard deviation of the trials reducing to 0.035, 0.06 and 0.061 for AA6061-T6, MS and OHNS consumable pins, respectively. The load-displacement graphs for the joints are shown in Figure 5.8a.

Table 5.6 Maximum load (failure load) during lap shear test for the consumable pin FSSW joints

Condition	Maximum load (kN)			Standard deviation
	Sample 1	Sample 2	Sample 3	
Consumable pin FSSW (material = AA6061-T6)	2.62	2.66	2.59	0.035
Consumable pin FSSW (material = MS)	2.48	2.6	2.54	0.06
Consumable pin FSSW (material = OHNS)	2.57	2.49	2.61	0.061

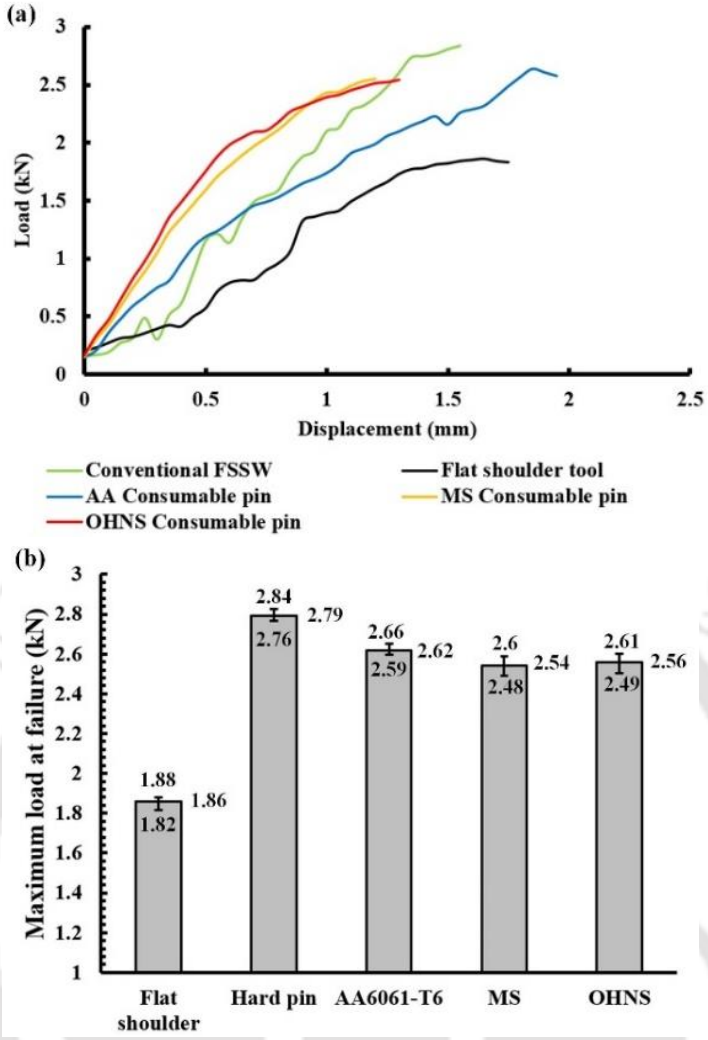

Figure 5.8 Comparison of lap shear test for different consumable pin FSSW and conventional FSSW joints: (a) load evolution (b) average maximum load bearing capacities for different joints

The maximum load bearing capacity was determined for each consumable pin material, conventional FSSW using flat shoulder pinless tool and a tool with hard pin. Average maximum load bearing capacities (three samples for each case) were calculated for the conventional FSSW using flat shoulder pinless tool, FSSW using hard pin tool, AA6061-T6, MS and OHNS consumable pin tool as 1.86 kN, 2.79 kN, 2.62 kN, 2.54 kN and 2.56 kN, respectively (Figure 5.8b). It can be observed from the results that the joint produced by conventional FSSW using a tool with hard pin has the maximum load bearing capacity in lap shear test. The load bearing capacity of the joint produced by conventional FSSW using a flat shoulder pinless tool is the minimum. The average load bearing capacity of joint produced by conventional FSSW using a tool having hard pin is 50% more than the maximum load bearing capacity of joint produced by flat shoulder pinless tool. The penetration depth of the SZ for the flat shoulder pinless tool is very low, which results in the low strength of the joint. The average joint strengths for welds produced using AA6061-T6, MS and OHNS consumable pins are 40.8%, 36.6% and 37.6% more than joints produced by conventional flat shoulder pinless tool. The increase in joint strength can again be attributed to increase in depth

of SZ in the weld. The consumable pins contributed to stirring of material within the workpiece in the weld zone resulting in increased SZ depth and thus the improved joint strength. However, the amount of stirring was less compared to the joint produced by conventional FSSW with a hard pin tool, which showed the maximum joint strength. It is also observed that although the SZ depths for MS and OHNS consumable pin are more than AA6061-T6 consumable pin, the AA6061-T6 consumable pin shows slightly higher joint strength. The reason could be the formation of brittle intermetallic compounds at the steel-aluminium interface during welding (Khan et al., 2017). The argument can be further substantiated by observing the extension at failure for the consumable pins, which is highest for the AA6061-T6. As compared to AA6061-T6 consumable pin, the extensions for MS and OHNS consumable pin were 39% and 34% lower, respectively. Maximum extension at failure for conventional FSSW using flat shoulder pinless tool, FSSW using hard pin tool, AA6061-T6, MS and OHNS consumable pin tool are observed as 1.8 mm, 1.6mm, 2.05 mm, 1.25 mm and 1.35 mm, respectively. It shows that the joint using AA6061-T6 consumable pin is comparatively more ductile as compared to the other joints, thus helps improve the joint quality. The typical lap shear test joint strengths reported in literature for conventional FSSW of similar sized AA6061-T6 sheets lie in the range 0.6−3.7 kN depending on process parameters (Gard and Bhattacharya, 2017). Yazdi et al. (2019) reported lower joint strengths for pinless tools. In this study using consumable pin FSSW, a comparable joint strength to that mentioned in literature was achieved, without an exit hole.

5.4.2 Microhardness

Figure 5.9a−e shows the variation of microhardness for different FSSW joint cross-sections. The hardness dropped sharply in the weld zone for all the welds. AA6061-T6 is precipitation hardened aluminium alloy with base material microhardness tested as 102 HV. The hardness depends on the precipitate distribution, such as Mg_2Si. Hardness reduction in the weld zone can be attributed to the dissolution of the precipitates and grain growth during FSSW. The hardness in the SZ is found to be high and gradually decreases through the TMAZ and reaches a minimum value and again increases towards base material exhibiting a ‘W’ shape appearance. The observation concurred with literature and according to literature the region where hardness is minimum is the HAZ (Venukumar et al., 2013). Cao et al. (2016) found similar trend in microhardness distribution during Refill FSSW or friction spot welding of AA6061-T6 sheets. SZ is associated with high temperature and severe plastic deformation, which leads to dynamic recrystallization and fine grain structure. Thus, hardness increase in SZ is due to the fine grains and fine precipitates. The microhardness in case of consumable pin remained almost constant for Line B. In Line A, the variations of hardness values showed that the HAZ is less pronounced as compared to conventional FSSW with and without pin. Due to this homogeneous nature of the weld zone, the AA6061-T6 consumable pin joint showed higher lap shear strength (refer Section 5.4.1) as compared to both MS and OHNS consumable pin

joints, where there is a pronounced change in hardness while moving from one material to another. The sudden increase in hardness in Line A as shown in Figure 5.9 (d and e) are the indentations on harder MS and OHNS consumable pin which remained in the joint.

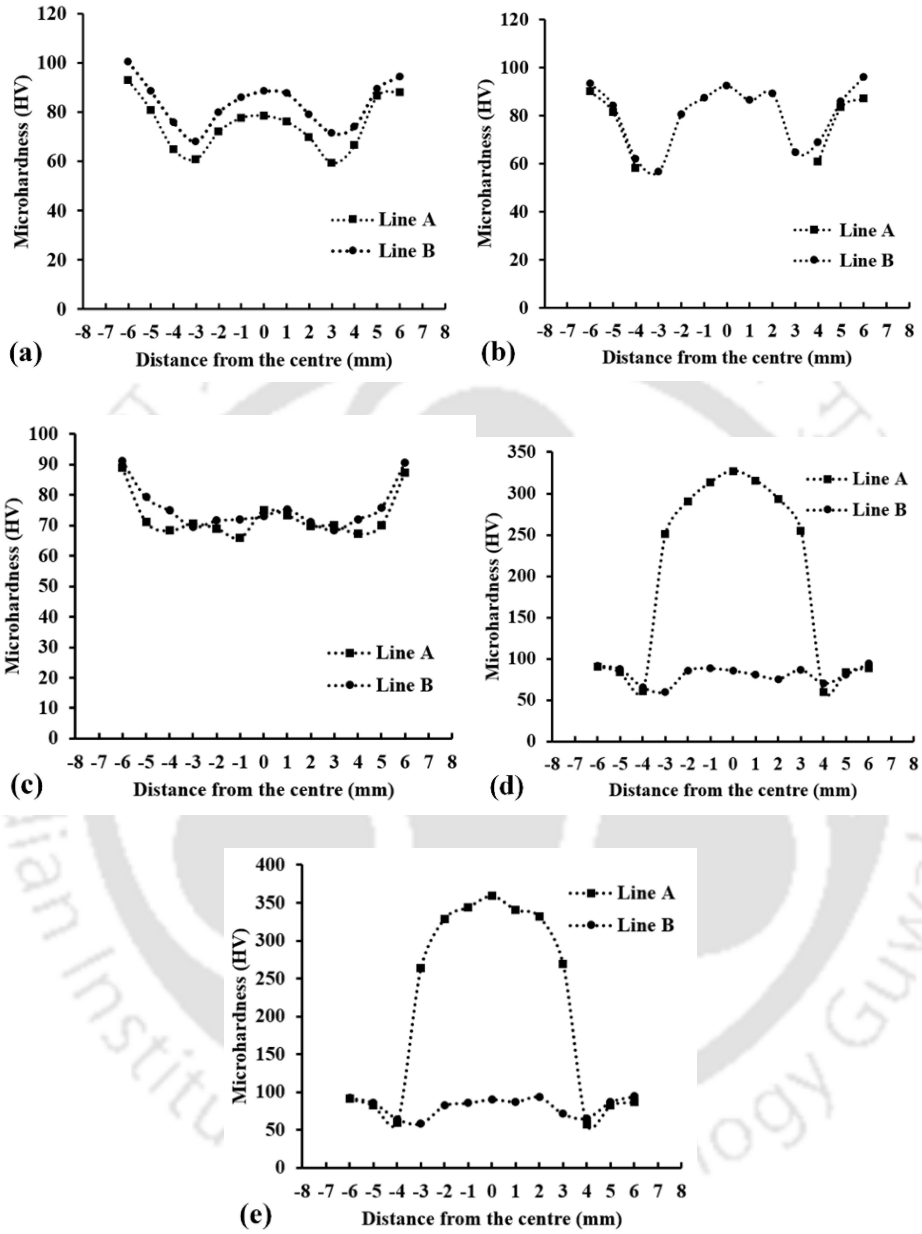

Figure 5.9 Microhardness plots for FSSW using (a) flat shoulder pinless tool (b) conventional hard pin tool (c) AA6061-T6 consumable pin (d) MS consumable pin (e) OHNS consumable pin

5.4.3 Microstructure and Joint Composition Analysis

The different weld cross-sections for joints produced by the consumable pins along with microstructure at different zones produced during welding *viz.* BM, HAZ, TMAZ and SZ are shown in Figure 5.10a−d. The cross-sections and microstructures are compared with welds made with conventional FSSW using a flat shoulder tool and a tool with a hard pin. The welds produced using

MS and OHNS consumable pins showed similar microstructure and properties; hence cross-section of joint produced by MS consumable pin only is shown. The microstructures reveal the material flow characteristics during the various FSSW processes.

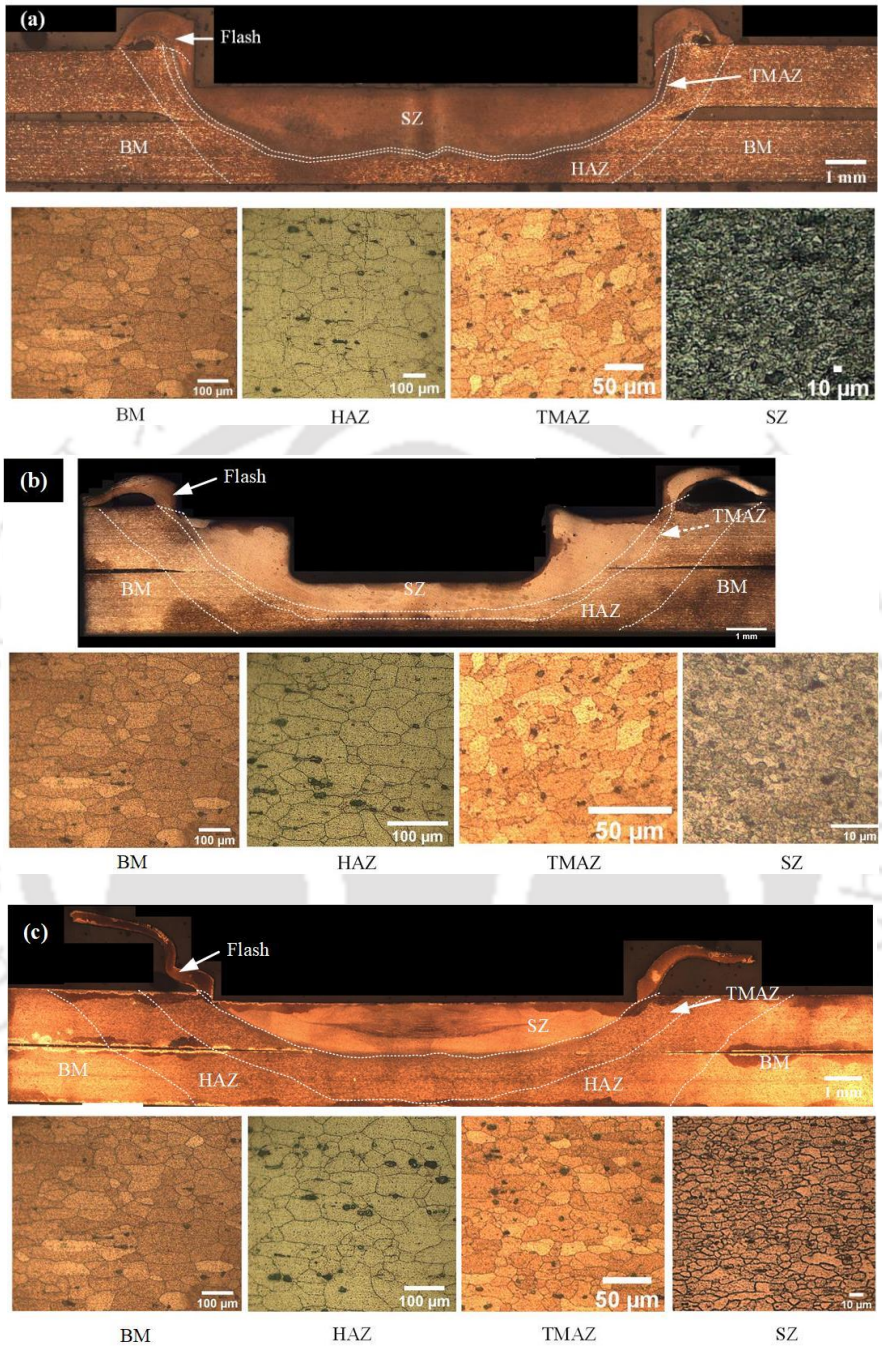

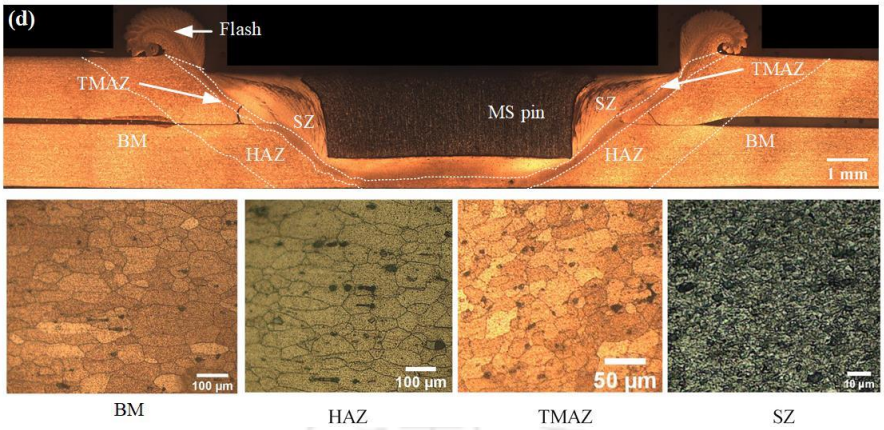

Figure 5.10 Macrostructure (at 5X magnification) and microstructure at different zones of the weld cross sections for FSSW using (a) flat shoulder pinless tool (b) hard pin tool (c) AA6061-T6 consumable pin (d) MS consumable pin. Magnifications used: BM (10X), HAZ (10X), TMAZ (25X), SZ (50X)

It is observed that the depth of SZ produced by the hard pin FSSW tool and MS consumable pin tool are almost equal. The flat shoulder pinless tool resulted in excessive flash at the outer vicinity of the tool shoulder due to excessive plunge force experienced by the workpiece. The SZ of the AA6061-T6 consumable showed a U-shaped SZ with traces of unstirred material at the centre of the weld. Although the depth of SZ is higher for FSSW using MS consumable pin as compared to AA6061-T6 consumable pin, the former joint contains defects in the form of cracks (Figure 5.11a) as well as sharp interfaces between the two sheets (Figure 5.11b), which results in reduction of joint strength during lap shear test. In all the joints it is observed that the grain size in the SZ is much smaller than the rest of the zones. The grain size increases when moving to the TMAZ, which can be considered as a transition zone between the smaller grains of the SZ and larger grains of the HAZ. The grains of the HAZ become larger due to grain growth as this zone experiences heat and rise in temperature during welding. TMAZ, although experiences larger amount of heat compared to HAZ, it also undergoes plastic deformation, which results in reduced grain size. Microstructures explain the trend in the microhardness distribution across the cross-section. The finer grain size in the SZ region gives higher microhardness according to Hall-Petch law. The microhardness lowers as we approach the HAZ which has the largest grain size. It is also observed that the TMAZ in case of AA6061-T6 consumable pin FSSW is spread wider and thus has more area with finer grains. This explains the relatively uniform high microhardness distribution in case of AA6061-T6 consumable pin FSSW. Thus, the microstructure can also be correlated to the microhardness of the joints as discussed in Section 5.4.2.

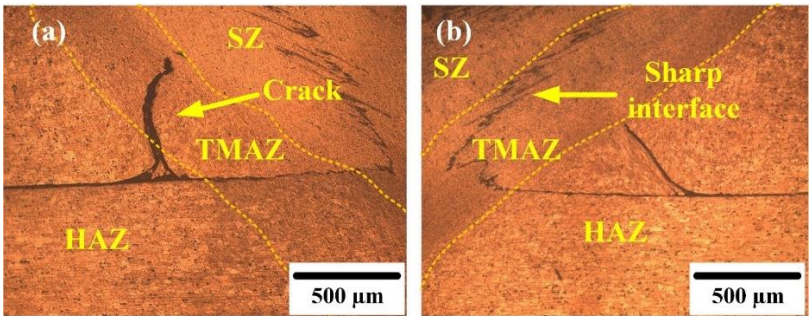

Figure 5.11 Defects seen in joint made with MS consumable pin: (a) crack (b) sharp interface between two aluminium alloy sheets (10X magnification)

Energy-dispersive X-ray spectroscopy (EDS) was performed at the interface of the consumable pin and base material to analyse the chemical composition after welding. In case of the AA6061-T6 consumable pin, since consumable pin and base material are of the same composition, the pin assimilated into the base material uniformly. It can be observed in Figure 5.12a, that there is a homogeneous chemical composition at the interface of consumable pin and base material. However, in case of MS consumable pin, a sharp interface can be observed with MS on one side and AA6061-T6 on the other side. Intermixing of material can be observed in some locations as Fe element was detected on the AA6061-T6 side (Figure 5.12b). However, there was no movement of Al into the MS consumable pin side. From XRD (X-ray diffraction) analysis, it was found that IMCs were formed at the interface of MS consumable pin and AA6061-T6 base material. The peaks on the XRD plot were compared to JCPDS (Joint committee on powder diffraction standards) data, which revealed the presence of Fe_2Al_5 (Aghajani Derazkola and Khodabakhshi, 2019) (Figure 5.12c). EDS analysis at the IMC layer confirms the finding as Fe and Al percentages were found to be approximately 28% and 70%, respectively. FeAl, $FeAl_3$, Fe_3Al, Fe_4Al_{13} are some other IMCs typically formed during FSW of steel and aluminium alloys, depending on temperature at the weld region (Wan and Huang, 2017). Fe_2Al_5 is a brittle compound. The IMC formation was responsible for weakening of joint strength in case of FSSW with MS consumable pin.

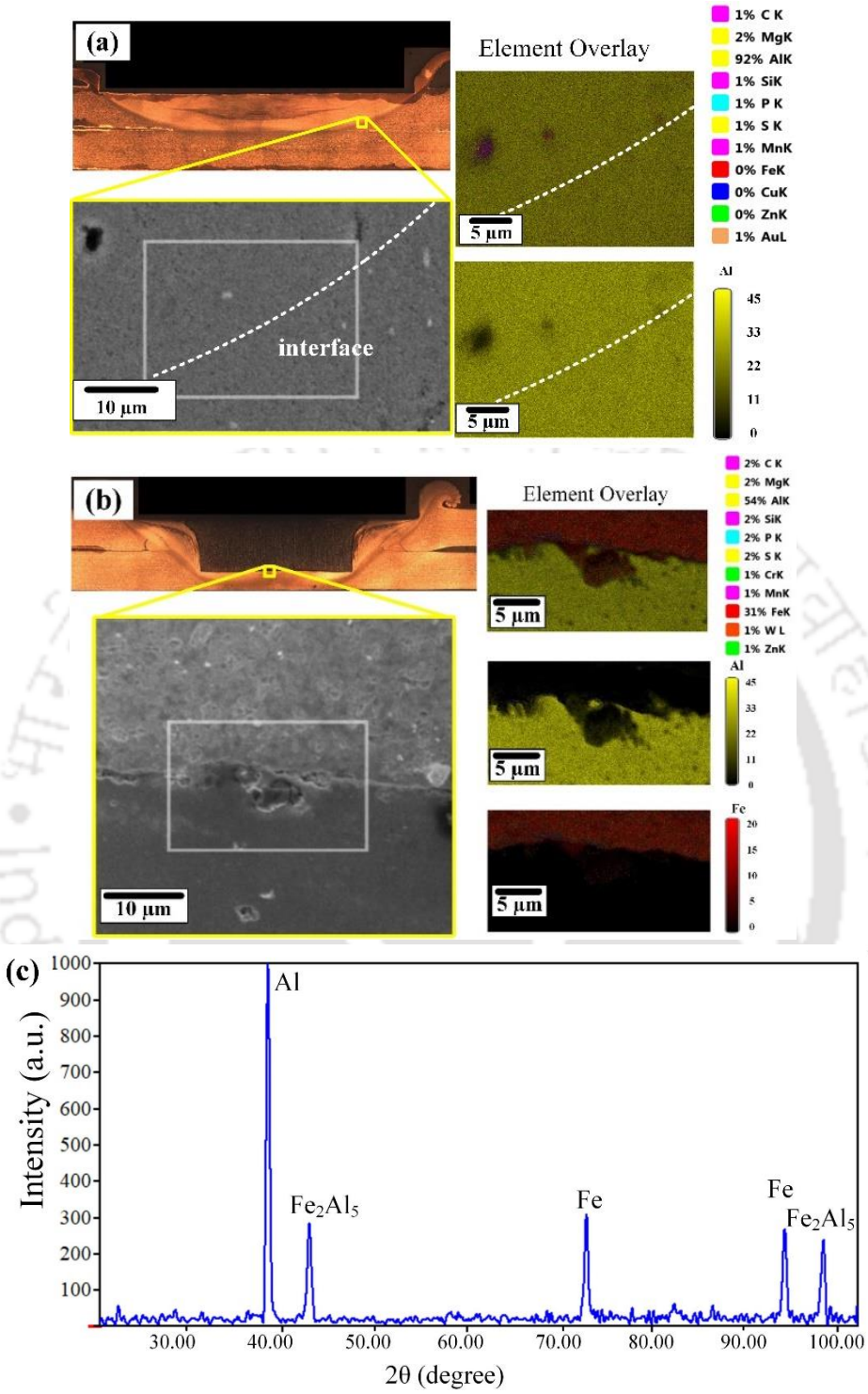

Figure 5.12 Chemical composition analysis at the interface of consumable pin and workpiece material post FSSW for (a) AA6061-T6 consumable pin (b) MS consumable pin and (c) XRD plot at the interface of MS consumable pin and AA6061-T6 workpiece showing IMC formed

5.4.4 Failure Modes

The different modes of failure in the welds during lap shear test were studied (Figure 5.13). It was observed that joint with FSSW using pinless tool failed due to partial nugget fracture. In this type of fracture, failure occurs at the softer region near the nugget region (Rana et al., 2018). Large

amount of thinning of the upper sheet occurs when producing a joint using pinless tool, thus it weakens the region near the weld nugget where the failure occurs. On the other hand, in case of the conventional FSSW using a hard pin tool, the failure mode observed was interfacial separation. The exit hole defect results in a smaller bonded area between the two sheets, which results in separation of the sheets when subjected to shear loading during lap shear test (Wang et al., 2020). Failure occurs at the circumference of the exit hole defect. The joints made using AA6061-T6 consumable pin failed by nugget pull-out failure. In this type of failure, the nugget remains attached to one of the sheets and failure occurs around it. Both MS and OHNS consumable pin FSSW joints showed combination of nugget pull-out and interfacial separation type of failure. It can be observed that the MS and OHNS consumable pin remains intact and attached to the lower sheet. Failure occurs at the boundary of the consumable pins where a sudden change in microhardness was observed (Figure 5.9). The bonded region of the two AA6061-T6 sheets is also small, leading to interfacial separation in the area surrounding the consumable pin. The presence of brittle intermetallic compounds at the interface of MS and OHNS with the AA6061-T6 sheet further weakens the joint in that region.

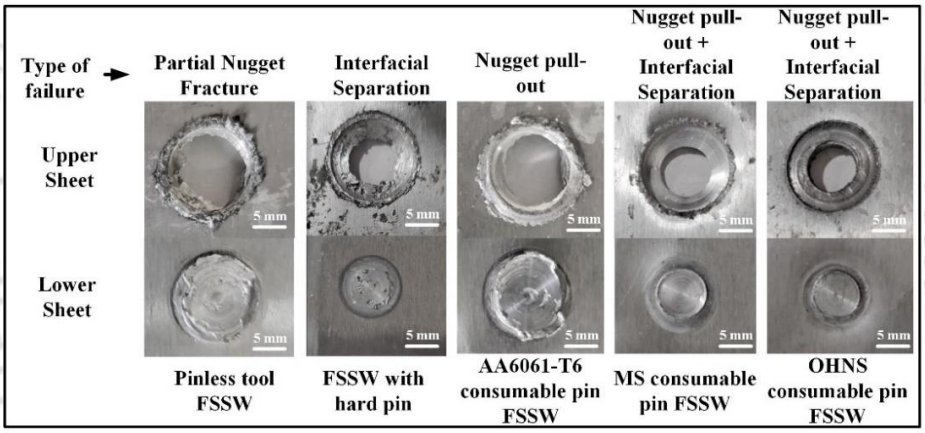

Figure 5.13 Different modes of failure in the joints produced during welding of AA6061-T6 sheets

It can be observed in Figure 5.14 that the fractured surface in case of MS and OHNS consumable pin FSSW contains lesser number of dimples as compared to welds made using pinless tool, hard pin tool and AA6061-T6 consumable pin, when observed under scanning electron microscope (SEM). The fractography study revealed that the fractured surface of MS and OHNS consumable pin FSSW joints contained dimples as well as flat surfaces, indicating a combination of ductile and brittle modes of failure. When failure occurs with little or no plastic deformation, a smooth and flat surface appearance is observed, denoting brittle mode of failure (Bonhomme et al., 2009; Wouters and Froven, 1996). Higher density of dimples in pinless tool, hard pin tool and AA6061-T6 consumable pin FSSW implies ductile mode of failure (Saravanan et al., 2016). A high density of fine equiaxed dimples in fractography denotes ductile failure (Garg et al., 2020). The larger size dimples present in AA6061-T6 consumable pin FSSW as compared to pinless tool FSSW is due to larger plastic deformation in case of the former (Agrawal et al., 2021).

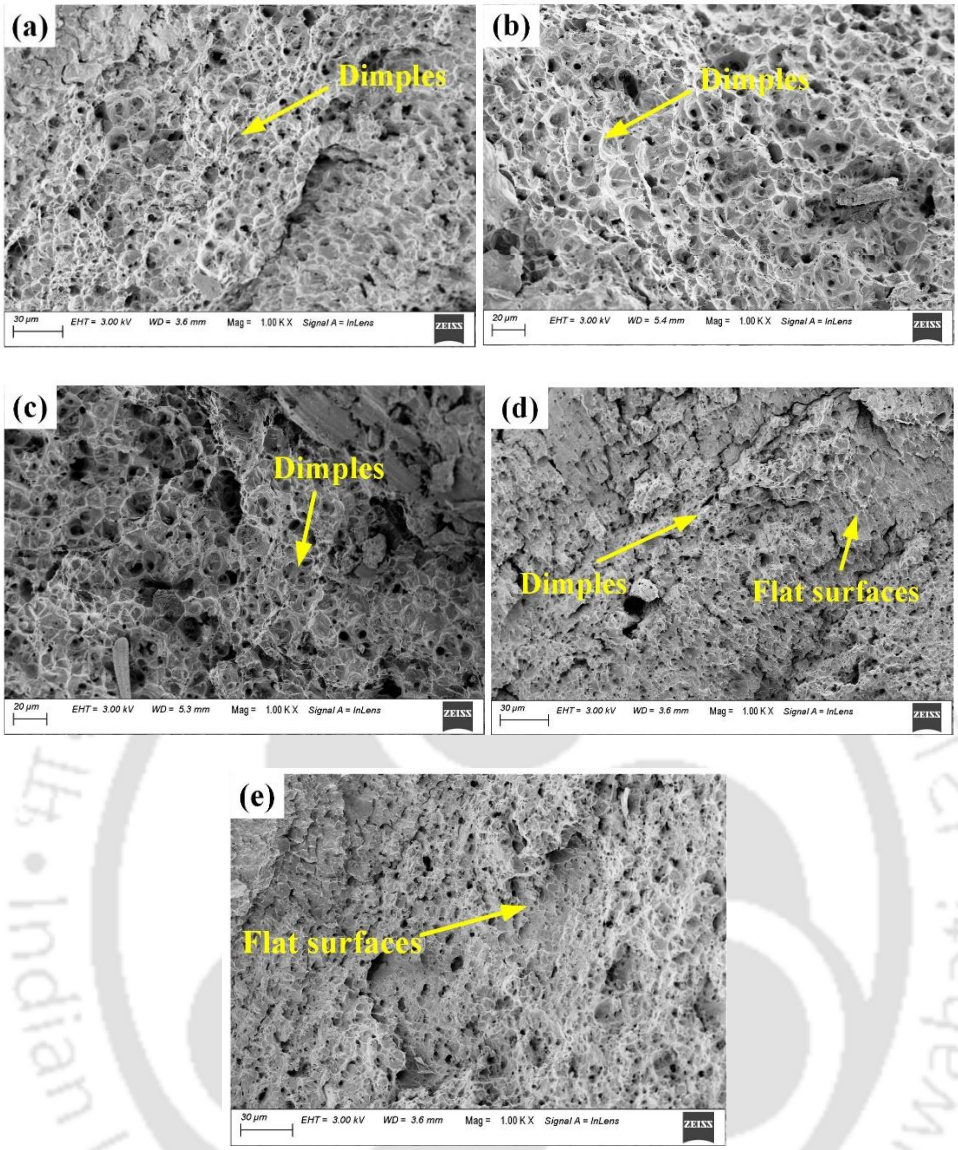

Figure 5.14 SEM images (1000X magnification) of fractured surfaces during lap shear test of FSSW joints produced by (a) pinless tool (b) tool with rigid pin (c) AA6061-T6 consumable pin (d) MS consumable pin (e) OHNS consumable pin

5.4.5 FE Simulation Results

FE simulation of FSSW using consumable pin was performed in DEFORM-3D. The model was validated by comparing experimental and simulation torque during welding. A reasonably acceptable match in torque evolution between experimental and FE simulation was obtained using the model. For AA6061-T6 consumable pin, the average experimental and simulation torque in the range of 0 to 10 s were found to be 8309 N·mm and 8814 N·mm, respectively. For MS consumable pin, average experimental torque was 7799 N·mm and average simulation torque was 8160 N·mm. On the other hand, 7761 N·mm and 8320 N·mm were found to be average experimental and simulation torque, respectively for OHNS consumable pin. Average error between experimental and simulation torque was found to be 6%, 4.74% and 7.2% for FSSW using AA6061-T6, MS and

OHNS consumable pins, respectively. The comparison between experimental and simulation torque for FSSW using different consumable pin materials is shown in Figure 5.15. The average torque during welding for conventional FSSW with hard pin was reported to be 7998 N·mm in Chapter 3, which is comparable to average torque during FSSW using MS and OHNS consumable pins. However, the average torque during welding with AA6061-T6 consumable pin was higher than conventional FSSW with hard pin as well as MS and OHNS consumable pins. This could be due to extra torque utilized in plastic deformation of the AA6061-T6 consumable pin. The deformation for AA6061-T6 was observed to be more than MS and OHNS consumable pins.

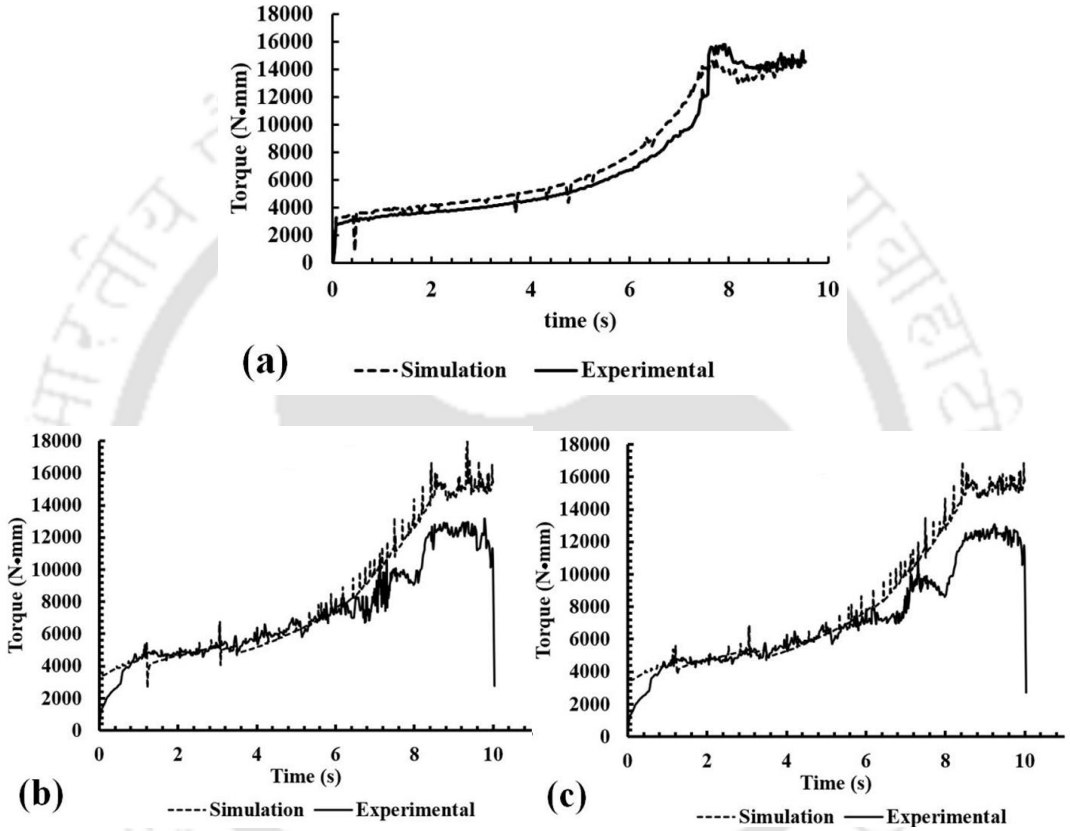

Figure 5.15 Comparison of torque evolution from experiments and FE simulation for FSSW using (a) AA6061-T6 consumable pin (b) MS consumable pin (c) OHNS consumable pin

It can be observed from Figure 5.15 that the torque increases gradually as the pin and shoulder is plunged inside the workpiece. In case of conventional FSSW, it is observed in literature that there is a sudden increase in torque as the shoulder touches the workpiece, which is not observed in case of FSSW using consumable pin. The reason may be due to deformation of the pin, which bulges outwards at the tool-pin interface, covering a part of the tool as the tool is plunged downwards. This results in a gradually increasing contact area between the workpiece and the tool, thus a gradual increase in torque as well. It is also observed that the torque evolution for both MS and OHNS consumable pins are similar due to their comparable material properties. Torque predicted by FE simulation is slightly overestimated for all cases, implying that there may be slip between pin and shoulder in case of experiments.

The temperature generated during welding was analyzed at two points, P1 and P2, taken on the upper surface of the workpiece at a distance of 5 mm and 15 mm from the shoulder edge, respectively. Temperature evolution from experiments and FE simulations is compared in Figure 5.16 (a−c). The experimental temperatures at P1 and P2 were taken as the average of three trials for each welding condition at the respective points. There was good repeatability with an average coefficient of variation as 4%. However, the simulations over-predicted the temperature, although the trend of time-temperature curves was in good agreement. The quantitative error in the range of 10–12% at P1 and 14–16% at P2 may be due to variation in thermal properties. These properties were taken from DEFORM-3D database and were not verified experimentally in this study. Moreover, point P2 was close to the clamping setup and some amount of heat dissipated out through the setup. Although heat dissipation through the base plate was considered in the FE model, heat dissipation through clamping setup was not modelled in order to reduce complexity and time of the simulation. Nevertheless, as the qualitative prediction is good, it is possible to reduce the error by model-updating (mainly by adjusting the thermal properties). However, the same was not done here considering the focus and scope of present work.

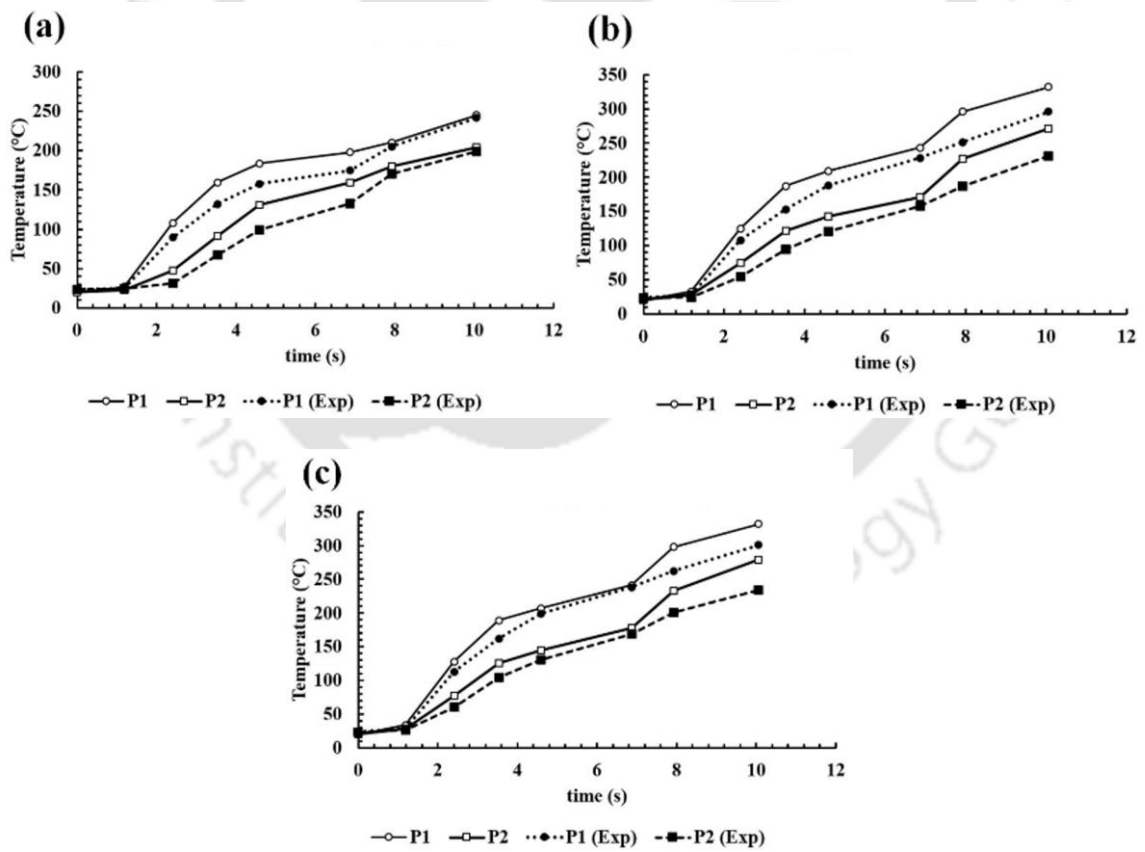

Figure 5.16 Temperature evolution during FSSW with (a) AA6061-T6 consumable pin (b) MS consumable pin (c) OHNS consumable pin

The peak temperature generated using AA6061-T6 consumable pin is less compared to MS and OHNS consumable pin FSSW. As AA6061-T6 is softer compared to MS and OHNS, the

stirring of workpiece material is comparatively lesser and consequently, heat generated due to plastic deformation of the workpiece is also less. However, in case of the weld made using AA6061-T6 consumable pin (Figure 5.17a), the temperature distribution during plunging is different from weld made using MS and OHNS consumable pins. Figure 5.17 shows the temperature contours at the joint cross-sections and upper surfaces of the joints made using different consumable pins. The temperature distribution in case of FSSW by MS and OHNS consumable pins is similar to that of conventional FSSW process. The temperature distribution follows a V-shaped pattern for all conditions, which is similar to the shape of the SZ as observed in Section 5.4.3.

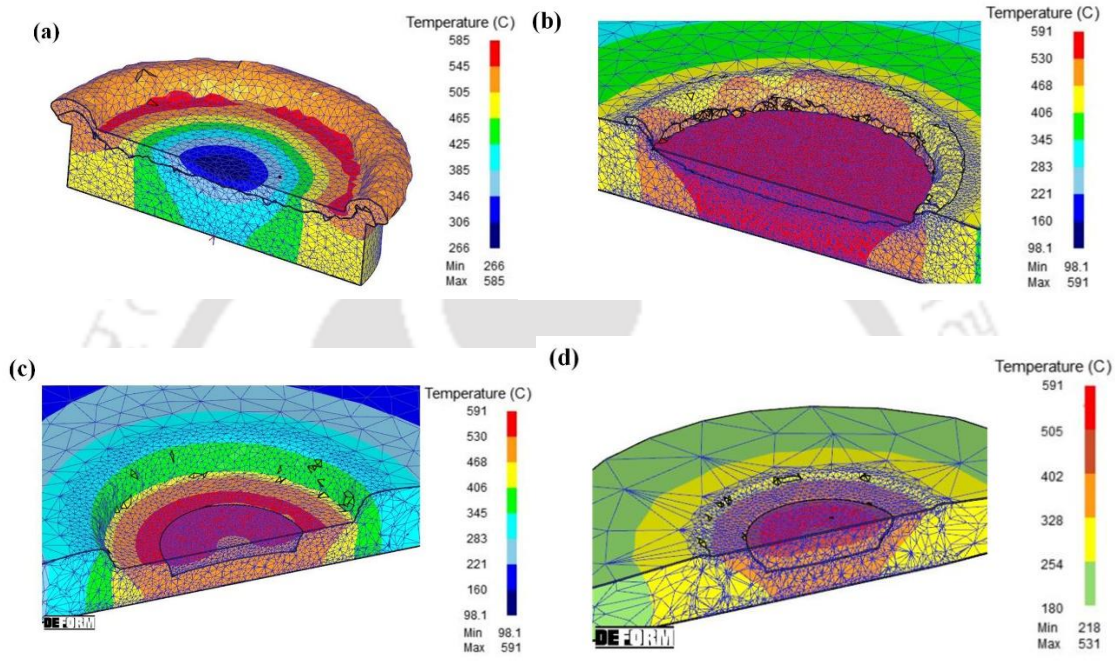

Figure 5.17 Temperature contour at the joint cross-section for (a) AA6061-T6 consumable pin during plunging (b) AA6061-T6 consumable pin during dwelling (c) MS consumable pin and (d) OHNS consumable pin during dwelling

The reason for the unique temperature distribution in case of AA6061-T6 consumable pin is due to unique characteristics of heat generated due to friction as well as severe plastic deformation of the consumable pin. Plastic deformation of the pin at the outer edges is higher as compared to its inner parts. The plastic deformation inside the consumable pin increases with increasing radius of the pin due to increased tangential velocity of material at the outer radii. Thus, the temperature is higher at the periphery of the pin compared to its interior. Thus, although peak temperature produced in case of AA6061-T6 consumable pin FSSW is less, it is produced at the outer boundary of the pin, resulting in a wider TMAZ area as seen in Section 5.4.3. The temperature in this region is high enough for the grains to undergo dynamic recrystallization and the finer microstructures results in a relatively higher uniformly distributed microhardness in the weld zone (Section 5.4.2). During dwelling, the temperature distribution becomes similar to conventional FSSW due to more prominent effect of the tool shoulder.

5.4.6 Mechanism of Joint Formation

It is known from literature that in order to produce effective FSSW joint the depth of SZ should be high. Flat shoulder pinless tools are unable to produce sufficient SZ depth without using excessive plunge depth (Aota and Ikeuchi, 2009). Conventional FSSW with hard pin aids in increasing the SZ depth and thus improves the joint quality. The primary intention of using a consumable pin is also to increase the SZ depth in the weld zone while delivering a joint without exit hole. The mechanism of joint formation during FSSW using consumable pin and conventional FSSW (FSSW with hard pin) is discussed in this section.

Figure 5.18 shows the deformation behaviour and material flow of the AA6061-T6 consumable pin and the workpiece. There are five stages during the process.

Stage 1: The consumable pin is placed on an indentation mark of identical diameter on the upper face of sheet and downward axial force is applied using a hard flat shoulder tool.

Stage 2: The tool starts rotating and the friction between the shoulder and the pin causes the pin to rotate along with the tool. This initiates material stirring, depicted by arrows on the upper and the bottom face of the sheet.

Stage 3: The deformation of the pin increases with increase in plunge depth.

Stage 4: Although the upper part is highly deformed, rotation of the pin continues. With the pin rotation, the workpiece material continues to get stirred.

Stage 5: The rotation of the pin ceases when the hard shoulder of the tool touches the workpiece. While stirring of workpiece material continues due to the rotating shoulder of the tool, the consumable pin gets assimilated into the workpiece and the consumable material stirs along with workpiece material. The blue arrows in circular motion on the bottom face of the workpiece show stirring of workpiece material up to bottom face.

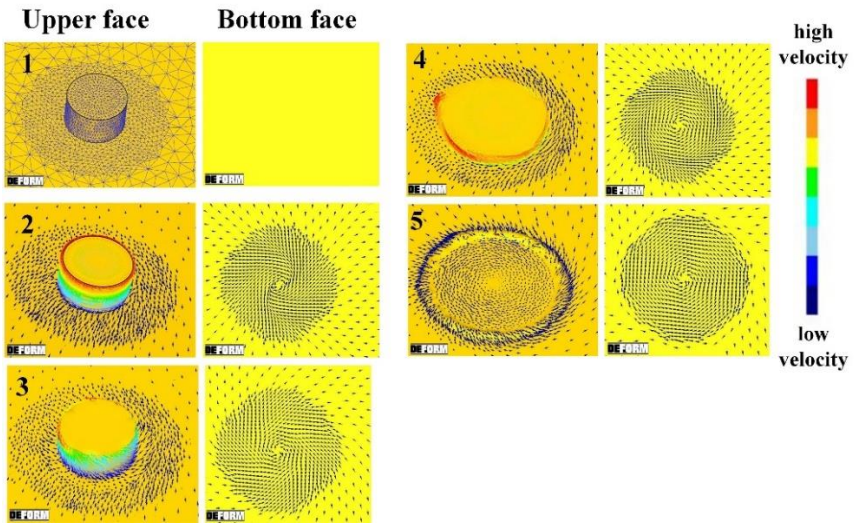

Figure 5.18 Joint formation using consumable pin depicting material velocity during welding

Three points on the workpiece in the vicinity of the pin, T1 (just below top surface), M1 (middle of workpiece) and B1 (just above bottom surface) were tracked during simulation to understand the material movement (Figure 5.6). Apart from stirring of material in the horizontal plane, there is swirling motion around the pin in vertical plane as well. It is observed in Figure 5.19a that T1 is stirred in a spiral motion. M1 is stirred less in the horizontal plane; however, vertical movement around the pin is more pronounced. Point B1 shows very little movement in both vertical and horizontal directions. The vertical motion of material can be seen by observing the microstructure around the SZ as shown in Figure 5.19c. In comparison to conventional FSSW, the stirring of material at larger depths is low. It can be seen in Figure 5.19b that for conventional FSSW, although stirring of material for top point T1 is similar, stirring at middle point, M1 and bottom point, B1 are more as compared to consumable pin FSSW. Thus, it can be observed that the consumable pin contributed to stirring of the workpiece material similar to a conventional hard pin; however, amount of stirring was less at higher depths as compared to hard pin.

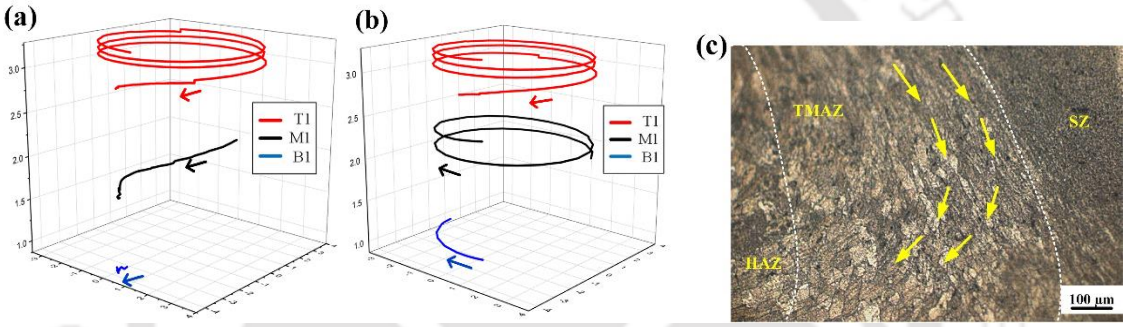

Figure 5.19 Material flow during FSSW (a) using AA consumable pin: tracking three points in the vicinity of the pin (b) conventional FSSW with hard pin: three points in the vicinity of the pin tracked (c) vertical motion of material in the weld cross-section (20X magnification)

The material in the vicinity of the consumable pin is stirred around it in spiral motion, leading to mixing of materials at the interface of the sheets. The heat generated due to friction and plastic deformation helps in softening the workpiece for the stirring to take place, similar to conventional FSSW. However, in conventional FSSW where the exit hole remains after tool retractions, in case of FSSW using consumable pin, the pin after completely entering inside the workpiece, stops rotating and gets assimilated into the workpiece. The rotating hard shoulder during dwelling ensures further stirring and mixing of pin and workpiece material leading to a seamless bonding. The consumable pin increases the depth of stirring zone as compared to flat shoulder pinless tool and produces effective FSSW joint without exit hole defect. Thus, from the experimental observations and simulation results, it is proposed that the consumable pin stirs the material around it in the weld, leading to better mixing, which at elevated temperature under high downwards plunge force results in all components bonding together and in joint formation.

5.5 Conclusion

A novel method of producing exit-hole-free FSSW joint using a consumable pin was successfully demonstrated. The process was able to produce the joints using a cost-efficient, simple tool and setup. The method is a single-step process for producing effective exit-hole-free FSSW joints, which is both fast and cost-effective. The weld quality analysed using lap shear test, microhardness and microstructure studies showed proper joining and improved joint strength over conventional flat shoulder FSSW. The following conclusions can be drawn from the study:

(i) The joints produced using consumable pin were compared to conventional FSSW using a pinless flat shoulder tool and a tool with hard pin. It was found that the use of consumable pin significantly increased the joint strength in lap shear test (36−40% higher) as compared to conventional FSSW using a pinless flat shoulder tool. However, joint strength was slightly lower as compared to FSSW using tool with a hard pin for the same process parameters. Therefore, depending on the application, the slight decrease in joint strength may be overlooked to opt for an exit-hole-free FSSW joint.

(ii) Among the different consumable pin materials used, *viz.* AA6061-T6, MS and OHNS, the best weld quality was achieved for welding using AA6061-T6. Although stirring and temperature produced in case of MS and OHNS consumable pins were more compared to AA6061-T6 consumable pin, the joints produced using the former pins showed ~3% lower failure load and 34−39% lesser elongation at failure during lap shear test. It is due to the formation of brittle intermetallic compounds (Fe_2Al_3) at the dissimilar material interface. A sharp interface and cracks were also observed in MS and OHNS consumable pin FSSW. On the other hand, a seamless bonding with homogeneous chemical composition was observed in case of AA6061-T6 consumable pin. Thus, AA6061-T6 is more suitable as the pin material for consumable pin FSSW of AA6061-T6 sheets.

(iii) FE simulation of the welding process using DEFORM-3D was able to predict torque and temperature during welding within 10% and 15% errors, respectively. Simulated temperature contour and microstructure analysis at the cross-section of the AA6061-T6 consumable pin FSSW joint showed wider TMAZ area, resulting in a uniform distribution of refined grains due to dynamic recrystallization leading to uniform microhardness and higher joint strength. From the study of material flow and deformation behaviour of the consumable pin during the welding, joint formation mechanism during FSSW using consumable pin was explained. The consumable pin aids in stirring the workpiece material resulting in better mixing and under high downwards plunge forge, at elevated temperature due to friction and plastic deformation, results in bonding of the two sheets. The consumable pin gets assimilated into the workpiece material and produces an exit-hole-free FSSW joint.

Chapter 6

Effect of Rotational Speed on Exit-Hole Free FSSW with Consumable Pin

6.1 Introduction

In order to have proper control over the process and optimise the weld quality, studies on the effect of process parameters on FSSW joints have been performed for both conventional FSSW and exit-hole-free FSSW. The rotational speed of the tool is one of the key parameters affecting joint quality as it primarily determines the amount of heat input into the weld zone due to the rubbing action of the tool and workpiece surfaces and subsequent plastic deformation of the workpiece material (Arora et al., 2009). It is observed in literature that an increase in tool rotational speed results in increase in temperature of the SZ. It is important to assess the relationship between rotational speed and heat input as an insufficient heat input at lower rotational speed results in inadequate plasticization, whereas, higher heat input at higher rotational speeds causes dissolution, undesirable grain coarsening and lowering dislocation density, leading to decrease in joint strength. It is recommended to keep the rotational speed moderately low; enough to cause plasticization of the workpiece while maintaining SZ properties closer to the BM (Hao et al., 2013; Jambhale et al., 2015; Merzoug et al., 2010). A lower rotational speeds is also recommended in case of refill FSSW to ensure good material flow and high tensile shear force (Lage et al., 2019; Ferreira et al., 2020). Tier et al. (2013) found that the joint strength decreased with increase in rotational speed from 900 to 1900 RPM during RFSSW due to unwanted grain growth. Similar to conventional FSSW, rotational speed was found to contribute maximum in determining nugget width and joint strength in RFSSW (de Castro et al., 2018).

This chapter investigates the effect of rotational speed on the weld quality during FSSW using consumable pin. Weld quality is assessed by lap shear strength, microhardness distribution and microstructure in the cross-section of the joints. Fracture analysis of the joints was performed. In order to gain more insight about the process, FE simulations were conducted using DEFORM-3D. Temperature distribution, force and torque evolution and material flow during FSSW were predicted using simulation and compared with experimental results. Lap shear tests were also simulated to predict weld strength and fracture using Freudenthal damage model and Cockcroft-Latham damage model. Such simulations helped predicting weld strength beyond the experimental limits of machines used in this study.

6.2 Experimental Details

The welding operation was performed on two AA6061-T6 sheets of dimension 150 mm ×150 mm ×1.5 mm placed in lap configuration. A flat shoulder tool of H13 tool steel material was used along with an AA6061-T6 consumable pin. The working principle of the welding technique is discussed in Chapter 5.

In this study, the rotational speed of the tool was varied, while keeping all other parameters constant, to understand its influence on joint formation and joint strength. The diameter of the tool used was 12 mm. The consumable pin was of 6 mm diameter and 2.5 mm length. A constant plunge rate of 20 mm/min and dwell time of 10 s was used for all experiments. Five different rotational speeds viz., 360, 462, 557, 900, 1200 revolutions per minute (RPM) were used. The corresponding surface speed at the outer diameter of the tool varied from 226 mm/s to 753 mm/s for 360 RPM to 1200 RPM. Torque and plunge force during the experiment was recorded using strain-gage based integrated sensors in the machine (strain data logger-MP31C09). Two K-type thermocouples were attached to the workpiece to record the temperature during welding. The thermocouples were attached on the top surface of the workpiece at 5 mm and 10 mm from the tool edge (Figure 6.1).

In order to study the effect of rotational speed on joint strength, lap shear test was performed. The samples were prepared according to AWS B4.0-2007 standards and the joint strength was evaluated in a universal testing machine with uniform cross-head speed of 1 mm/min at room temperature. Lap shear test on three samples for each set of process parameters were performed and the mean value was taken as the final joint strength. The fractured joints after the lap shear test were also analysed for their mode of failure. Fractography analysis after lap shear test was performed using field emission scanning electron microscope (FESEM – Zeiss, Model: Gemini). The microhardness at the cross section of the welds was evaluated using a Vickers microhardness tester by OmniTech (model MVH-11). Two lines, upper line and lower line, were taken at 1 mm from the top and 0.5 mm from the bottom surface of the workpiece, respectively (Figure 6.2). On each line the readings were taken at 13 equidistant positions, which were 1 mm apart (marked A−M in Figure 6.1). The microhardness at each position was evaluated as the average of three readings taken above the line, on the line and below the line, such that the indentations do not overlap. For all the positions, 200 g force was applied with 10 s dwell time to make the indentations. For analysing the microstructure, the joints were sectioned at the centre of the weld spot perpendicular to the top surface. The sectioned joints were mounted on an epoxy resin mount and polished using silicon carbide emery paper. A detailed description of the characterization process along with material properties and chemical composition of base material and consumable pin are discussed in Chapter 5. The assumptions regarding flow stress and other properties and their incorporation into simulation are also discussed in detail in Chapter 5.

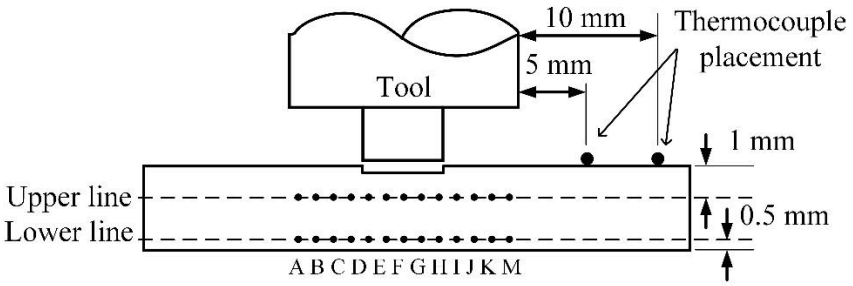

Figure 6.1 Schematic diagram of cross-section of the joint with microhardness testing positions and thermocouple placements (not-to-scale)

6.3 FE Simulation of FSSW using a Consumable Pin and Lap Shear Test

FE simulation of FSSW and subsequent lap shear test was performed using commercial FE analysis software DEFORM-3D (version 11.2). The simulation consisted of two stages. In stage 1, FSSW using consumable pin was simulated. The changes in material properties after the simulation were retained and passed on to stage 2, where lap shear test simulation was performed. The details of the formulation used are discussed in this section.

6.3.1 FSSW Simulation

Lagrangian implicit code with adaptive remeshing was used to develop a fully coupled temperature-displacement model that calculated temperature and displacement at each node simultaneously. Sparse solver with direct iteration was used to converge to the solution. The maximum time increment used for each step was 0.05 s. If a lower time increment was required for convergence, the software automatically decreased it to smaller time step. The tool and consumable pin dimensions were as that of experiments. A continuum-based model was used while modelling the workpiece as used by Buffa et al. (2006) as discussed in Chapter 5. The workpiece in this study was modelled according to dimensions of lap shear test, since the retained material properties after FSSW simulation were passed on to the next stage, where lap shear test was simulated on the same workpiece. The workpiece in this study was modelled according to dimensions of lap shear test. However, the centre of the overlapped portion was modelled as a continuum of 12 mm diameter with thickness as the total thickness of the two sheets, i.e., 3 mm (Figure 6.2). The diameter of the continuum zone was chosen equal to the diameter of the tool shoulder as most of the stirring occurs in the region beneath the tool shoulder region (Mishra and Ma, 2005). FSSW simulation was performed over this continuum region. The stirring of material in this continuum zone helped in comparing the effect of stirring and plastic deformation at elevated temperature and strain rate on flow stress, strain hardening and residual stresses, which in turn governed joint strength with respect to rotational speed. To verify the assumption and determine the sensitivity of the continuum zone diameter, two more simulations were conducted for welding at 1200 RPM and subsequent lap shear

test. Increasing or decreasing the size of the continuum zone increases the error in lap shear strength prediction because of unrealistic assumption (Table 6.1). A zone of 12 mm diameter (equal to shoulder diameter) only provides reasonable results.

Table 6.1 Variation of lap shear strength prediction with change in continuum diameter for welding at 1200 RPM (using Cockcroft-Latham damage model)

Continuum diameter	Experimental lap shear strength	Simulated lap shear strength	Error %
11 mm	3.5 kN	3.32 kN	5.2
12 mm	3.5 kN	3.64 kN	4.1
13 mm	3.5 kN	3.77 kN	7.7

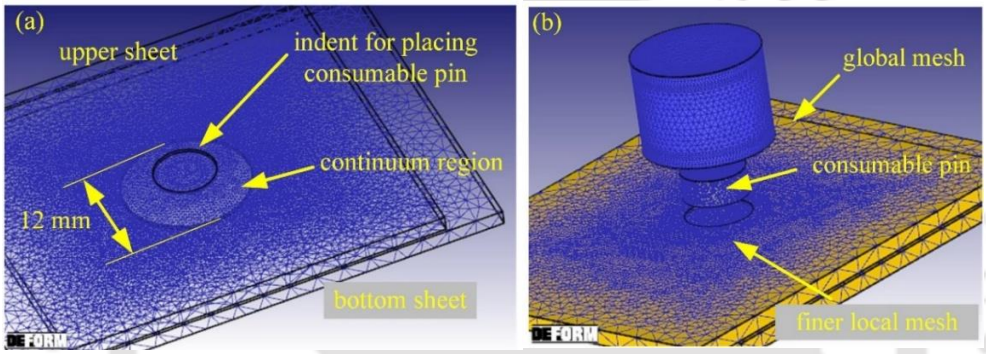

Figure 6.2 FE simulation of FSSW using consumable pin: (a) wireframe diagram showing continuum region (b) components of the welding process with global and local mesh

The tool was meshed using Tetrahedral mesh of 1 mm as the minimum element size. Since the tool was modelled as a rigid body, mesh size had no effect on the simulation. The workpiece was meshed with tetrahedral elements of 2 mm global element size and 0.3 mm local element size at interfaces and regions undergoing deformation (Figure 6.2b). The consumable pin was also meshed throughout with tetrahedral elements of 0.3 mm size. Mesh sensitivity analysis was performed to arrive at the optimal mesh size for the simulation as discussed in Chapter 5. The simulated and experimental torque were compared to find the error in prediction for each of the trials. The material properties for the workpiece was derived from tensile tests as discussed in Section 5.2.2. The load-displacement data at four different temperatures were converted to true stress-strain data for AA6061-T6 and the true plastic stress-strain data was provided as material input for base sheets. Material properties of the consumable pin were derived from compression test of AA6061-T6 at four different temperatures. The strength coefficient (K) and strain hardening exponent (n) were derived by fitting the true stress-strain data in the Hollomon power law and same was used to extrapolate flow stress at large strains. Experimentally found plastic stress versus strain at 3×10^{-4} s^{-1} strain rate was given as input for the simulation, which showed good match with material properties in DEFORM-3D database at the same strain rate and temperatures (< 5% error). The material properties at strain rate of 10 s^{-1} were given as input from DEFORM-3D database for

AA6061-T6 at four different temperatures as per experiments. Using the data at the two strain rates, material properties at other strain rates were either interpolated or extrapolated. Actually, there is not a high variation in the stress-strain curves at 3×10^{-4} s^{-1} and 10 s^{-1} and most of the strain-rates are near this range only. Hence, interpolation or extrapolation of properties is justified. The thermal properties of AA6061-T6 are used from DEFORM-3D database; simulations are carried out with thermal conductivity as 180.2 W/m•K, specific heat capacity as 903 J/kg•K and coefficient of thermal expansion as 22×10^{-6}/°C.

During the FSSW process, heat generated from friction and plastic deformation was used to calculate the temperature distribution using Fourier heat conduction equation. The contact properties at the interfaces and boundary conditions used during the FSSW were discussed in Chapter 5. The model was validated by comparing simulated and experimental torques during welding at different rotational speeds, which showed prediction error in the range of 4−7% using the model (Table 6.2).

Table 6.2 Comparison of average torque and plunge force from simulation and experiment at different rotational speeds

Rotational speed (RPM)	Experimental torque (N·mm)	Simulated torque (N·mm)	% error for torque	Experimental plunge force (N)	Simulated plunge force (N)	% error for plunge force
360	7816	8133	4	417	439	5.2
462	7981	8472	5.7	420	440	4.7
557	8309	8814	6	403	428	6.2
900	8972	9519	6.1	397	419	5.6
1200	9113	9586	5.2	387	406	4.9

6.3.2 Lap Shear Test Simulation using Damage Models

The lap shear test was simulated in DEFORM-3D as a subsequent stage to the FSSW simulation. DEFORM-3D allows material and thermal properties at the end of the simulation to be passed on to the next stage. Thus, the change in material properties due to severe plastic deformation and elevated temperature at high strain rates during FSSW simulation was preserved and passed on to the lap shear simulation. This included plastic material behaviour of the weld spot area, i.e. flow stress, strain hardening parameters and residual stresses due to plastic deformation and thermal cycle. After the FSSW welding simulation was completed, the tool was removed, and new boundary conditions were applied to the welded workpiece. The boundary conditions applied were (i) one end of the upper sheet was fixed in all directions, (ii) the opposite end of the bottom sheet was given velocity of 1 mm/min in the positive *x*-direction (Figure 6.3), (iii) the top surface of the upper sheet and bottom surface of the bottom sheet was assigned zero velocity in *z*-direction to avoid sheet

bending. The mesh was imported from stage 1, i.e., FSSW simulation, along with material and thermal properties. Element deletion was introduced in this stage by incorporating damage models in material properties. Two damage models namely, Freudenthal (1950) damage model and Cockcroft-Latham (1968) damage model were used in this study and compared for their efficacy. In Freudenthal model, damage is given as

$$D = \int_0^{\bar{\varepsilon}_f} \bar{\sigma} d\bar{\varepsilon}\,, \tag{6.1}$$

where $\bar{\varepsilon}_f$ is the effective strain at fracture, $\bar{\sigma}$ is the effective stress and $\bar{\varepsilon}$ is the effective strain.

On the other hand, in Cockcroft-Latham model, damage is given as

$$D = \int_0^{\bar{\varepsilon}_f} \sigma_1 d\bar{\varepsilon}\,, \tag{6.2}$$

where σ_1 is the maximum principal stress (Eom et al., 2014; Heidari et al., 2020). Fracture initiates when the value of D exceeds a critical damage value C_f. When $D - C_f < 0$, there is no failure, and if $D - C_f > 0$, there is failure (Barik et al., 2022). The value of critical damage constant was calculated from uniaxial tensile test data of AA6061-T6. In this study, C_f = 34 MPa was obtained for both the cases considering uniaxial tensile tests and assuming the base sheets as isotropic. The sheets are assumed as isotropic materials during FSSW and lap shear test simulations following von Mises yield function.

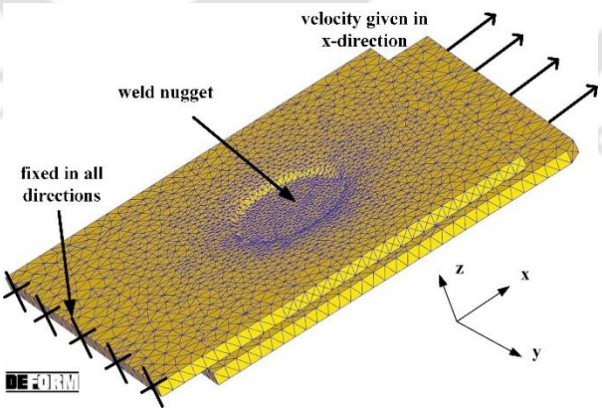

Figure 6.3 Boundary conditions used during lap shear test simulation

6.4 Results and Discussion

The effect of change in rotational speed during FSSW using consumable pin is assessed by comparing the joint strengths during lap shear test, microhardness and microstructure comparison,

analysis of failure, temperature and material flow during welding. The results are discussed in this section.

6.4.1 Joint Strength

It is observed from lap shear test data (Figure 6.4a) that the maximum load bearing capacity initially increased with increase in rotational speed up to 900 RPM. There is a marginal decrease at 1200 RPM. The mean value of maximum load at failure for 360, 462, 557, 900 and 1200 RPM are 1.4, 1.52, 2.7, 3.79 and 3.5 kN, respectively (Table 6.3), indicating 1.7 times increase in failure load between minimum and maximum values. The standard deviations for the tests were found to be in the range of 0.04−0.08. Considering the weld spot area to be 113 mm^2, the corresponding average shear strengths are calculated as 12.4, 13.4, 23.9, 33.5 and 30.9 MPa, respectively. A similar trend is observed in elongation at failure with respect to increase in rotational speed. The maximum value is about 2.16 mm at 900 RPM (Figure 6.4b) and only a minor increase is seen after 900 RPM (Figure 6.4b). Moreover, there is a sharp improvement in maximum load at failure as well as elongation at failure at 557 RPM.

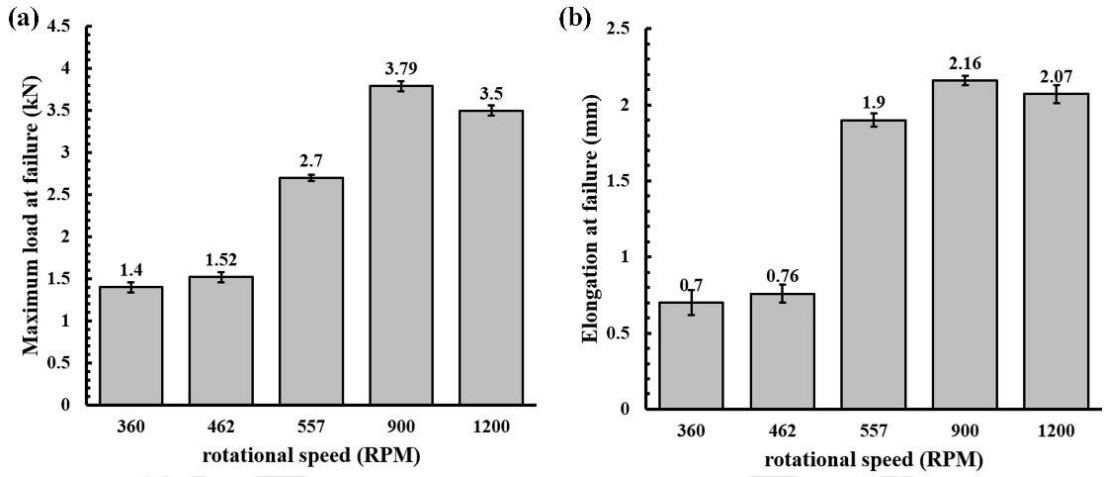

Figure 6.4 Lap shear test results at different rotational speeds: (a) maximum load at failure (b) elongation at failure

Due to machine limitations, the experimental study was carried out only up to 1200 RPM. However, from the simulation of consumable pin FSSW and subsequent lap shear test simulation, the study was further extended to higher rotational speeds. Lap shear test simulations were performed for 360, 462, 557, 900 and 1200 RPM and compared to the maximum load bearing capacity from experiments. In this study, Freudenthal damage model and Cockcroft-Latham damage models were implemented in the lap shear test simulation. There is only a marginal difference in their predictions of maximum load at failure (Table 6.3). However, the results predicted by Cockcroft-Latham damage model are closer to experimental results; and hence considered as the preferred damage model for this study. Figure 6.5 shows the comparison of simulation and experimental load-displacement curve during lap shear test for joint at different

rotational speeds. The chosen damage models provided prediction error of only 4−7% in lap shear test. Due to the assumption of continuity of the sheets, simpler damage models were able to encompass the damage behaviour during lap shear test without considering delamination. In future work, models like ductile damage model (Beygi et al., 2022) and void growth model (He et al., 2008) can be used for simulations.

Table 6.3 Comparison of average experimental and simulated lap shear test results along with prediction using damage models

Rotational speed (RPM)	Maximum load at failure (kN)	Elongation at failure (mm)	Comparison of simulated and experimental maximum load at failure (kN)			
			Cockcroft-Latham	error (%)	Freudenthal	error (%)
360	1.4	0.7	1.65	18	1.66	18.8
462	1.52	0.76	1.76	16.2	1.75	15
557	2.7	1.9	2.86	6	2.88	6.8
900	3.79	2.15	3.97	4.8	3.98	5
1200	3.5	2.07	3.64	4.1	3.67	4.8
1500	-	-	3.42	-	3.51	-
2000	-	-	3.17	-	3.22	-

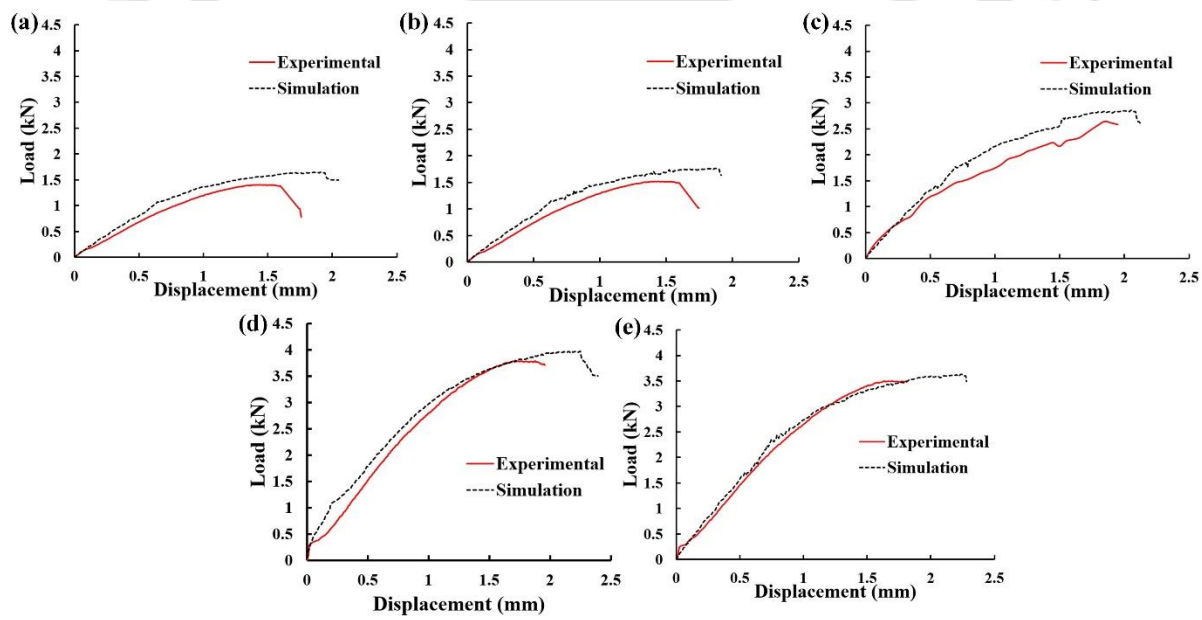

Figure 6.5 Comparison of load evolution from experiments and simulations (using Cockcroft-Latham damage model) during lap shear test for FSSW at (a) 360 RPM (b) 462 RPM (c) 557 RPM (d) 900 RPM (e) 1200 RPM

The errors for 360 and 462 RPM are 18% and 16.2%, which are on the higher side. The joints made at 360 and 462 RPM had very small bond lengths and contained defects, as discussed later in Section 6.4.4. Effective joints are produced only at 557 RPM and above. The FE model did

not consider defects in the joints and thus resulted in inaccurate prediction. However, the model yields good predictions for 557, 900 and 1200 RPM with an acceptable error of 6%, 4.8% and 4.1%, respectively (Table 6.3). Using the same model after validation, simulations of consumable pin FSSW and lap shear tests were performed for two more rotational speeds, viz., 1500 and 2000 RPM. The predicted maximum load at failure for 1500 and 2000 RPM are 3.42 and 3.17 kN, respectively. Thus, a decrease in joint strength is observed beyond 900 RPM, both in experiments and FE simulations.

6.4.2 Fracture Analysis

The joint failure during lap shear test was studied using fractography as well as visual inspection. It can be observed from fractography results that all the joints failed in ductile mode of failure. The fractured surfaces, when observed under FESEM revealed dimples with varied density (Figure 6.6). A smooth and flat surface during fractography denotes brittle mode of failure (Bonhomme et al., 2009; Wouters and Froyen, 1996). Whereas, a high density of fine equiaxed dimples denotes ductile failure (Garg et al., 2020; Saravanan et al., 2016). Larger sized dimples present in case of 1200 RPM as compared to 360 RPM are due to higher plastic deformation, denoting higher stirring at higher rotational speeds (Agrawal et al., 2021). It can also be inferred that the joint strengths were not affected by formation of brittle regions in any of the joints. The variation in strength was primarily dependent on the amount of stirring and material mixing due to change in rotational speed.

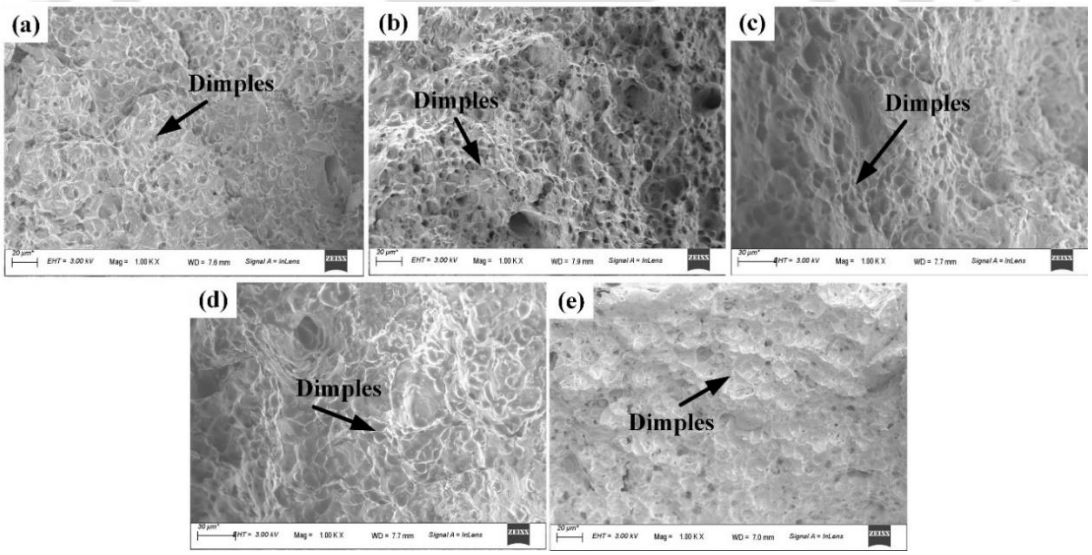

Figure 6.6 FESEM images (1000X magnification) of fractured surface during lap shear test for (a) 360 RPM (b) 462 RPM (c) 557 RPM (d) 900 RPM (e) 1200 RPM

The types of failure for the joints are shown in Figure 6.7. FSSW performed at 360 and 462 RPM show ‘interfacial separation’ mode of fracture. This type of failure occurs when bond length between the two sheets is small and fails at the interface when a shear load is applied (Rana et al., 2018; Wang et al., 2020). The welds at 557, 900 and 1200 RPM failed by ‘nugget pull-out’. In nugget pull-out, fracture occurs around the nugget while the nugget remains attached to one of the

sheets. The analysis confirms that the bond area between the two sheets was lower for welding at rotational speeds below 557 RPM. At higher rotational speeds, i.e., 557, 900 and 1200 RPM, the sheets were bonded properly in the nugget region and failure occurred only at the boundary of nugget and base material. This is due to change in material properties, which is discussed in subsequent sections. Figure 6.8 shows comparison between failure type between experiment and lap shear test simulation for joints at 557, 900 and 1200 RPM, which shows a good match. Stress concentration around the weld nugget is visible before failure.

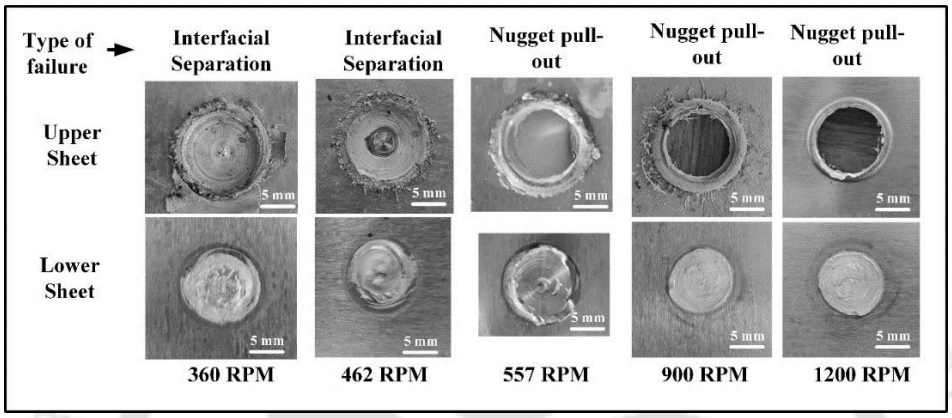

Figure 6.7 Different failure modes with variation of rotational speed

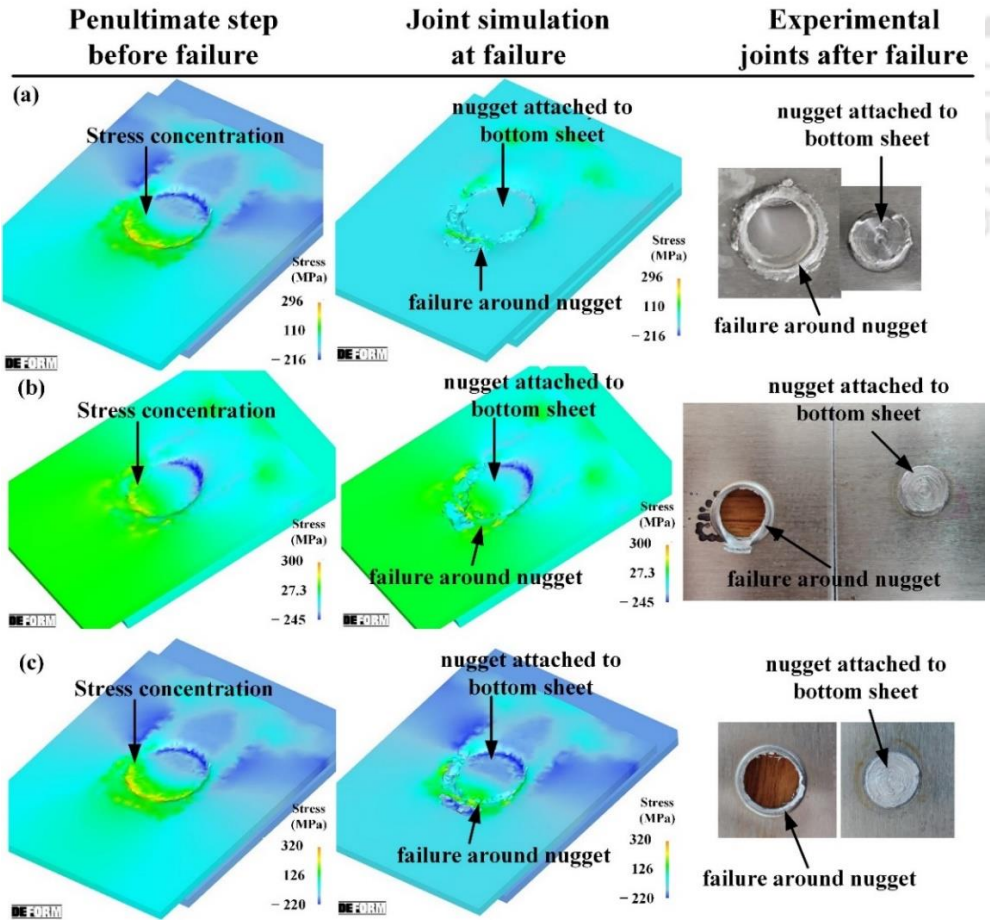

Figure 6.8 Comparison of fracture mode from FE simulations and experiments for FSSW at (a) 557 RPM (b) 900 RPM (c) 1200 RPM

6.4.3 Energy during Welding

The energy required for welding was calculated using torque and plunge force during welding using Eq. (3.4) discussed in Chapter 3. It was found that as the rotational speed was increased, the energy required during welding also increased. The energy consumption at 360, 462, 557, 900 and 1200 RPM are 4.68 kJ, 4.83 kJ, 5.18 kJ, 5.97 kJ and 6.24 kJ, respectively. An increase in rotational speed from 360 RPM to 900 RPM results in 27.5% increase in heat input during welding. Although the rotational speed was increased almost three times (360 to 900 RPM), the energy input only increased by 27.5% with 1.7 times increase in joint strength. Su et al. (2006), during conventional FSSW of AA6061-T6 sheets with comparable process parameters, reported a similar observation of increase in energy applied from 3 kJ to 6 kJ with increase in rotational speed from 500 to 1000 RPM.

6.4.4 Microstructure

The cross-sections about the weld centreline for joints produced at different rotational speeds and their associated microstructure in different weld zones are shown in Figure 6.9. Four distinct zones can be observed namely, BM, HAZ, TMAZ and SZ. All the joints show a U-shaped SZ. The grains in the SZ are smallest for all the joints. SZ experiences highest amount of plastic deformation due to stirring and undergoes dynamic recrystallisation, which leads to fine equiaxed grains (Rana and Narayanan, 2021). On the other hand, the HAZ experiences increase in temperature without plastic deformation leading to grain growth. HAZ shows the largest grain size. TMAZ, that lies between the SZ and HAZ, experiences rise in temperature as well as stirring and plastic deformation. This results in smaller grain size as compared to HAZ, but bigger than SZ. It acts as a transition zone between SZ and HAZ (Figure 6.9). The average grain size in each of the zones was calculated by line intercept method using 10 lines. The average grain size in HAZ increased from 80 µm to 105 µm with increase in rotational speed from 360 to 1200 RPM. SZ and TMAZ experienced a decrease from 13 µm to 9 µm and 31 µm to 20 µm, respectively with increase in rotational speed from 360 to 900 RPM. There is minor variation of grain size in SZ and TMAZ with further increase of rotational speed to 1200 RPM (Figure 6.10).

As discussed in Section 6.4.3, the heat input increases with increase in rotational speed. The increase in heat input promotes grain growth. However, with increase in rotational speed, the amount of stirring and plastic deformation also increases, which promotes recrystallisation and finer grains. Thus, two opposing phenomena take place with increase in rotational speed. It can be observed from Figure 6.10 that the average grain size in the SZ and TMAZ decreases as rotational speed is increased from 360 to 900, and becomes stable with further increase in rotational speed. The recrystallisation phenomenon dominates up to 900 RPM, and further increase in rotational

speed leads to higher heat input and increased grain growth. The average grain size in the HAZ increased monotonously with increase in rotational speed.

It can be observed from the macrostructure of the joints that the radial bond length, measured from the weld centreline to end of bonded region (Figure 6.9), in case of 360 and 462 RPM are 2.1 mm and 1.8 mm, respectively. Whereas, the bond lengths for 557, 900 and 1200 RPM are 4.7 mm, 6.4 mm and 5.6 mm, respectively. There is a marked increase in bond length with increase in rotational speed. The reason for low lap shear strength of joints produced by 360 and 462 RPM is due to the small bond length. Effective joining can be considered to take place at 557 RPM and above.

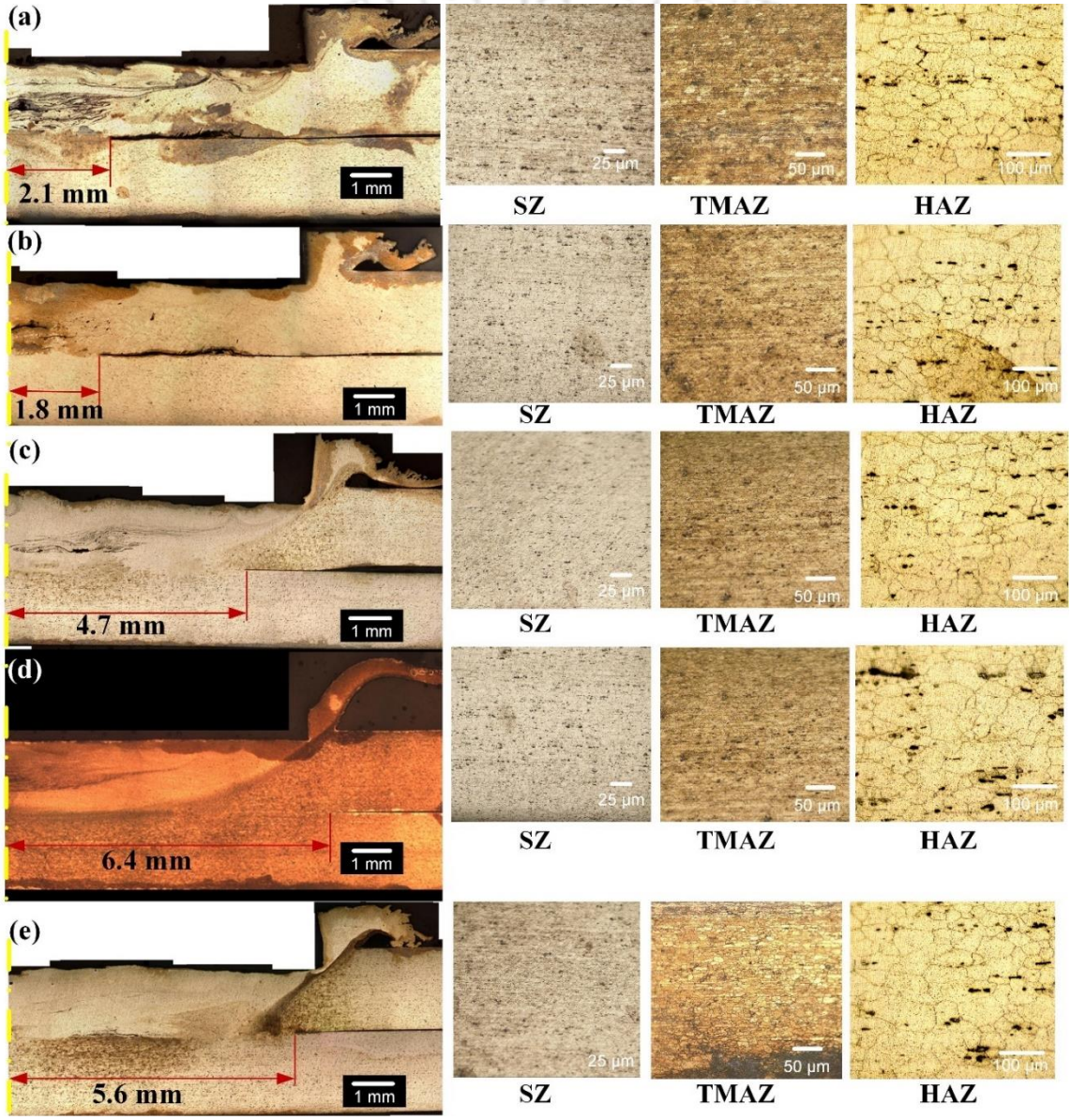

Figure 6.9 Weld cross-section (5X magnification) about the centreline along with radial bond length and HAZ (10X), TMAZ (25X), SZ (50X) for (a) 360 RPM (b) 462 RPM (c) 557 RPM (d) 900 RPM (e) 1200 RPM

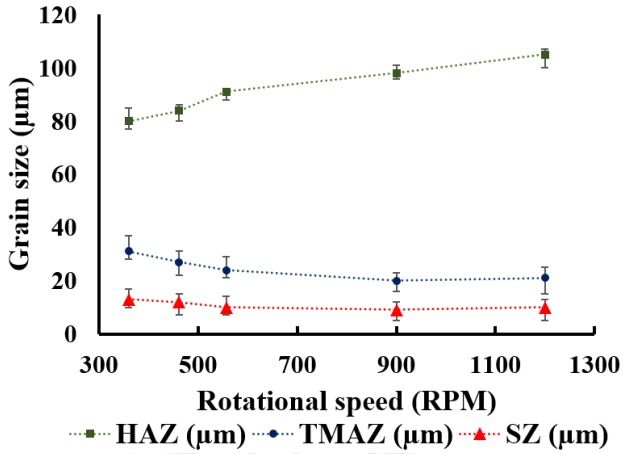

Figure 6.10 Variation of grain size in HAZ, TMAZ and SZ with increase in rotational speeds

6.4.5 Microhardness

The microhardness distributions in the weld cross-section for welds produced with different rotational speeds at upper and lower lines are shown in Figure 6.11. The base material microhardness is 102 HV. As compared to base material, there is a decrease in microhardness in the weld region for all the joints. Since AA6061-T6 is a precipitation hardened aluminium alloy, the hardness depends on the distribution of precipitates like Mg_2Si. The observation is consistent with literature, which states minimum and maximum microhardness found at HAZ and SZ, respectively for conventional and refill FSSW (Venukumar et al., 2013; Cao et al., 2016). The fine grains and precipitates of the SZ (Section 6.4.4) impart higher microhardness. The average grain size discussed in Section 6.4.4 explains the variation of microhardness distribution according to Hall-Petch relationship. The microhardness on lower line shows higher hardness compared to the upper line, as the lower line is less affected by temperature and plastic deformation during welding, thus retaining properties closer to BM (Figure 6.11b). As the rotational speed is increased, the ratio of BM to HAZ hardness and SZ to HAZ hardness on the upper line increases. This sharp variation of hardness at the weld-BM interface is partly responsible for the weakening of joint strength. The observation of stress concentration around the weld and nugget pull-out failure in Section 6.4.2 also confirms the same.

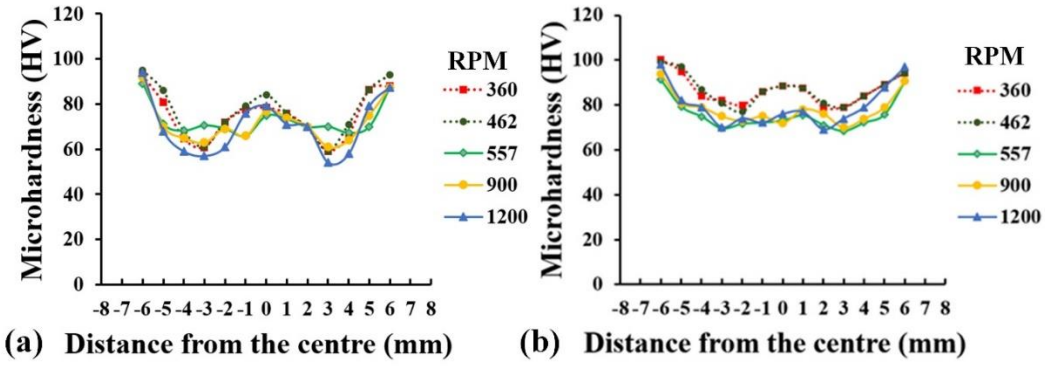

Figure 6.11 Distribution of microhardness (± 5 % variation) for different rotational speeds: (a) upper line (b) lower line

6.4.6 Temperature Distribution and Material Flow

The temperature during welding was recorded at two points, P1 and P2, on the upper surface of the top sheet during welding. The temperature evolution at points P1 and P2 from experiments and FE simulations are compared at different rotational speeds (Figure 6.12). The average prediction error at P1 is in the range of 4−7%, and at P2, it is in the range of 4−8%. Though the errors are in acceptable range, the deviation is due to assumption of the thermal properties of the materials from DEFORM-3D database, which was not verified experimentally. Considering the model's capability to predict temperature within acceptable errors, the model was used to predict the temperature contour in the joint cross-section as well as the consumable pin.

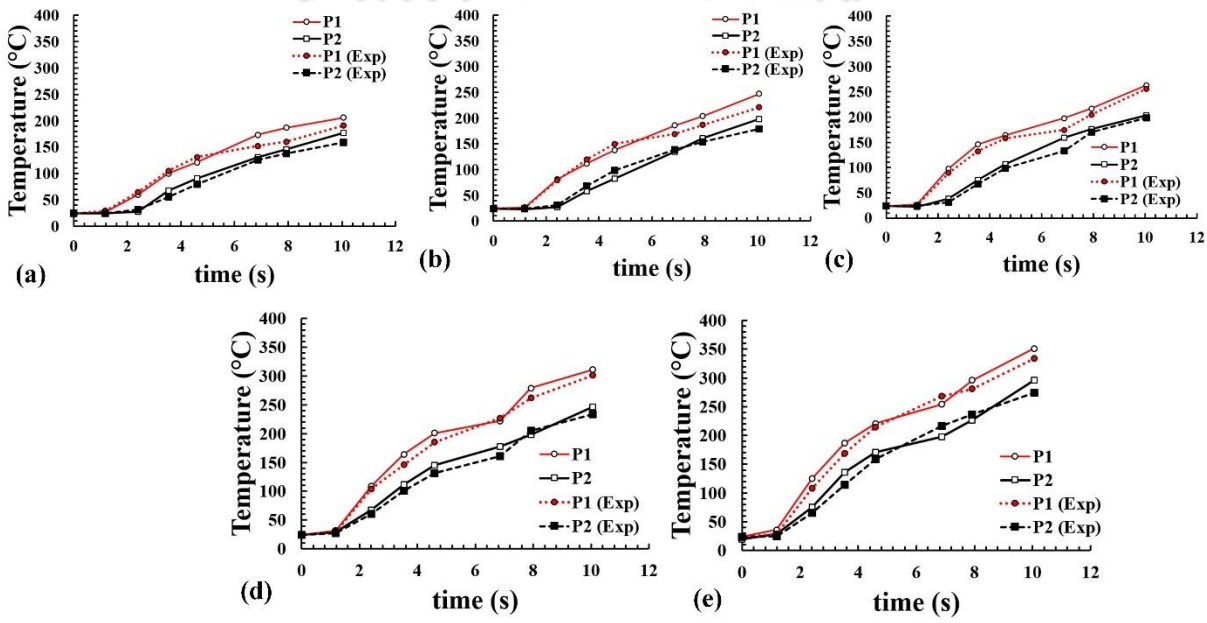

Figure 6.12 Comparison of temperature evolution from experiments and FE simulations at P1 and P2 for (a) 360 RPM (b) 462 RPM (c) 557 RPM (d) 900 RPM (e) 1200 RPM

Figure 6.13 shows the typical temperature contours at the upper surface and cross-section of the joints made at 360 RPM and 1200 RPM. With increase in rotational speed, the peak temperature also increases. The observation matches the increase in average grain size in HAZ due to grain growth with increase in rotational speed (Figure 6.10). The peak temperature zone was smaller in case of the joint made at 360 RPM, implying lesser plasticisation of material at the bottom of the workpiece as compared to joint made at 1200RPM. The temperature distribution at the cross-section for the joint made at 1200 RPM is a V-shaped contour, which matches the shape of the SZ observed in Section 6.4.4.

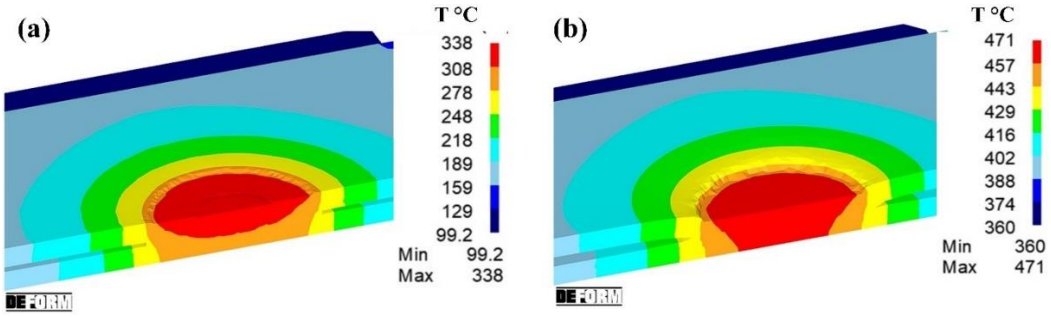

Figure 6.13 Typical temperature distribution on the weld cross-section and upper surface of the workpiece for (a) 360 RPM (b) 1200 RPM

Figure 6.14 shows peak temperature generated in the consumable pin and the predicted penetration depth of consumable pin inside the workpiece. The penetration depth increased with increase in rotational speed up to 900 RPM (Figure 6.15). A higher rotational speed resulted in higher stirring and increased temperature of the workpiece, thereby softening the workpiece. However, the penetration depth at 1200 RPM was slightly lower, which could be due to its softening prior to penetration inside the workpiece resulting from higher temperature generated in the pin at 1200 RPM. The observation is further verified by simulation of material stirring at three points, T1, T2 and T3, taken inside the workpiece below the tool at 0.5 mm, 1.5 mm and 2.9 mm depth, respectively (Figure 6.16). Simulation of the material flow can give a qualitative idea of stirring within the workpiece and resulting joint quality (Dialami et al., 2015). At all the rotational speeds, a good amount of stirring took place at T1. Stirring increased with increase in rotational speed. A similar observation was made for T2, where stirring increased with increase in rotational speed up to 900 RPM. At 1200 RPM, stirring was observed to be marginally lower than 900 RPM due to reduced penetration depth of the consumable pin. Stirring at T3 was observed to be very minimal for all rotational speeds. The material flow analysis further conforms to the joint strength trend observed during the lap shear test.

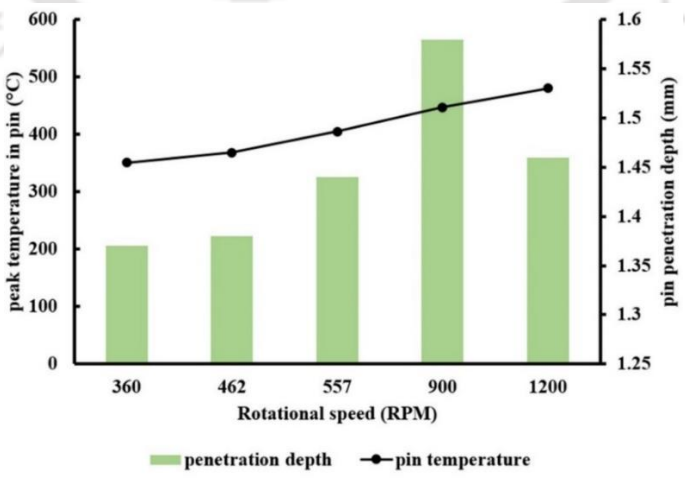

Figure 6.14 Peak temperature generated in the consumable pin during welding and pin penetration depths at different rotational speeds

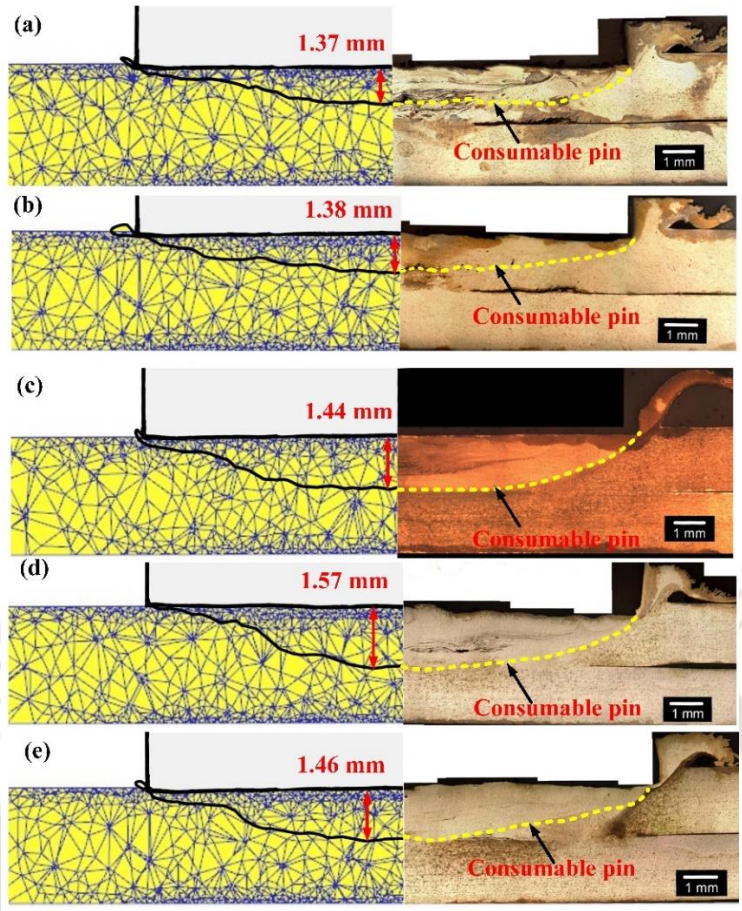

Figure 6.15 Simulated and experimental penetration depth of consumable pin after welding at (a) 360 RPM (b) 462 RPM (c) 557 RPM (d) 900 RPM (e) 1200 RPM

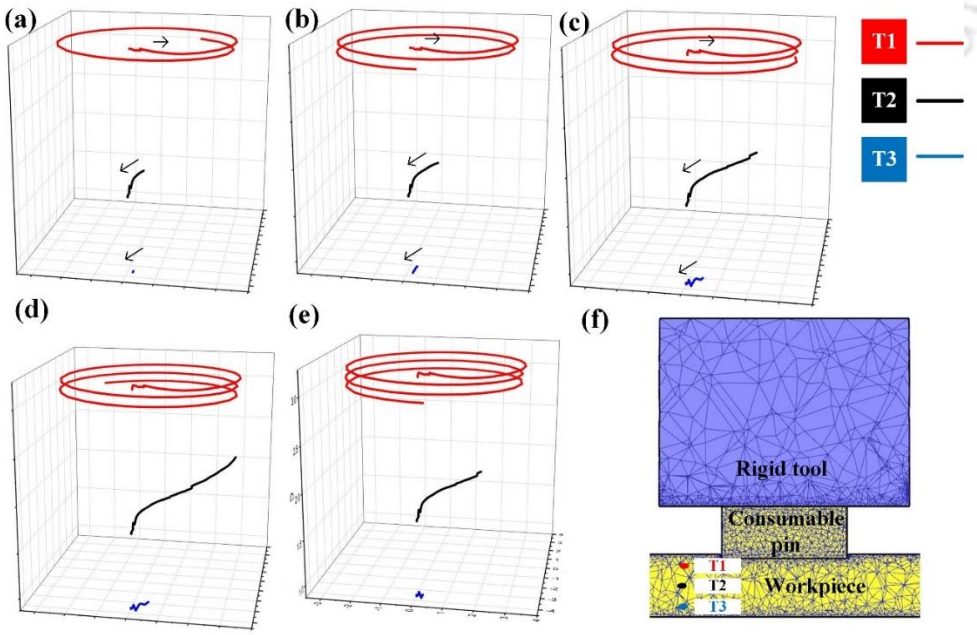

Figure 6.16 Material flow pattern at three points T1, T2, T3 for (a) 360 RPM (b) 462 RPM (c) 557 RPM (d) 900 RPM (e) 1200 RPM (f) location of points T1, T2, T3

Overall, the effect of rotational speed on the inter-related phenomena during welding, leading to determination of joint quality can be summarized as follows:

- With the increase in rotational speed heat input increases resulting in an increase in the temperature.
- For the HAZ, which does not experience plastic deformation, the grain size increases with increase in temperature. However, for SZ and TMAZ, which experience severe plastic deformation along with temperature rise, grain size reduces up to 900 RPM due to dominant role of recrystallization. Beyond 900 RPM, grain size becomes stable as grain growth due to the rise in temperature and finer grains due to dynamic recrystallization balance each other.
- Finer grains result in higher microhardness. Due to the variation in grain size, the ratio of BM to HAZ hardness and SZ to HAZ hardness increases with increasing rotational speed.
- Increase in rotational speed promotes higher plasticisation of material at elevated temperatures, resulting in increased penetration depth and stirring up to 900 RPM. At 1200 RPM, both pin penetration and stirring are lower due to higher than optimal heat input.

The bond length increases with increase in rotational speed up to 900 RPM and then decreases on further increase of speed. Increase in the speed increases plasticization, which is favourable for bond formation. However, it also causes softening of pin, which discourages proper bond formation. Thus, there is an optimum speed for proper bond formation. The findings are summarised in Figure 6.17.

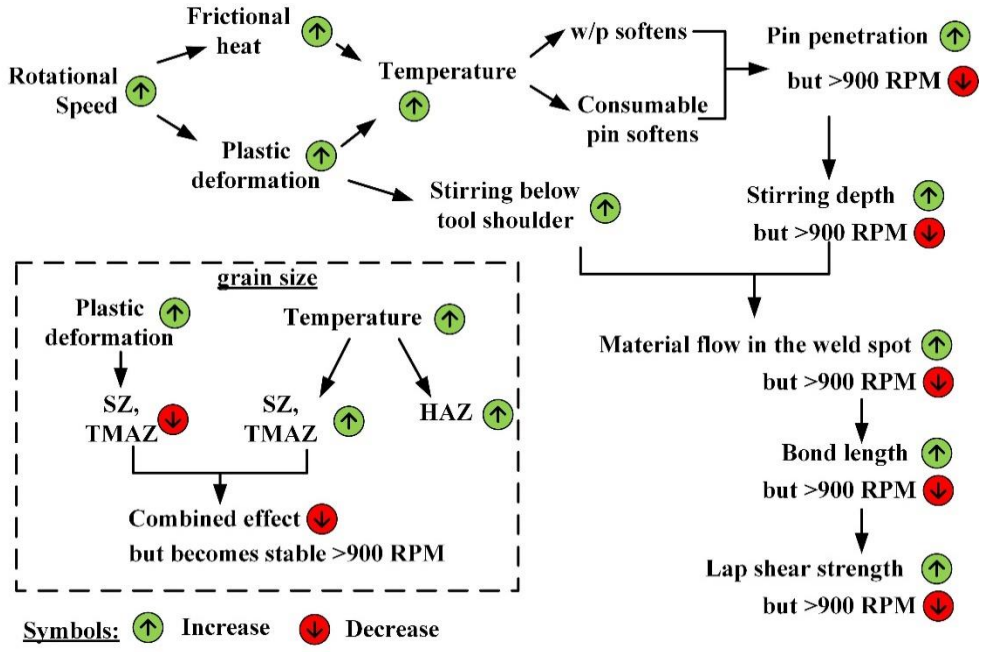

Figure 6.17 Effect of variation of rotational speed on different parameters during FSSW using consumable pin

6.5 Conclusion

This chapter studies the effect of rotational speed on joint quality during FSSW using a consumable pin. Joints produced at five rotational speeds, viz. 360, 462, 557, 900 and 1200 RPM were investigated. The joint quality was analyzed using lap shear test, microstructure analysis and microhardness study. FE simulation of FSSW was performed to estimate the torque, force, and temperature evolution during stirring. After stirring simulation, FE simulation of lap shear test was also conducted to estimate fracture and joint strength using Cockcroft-Latham damage model and Freudenthal damage model. The following conclusions are drawn from the study:

1) The experimental joint strength in lap shear test increased with increase in rotational speed from 360 RPM to 900 RPM; further increase in rotational speed resulted in a marginal decrease in joint strength. A 1.7 times increase in joint strength was observed for FSSW formed at 900 RPM as compared to that formed at 360 RPM.
2) FE simulation of the lap shear test successfully predicted the failure load for joints produced at 360, 462, 557, 900 and 1200 RPM with error in the range of 4−7%. This model was also used to predict the failure load for FSSW at 1500 and 2000 RPM, which were beyond experimental limits. During lap shear test simulation, Cockcroft-Latham damage model predicted the failure load closer to the experimental values as compared to Freudenthal damage model, indicating that mainly the greatest principal stress influences the fracture behavior.
3) The failure analysis revealed that joints at 360 and 462 RPM failed by interfacial failure mode during the lap shear test, suggesting poor joint quality. Joints at 557, 900 and 1200 RPM failed by nugget pull-out mode indicating good joining at the nugget region.
4) Energy input and temperature in both the workpiece and consumable pin increased with increase in the rotational speed. There was a 27.5% increase in energy input as the rotational speed was increased from 360 to 900 RPM.
5) Welding at 1200 RPM resulted in lower joint strength than that obtained by welding at 900 RPM. This may be attributed to (i) sharp change of microhardness at the BM-HAZ interface, (ii) lower pin penetration depth, and (iii) lower stirring at middle region of joint cross-section.

Chapter 7

Effect of Plunge Rates on Exit-hole-free FSSW with a Consumable Pin

7.1 Introduction

The process parameters determine the quality of weld produced by any process. Along with rotational speed discussed in Chapter 6, the plunge rate of the FSSW tool is one of the important process parameters influencing plastic deformation, heat input and overall joint quality (Suryanarayanan and Sridhar, 2021; Çam et al., 2022). Su et al. (2006) reported that as the plunge rate increases, the width of the SZ decreases, negatively impacting joint strength. An increase in plunge rate reduces the heat input as it reduces the thermal cycle duration (Suryanarayanan and Sridhar, 2020). It was found in literature review that a lower plunge rate is recommended to keep the torque and axial forces low, however, too low axial force may result in low heat input and defects. An optimum plunge rate of 6 mm/min was suggested. An optimum plunge rate is important to achieve good joint quality. This chapter examines the impact of plunge rate on weld quality during exit-hole free FSSW with a consumable pin. To evaluate weld quality, the study employs lap shear strength testing, microhardness distribution analysis, and microstructure examination of the cross-sections of the joints. Additionally, fracture analysis of the joints is conducted. To further understand the FSSW process, FE simulations using DEFORM-3D are carried out to predict temperature distribution, force and torque evolution, and material flow during the welding process. These simulations are then compared to the experimental results. The study also uses simulation to predict the lap shear strength and fracture using the Freudenthal damage model and Cockcroft-Latham damage model. This approach allows for predictions of weld strength beyond the limitations of the machines used in the study.

7.2 Experimental Details

The welding was performed on two sheets of AA6061-T6 aluminum alloy, as described in Chapter 5. This study investigates the impact of tool plunge rate on joint formation and strength by varying the plunge rate while keeping all other parameters constant. The tool used had a diameter of 12 mm, and the AA6061-T6 consumable pin was 6 mm in diameter and 2.5 mm in length. A rotational speed of 900 RPM and dwell time of 10 s were employed for all experiments. Five different plunge rates, 6, 10, 15, 20 and 35 mm/min were used. The plunge rates were chosen based on frequently used plunge rates in literature and trial experiments. Torque and plunge force were recorded during the experiment using strain-gage based integrated sensors in the machine (strain data logger-MP31C09). Temperature during welding was monitored by attaching two K-type thermocouples to

the workpiece, on the top surface at 5 mm and 10 mm from the tool edge as described in Chapter 6.

The characterization methods are described in detail in Chapter 5. The samples were prepared according to the AWS B4.0-2007 standards for lap shear test, and the joint strength was measured using a universal testing machine (UTM) with a uniform cross-head speed of 1 mm/min at room temperature. Three samples for each set of process parameters were tested and the mean value was taken as the final joint strength. The fractured joints after the lap shear test were analyzed to determine their mode of failure. Fractography analysis was performed using a field emission scanning electron microscope (FESEM – Zeiss, Model: Gemini). The microhardness at the cross-section of the welds was evaluated on A to M locations using a Vickers microhardness tester by OmniTech (model MVH-11) as described in Chapter 5. The microstructure of the joints was analyzed by sectioning them at the center of the weld spot, perpendicular to the top surface and polishing using silicon carbide emery paper. The cross-sections were then etched using modified Poulton's reagent comprising 10 ml HNO_3, 16 ml chromic acid solution (3g H_2CrO_4 in 10 ml H_2O), 12 ml HCl, 6 ml HNO_3, 1 ml HF (48% concentration), and 1 ml H_2O. The samples were dipped in the etchant for 5 s and washed under running water for 10 s. The process was repeated twice and observed under an optical microscope (Carl Zeiss- Axiotech model). The base material tensile properties (using ASTM E8/E8M standards) and consumable pin compressive properties (using ASTM E9 standards) were evaluated at four temperatures: RT, 100 °C, 200 °C, and 400 °C (reported in Chapter 5). The engineering stress-strain data from the tests were converted into true plastic stress-strain data, and strength coefficient (*K*), strain hardening exponent (*n*) were evaluated by curve fitting using Hollomon power law given by $\sigma = K\varepsilon^n$.

7.3 FE Simulation of FSSW using a Consumable Pin and Lap Shear Test

FSSW simulation followed by lap shear test simulation was conducted using DEFORM-3D (v11.2) software. The simulation comprised two phases. Phase 1 simulated the FSSW process using a consumable pin. The altered material properties from this stage were carried over to phase 2, which simulated the lap shear test. The simulation methodology is discussed in detail in Chapter 6. In this study the plunge rates during simulation were varied. The validation of the model was performed by comparing experimental and simulated welding torque. Table 7.1 compares the average torque during simulation and experiment from 0 to 2.5 mm plunge depth for the plunge rates used. The model produced a reasonably accurate match with prediction error within 4−6%. Similar to Chapter 6, during lap shear test two damage models, the Freudenthal model and Cockcroft-Latham model, were used and compared in the study.

Table 7.1 Comparison of average torque and plunge force from simulation and experiment at different plunge rates

Plunge rate (mm/min)	Experimental torque (N·mm)	Simulated torque (N·mm)	% error for torque	Experimental plunge force (N)	Simulated plunge force (N)	% error for plunge force
6	8256	8652	4.8	358	377	5.4
10	8387	8890	6	371	396	6.7
15	8611	9085	5.5	382	402	5.2
20	8972	9501	5.9	397	419	5.6
35	9493	9910	4.4	438	456	4.1

7.4 Results and Discussion

An evaluation of the impact of plunge rate during FSSW with a consumable pin was carried out by lap shear tests, fractography, microhardness measurements, microstructure analysis, temperature evolution and deformation behavior of consumable pin during welding. The outcomes are presented and analyzed in this section.

7.4.1 Lap Shear Test

The lap shear strength obtained for welding with different plunge rates is shown in Figure 7.1. The maximum load at failure for welding at 6, 10, 15, 20 and 35 mm/min plunge rates are 3.94, 3.97, 4.1, 3.79 and 3.07 kN, respectively. The standard deviations for the tests were found to be in the range of 0.06−0.14. Considering joint cross-sectional area as 113 mm^2, average shear strengths are 34.9, 35.1, 36.2, 33.5 and 27.1 MPa for welding at 6, 10, 15, 20 and 35 mm/min plunge rates, respectively. It can be observed that the joint strength increases marginally with increase in plunge rate from 6 to 15 mm/min, and further increase lead to decrease in joint strength (Figure 7.1). There is a 4% increase in joint strength for welding at 15 mm/min compared to welding at 6 mm/min. Whereas, a 26% decrease in joint strength is observed for welding at 35 mm/min plunge rate compared to welding at 15 mm/min. Similarly, the elongation at failure increased up to welding at 20 mm/min and decreased on further increase in plunge rate (Figure 7.1). This observation is unlike conventional FSSW, where the joint strength decreases monotonously as the plunge rate is increased due to lower heat input. In case of consumable pin FSSW, the difference in trend of joint strength is observed due to the unique deformation behavior of the consumable pin during plunging. The heat input and temperature of the workpiece and the consumable pin play the major role in determining the penetration depth, stirring and thereby joint strength, which is discussed later in Section 7.4.5.

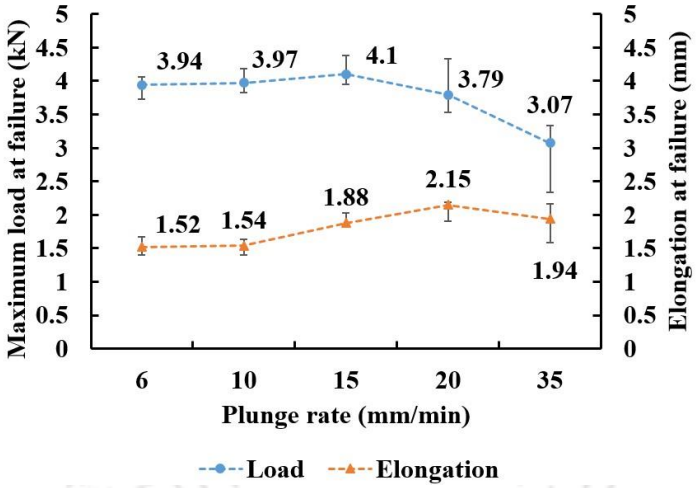

Figure 7.1 Lap shear test results at different plunge rates showing maximum load at failure and elongation at failure

The joint failure during lap shear testing was analyzed through fractography and visual inspection. Fractography results showed that all joints failed in a ductile manner. The results suggest that joint strength was not influenced by the formation of brittle regions, and that the strength variation was primarily determined by the extent of stirring and material mixing. Examination of the fractured surfaces under FESEM revealed dimples with varying densities (Figure 7.2a−e). The presence of larger dimples for welding at 15 mm/min can be attributed to higher plastic deformation, indicative of greater stirring at depth (Agrawal et al., 2021). All the joints failed by nugget pull-out mode of failure, indicating the sheets were properly bonded in the nugget region, leading to failure only at the nugget-BM boundary (Figure 7.2f).

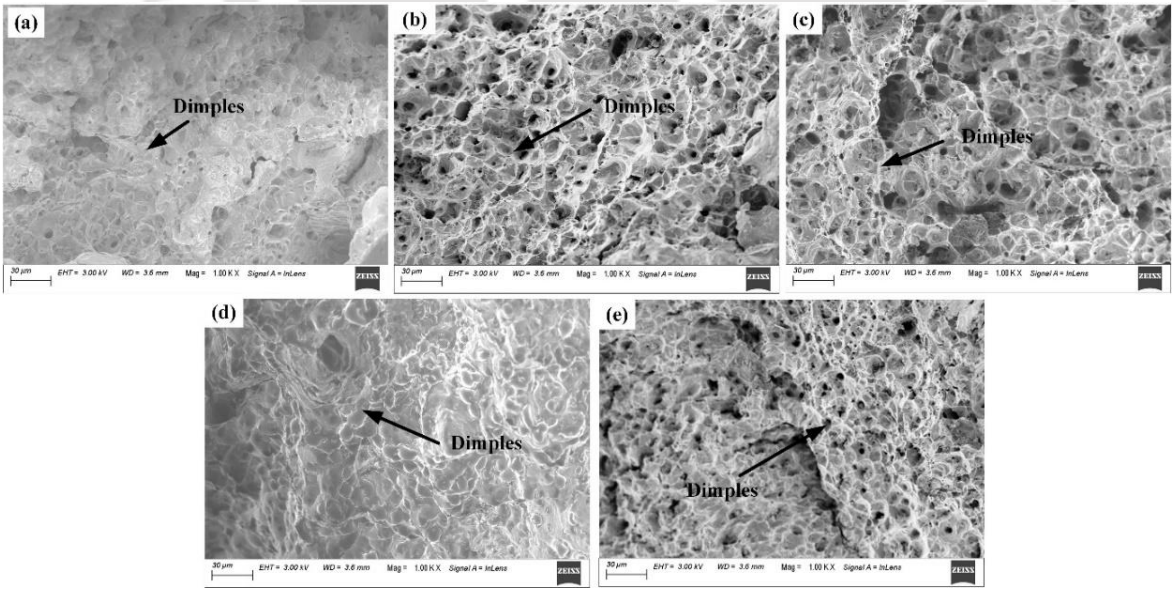

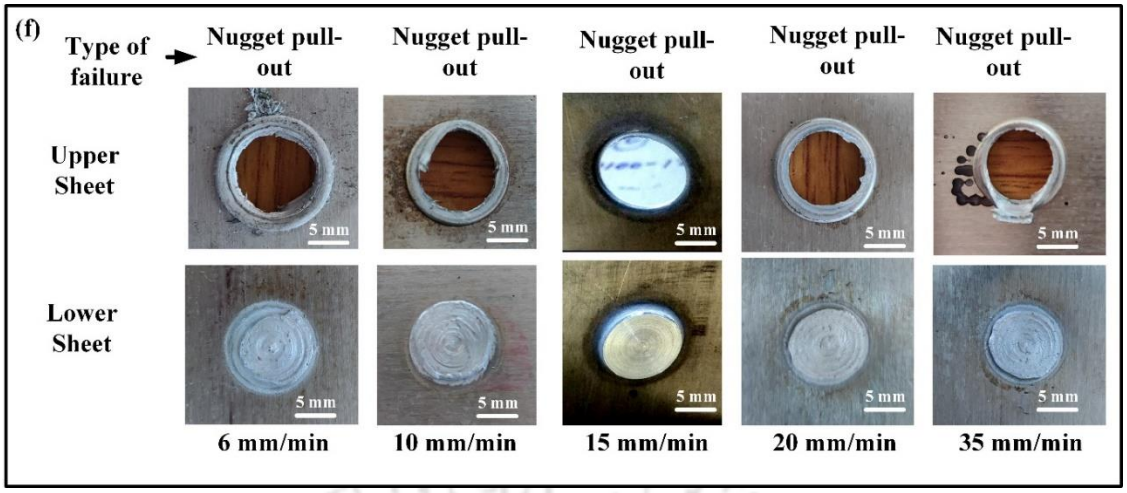

Figure 7.2 FESEM images of fractured surfaces for FSSW at (a) 6 mm/min (b) 10 mm/min (c) 15 mm/min (d) 20 mm/min (e) 35 mm/min (f) nugget pull-out mode of failure at different plunge rates

7.4.2 Energy during Welding

From experimental torque and plunge force generated during welding, the energy required for different plunge rates was calculated using Eq. (3.4). The energy during welding decreased as the plunge rate was increased. Energy input into the weld at 6, 10, 15, 20 and 35 mm/min plunge rates were 6.78 kJ, 6.53 kJ, 6.21 kJ, 5.97 kJ and 5.82 kJ, respectively. Although torque and plunge force increased with increase in plunge rate, the duration of each thermal cycle decreased with increase in plunge rate. Plunging time for welding at 6, 10, 15, 20 and 35 mm/min plunge rates were 25 s, 15 s, 10 s, 7.57 s and 4.3 s, respectively. Thus, the overall energy input decreased. It is important to note that although there is only 4% increase in joint strength when welding at plunge rate of 15 mm/min compared to 6 mm/min, it was achieved at 8.5% lower energy input. On the other hand, welding at 35 mm/min plunge rate results in 6.2% lower energy input compared to plunge rate of 15 mm/min, however, joint strength decreased by 25%. Thus, plunge rate of 15 mm/min is suggested as the preferred plunge rate for consumable pin FSSW of AA6061-T6 sheets.

7.4.3 Microstructure

Four main microstructure zones are identified at the cross-section of the joints: the BM, HAZ, TMAZ, and SZ (Figure 7.3). The average grain size calculated using line intercept method, in the HAZ decreased from 118 µm to 84 µm with increase in plunge rate from 6 to 35 mm/min. SZ and TMAZ experienced a decrease in average grain size, from 13 µm to 9 µm and 29 µm to 20 µm, respectively, as plunge rate increased from 6 to 35 mm/min (Figure 7.4).

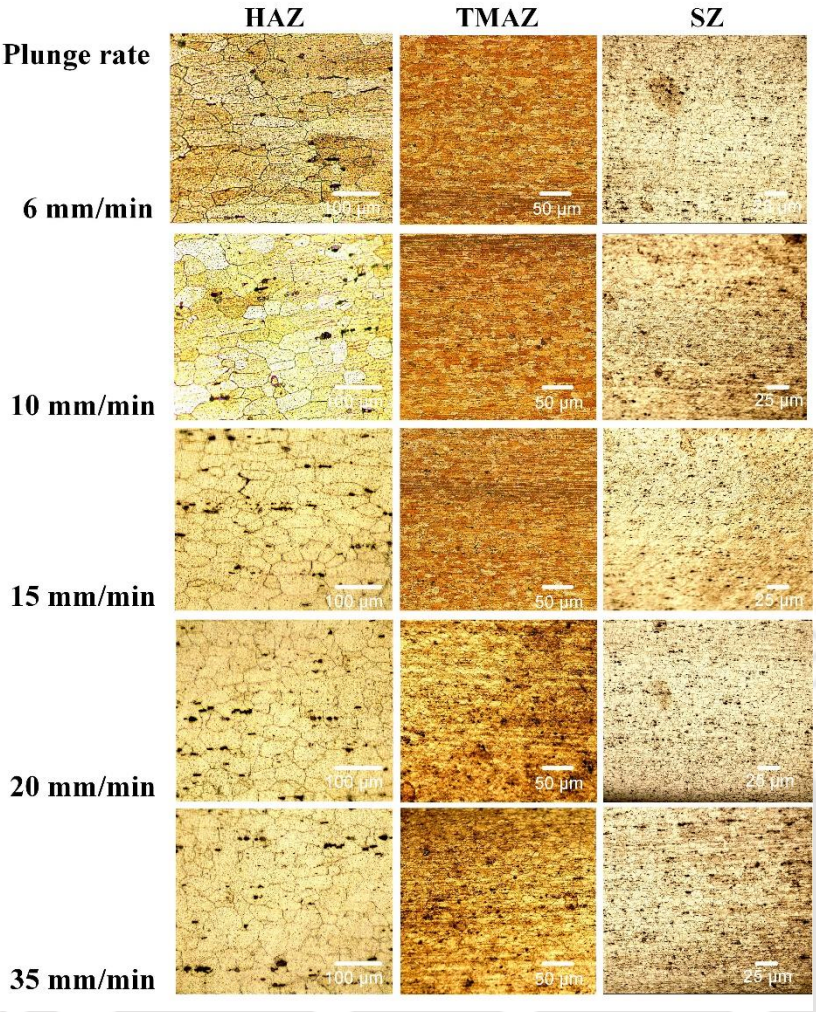

Figure 7.3 Weld zones and microstructure for FSSW at different plunge rates

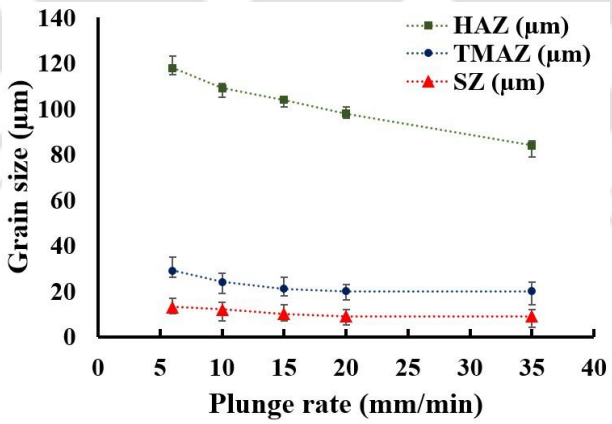

Figure 7.4 Change in average grain size with respect to plunge rate in different weld zones

7.4.4 Microhardness

The microhardness in the weld cross-sections of joints made at different plunge rates is depicted in Figure 7.5. The hardness of AA6061-T6 base sheet is 102 HV. The variation in microhardness distribution is explained by the comparison of average grain size discussed in Section 7.4.3. Welding at 6 mm/min experiences the highest heat input and thus show higher grain growth and

larger grain size leading to lower microhardness on the upper line at HAZ, TMAZ and SZ. Welding at 15 mm/min results in higher stirring leading to finer and equiaxed grains. This is evident from higher microhardness at the SZ on the upper line. On the lower line present at a higher depth, stirring is more for welding at 15 mm/min plunge rate due to higher penetration of the pin, however not high enough to produce fine equiaxed grains. Penetration depth of consumable pin for welding at 6 mm/min is lower, resulting in lesser stirring and the workpiece maintained its hardness closer to BM. A sharp variation of hardness at the nugget-BM interface is observed for welding at all the plunge rates, which contributes to weakening joint strength. This is supported by the observation of nugget pull-out failure.

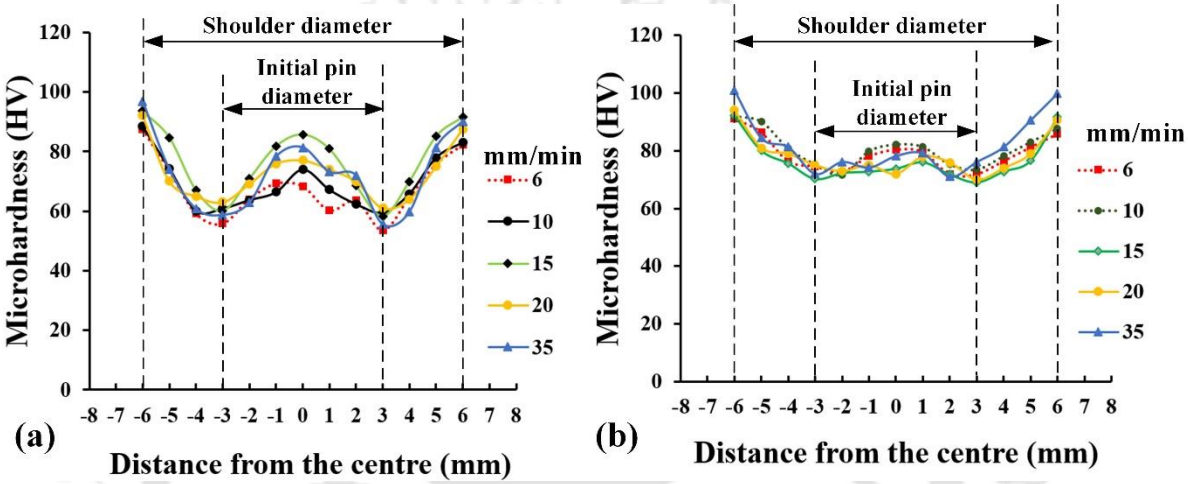

Figure 7.5 Microhardness for FSSW at different plunge rates: (a) upper line (b) lower line

7.5 Simulation Results

FE simulation results were validated by comparing the experimental and simulation torque and plunge force, as shown in Table 7.1 (Section 7.3). Figure 7.6a compares load vs displacement curve during experimental and simulated lap shear tests for weld produced at 15 mm/min plunge rate. The FE model using Cockcroft-Latham damage model was able to predict the load vs displacement curve with an error of 5.1%, while Freudenthal model predicted with 5.6% error for welding at 15 mm/min plunge rate (Table 7.2). FE simulation showed stress concentration around the weld nugget boundary (Fig 7.6b) and failure at the high stress concentration region. This observation coincided with nugget pull-out failure observed during experiments (Figure 7.6c). The Cockcroft-Latham damage model was able to predict the maximum load at failure during lap shear test with an error of 4−7% compared to experiments (Table 7.2). Owing to the capability of the FE model to predict lap shear load, it was further used to predict the maximum load at failure for two different plunge rates, 12 and 25 mm/min, within the range of experimental plunge rates. The maximum load at failure predicted by the model conformed to the trend observed in experimental results (Table 7.2).

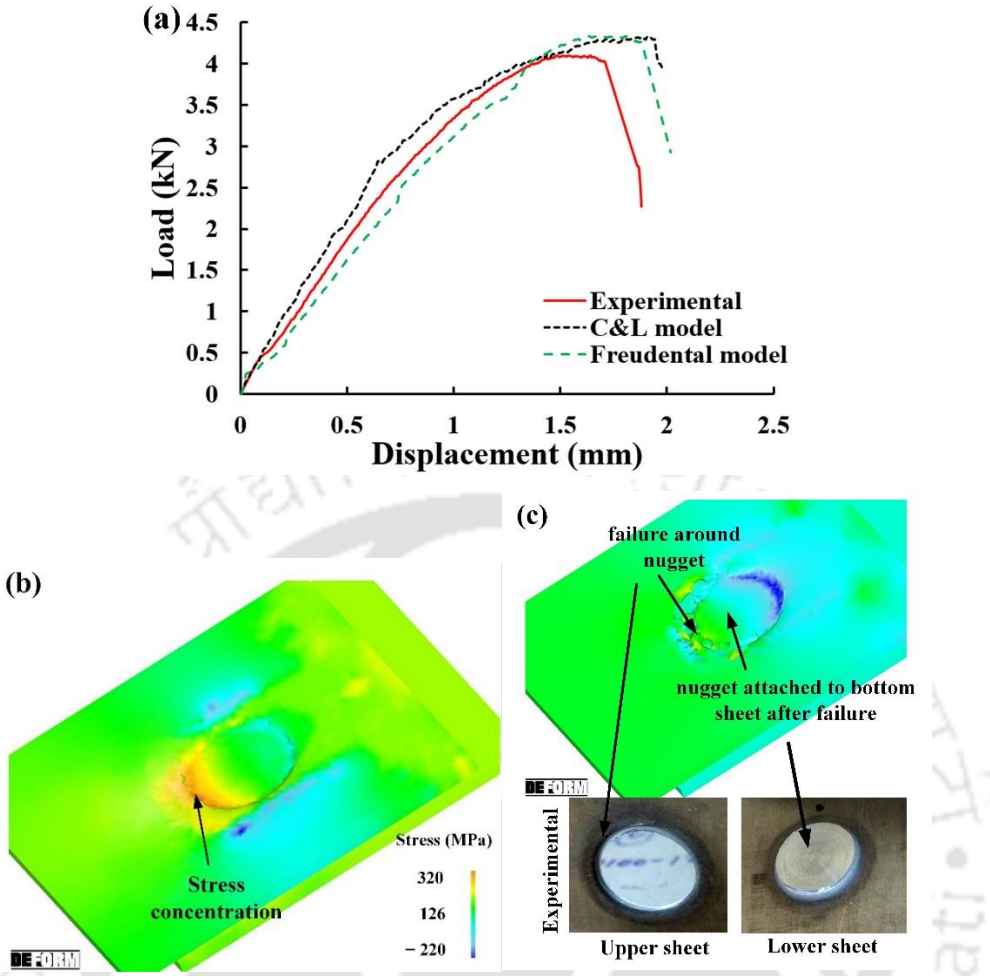

Figure 7.6 Comparison of experimental and simulated lap shear test for FSSW at 15 mm/min plunge rate: (a) load vs displacement curve (b) simulated stress concentration and failure during lap shear test (c) simulated failure and comparison to experimental failure

Table 7.2 Comparison of average experimental and simulated lap shear test results along with prediction using damage models

Plunge rate (mm/min)	Maximum load at failure (kN)	Comparison of simulated and experimental maximum load at failure (kN)			
		Cockcroft-Latham	error (%)	Freudenthal	error (%)
6	3.94	4.17	5.8	4.18	6.1
10	3.97	4.16	4.9	4.19	5.4
15	4.1	4.31	5.1	4.33	5.6
20	3.79	3.97	4.8	4.01	5.9
35	3.07	3.26	6.4	3.27	6.6
12	-	4.12	-	4.15	-
25	-	3.71	-	3.77	-

The temperature evolution from experiments was compared to results from FE simulations at various plunge rates. Figure 7.7a and 7.7b depict results for FSSW at 15 mm/min plunge rate. A

good agreement is observed at P1 and P2 locations. Moreover, the average error in prediction for all plunge rates was 4−7% at P1 and 4−8% at P2. The influence of plunge rate on temperature evolution during plunging is depicted in Figure 7.7c and 7.7d, respectively. At both the locations, P1 and P2, temperature decreased with increase in plunge rate. The observation is consistent with energy calculated during FSSW in Section 7.4.2.

The validated FE model was used to predict the temperature in the joint cross-section and the consumable pin based on its ability to accurately predict temperature at P1 and P2. Temperature contours at the top surface and cross-section are shown in Figure 7.8a for joint made at 15 mm/min plunge rate. The temperature distribution is consistent with the different weld zones observed during welding as discussed in Section 7.4.3. The high temperature in the SZ (470−496 °C), along with severe plastic deformation, helped in dynamic recrystallization leading to finer grains. HAZ experienced a temperature between 390 to 470 °C leading to grain growth and larger grain size. The decrease in temperature as plunge rate is increased (Figure 7.7c and 7.7d) explains the decrease in grain size in different weld zones with increase in plunge rate (Figure 7.4).

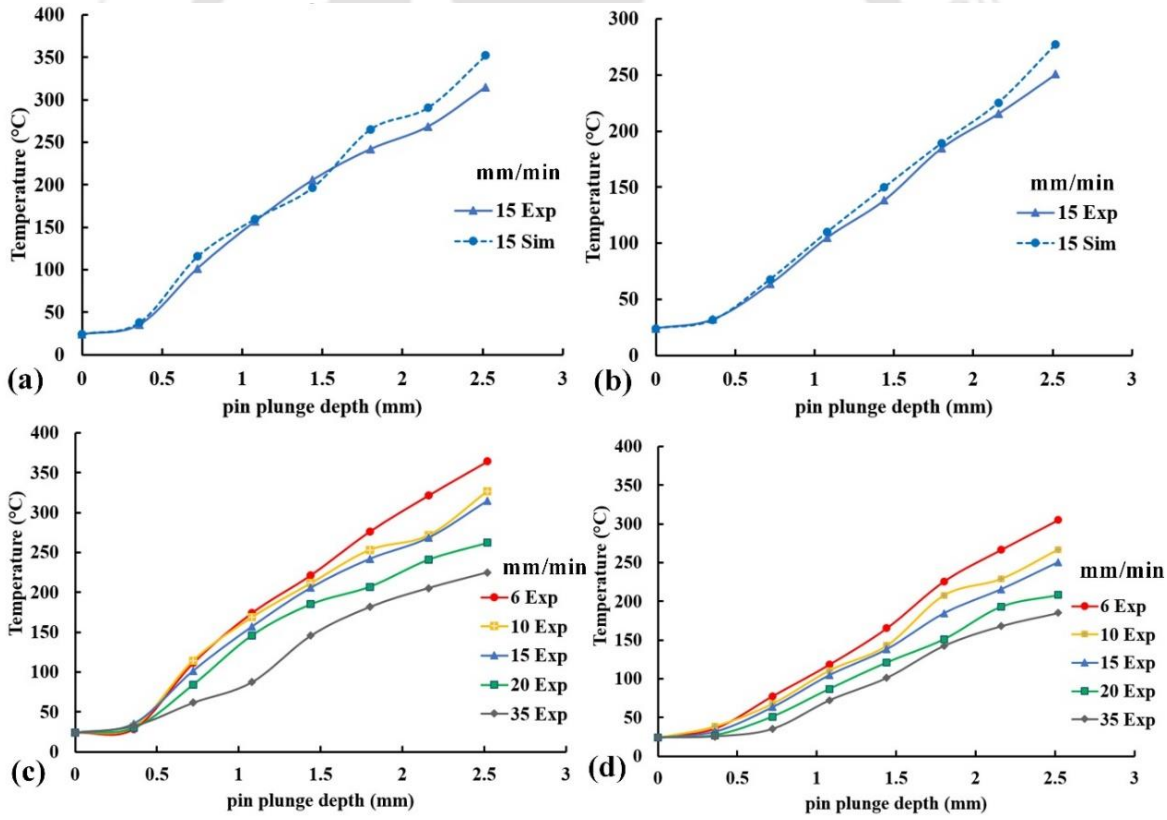

Figure 7.7 Comparison of experimental and simulated temperature variation with time: (a) at P1 (b) at P2; comparison of temperature vs time at different plunge rates (c) at P1 (d) at P2

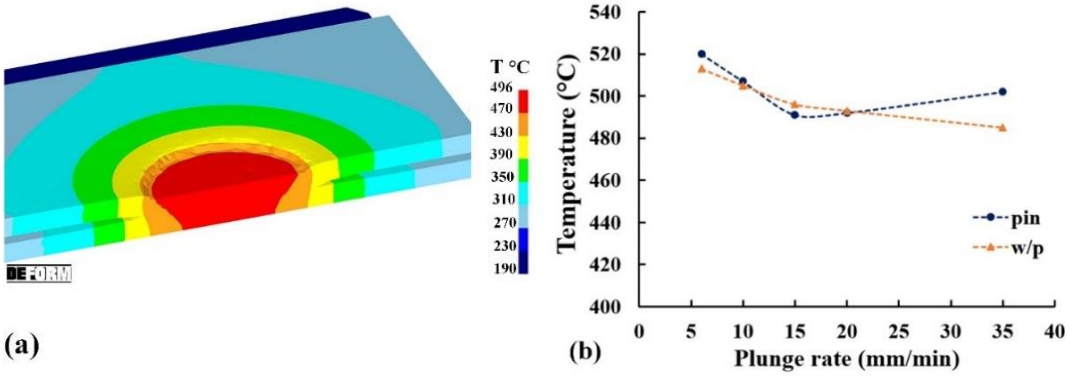

Figure 7.8 Temperature from FE simulations (a) contour at the cross-section and top surface of workpiece (b) maximum temperature on workpiece and consumable pin during plunging at different plunge rates

The unique deformation behavior of the consumable pin is dependent on the heat produced and temperature generated. The deformation behavior determines the penetration depth of the pin and stirring of workpiece material and thus the bond length and joint strength. The temperature of the workpiece during plunging decreases as the plunge rate is increased due lesser process duration. The temperature of the consumable pin also decreases as plunge rate is increased, however, at plunge rates higher than 15 mm/min, the temperature of the consumable pin increases. Although process duration is less, the heat generated due to combined effect of friction and high plastic deformation rate at increased plunge rates result in overall increase in temperature of the consumable pin. It is observed that the consumable pin temperature is higher than the workpiece at plunge rates of 6 mm/min and 10 mm/min (Figure 7.8b). For plunge rates above 20 mm/min, the consumable pin temperature again increases above workpiece temperature, as it experiences more severe plastic deformation rates. At these plunge rates, the consumable pin softens prior to penetration inside the workpiece leading to lesser penetration depth and stirring inside the workpiece (Fig 7.9). The penetration depths of the consumable pins for welding at 6, 10, 15, 20 and 35 mm/min plunge rates are 1.41, 1.48, 1.63, 1.57 and 1.31 mm, respectively. The effect on stirring as a result of penetration depth is reflected in the half-bond lengths of 5.3, 4.8, 6.4, 5.8 and 3.2 mm for welding at 6, 10, 15, 20 and 35 mm/min plunge rates, respectively (Figure 7.9). FSSW at 15 mm/min plunge rate showed the lower consumable pin temperature compared to workpiece, resulting in the higher penetration depth. The consumable pin was able to penetrate more and stir the workpiece material more compared to welding at other plunge rates (in the range 6−35 mm/min) leading to its highest bond length and lap shear strength. Welding at 35 mm/min showed highest consumable temperature compared to workpiece resulting in maximum softening of the consumable pin leading to lowest penetration depth, bond length and lap shear strength.

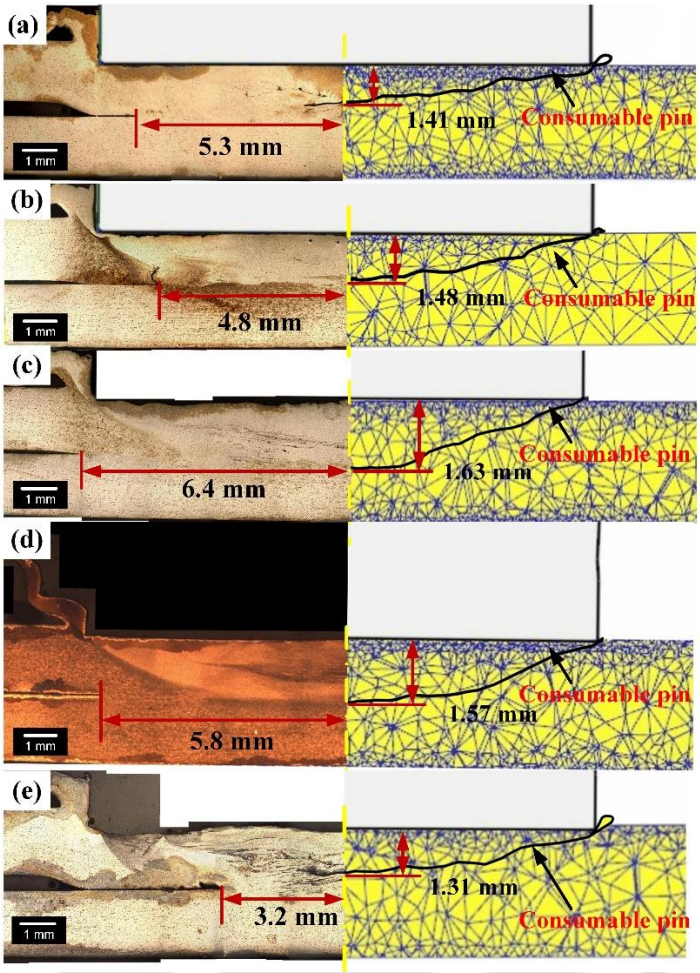

Figure 7.9 Depiction of penetration depth of consumable pin and half-bond length for welding at (a) 6 (b) 10 (c) 15 (d) 20 (e) 35 mm/min plunge rates

7.6 Conclusion

The effect of plunge rate on joint quality during exit-hole-free FSSW using a consumable pin was investigated in this chapter. The joints produced at 6, 10, 15, 20 and 35 mm/min were analyzed by lap shear test, microstructure and microhardness tests. FE simulations of the welding process and subsequent lap shear test simulation were performed to investigate torque, plunge force, lap shear strength and temperature evolution. The following conclusions are made:

1) Unlike conventional FSSW where joint strength decreased monotonously with increasing plunge rate, the lap shear strength in FSSW using consumable pin increased from welding at 6 mm/min to welding at 15 mm/min. Further increase in plunge rate resulted in decrease in joint strength.
2) There was 4% increase in joint strength and 8.5% lower energy input for welding at 15 mm/min plunge rate compared to 6 mm/min. Welding at 35 mm/min plunge rate required 6.2% lower energy as compared to welding at 15 mm/min, however, the joint strength also decreased by 25%. For FSSW of AA6061-T6 sheets using consumable pin, 15 mm/min is suggested as the optimized plunge rate.

3) FE simulations of the lap shear test were able to predict the maximum load at failure for welding at different plunge rates with an error of 4−7%. Lap shear strengths for welding at 12 and 25 mm/min plunge rates were predicted, which conformed to the experimental trend in joint strength. The model can be useful in predicting weld strength for any plunge rate without undergoing physical experimentation, saving material and labor expenses, which is industrially beneficial. The prediction capability of Cockcroft-Latham damage model was found to be better than Freudenthal damage model in this process.
4) The FE model was able to predict torque, plunge force and temperature with an error of 4−6%, 4−7% and 4−8%, respectively, with respect to experimental values. The predicted temperature contours helped understand microstructure changes at different zones as well as deformation and flow behavior of workpiece and the consumable pin.
5) The temperature dependent deformation behavior of the consumable pin determines the penetration depth of the pin, stirring of workpiece material, the bond length, and overall joint strength during FSSW using consumable pin. At plunge rates between 10 and 20 mm/min, temperature of the consumable pin was lower than the workpiece, which resulted in higher penetration depth and stirring leading to higher joint strengths.

Chapter 8

Improving Process Efficiency of FSSW using Consumable Pin by Application of Adhesive and Lubrication

8.1 Introduction

The process of FSSW using consumable pin described in Chapter 5 was able to produce exit-hole-free joints; however, it involved an additional step of machining an indent on the workpiece to ensure stability of the tool and consumable pin axes. This increases production time for each spot welding. Production time is an important aspect of all manufacturing and industrial applications. Shorter production time, fewer machine or parts requirement and capability of automation improve production efficiency. It is also discussed in Chapter 3 that the energy required for welding during FSSW can be reduced by use of lubricants. Use of lubricants during FSSW resulted in more than 50% reduction in energy requirement for weld formation with insignificant change in joint strength.

In this chapter, some strategies are discussed for removal of the additional machining step and reduction of energy requirement during welding by use of lubricants to improve the production efficiency of FSSW using consumable pin. Different lubricants are used to check the effect of lubrication on joint strength and energy required for weld formation.

8.2 Different Pin Retaining Strategies

As described in Section 5.2.1, the method of FSSW using consumable pin involved placing the consumable pin on an indent created on the workpiece, in order to keep the axes of the tool and consumable pin aligned during the initial stages of tool rotation and bring in better stability and control over the process. However, creation of the indent was an additional process involving use of separate tool and taking up production time. To remove the additional step three different techniques are proposed:

I. Tool shoulder with indent: Instead of machining the indent on the upper sheet, the indent of 1 mm depth was machined on the tool shoulder, equal to consumable pin diameter. This allowed for creating the indent only once and eliminated the machining step to be repeated for each spot weld (Figure 8.1a).

II. Consumable pin glued to flat shoulder tool using cyanoacrylate adhesive: The axes of the consumable pin and tool shoulder were aligned, and the consumable pin was joined to the shoulder using cyanoacrylate adhesive (Fevikwik) (Figure 8.1b). Curing time for the adhesive was 5 min. No indent was created on sheet or tool.

III. Consumable pin glued to flat shoulder tool using epoxy-based adhesive: The consumable pin was joined to the shoulder after aligning their axes using epoxy-based adhesive (Araldite) (Figure 8.1c). Curing time for the epoxy-based adhesive was 24 h. No indent was created on sheet or tool as well.

For all the cases, rotational speed of 900 RPM, plunge rate of 15 mm/min, plunge depth of 0.2 mm and dwell time of 10 s were used. Tool shoulder used was 12 mm in diameter and consumable pin was of 6 mm diameter and pin length 3.5 mm in case (I) and 2.5 mm in case (II) and (III). No indent was present on the workpiece. The lap shear strength for all the cases is shown in Table 8.1.

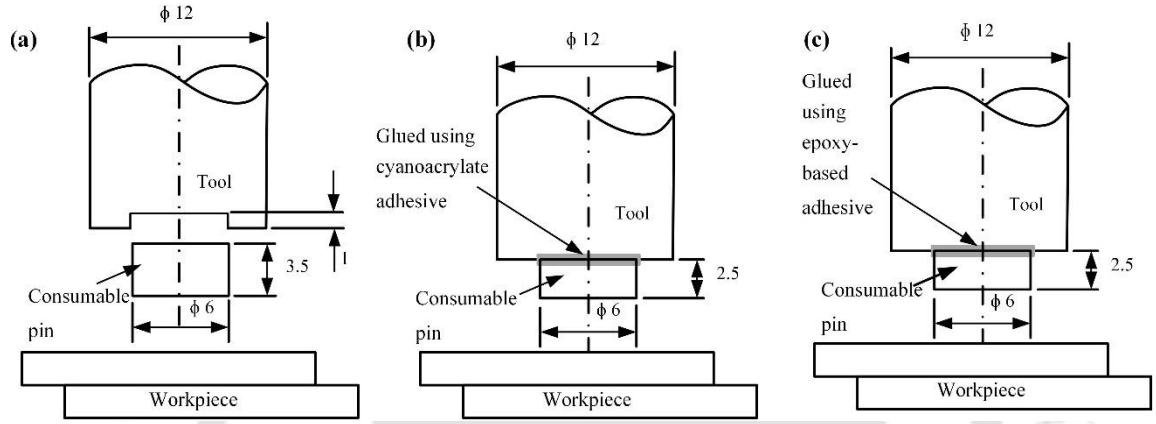

Figure 8.1 Schematics of different consumable pin FSSW techniques: (a) shoulder with indent (b) consumable pin glued using Fevikwik (c) consumable pin glued using Araldite (all dimensions are in mm)

Table 8.1 Maximum load at failure in lap shear test for the different techniques used for consumable pin FSSW

	Maximum load at failure (kN)			
	Case I	**Case II**	**Case III**	**FSSW using consumable pin**
Trial 1	3.98	3.91	4.13	4.07
Trial 2	4.07	4.09	4.02	4.19
Trial 3	4.15	4.1	3.97	4.04
Average	**4.07**	**4.03**	**4.04**	**4.1**

The maximum loads at failure during lap shear test for all the cases (I, II and III) are almost equal. Moreover, maximum load at failure for welding at same process parameters for consumable pin FSSW with indent on the workpiece was 4.1 kN, which is within 5% variation (Table 7.2). Thus, it is observed that use of indent on tool or gluing consumable pin directly to flat tool shoulder is able to produce joints of comparable strength as consumable pin FSSW with indent on the workpiece. However, in case (I), the weld nugget had a protruding extension of the shape of the tool indent (Figure 8.2a), which would need further machining. Such, problem was not observed for case (II) and (III), where an exit-hole-free joint was produced without further processing (Figure 8.2b and 8.2c).

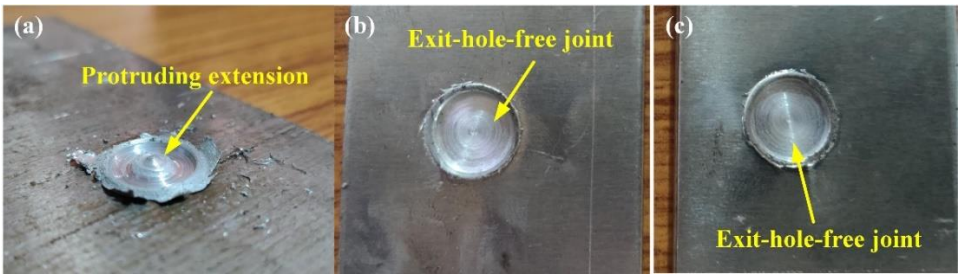

Figure 8.2 FSSW joints produced using consumable pin: (a) with indent on tool shoulder, (b) glued using cyanoacrylate adhesive (Fevikwik) (c) consumable pin glued using epoxy-based adhesive (Araldite)

Thus, use of adhesive to glue the consumable pin to the tool shoulder, aligning their axes, proved to be the most efficient way to produce exit-hole-free FSSW joints using consumable pin. It reduced the additional step of machining an indent on the workpiece or tool. In order to achieve a continuous production using adhesive joined consumable pin tools, multiple tools can be prepared and used one after another to make the joints. At the end of all welding operations, the tools can be reused by gluing the consumable pins to the shoulders again in batches. This could be performed by an unskilled worker. The flow chart of the proposed production cycle is shown in Figure 8.3. Between the adhesives, cyanoacrylate-based adhesive (Fevikwik) is suggested over epoxy-based adhesive (Araldite), since curing time for the former is within 5 mins, whereas the later takes 24 h to cure.

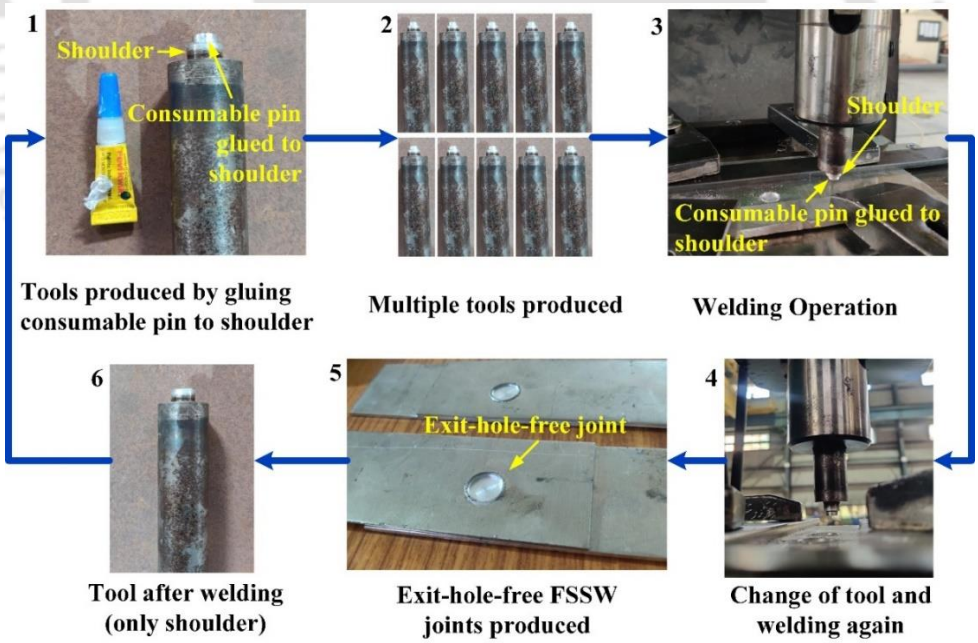

Figure 8.3 Flow chart of production cycle for exit-hole-free FSSW using adhesive joined consumable pin

8.3 Application of Lubricants to FSSW with Consumable Pin

The study is conducted on FSSW using adhesive-bonded consumable pin, as discussed in Section 8.2. Use of cyanoacrylate-based adhesive (Fevikwik) is considered for the study. The primary aim of application of lubricant is to reduce the friction between the tool shoulder and the workpiece. The use of adhesive-bonded consumable pin ensured no lubricant entering the interface between

consumable pin and tool shoulder. This ensured continuous rotation of the consumable pin with the rotating tool. Thus, only this mode of pin retaining strategy was tested with application of lubricants.

In this study, similar lubrication conditions as discussed in Section 3.1 were employed. To investigate the effects of different lubricants, three types of lubricants were utilized: solid (Chisel paste by Cauldron Petrotech India Pvt. Ltd.), liquid (ST Forge Star E), and MoS_2 bonded coating spray lubricants (Release-On). The other process parameters remained unchanged throughout the experiments. The tool rotational speed was set at 900 RPM, the plunge rate at 15 mm/min, and the dwell time at 10 s. The solid lubricant was generously applied to all the surfaces involved in the FSSW process. For the liquid lubricant, a mixture of water and lubricant in the ratio of 1:1 was poured onto the interacting surfaces during the welding process. As for the coated lubricant, it was sprayed onto the tool, adhesive-bonded consumable pin, and the workpiece. The coated lubricant was then allowed to cure for 5 mins before initiating the welding process. Throughout the welding procedure, torque and plunge force were continuously recorded using strain-gage based integrated sensors in the machine (strain data logger-MP31C09). Furthermore, the joint strength was evaluated through lap shear testing using a universal testing machine (UTM) at room temperature, employing a cross head speed of 1 mm/min.

The lap shear strength of each condition was determined by conducting three evaluations and taking the average value. Table 8.2 presents the lap shear strengths for each lubrication condition and comparing them to the unlubricated condition. The results indicate a slight reduction in joint strength for all cases. There was a reduction of 5.7% for the solid lubricant, 6.7% for the liquid lubricant, and 7.9% for the coated lubricant. This decrease can be attributed to the slight reduction in heat input resulting from the decreased friction. However, the joint strength did not degrade significantly due to the involvement of the consumable pin, which contributed to stirring and plastic deformation as it penetrated the workpiece. As explained in Chapter 3.1, the lubricant on the pin's surface gets scraped off during penetration. While the joint strength experienced a slight reduction, there was a notable decrease in torque and plunge force during welding for all lubrication conditions. This reduction in torque and force translated to a lower energy requirement for weld formation. The energy required was calculated using Eq. (3.4), taking into account the torque and plunge force values for each condition. The results showed a reduction of 38% for the solid lubricant, 35% for the liquid lubricant, and 42% for the coated lubricant. It is worth noting that despite the significant reduction in energy requirement for weld formation due to application of lubricants, only a marginal decrease in joint strength was observed. Among the various lubricants, the coated lubricant resulted in maximum energy efficiency. Solid lubricant delivered a good balance of joint strength and energy efficiency.

Table 8.2 Comparison of joint properties with application of different lubricants

	Max. load at failure during lap shear test (kN)				% reduction	Avg. *T* (N·mm)	Avg. *F* (N)	Energy (kJ)	% reduction
	Trial 1	Trial 2	Trial 3	Average					
Unlubricated	3.91	4.09	4.1	4.03	NA	8972	428	6.21	NA
Solid	3.8	3.83	3.77	3.8	5.7%	5386	381	3.85	38%
Liquid	3.78	3.79	3.71	3.76	6.7%	5819	375	4.03	35%
Coated Lubricant	3.66	3.74	3.73	3.71	7.9%	5168	376	3.61	42%

8.4 Optimization of Process Parameters

The process parameters used for FSSW using consumable pin were optimized using G.E.P. Box's evolutionary optimization method. It is established in Section 8.2 that the joint strength achieved by different pin retaining strategies lie within 5% variation. Thus, the optimization process is carried out for FSSW using consumable pin to take advantage of available data from previous chapters. In this study, the process parameters viz., rotational speed and plunge rate form a 2-dimensional case with lap shear strength as the desired functional value. Initial best point, $\bar{x}$ is assumed as 900 RPM and 15 mm/min, denoted by S_0. The initial best rotational speed is assumed based on optimum rotational speed given in Chapter 6. The initial best plunge rate was chosen based on Chapter 7.

The functional value is evaluated at 5 points by giving ± 10% variation to $\bar{x}$. However, due to machine limitations, the functional values were evaluated at closest available process parameters. The process parameters are depicted in Figure 8.4 and the functional values evaluated are shown in Table 8.3. It is observed from experiments that the highest value of lap shear strength is obtained at S_0 i.e. rotational speed of 900 RPM and plunge rate of 15 mm/min. However, FE simulation could be used to assess the lap shear strengths at process parameters beyond machine limits.

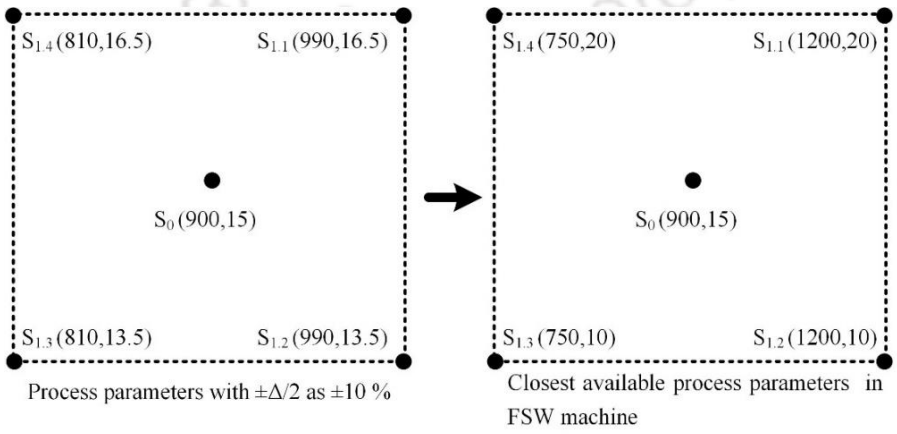

Figure 8.4 Hypercube (2-dimensional) formed for Box's evolutionary optimization

Table 8.3 Functional values at corner points of hypercube (2-dimensional)

Point	Rotational speed (rpm)	Plunge rate (mm/min)	Lap shear strength (kN)	Elongation at failure (mm)
S_0	900	15	4.1	2.15
$S_{1.1}$	1200	20	3.4	1.87
$S_{1.2}$	1200	10	3.44	1.93
$S_{1.3}$	750	10	3.88	1.97
$S_{1.4}$	750	20	3.81	1.96

Considering the superior ability of the FE model described in Chapter 5 and 6, to predict lap shear strength at any a given process parameter, the lap shear strengths at the corner points of the 2-dimensional hypercube with ±10% variation were evaluated (Table 8.4). The highest simulated lap shear strength was achieved at 900 RPM and 15 mm/min. Thus, from experiments and simulation, this point can be concluded as the optimum combination of process parameters for highest lap shear strength. It was also observed that lap shear strength was more sensitive to variation of rotational speed compared to plunge rate.

Table 8.4 Simulated functional values at corner points of hypercube (2-dimensional)

Point	Rotational speed (rpm)	Plunge rate (mm/min)	Lap shear strength (kN)
S_0	900	15	4.31
$S_{1.1}$	990	16.5	4.09
$S_{1.2}$	990	13.5	4.11
$S_{1.3}$	810	13.5	4.18
$S_{1.4}$	810	16.5	4.17

8.5 Conclusion

The findings of this study are summarized as the following conclusions:

1. The study proposed an approach to enhance production efficiency by joining the consumable pin to the tool shoulder using adhesive. This technique eliminated the need for producing an indent on the workpiece for alignment of axes, thus reducing an additional machining step. The results indicated that employing the adhesive-bonded consumable pin method resulted in exit-hole-free FSSW joints with comparable joint strength to the traditional approach. A scheme of production cycle was also proposed for industrial application, where the tools with adhesive-bonded consumable pins are reused in batches.

2. The experimental investigation included the application of solid, liquid, and coated lubricants in FSSW with consumable pin. The results revealed a slight reduction in joint strength for all

lubrication conditions compared to the unlubricated condition. However, the decrease in joint strength was minimal (within 5%), indicating that the lubricants did not significantly compromise the overall strength of the joints.

3. The application of lubricants in FSSW with consumable pin resulted in a significant reduction in torque and plunge force, which translated into a lower energy requirement for weld formation. The energy calculations showed that the lubricated conditions exhibited a notable decrease in energy requirements compared to the unlubricated condition (35–42%). Additionally, the use of lubricants in the welding process did not compromise the control and stability of the process, as the joint strength reduction was minimal.

4. Furthermore, the application of lubricants in conjunction with adhesive-bonded consumable pin FSSW provides a significant advantage in terms of improved production efficiency. The integration of lubricants reduces the energy requirement for weld formation while maintaining good joint strength. This combination of lubrication and adhesive bonding not only streamlines the welding process by eliminating the need for additional machining steps but also ensures the production of joints with satisfactory strength. Thus, the utilization of lubricants in FSSW using adhesive-bonded consumable pin offers a promising approach for achieving higher production efficiency, lower energy consumption, and reliable joint performance of exit-hole-free joints.

5. Use of G.E.P. Box's evolutionary optimization during welding to maximize lap shear strength revealed that welding at 900 RPM rotational speed and 15 mm/min plunge rate are the optimum combination of process parameters. FE simulations were helpful in assessment of joint strength at process parameters outside machine limits.

Chapter 9

Epilogue

9.1 Introduction

This thesis involves advances in welding techniques for sustainability and defect-free joints, focusing on FSSW. The research delves into a comprehensive analysis of friction and heat generation occurring at the contacting surfaces during FSSW. An inverse approach is proposed to model friction during FSSW. Notably, this study tackles the issue of exit-hole formation by presenting two novel approaches. The first involves refilling exit-holes using waste aluminum chips, ensuring the creation of exit-hole-free FSSW joints. The second approach introduces use of a consumable pin during FSSW, effectively eliminating exit-holes. The research explores various consumable pin materials and evaluates the influence of key process parameters, viz. rotational speed and plunge rate, on joint quality in FSSW using consumable pins. Comprehensive evaluations through lap shear tests, macrostructure, microstructure analysis, and microhardness studies are conducted at different process parameters. Moreover, a predictive FE model is developed to simulate the welding process and accurately determine lap shear strength for welding at specific process parameters. In addition, the study investigates adhesive-bonded consumable pins to the tool shoulder for improving process efficiency. The combined application of lubricants and adhesive-bonded consumable pin during FSSW is also explored, offering enhanced production efficiency while maintaining satisfactory joint strength. The overall conclusions of the thesis are discussed in the following section.

9.2 Overall Conclusions

The overall conclusions from the studies can be summarized as follows:

- **Role of Plastic Deformation and Friction in heat generation during FSSW:** Plastic deformation plays a more important role in joint formation during FSSW than friction. Use of lubricants in FSSW reduced torque and plunge force due to reduced friction between the tool shoulder and workpiece. Lubricants resulted in over 50% reduction in energy requirement for weld formation, with insignificant change in joint strength. FSSW could be referred to as stir spot welding (SSW) to highlight the predominant role of plastic deformation.
- **Inverse estimation of friction in FSSW:** A friction model with temperature-dependent parameters was developed for simulating the FSSW process. The model accurately predicted friction parameters, torque, plunge force, and temperature. A typical case study

using AA6061-T6 sheets and H13 grade steel tool yielded friction values for the pin-workpiece and shoulder-workpiece interfaces. The friction model could predict temperature, torque, and plunge force for tools of different sizes.

- **Exit-Hole Refilling using waste chips:** A novel method was used to successfully refill the exit-hole in FSSW using waste aluminium chips. It showed higher load-bearing capacity compared to conventional FSSW with pin and pin-less tools. A seamless bonding of the two plates was observed in the weld spot cross-section, with no trace of the exit-hole.
- **Exit-hole-free FSSW using consumable pin:** A novel method of producing exit-hole-free FSSW using consumable pin was successfully demonstrated. FSSW using consumable pin exhibited higher joint strength compared to pin-less flat shoulder tools, with a slight decrease compared to hard pin tools. AA6061-T6 consumable pin yielded the best weld quality, while MS and OHNS formed brittle intermetallic compounds at dissimilar material interfaces. FE simulation accurately predicted torque, temperature, and microstructure changes, confirming wider TMAZ area and uniform microhardness in AA6061-T6 consumable pin joints.
- **Effect of rotational speed on joint quality for FSSW using consumable pin:** Joint strength in lap shear tests increased with increasing rotational speed up to 900 RPM. Further increase in rotational speed resulted in a marginal decrease in joint strength. FE simulation successfully predicted the failure load for different rotational speeds. Cockcroft-Latham damage model provided more accurate results than the Freudenthal damage model.
- **Effect of plunge rate on joint quality for FSSW using consumable pin:** Lap shear strength in consumable pin FSSW increased from 6 mm/min to 15 mm/min plunge rate and decreased thereafter. Welding at 15 mm/min plunge rate resulted in a 4% higher joint strength and 8.5% lower energy input compared to 6 mm/min. FE simulation accurately predicted torque, plunge force, lap shear strength, and temperature evolution.
- **Integration of adhesive-bonded consumable pin and application of lubricant to FSSW using consumable pin:** A method was proposed to enhance production efficiency by joining the consumable pin to the tool shoulder using adhesive. The adhesive-bonded consumable pin method produced exit-hole-free joints with comparable joint strength to earlier approach of machining an indent on the workpiece. A production cycle scheme was suggested for industrial application, with tools and adhesive-bonded consumable pins reused in batches. The use of lubricants in the welding process reduced torque, plunge force, and energy requirements without compromising process control and stability. This combination of lubrication and adhesive bonding offers a promising approach for achieving high-quality FSSW joints.

9.3 Scope for Future Work

Based on the review conducted and work carried out during the thesis, some future scopes of research are listed:

- During experiments with FSSW using consumable pin, the process may be implemented with assisted heat input to preheat the workpiece, thereby softening it and facilitating higher penetration and stirring by the consumable pin.
- One major concern in FSW/FSSW simulations is the extensive simulation time. Research to shorten the simulation duration can accelerate studies and enhance productivity in the field of FSW/FSSW. Therefore, it would be highly valuable to engage in research aimed at reducing the simulation time of FSW.
- More advanced damage models can be implemented in lap shear test simulations. A major assumption in this study was the continuum assumption where the two sheets were considered as one during FSSW simulation. A model may be developed without considering continuum which would give better idea of bond length and joint strength during lap shear test.
- A continuous feed mechanism of the consumable pin may be developed, where the consumable pin may be fed forward through the shoulder, after each weld. The consumable pin will get assimilated in the workpiece after weld and a new consumable pin will be fed from inside the tool system for the next weld. This will increase the production speed.
- The physical deformation behavior of the consumable pin during FSSW may be recorded in real time with high speed camera to have a better understanding of the consumable pin behavior.
- An analytical model that evaluates various parameters, such as torque and energy, during FSSW with consumable pin would greatly contribute to gaining insights into the intricate interactions involved in FSSW. An analytical approach would allow for a comprehensive analysis of the process, enabling researchers to optimize parameters, improve performance, and refine the FSSW technique.
- The portability of the FSW process is a significant challenge that limits its widespread usage in various industries. Therefore, conducting research focused on addressing the portability issues of FSW would be highly valuable for the industry. By developing innovative techniques, tooling, or approaches that enhance the portability of FSW, researchers can promote its adoption in diverse applications and expand its industrial applicability.

References

Abbasnejad Dizaji, S., Darendeliler, H., and Kaftanoğlu, B. (2016). Effect of hardening models on different ductile fracture criteria in sheet metal forming. International Journal of Material Forming, 9, 261–267.

Aghajani Derazkola, H., and Khodabakhshi, F. (2019). Intermetallic compounds (IMCs) formation during dissimilar friction-stir welding of AA5005 aluminum alloy to St-52 steel: Numerical modeling and experimental study. The International Journal of Advanced Manufacturing Technology, 100, 2401–2422.

Agrawal, A. K., Narayanan, R. G., and Kailas, S. V. (2021). Formability and instability evaluation of friction stir processed AA6063-T6 tubes during end forming and numerical prediction. Journal of Materials Engineering and Performance, 30, 973–993.

Ahmed, M. M., El-Sayed Seleman, M. M., Ahmed, E., Reyad, H. A., Alsaleh, N. A., and Albaijan, I. (2022). A novel friction stir deposition technique to refill keyhole of friction stir spot welded AA6082-T6 dissimilar joints of different sheet thicknesses. Materials, 15(19), 6799.

Akbari, M., Asadi, P., Givi, M. B., and Zolghadr, P. (2016). A cellular automaton model for microstructural simulation of friction stir welded AZ91 magnesium alloy. Modelling and Simulation in Materials Science and Engineering, 24(3), 035012.

Al–Badour, F., Merah, N., Shuaib, A., Bazoune, A. (2013). Coupled Eulerian Lagrangian finite element modeling of friction stir welding processes. Journal of Material Processing Technology, 213(8), 1433–1439.

Allen, C.D., Arbegast, W.J. (2005). Evaluation of friction spot welds in aluminum alloys. SAE International, 2005-01-1252, 107–113.

Álvarez, A. I., García, M., Pena, G., Sotelo, J., and Verdera, D. (2014). Evaluation of an induction-assisted friction stir welding technique for super duplex stainless steels. Surface and Interface Analysis, 46(10–11), 892–896.

Amancio–Filho, S.T., Sheikhi, S., Santos, J.F.D., and Bolfarini, C. (2008). Preliminary study on the microstructure and mechanical properties of dissimilar friction stir welds in aircraft aluminium alloys 2024–T351 and 6056–T4. Journal of Materials Processing Technology, 206, 132–142.

Amini, A., Asadi, P., and Zolghadr, P. (2014). Advances in Friction Stir Welding and Processing. Woodhead Publishing Limited, Cambridge, U.K.

Aonuma M., Nakata K. (2010). Effect of calcium on intermetallic compound layer at interface of calcium added magnesium–aluminum alloy and titanium joint by friction stir welding. Materials Science and Engineering: B, 173, 135–138.

Aota, K., Ikeuchi, K. (2008). Development of friction stir spot welding using rotating tool without probe and its application to low carbon steel plates. Quarterly Journal of the Japan Welding Society, 26, 54–60.

Arbegast, W.J. (2003). Hot Deformation of Aluminum Alloys III. In Hot Deformation of Aluminum Alloys III, TMS, Warrendale, PA, USA.

Arici, A., and Selale, S. (2007). Effects of tool tilt angle on tensile strength and fracture locations of friction stir welding of polyethylene. Science and Technology of Welding and Joining, 12(6), 536–539.

Arora, A., Nandan, R., Reynolds, A. P., and DebRoy, T. (2009). Torque, power requirement and stir zone geometry in friction stir welding through modeling and experiments. Scripta Materialia, 60(1), 13–16.

Arora, A., De, A. and DebRoy, T. (2011). Toward optimum friction stir welding tool shoulder diameter. Scripta Materialia, 64 (1), 9–12.

Asadi, P., Mahdavinejad, R. A., and Tutunchilar, S. (2011). Simulation and experimental investigation of FSP of AZ91 magnesium alloy. Materials Science and Engineering: A, 528(21), 6469–6477.

Asadi, P., Givi, M. K. B., and Akbari, M. (2015). Microstructural simulation of friction stir welding using a cellular automaton method: a microstructure prediction of AZ91 magnesium alloy. International Journal of Mechanical and Materials Engineering, 10(1), 20.

Asadi, P., Givi, M. K. B., and Akbari, M. (2016). Simulation of dynamic recrystallization process during friction stir welding of AZ91 magnesium alloy. The International Journal of Advanced Manufacturing Technology, 83(1–4), 301–311.

Assidi, M., Fourment, L., Guerdoux, S., and Nelson, T. (2010). Friction model for friction stir welding process simulation: Calibrations from welding experiments. International Journal of Machine Tools and Manufacture, 50(2), 143–155.

Aval, H.J., Serajzadeh, S., Kokabi, A.H. (2011). Thermo–mechanical and microstructural issues in dissimilar friction stir welding of AA5086–AA6061. Journal of Materials Science, 46, 3258–3268.

Awang, M. (2007). Simulation of friction stir spot welding (FSSW) process: study of friction phenomena. West Virginia University.

Awang, M., and Mucino, V. H. (2010). Energy generation during friction stir spot welding (FSSW) of Al 6061-T6 plates. Materials and Manufacturing Processes, 25(1–3), 167–174.

ASM International. (2003). Welding handbook: Welding processes, Vol. 2 (8th ed.). ASM International.

Aziz, S. B., Dewan, M. W., Huggett, D. J., Wahab, M. A., Okeil, A. M., and Liao, T. W. (2018). A fully coupled thermomechanical model of friction stir welding (FSW) and numerical studies on process parameters of lightweight aluminum alloy joints. Acta Metallurgica Sinica (English Letters), 31, 1–18.

Bahemmat, P., Haghpanahi, M., Givi, M.K.B., Seighalani, K.R. (2012). Study on dissimilar friction stir butt welding of AA7075–O and AA2024–T4 considering the manufacturing limitation. International Journal of Advanced Manufacturing Technology, 59, 939–953.

Barik, S. K., Narayanan, R. G., and Sahoo, N. (2022). Assessment of stress-strain constitutive models and failure models on the shock tube based impact forming of AA 5052-H32 sheet. Journal of Manufacturing Processes, 74, 573–591.

Baskoro, A. S., Hadisiswojo, S., Kiswanto, G., Winarto, Amat, M. A., and Chen, Z. W. (2020). Influence of welding parameters on macrostructural and thermomechanical properties in micro friction stir spot welded under high-speed tool rotation. The International Journal of Advanced Manufacturing Technology, 106, 163–175.

Behmand, S.A., Mirsalehi, S.E., Omidvar, H., Safarkhanian, M.A. (2015). Filling exit holes of friction stir welding lap joints using consumable pin tools. Science and Technology of Welding and Joining, 20(4), 330–336.

Behnagh, R. A., Samanta, A., Pour, M. A. M., Esmailzadeh, P., and Ding, H. (2019). Predicting microstructure evolution for friction stir extrusion using a cellular automaton method. Modelling and Simulation in Materials Science and Engineering, 27(3), 035006.

Benardos, N., and Meritens, A. (1881). Process of and apparatus for welding or uniting metals. U.S. Patent No. 237,845.

Benson, D.J. (1992). Computational methods in Lagrangian and Eulerian hydrocodes, Computer Methods in Applied Mechanics and Engineering, 99, 235–394.

Benson, D.J. (1997). A mixture theory for contact in multi-material Eulerian formulations. Computer methods in applied mechanics and engineering, 140(1–2), 59–86.

Bendzsak, G.B., North, T.B., Smith, C.B. (2000). An experimentally validated 3D model for friction stir welding, in: Proceedings of the Second International Symposium on Friction Stir Welding, Sweden.

Bevington, J. (1891). Spinning Tubes Mode of Welding the Ends of Wire, Rods, Etc, and Mode of Making Tubes. US patent 463134.

Beygi, R., Akhavan-Safar, A., Carbas, R., Barbosa, A. Q., Marques, E. A. S., and da Silva, L. F. M. (2022). Utilizing a ductile damage criterion for fracture analysis of a dissimilar aluminum/steel joint made by friction stir welding. Engineering Fracture Mechanics, 274, 108775.

Bhamji, I., Preuss, M., Threadgill, P. L., and Addison, A. C. (2011). Solid state joining of metals by linear friction welding: a literature review. Materials Science and Technology, 27(1), 2–12.

Bist, A., Saini, S. J., Sharma, B. (2016). A review of tool wear prediction during friction stir welding of aluminium matrix composite. Transactions of Nonferrous Metal Society of China, 26, 2003–2018.

Bonhomme, J., Argüelles, A., Viña, J., and Viña, I. (2009). Fractography and failure mechanisms in static mode I and mode II delamination testing of unidirectional carbon reinforced composites. Polymer Testing, 28(6), 612–617.

Blaha, F., and Langenecker, B. (1955). Tensile deformation of zinc crystal under ultrasonic vibration. Naturwissenschaften, 42, 556–561.

Brassington, W. D. P., and Colegrove, P. A. (2017). Alternative friction stir welding technology for titanium–6Al–4V propellant tanks within the space industry. Science and Technology of Welding and Joining, 22(4), 300–318.

Brown, K.H., Burns, S.P. and Christon, M.A. (2002) Coupled Eulerian-Lagrangian Methods for Earth Penetrating Weapon Applications, Sand Report: Sand2002-1014, Sandia National Lab.(SNL-NM), Albuquerque, N·m, United States; Sandia National Lab.(SNL-CA), Livermore, CA, United States.

Buffa, G., Donati, L., Fratini, L., Tomesani, L. (2006). Solid state bonding in extrusion and FSW: process mechanics and analogies. Journal of Material Processing Technology, 177, 344–347.

Buffa, G., Hua, J., Shivpuri, R., and Fratini, L. (2006b). Design of the friction stir welding tool using the continuum based FEM model. Materials Science and Engineering, 419, 381–388.

Buffa, G., Fratini, L., and Piacentini, M. (2008). On the influence of tool path in friction stir spot welding of aluminum alloys. Journal of Materials Processing Technology, 208(1–3), 309–317.

Buffa, G., Fratini, L., Shivpuri, R. (2007). CDRX modelling in friction stir welding of AA7075–T6 aluminum alloy: analytical approaches. Journal of Material Processing Technology, 191, 356–359.

Buffa, G., Campanile, G., Fratini, L. and Prisco, A. (2009). Friction stir welding of lap joints: influence of process parameters on the metallurgical and mechanical properties. Materials Science and Engineering A, 519 (1–2), 19–26.

Cao, X., and Liu, H. (2017). A review of keyhole plasma arc welding: From fundamentals to applications. Journal of Materials Processing Technology, 249, 62–77.

Carslaw, H. S., and Jaeger, J. C. (1959). Conduction of heat in solids, Oxford University Press, Amen House, London.

Cavaliere, P., De Santis, A., Panella, F., Squillace, A. (2009). Effect of welding parameters on mechanical and microstructural properties of dissimilar AA6082–AA2024 joints produced by friction stir welding. Materials and Design, 30(3), 609–616.

Cederqvist, L., Sorensen, C. D., Reynolds, A. P. and Oberg, T. (2009). Improved process stability during friction stir welding of 5 cm thick copper canisters through shoulder geometry and parameter studies. Science Technology of Welding and Joining, 14(2), 178–184.

Cengel, Y. A., and Boles, M. A. (2007). Thermodynamics: An Engineering Approach 6th Editon (SI Units). The McGraw-Hill Companies, Inc., New York.

Chang, W. S., Rajesh, S. R., Chun, C. K., and Kim, H. J. (2011). Microstructure and mechanical properties of hybrid laser–friction stir welding between AA6061–T6 Al alloy and AZ31 Mg alloy. Journal of Materials Science and Technology, 27(3), 199–204.

Chai, P., Hu, W., Ji, S., Ai, X., Lv, Z., and Song, Q. (2019). Refill friction stir spot welding dissimilar Al/Mg alloys. Journal of Materials Engineering and Performance, 28, 6174–6181.

Chao Y., Qi X. (1998). Thermal and thermo–mechanical modeling of friction stir welding of aluminum alloy 6061–T6. J. Journal of Materials Processing and Manufacturing Science, 7, 215–233.

Chao, Y. J., Qi, X., and Tang, W. (2003). Heat transfer in friction stir welding—experimental and numerical studies. Journal of Manufacturing Science and Engineering, 125(1), 138–145.

Chaudhary, S. S., and Bhavsar, K. H. (2016). A Review of Bobbin Tool Friction Stir Welding (FSW) Process. International Journal of Science Technology and Engineering, 2(10), 630–633.

Chen, Y. C., and Nakata, K. (2008). Friction stir lap joining aluminum and magnesium alloys. Scripta Materialia, 58(6), 433–436.

Choi, D. H., Lee, C. Y., Ahn, B. W., Choi, J. H., Yeon, Y. M., Song, K., and Jung, S. B. (2011). Hybrid friction stir welding of high-carbon steel. Journal of Materials Science and Technology, 27(2), 127–130.

Cockroft, M.G. and Latham, D.J. (1968). Ductility and the Workability of Metals. Journal of the Institute of Metals, 96, 33–39.

Cole, E. G., Fehrenbacher, A., Duffie, N. A., Zinn, M. R., Pfefferkorn, F. E., and Ferrier, N. J. (2014). Weld temperature effects during friction stir welding of dissimilar aluminum alloys 6061–T6 and 7075–T6. The International Journal of Advanced Manufacturing Technology, 71(1–4), 643–652.

Colegrove, P. A. and Shercliff, H. R. (2003). Two–dimensional CFD modelling of flow round profiled FSW tooling. Science and Technology of Welding and Joining, 9, 483–492.

Colegrove, P. A., and Shercliff, H. R. (2004). Development of Trivex friction stir welding tool Part 2–three–dimensional flow modelling. Science and Technology of Welding and Joining, 9(4), 352–361.

Colligan, K. (1999). Material flow behavior during friction welding of aluminum. Welding Journal, 75(7), 229s–237s.

Corral, J., Trillo, E. A., Li, Y., and Murr, L. E. (2000). Corrosion of friction-stir welded aluminum alloys 2024 and 2195. Journal of Materials Science Letters, 19, 2117–2122.

Das, S. (2010). Modeling mixed microstructures using a multi-level cellular automata finite element framework. Computational Materials Science, 47(3), 705–711.

Davies, C. H. J. (1995). The effect of neighbourhood on the kinetics of a cellular automaton recrystallisation model. Scripta Metallurgica Et Materialia, 33(7), 1139–1143.

de Castro, C. C., Plaine, A. H., de Alcântara, N. G., and dos Santos, J. F. (2018). Taguchi approach for the optimization of refill friction stir spot welding parameters for AA2198-T8 aluminum alloy. The International Journal of Advanced Manufacturing Technology, 99, 1927–1936.

DebRoy, T., Bhadeshia. HKDH. (2010). Friction stir welding of dissimilar alloys–a perspective. Science and Technology Welding and Joining, 15(4), 266–270.

Delany, F., Kallee, S.W. and Russell, M.J., (2007). Friction stir welding of aluminium ships. Electric Welding Machine, 6, 19–29.

Deng, L., Niu, P., Ke, L., Liu, J., Kang, J. (2023). Repairing of exit-hole in friction-stir-spot welded joints for 2024-T4 aluminum alloy by resistance welding. International Journal of Minerals, Metallurgy and Materials, 30(4), 660–669.

Derazkola, H.A., Aval, H.J., Elyasi, M. (2015). Analysis of process parameters effects on dissimilar friction stir welding of AA1100 and A441 AISI steel. Science and Technology Welding and Joining, 20(7), 553–562.

Dialami, N., Chiumenti, M., Cervera, M., Agelet de Saracibar, C., and Ponthot, J. P. (2015). Material flow visualization in friction stir welding via particle tracing. International Journal of Material Forming, 8, 167–181.

Dilip, J. J. S., Janaki Ram, G. D., and Stucker, B. E. (2012). Additive manufacturing with friction welding and friction deposition processes. International Journal of Rapid Manufacturing, 3(1), 56–69.

Dixit, U. S. (2009). Finite element methods for engineers. Cengage Learning.

Dixit, P. M., and Dixit, U. S. (2008). Modeling of metal forming and machining processes: by finite element and soft computing methods. Springer Science and Business Media.

Dixit, U. S., and Shufen, R. (2020). Finite element method modeling of hydraulic and thermal autofrettage processes. In Elsevier Series in Mechanics of Advanced Materials, Mechanics of Materials in Modern Manufacturing Methods and Processing Techniques, Elsevier, 31–69.

Dong, Z., Song, Q., Ai, X., and Lv, Z. (2019). Effect of joining time on intermetallic compound thickness and mechanical properties of refill friction stir spot welded dissimilar Al/Mg alloys. Journal of Manufacturing Processes, 42, 106–112.

Elangovan, K., Balasubramanian, V. (2007). Influences of pin profile and rotational speed of the tool on the formation of friction stir processing zone in AA2219 aluminum alloy. Material Science and Engineering A, 459, 7–18.

Elangovan, K., Balasubramanian, V., and Valliappan, M. (2008). Effect of tool pin profile and tool rotational speed on mechanical properties of friction stir welded AA6061 aluminium alloy. Materials and Manufacturing Processes, 23(3), 251–260.

Elmer, J.W., Evans, C.L., Embree, J.J., Gallegos, G.F. and Summers, L.T., (2014). Electron beam weldability of a group IAB iron meteorite. Science and Technology of Welding and Joining, 19(4), 295–301.

Eom, J., Kim, M., Lee, S., Ryu, H., and Joun, M. (2014). Evaluation of damage models by finite element prediction of fracture in cylindrical tensile test. Journal of Nanoscience and Nanotechnology, 14(10), 8019–8023.

Ericsson, M., and Sandström, R. (2003). Influence of welding speed on the fatigue of friction stir welds, and comparison with MIG and TIG. International Journal of Fatigue, 25(12), 1379–1387.

ESAB. (2012). Friction Stir Welding—The ESAB Way, ESAB, Korea.

Eslami, S., Ramos, T., Tavares, P. J., and Moreira, P. M. G. P. (2015). Shoulder design developments for FSW lap joints of dissimilar polymers. Journal of Manufacturing Processes, 20, 15–23.

Eslami, S., Tavares, P.J. and Moreira, P.M.G.P. (2017). Friction stir welding tooling for polymers: review and prospects. The International Journal of Advanced Manufacturing Technology, 89(5–8), 1677–1690.

Esmaeili, A., Givi, M. B., and Rajani, H. Z. (2011). A metallurgical and mechanical study on dissimilar Friction Stir welding of aluminum 1050 to brass (CuZn30). Materials Science and Engineering: A, 528(22–23), 7093–7102.

Feng, Z., Wang, X., David, S.A., Sklad, P. (2007). Modeling of residual stresses and property distributions in friction stir welds of aluminum alloy 6061-T6. Science and Technology of Welding and Joining, 12(4), 348–356.

Fernandez, G. J., and Murr, L. E. (2004). Characterization of tool wear and weld optimization in the friction-stir welding of cast aluminum 359+ 20% SiC metal-matrix composite. Materials Characterization, 52(1), 65–75.

Ferrando, W. A. (2012). Electrically assisted friction stir welding. US patent 8164021 B1.

Ferreira, A. C., Campanelli, L. C., Suhuddin, U. F. H., de Alcântara, N. G., and dos Santos, J. F. (2020). Investigation of internal defects and premature fracture of dissimilar refill friction stir spot welds of AA5754 and AA6061. The International Journal of Advanced Manufacturing Technology, 106, 3523–3531.

Feulvarch, É. (2005). Modélisation numérique du soudage par friction-malaxage (Friction Stir Welding). These de doctorat, Université Jean Monnet de Saint-Etienne.

Firouzdor, V., and Kou, S. (2010). Al-to-Mg friction stir welding: effect of material position, travel speed, and rotation speed. Metallurgical and Materials Transactions A, 41, 2914–2935.

Fratini, L., Buffa, G. (2005a) CDRX modelling in friction stir welding of aluminium alloys. International Journal of Machine Tools and Manufacture, 45, 1188–1194.

Fratini, L., Beccari, S., Buffa, G. (2005b). Friction stir welding fem model improvement through inverse thermal characterization. Transactions of the North American Manufacturing Research Institution of SME, 33, 259–66.

Fratini, L., Buffa, G., Shivpur, R. (2007). Improving friction stir welding of blanks of different thicknesses. Materials Science and Engineering: A, 459, 209–215.

Freudenthal, M. (1950). The Inelastic Behavior of Engineering Materials and Structures. John Wiley and Sons, New York.

Frigaard, O., Grong, O. (1998). Modeling of the heat flow phenomena in friction stir welding of aluminum alloys. Proceedings of the Seventh International Conference on Joints in Aluminum (INALCO ’98), Cambridge, 15–17.

Frigaard, O., Grong, O. (2001). A process model for friction stir welding of age hardening aluminum alloys. Metallurgical and Materials Transactions A, 137–148.

Fu, B., Qin, G., Li, F., Meng, X., Zhang, J., and Wu, C. (2015). Friction stir welding process of dissimilar metals of 6061-T6 aluminum alloy to AZ31B magnesium alloy. Journal of Materials Processing Technology, 218, 38–47.

Galvao, I., Oliveira, J. C., Loureiro, A., and Rodrigues, D. M. (2011). Formation and distribution of brittle structures in friction stir welding of aluminium and copper: influence of process parameters. Science and Technology of Welding and Joining, 16(8), 681–689.

Gan, W., Li, Z. T. and Khurana S. (2007). Tool materials selection for friction stir welding of L80 steel. Science and Technology of Welding and Joining, 12(7), 610–613.

Gandin, C. A., and Rappaz, M. (1994). A coupled finite element-cellular automaton model for the prediction of dendritic grain structures in solidification processes. Acta Metallurgica et Materialia, 42(7), 2233–2246.

Gao, J., Li, C., Shilpakar, U., and Shen, Y. (2015). Improvements of mechanical properties in dissimilar joints of HDPE and ABS via carbon nanotubes during friction stir welding process. Materials and Design, 86, 289–296.

Gao, Z., Niu, J. T., Krumphals, F., Enzinger, N., Mitsche, S., and Sommitsch, C. (2013). FE modelling of microstructure evolution during friction stir spot welding in AA6082-T6. Welding in the World, 57, 895–902.

Garg, A., Raturi, M., Garg, A., and Bhattacharya, A. (2020). Microstructure evolution and mechanical properties of double-sided friction stir welding between AA6061-T6 and AA7075-T651. CIRP Journal of Manufacturing Science and Technology, 31, 431–438.

Gerard, H., Ehrstrom J.C. (2004). Friction stir welding of dissimilar alloys for aircraft. Presented at the 5th International Symposium on Friction Stir Welding, Metz, France.

Gerlich, A., Su, P., Yamamoto, M., and North, T. H. (2007). Effect of welding parameters on the strain rate and microstructure of friction stir spot welded 2024 aluminum alloy. Journal of Materials Science, 42(14), 5589–5601.

Ghavimi, A. H., Aboutalebi, M. R., Seyedein, S. H. (2020). Exit-hole repairing in friction stir welding of AA5456 pipe using consumable pin. Materials and Manufacturing Processes, 35(11), 1240–1250.

Ghosh, M., Gupta, R. K., and Husain, M. M. (2014). Friction stir welding of stainless steel to Al alloy: effect of thermal condition on weld nugget microstructure. Metallurgical and Materials Transactions A, 45(2), 854–863.

Gong, P., Zuo, Y., Ji, S., Yan, D., and Shang, Z. (2022). A novel non-keyhole friction stir welding process. Journal of Manufacturing Processes, 73, 17–25.

Gould, J. E., and Feng, Z. (1998). Heat flow model for friction stir welding of aluminum alloys. Journal of Materials Processing and Manufacturing Science, 7(2), 185–194.

Gratecap, F., Girard, M., Marya, S., and Racineux, G. (2012). Exploring material flow in friction stir welding: Tool eccentricity and formation of banded structures. International Journal of Material Forming, 5(2), 99–107.

Gratecap Lienert, T. J., Stellwag Jr, W. L., Grimmett, B. B., and Warke, R. W. (2003). Friction stir welding studies on mild steel. Welding Journal, 82(1), 1S–9S.

Grujicic, M., He, T., Arakere, G., Yalavarthy, H.V., Yen, C-F. and Cheeseman, B.A. (2010). Fully coupled thermomechanical finite element analysis of material evolution during friction-stir welding of AA5083. Proceedings of the IMechE, Part B: Journal of Engineering Manufacture, 224, 609–625.

Guerdoux, S., Fourment, L., Miles, M., and Sorensen, C. (2004). Numerical simulation of the friction stir welding process using both Lagrangian and arbitrary Lagrangian Eulerian

formulations. In AIP Conference Proceedings (Vol. 712, No. 1, pp. 1259–1264). American Institute of Physics

Guerdoux S. and Fourment L. (2005). ALE formulation for the numerical simulation of friction stir welding, In Computational plasticity: fundamentals and applications: proceedings of the Eighth International Conference on Computational Plasticity, COMPLAS VIII, CIMNE, Barcelona.

Guo, J. F., Chen, H. C., Sun, C. N., Bi, G., Sun, Z., and Wei, J. (2014). Friction stir welding of dissimilar materials between AA6061 and AA7075 Al alloys effects of process parameters. Materials and Design (1980–2015), 56, 185–192.

Hang, Z. Y., Jones, M. E., Brady, G. W., Griffiths, R. J., Garcia, D., Rauch, H. A., and Hardwick, N. (2018). Non-beam-based metal additive manufacturing enabled by additive friction stir deposition. Scripta Materialia, 153, 122–130.

Hao, H. L., Ni, D. R., Huang, H., Wang, D., Xiao, B. L., Nie, Z. R., and Ma, Z. Y. (2013). Effect of welding parameters on microstructure and mechanical properties of friction stir welded Al–Mg–Er alloy. Materials Science and Engineering: A, 559, 889–896.

Hattel, J. H., Sonne, M. R., and Tutum, C. C. (2015). Modelling residual stresses in friction stir welding of Al alloys—a review of possibilities and future trends. The International Journal of Advanced Manufacturing Technology, 76(9–12), 1793–1805.

He, X., Gu, F., and Ball, A. (2014). A review of numerical analysis of friction stir welding. Progress in Materials Science, 65, 1–66.

Heidari, A., Ghassemi, A., and Atrian, A. (2020). A numerical and experimental investigation of temperature effects on the formability of AA6063 sheets using different ductile fracture criteria. The International Journal of Advanced Manufacturing Technology, 106(5–6), 2595–2611.

Hilgert, J., Schmidt, H. N. B., Dos Santos, J. F., and Huber, N. (2011). Thermal models for bobbin tool friction stir welding. Journal of Materials Processing Technology, 211(2), 197–204.

Hirasawa, S., Badarinarayan, H., Okamoto, K., Tomimura, T., and Kawanami, T. (2010). Analysis of effect of tool geometry on plastic flow during friction stir spot welding using particle method. Journal of Materials Processing Technology, 210(11), 1455–1463.

Hitachi (2018). Available from: http://www.hitachi–rail.com/products/rolling_stock/a_train/feature02.html: Retrieved on 20th January, 2023.

Honda (2012). Honda develops new technology to weld together steel and aluminum and achieves world's first application to the frame of a mass–production vehicle, 6 September, 2012. Available from: http://world.honda.com/: Retrieved on 20th January, 2023.

Honda (2013). Honda Develops New Technology to Join Steel and Aluminum with World's First Application to the Door Panel of Mass Production Vehicles – To reduce vehicle weight to improve fuel economy and dynamic performance, 18 February, 2013. Available from: http://world.honda.com/: Retrieved on 20th January, 2023.

Hovanski, Y., Upadhyay, P., Carsley, J., Luzanski, T., Carlson, B., Eisenmenger, M., Soulami, A., Marshall, D., Landino, B. and Hartfield–Wunsch, S. (2015). High–speed friction–stir welding to enable aluminum tailor–welded blanks. Jom, 67(5), 1045–1053.

Hossfeld M., Roos E. (2013). A new approach to modelling friction stir welding using the CEL method. In International Conference on Advances in Manufacturing and Engineering Technology. NEWTECH. Stockholm 179–190.

Hsu, T.T. (2012). The Finite Element Method in Thermomechanics, Allen and Unwin, London.

Huang, Y.X., Han, B., Tian, Y., Liu, H.J., Lv, S.X., Feng, J.C., Leng, J.S., Li, Y. (2011). New technique of filling friction stir welding. Science and Technology of Welding and Joining, 16, 497–501.

Huang, Y.X., Han, B., Lv, S.X., Feng, J.C., Liu, H.J., Leng, J.S., Li, Y. (2012). Interface behaviours and mechanical properties of filling friction stir weld joining AA2219. Science and Technology of Welding and Joining, 17, 225–230.

Hunt, F., Badarinarayan, H., and Okamoto, K. (2006). Design of Experiments for Friction Stir Stitch Welding of Aluminum Alloy 6022–T4–Friction Stir Welding of Aluminum for Automotive Applications (3)– (No. 2006–01–0970). SAE Technical Paper.

Hydroextrusions (2018). Available from: https://www.hydroextrusions.com/en–GLOBAL/industry/transportation/rail/: Retrieved on 20th January, 2023.

Jain, R., Pal, S. K., and Singh, S. B. (2017). Finite element simulation of temperature and strain distribution during friction stir welding of AA2024 aluminum alloy. Journal of The Institution of Engineers (India): Series C, 98(1), 37–43.

Jain, R., Pal, S.K. and Singh, S.B. (2018). Finite element simulation of pin shape influence on material flow, forces in friction stir welding. The International Journal of Advanced Manufacturing Technology, 94(5–8), 1781–1797.

Jambhale, S., Kumar, S., Kumar, S., (2015). Effect of Process Parameters and Tool Geometries on Properties of Friction Stir Spot Welds: A Review. Universal Journal of Engineering Science, 3, 6–11.

Jata, K. V., Sankaran, K. K., and Ruschau, J. J. (2000). Friction–stir welding effects on microstructure and fatigue of aluminum alloy 7050–T7451. Metallurgical and Materials Transactions A, 31(9), 2181–2192.

Ji, S. D., Meng, X. C., Li, Z. W., Ma, L., and Gao, S. S. (2016). Experimental study of stationary shoulder friction stir welded 7N01–T4 aluminum alloy. Journal of Materials Engineering and Performance, 25(3), 1228–1236.

Ji, S. D., Meng, X. C., Liu, J. G., Zhang, L. G., and Gao, S. S. (2014). Formation and mechanical properties of stationary shoulder friction stir welded 6005A–T6 aluminum alloy. Materials and Design (1980–2015), 62, 113–117.

Joo, S. (2013). Joining of dissimilar AZ31B magnesium alloy and SS400 mild steel by hybrid gas tungsten arc friction stir welding. Metals and Materials International, 19(6), 1251–1257.

Justman, R., West, M., Jasthi, B., Widener, C., and Boysen, A. (2013). Friction Stir Lap Welding Aluminum to Steel Using Scribe Technology. Master Thesis, Dakota School of Mines, USA.

Kallee, S.W. (2010). Industrial applications of friction stir welding, in: D. Lohwasser and Z. Chen (eds), Friction Stir Welding from Basics to Applications. Woodhead Publishing Limited, Cambridge, UK, 118–163.

Kang, S. W., and Jang, B. S. (2013). A study on computational fluid dynamics simulation of friction stir welding. In Analysis and Design of Marine Structures–Proceedings of the 4th International Conference on Marine Structures, Marstruct, 433–439.

Kar, A., Kailas, S. V., and Suwas, S. Effect of Mechanical Mixing in Dissimilar Friction Stir Welding of Aluminum to Titanium with Zinc Interlayer. Transactions of the Indian Institute of Metals, 1–4.

Karthikeyan, R., and Balasubramanian, V. (2010). Predictions of the optimized friction stir spot welding process parameters for joining AA2024 aluminum alloy using RSM. The International Journal of Advanced Manufacturing Technology, 51, 173–183.

Kasai, H., Morisada, Y., and Fujii, H. (2015). Dissimilar FSW of immiscible materials: steel/magnesium. Materials Science and Engineering: A, 624, 250–255.

Katre S., Karidi S., Durga Rao B., Ramulu P.J., Narayanan R.G. (2015). Springback and Formability Studies on Friction Stir Welded Sheets. In: Narayanan R., Dixit U. (eds)

Advances in Material Forming and Joining. Topics in Mining, Metallurgy and Materials Engineering. Springer, New Delhi.

Kawasaki (2002). Kawasaki Becomes First in Japan to Perfect Friction Stir Welding Technology (August, 2002). Available from: https://global.kawasaki.com/en/corp/newsroom/news/detail/ba020828.html: Retrieved on 20th January, 2023.

Kawasaki (2018). Available from: https://global.kawasaki.com/en/corp/sustainability/green_products/efACE_Standard_Railcar.html: Retrieved on 20th January, 2023.

Khan, M. I., Kuntz, M. L., Su, P., Gerlich, A., North, T., and Zhou, Y. (2007). Resistance and friction stir spot welding of DP600: A comparative study. Science and Technology of Welding and Joining, 12(2), 175–182.

Khan, N. Z., Siddiquee, A. N., and Khan, Z. A. (2017a). Friction Stir Welding: Dissimilar Aluminium Alloys. CRC Press.

Khan, N. Z., Siddiquee, A. N., Khan, Z. A., and Mukhopadhyay, A. K. (2017). Mechanical and microstructural behavior of friction stir welded similar and dissimilar sheets of AA2219 and AA7475 aluminium alloys. Journal of Alloys and Compounds, 695, 2902–2908.

Khandkar, M. Z. H., and Khan, J. A. (2001). Thermal modeling of overlap friction stir welding for Al–alloys. Journal of Materials Processing and Manufacturing Science, 10, 91–105.

Khandkar, M. Z. H., Khan, J. A., and Reynolds, A. P. (2003). Prediction of temperature distribution and thermal history during friction stir welding: input torque based model. Science and Technology of Welding and Joining, 8(3), 165–174.

Khandkar, M. Z. H., Khan, J. A., Reynolds, A. P., and Sutton, M. A. (2006). Predicting residual thermal stresses in friction stir welded metals. Journal of Materials Processing Technology, 174(1–3), 195–203.

Khoei, A. R., Anahid, M., and Mofid, M. (2003). An application of arbitrary Lagrangian-Eulerian method in numerical simulation of forming processes using cap plasticity model. In 12th International Science Conference on Achievements in Mechanical and Materials Engineering, AMME.

Khosa, S. U., Weinberger, T., and Enzinger, N. (2010). Thermo-mechanical investigations during friction stir spot welding (FSSW) of AA6082-T6. Welding in the World, 54, R134–R146.

Kim, Y. G., Fujii, H., Tsumura, T., Komazaki, T., and Nakata, K. (2006). Effect of welding parameters on microstructure in the stir zone of FSW joints of aluminum die casting alloy. Materials Letters, 60(29–30), 3830–3837.

Kohn, G., Greenberg, Y., Makover, I. and Munitz, A. (2002). Laser assisted friction stir welding. Welding Journal, 81, 46–48.

Kou, S. and Cao, G. (2006). Arc–enhanced friction stir welding.US patent 707 647.

Kubit, A., Kluz, R., Trzepieciński, T., Wydrzyński, D., and Bochnowski, W. (2018). Analysis of the mechanical properties and of micrographs of refill friction stir spot welded 7075-T6 aluminium sheets. Archives of Civil and Mechanical Engineering, 18, 235–244.

Kumagai, M., and Tanaka, S. (2001). Method of Spot Joining for Aluminum Alloy. Japan Patent, 259863.

Kumar, K. S. V. K., and Kailas, S. V. (2008). The role of friction stir welding tool on material flow and weld formation. Materials Science and Engineering: A, 485(1–2), 367–374.

Kumar, R., Pancholi, V., and Bharti, R. P. (2018). Material flow visualization and determination of strain rate during friction stir welding. Journal of Materials Processing Technology, 255, 470–476.

Kumar, N., Prasad, V., Singh, P., Singh, R. K., and Kumar, R. (2018). A review on friction welding of metals and alloys: applications, challenges and prospects. Journal of Materials Research and Technology, 7(4), 453–466.

Kumar, K., Kalyan, C., Kailas, S. V., and Srivatsan, T. S. (2009). An investigation of friction during friction stir welding of metallic materials. Materials and Manufacturing Processes, 24(4), 438–445.

Kwon, Y. J., Shigematsu, I., and Saito, N. (2004). Mechanical property improvements in aluminum alloy through grain refinement using friction stir process. Materials transactions, 45(7), 2304–2311.

Lage, S. B. M., Campanelli, L. C., de Bribean Guerra, A. P., Shen, J., dos Santos, J. F., da Silva, P. S. C. P., and Bolfarini, C. (2019). A study of the parameters influencing mechanical properties and the fatigue performance of refill friction stir spot welded AlMgSc alloy. The International Journal of Advanced Manufacturing Technology, 100, 101–110.

Lan, S., Liu, X., and Ni, J. (2016). Microstructural evolution during friction stir welding of dissimilar aluminum alloy to advanced high–strength steel. The International Journal of Advanced Manufacturing Technology, 82(9–12), 2183–2193.

Lan, Y. J., Li, D. Z., and Li, Y. Y. (2004). Modeling austenite decomposition into ferrite at different cooling rate in low-carbon steel with cellular automaton method. Acta Materialia, 52(6), 1721–1729.

Lancaster, J. F. (1999). The use of adhesives for making structural joints. Metallurgy of Welding, 6, 54–84.

Langenecker, B. (1966). Effects of ultrasound on deformation characteristics of metals. IEEE Transactions on Sonics and Ultrasonics, 13, 1–8.

Liechty, B. C., and Webb, B. W. (2007). The use of plasticine as an analog to explore material flow in friction stir welding. Journal of Materials Processing Technology, 184(1–3), 240–250.

Li, D., Yang, X., Cui, L., He, F., and Zhang, X. (2015). Investigation of stationary shoulder friction stir welding of aluminum alloy 7075–T651. Journal of Materials Processing Technology, 222, 391–398.

Li, J. Q., and Liu, H. J. (2014). Effects of tool rotation speed on microstructures and mechanical properties of AA2219–T6 welded by the external non–rotational shoulder assisted friction stir welding. Materials and Design, 43, 299–306.

Li, B., Zhang, Z., Shen, Y., Hu, W., and Luo, L. (2014a). Dissimilar friction stir welding of Ti–6Al–4V alloy and aluminum alloy employing a modified butt joint configuration: Influences of process variables on the weld interfaces and tensile properties. Materials and Design, 53, 838–848.

Li, W. Y., Fu, T., Hütsch, L., Hilgert, J., Wang, F. F., Dos Santos, J. F., and Huber, N. (2014b). Effects of tool rotational and welding speed on microstructure and mechanical properties of bobbin-tool friction-stir welded Mg AZ31. Materials and Design, 64, 714–720.

Lorrain, O., Serri, J., Favier, V., Zahrouni, H. and Hadrouz, M.E. (2009). A contribution to a critical review of friction stir welding numerical simulation. Journal of Mechanics of Materials and Structures, 4(2), 351–370.

Lin, P. C., Pan, J., and Pan, T. (2008). Failure modes and fatigue life estimations of spot friction welds in lap–shear specimens of aluminum 6111–T4 sheets. Part 2: Welds made by a flat tool. International Journal of Fatigue, 30(1), 90–105.

Liu, G., Murr, L. E., Niou, C. S., McClure, J. C., and Vega, F. R. (1997). Microstructural aspects of the friction–stir welding of 6061–T6 aluminum. Scripta Materialia, 37(3), 355–361.

Liu, H. J., Feng, J. C., Fujii, H., and Nogi, K. (2005). Wear characteristics of a WC–Co tool in friction stir welding of AC4A+ 30 vol% SiCp composite. International Journal of Machine Tools and Manufacture, 45(14), 1635–1639.

Liu, X. C., and Wu, C. S. (2016). Elimination of tunnel defect in ultrasonic vibration enhanced friction stir welding. Materials and Design, 90, 350–358.

Liu, F.C., Hovanski, Y., Miles, M.P., Sorensen, C.D. and Nelson, T.W., (2018). A review of friction stir welding of steels: Tool, material flow, microstructure, and properties. Journal of Materials Science and Technology, 34(1), 39–57.

Lotfi, A. H., and Nourouzi, S. (2014). Predictions of the optimized friction stir welding process parameters for joining AA7075-T6 aluminum alloy using preheating system. The International Journal of Advanced Manufacturing Technology, 73(9–12), 1717–1737.

Luijendijk, T. (2000). Welding of dissimilar aluminium alloys. Journal of Materials Processing Technology, 103, 29–35.

Maalekian, M. (2007). Friction welding–critical assessment of literature. Science and Technology of Welding and Joining, 12(8), 738–759.

Madej, L., Hodgson, P. D., and Pietrzyk, M. (2009). Development of the multi-scale analysis model to simulate strain localization occurring during material processing. Archives of Computational Methods in Engineering, 16(3), 287–318.

Mahoney, M., R.S. Mishra, T. Nelson, (2001). Friction Stir Welding and Processing. TMS, Warrendale, PA, USA.

Malik, V., Sanjeev, N. K., Hebbar, H. S., and Kailas, S. V. (2014). Time efficient simulations of plunge and dwell phase of FSW and its significance in FSSW. Procedia Materials Science, 5, 630–639.

Maltin, C. A., Nolton, L. J., Scott, J. L., Toumpis, A. I., and Galloway, A. M. (2014). The potential adaptation of stationary shoulder friction stir welding technology to steel. Materials and Design, 64, 614–624.

Mehta, K. P., Patel, R., Vyas, H., Memon, S., and Vilaça, P. (2020). Repairing of exit-hole in dissimilar Al-Mg friction stir welding: Process and microstructural pattern. Manufacturing Letters, 23, 67–70.

Mehta, K., Astarita, A., Carlone, P., Della Gatta, R., Vyas, H., Vilaça, P., and Tucci, F. (2021). Investigation of exit-hole repairing on dissimilar aluminum-copper friction stir welded joints. Journal of Materials Research and Technology, 13, 2180–2193.

Meran, C., Kovan, V., and Alptekin, A. (2007). Friction stir welding of AISI 304 austenitic stainless steel. Materialwissenschaft und Werkstofftechnik: Entwicklung, Fertigung, Prüfung, Eigenschaften und Anwendungen technischer Werkstoffe, 38(10), 829–835.

Messler, R. W. (1999). Principles of Welding. Wiley–VCH Verlag, Weinheim, Germany.

Merzoug, M., Mazari, M., Berrahal, L., and Imad, A. (2010). Parametric studies of the process of friction spot stir welding of aluminium 6060-T5 alloys. Materials and Design, 31(6), 3023–3028.

Mijajlović, M., and Milčic, D. (2012). Analytical model for estimating the amount of heat generated during friction stir welding: application on plates made of aluminium alloy 2024 T351. Welding Processes, 247–274.

Mishra, R. S., and Ma, Z. Y. (2005). Friction stir welding and processing. Materials science and engineering: R: reports, 50(1–2), 1–78.

Mofid, M. A., Abdollah–Zadeh, A., and Ghaini, F. M. (2012). The effect of water cooling during dissimilar friction stir welding of Al alloy to Mg alloy. Materials and Design, 36(12), 161–167.

Mousavi, S. A., Habibi, S., and Khoramshahi, M. (2019). The effect of preheating temperature on the mechanical properties and microstructure of Al-Cu exothermic weld joint. Journal of Manufacturing Processes, 43, 204–213.

Muthukumaran, S., and Mukherjee, S. K. (2008). Multi–layered metal flow and formation of onion rings in friction stir welds. The International Journal of Advanced Manufacturing Technology, 38(1–2), 68–73.

Nandan, R., Roy, G. G., Lienert, T. J., and DebRoy, T. (2006). Numerical modelling of 3D plastic flow and heat transfer during friction stir welding of stainless steel. Science and Technology of Welding and Joining, 11(5), 526–537.

NASA (2001). Space Shuttle Technology Summary, Friction Stir Welding. NASA, Maryland.

Neto, D. M., and Neto, P. (2013). Numerical modeling of friction stir welding process: a literature review. The International Journal of Advanced Manufacturing Technology, 65(1–4), 115–126.

Nikkeikin (2018). FSW (Friction Stir Welding) Technology from Plate to Sheet. Available from: http://www.nikkeikin.com/products/board/p29.html: Retrieved on 20th January, 2023.

Oguzie, E.E. (2007). Corrosion inhibition of aluminium in acidic and alkaline media by Sansevieria trifasciata extract. Corrosion Science, 49(3), 1527–1539.

Ohashi, R., Fujimoto, M., Mironov, S., Sato, Y. S., and Kokawa, H. (2009). Effect of contamination on microstructure in friction stir spot welded DP590 steel. Science and Technology of Welding and Joining, 14(3), 221–227.

Okamoto, K., Hunt, F., and Hirano, S. (2005). Development of Friction Stir Welding Technique and Machine for Aluminum Sheet Metal Assembly–Friction Stir Welding of Aluminum for Automotive Applications (2)– (No. 2005–01–1254). SAE Technical Paper.

Oosterkamp, A., Oosterkamp, L. D., and Nordeide, A. (2004). Kissing bond' phenomena in solid–state welds of aluminum alloys. Welding Journal, 83(8), 225S–232S.

Oeystein, G., Ove, K. A., Midling, O. T. and Hydro, N. (1999). Modified friction stir welding. International patent application, WO1999039861 A1.

Orowan, E., (1943). The calculation of roll pressure in hot and cold flat rolling. Proceedings of Institution of Mechanical Engineers, 150 (1), 140–167.

Padhy, G. K., Wu, C. S., and Gao, S. (2018). Friction stir based welding and processing technologies–processes, parameters, microstructures and applications: A review. Journal of Materials Science and Technology, 34(1), 1–38.

Palanivel, R., Mathews, P. K., and Murugan, N. (2013). Optimization of process parameters to maximize ultimate tensile strength of friction stir welded dissimilar aluminum alloys using response surface methodology. Journal of Central South University, 20(11), 2929–2938.

Palanivel, S., Nelaturu, P., Glass, B., and Mishra, R. S. (2015a). Friction stir additive manufacturing for high structural performance through microstructural control in an Mg based WE43 alloy. Materials and Design, 65, 934–952.

Palanivel, S., Sidhar, H., and Mishra, R. S. (2015b). Friction stir additive manufacturing: Route to high structural performance. JOM, 67(3), 616–621.

Palm F. (2004). Laser supported friction stir welding method. US patent 6793118

Pan, T., Joaquin, A., Wilkosz, D. E., et al. (2004). Spot friction welding for sheet aluminum joining. Proceedings of the Fifth International Conference on Friction Stir Welding, 14–16.

Park, S. K., Hong, S. T., Park, J. H., Park, K. Y., Kwon, Y. J., and Son, H. J. (2010). Effect of material locations on properties of friction stir welding joints of dissimilar aluminium alloys. Science and Technology of Welding and Joining, 15(4), 331–336.

Park, S. H. C., Sato, Y. S., Kokawa, H., Okamoto, K., Hirano, S., and Inagaki, M. (2009). Boride formation induced by pcBN tool wear in friction-stir-welded stainless steels. Metallurgical and Materials Transactions A, 40(3), 625–636.

Pashazadeh, H., Teimournezhad, J., and Masoumi, A. (2014). Numerical investigation on the mechanical, thermal, metallurgical and material flow characteristics in friction stir welding of copper sheets with experimental verification. Materials and Design, 55, 619–632.

Patel, C., Das, S., and Narayanan, R. G. (2013). CAFE modeling, neural network modeling, and experimental investigation of friction stir welding. Proceedings of the Institution of Mechanical Engineers, Part C: Journal of Mechanical Engineering Science, 227(6), 1164–1176.

Polt W. (September 2004). Boeing Frontiers. Available from: http://www.boeing.com/: Retrieved on 20th January, 2023.

Prado, R. A., Murr, L. E., Soto, K. F., and McClure, J. C. (2003). Self–optimization in tool wear for friction–stir welding of Al 6061+ 20% Al2O3 MMC. Materials Science and Engineering: A, 349(1–2), 156–165.

Priyadarshini, A., Pal, S.K., Samantaray, A.K., 2012. Finite element modeling of chip formation in orthogonal machining. Statistical and Computational Techniques in Manufacturing, 101–144.

Qian, M., and Guo, Z. X. (2004). Cellular automata simulation of microstructural evolution during dynamic recrystallization of an HY-100 steel. Materials Science and Engineering: A, 365(1–2), 180–185.

Rai, R., De, A., Bhadeshia, H. K. D. H., and DebRoy, T. (2011). friction stir welding tools. Science and Technology of welding and Joining, 16(4), 325–342.

Rajakumar, S., Muralidharan, C., and Balasubramanian, V. (2011). Influence of friction stir welding process and tool parameters on strength properties of AA7075–T6 aluminium alloy joints. Materials and Design, 32(2), 535–549.

Rajpoot, Y. S., Narayanan, R. G., and Das, S. (2018). Predicting the effect of tool configuration during friction stir welding by cellular automata finite element analyses. International Journal of Manufacturing Research, 13(4), 359–381.

Ramulu, P. J., Kailas, S. V., and Narayanan, R. G. (2013). Influence of tool rotation speed and feed rate on the forming limit of friction stir welded AA6061-T6 sheets. Proceedings of the

Institution of Mechanical Engineers, Part C: Journal of Mechanical Engineering Science, 227(3), 520–541.

Ramulu, P. J., Narayanan, R. G., and Kailas, S. V. (2013a). Forming limit investigation of friction stir welded sheets: influence of shoulder diameter and plunge depth. The International Journal of Advanced Manufacturing Technology, 69(9–12), 2757–2772.

Rana, P.K., Narayanan, R.G. and Kailas, S.V., (2018). Effect of rotational speed on friction stir spot welding of AA5052–H32/HDPE/AA5052–H32 sandwich sheets. Journal of Materials Processing Technology, 252, 511–523.

Rana, P. K., Narayanan, R. G., and Kailas, S. V. (2019). Friction stir spot welding of AA5052-H32/HDPE/AA5052-H32 sandwich sheets at varying plunge speeds. Thin-Walled Structures, 138, 415–429.

Rana P.K., Ganesh Narayanan R., Kailas S.V. (2019) Influence of Tool Plunge Depth During Friction Stir Spot Welding of AA5052-H32/HDPE/AA5052-H32 Sandwich Sheets. In: Dixit U., Narayanan R. (eds) Strengthening and Joining by Plastic Deformation. Lecture Notes on Multidisciplinary Industrial Engineering. Springer, Singapore.

Rao, S.S. (2010) Engineering Optimization: Theory and Practice. 3rd edn. New Age International (P) Ltd., Delhi.

Rao, S.S. (2019) Engineering Optimization: Theory and Practice. 5th ed. John Wiley and Sons, New Jersey.

Ravi, K. K., Narayanan, R. G., and Rana, P. K. (2018). Friction Stir Spot Welding of Al6082-T6/HDPE/Al6082-T6/HDPE/Al6082-T6 sandwich sheets: hook formation and lap shear test performance. Journal of Materials Research and Technology, 8(1), 615–622.

Reimann, M., Goebel, J., dos Santos, J.F. (2017). Microstructure and mechanical properties of keyhole repair welds in AA7075-T651 using refill friction stir spot welding. Materials and Design, 132, 283–294.

Reimann, M., Gartner, T., Suhuddin, U., Göbel, J., and dos Santos, J. F. (2016). Keyhole closure using friction spot welding in aluminum alloy 6061–T6. Journal of Materials Processing Technology, 237, 12–18.

Reynolds, A. P. (2000). Visualisation of material flow in autogenous friction stir welds. Science and technology of welding and joining, 5(2), 120–124.

Rhodes, C. G., Mahoney, M. W., Bingel, W. H., Spurling, R. A., and Bampton, C. C. (1997). Effects of friction stir welding on microstructure of 7075 aluminum. Scripta Materialia, 36(1), 341–355.

Richards, D. G., Prangnell, P. B., Williams, S. W., & Withers, P. J. (2008). Global mechanical tensioning for the management of residual stresses in welds. Materials Science and Engineering: A, 489(1-2), 351–362.

Rodelas, J., and Lippold, J. (2013). Characterization of engineered nickel-base alloy surface layers produced by additive friction stir processing. Metallography, Microstructure, and Analysis, 2(1), 1–12.

Rosenberg, J. (2015). Welding and metal fabrication. Industrial Press, Norwalk, CT, USA.

Russel, M., and Shercliff, H. (1999). Analytical modeling of microstructure development in friction stir welding. 1st International symposium on friction stir welding, USA.

Russell, M.J., Threadgill, P.L., Thomas, M.J. (2007). Static shoulder friction stir welding of Ti–6Al–4V. 11th World Conference on Titanium, Kyuoto, Japan Institute of Metals, 1095–1098.

Russell, M. J., Blignault, C., Horrex, N. L., and Wiesner, C. S. (2008). Recent developments in the friction stir welding of titanium alloys. Welding in the World, 52(9–10), 12–15.

Salimi, S., Bahemmat, P., and Haghpanahi, M. (2016). Analytical model for the temperature field around a nonuniform three-dimensional moving heat source: friction stir welding modelling. Journal of Engineering Mathematics, 98(1), 71–91.

Saluja, R. S., Narayanan, R. G., and Das, S. (2012). Cellular automata finite element (CAFE) model to predict the forming of friction stir welded blanks. Computational Materials Science, 58, 87–100

Samanta, A., Shen, N., Ji, H., Wang, W., Li, J., and Ding, H. (2018). Cellular automaton simulation of microstructure evolution for friction stir blind riveting. Journal of Manufacturing Science and Engineering, 140(3), 031016.

Santos, T. G., Miranda, R. M. and Vilaca, P. (2014). Friction stir welding assisted by electrical Joule effect. Journal of Material Processing Technology, 214, 2127–2133.

Saravanan, V., Rajakumar, S., and Muruganandam, A. (2016). Effect of friction stir welding process parameters on microstructure and mechanical properties of dissimilar AA6061-T6 and AA7075-T6 aluminum alloy joints. Metallography, Microstructure, and Analysis, 5, 476–485.

Sathyaseelan, P., Manickavasagam, V. M., Ravichandran, P., Prasad, D. V. S. S. S. V., Ramana Murty Naidu, S. C. V., Pradeep Kumar, S., and Kerga, G. A. (2022). Effect of Dwell Time on Fracture Load of Friction Stir Spot Welded Dissimilar Metal Joints. Advances in Materials Science and Engineering, Article 2163507.

Sato, Y. S., Urata, M., and Kokawa, H. (2002). Parameters controlling microstructure and hardness during friction–stir welding of precipitation–hardenable aluminum alloy 6063. Metallurgical and Materials Transactions A, 33(3), 625–635.

Sato, Y. S., Harayama, N., Kokawa, H., Inoue, H., Tadokoro, Y., and Tsuge, S. (2009). Evaluation of microstructure and properties in friction stir welded superaustenitic stainless steel. Science and Technology of welding and Joining, 14(3), 202–209.

Seidel, T. U., and Reynolds, A. P. (2003). Two–dimensional friction stir welding process model based on fluid mechanics. Science and technology of welding and joining, 8(3), 175–183.

Schilling, C., and dos Santos, J. (2004). U.S. Patent No. 6,722,556. Washington, DC: U.S. Patent and Trademark Office.

Schmidt, H., Hattel, J., and Wert, J. (2003). An analytical model for the heat generation in friction stir welding. Modelling and simulation in materials science and engineering, 12(1), 143.

Schmidt, H., and Hattel, J. (2005). Modelling heat flow around tool probe in friction stir welding. Science and Technology of Welding and joining, 10(2), 176–186.

Schmidt, H. N. B., Dickerson, T. L., and Hattel, J. H. (2006). Material flow in butt friction stir welds in AA2024–T3. Acta Materialia, 54(4), 1199–1209.

Sellars, C. M., and Tegart, W. M. (1972). Hot workability. International Metallurgical Reviews, 17(1), 1–24.

Shi, Q. Y., Dickerson, T. L., and Shercliff, H. R. (2003). Thermomechanical FE modelling of friction stir welding of Al-2024 including tool loads. In Friction Stir Welding: Proceedings of the 4th International Symposium on Friction Stir Welding. TWI Limited.

Shi, L., Wu, C. S., and Liu, H. J. (2014). Modeling the material flow and heat transfer in reverse dual–rotation friction stir welding. Journal of Materials Engineering and Performance, 23(8), 2918–2929.

Shi, L., Wu, C. S., and Liu, H. J. (2015a). Analysis of heat transfer and material flow in reverse dual–rotation friction stir welding. Welding in the World, 59(5), 629–638.

Shi, L., Wu, C. S., and Liu, H. J. (2015b). The effect of the welding parameters and tool size on the thermal process and tool torque in reverse dual–rotation friction stir welding. International Journal of Machine Tools and Manufacture, 91, 1–11.

Shojaeefard, M. H., Akbari, M., Khalkhali, A., Asadi, P., and Parivar, A. H. (2014). Optimization of microstructural and mechanical properties of friction stir welding using the cellular automaton and Taguchi method. Materials and Design, 64, 660–666.

Shterenlikht, A., and Howard, I. C. (2006). The CAFE model of fracture—application to a TMCR steel. Fatigue and Fracture of Engineering Materials and Structures, 29(9-10), 770–787.

Shtrikman, M. M. (2015). Trends in the development of the friction stir welding process. Welding International, 29(3), 230–239.

Siddiq, A. and Sayed, T. E. (2012). Ultrasonic–assisted manufacturing processes: variational model and numerical simulation. Ultrasonics 52, 521–529.

Silva, A. A. M. Da, Arruti, E., Janeiro, G., Aldanondo, E., Alvarez, P., and Echeverria, A. (2011). Material flow and mechanical behaviour of dissimilar AA2024–T3 and AA7075–T6 aluminium alloys friction stir welds. Materials and Design, 32(4), 2021–2027.

Simar, A., and Avettand–Fènoël, M. N. (2017). State of the art about dissimilar metal friction stir welding. Science and Technology of Welding and Joining, 22(5), 389–403.

Sinclair, P. C., Longhurst, W. R., Cox, Ch. D. and Lammlein, D. H. (2010). Heated friction stir welding: an experimental and theoretical investigation into how preheating influences process forces. Mater. Manuf. Processes, 25, 1283–1291.

Skrzat, A. (2012). Application of coupled Eulerian-Lagrangian approach in metal forming simulations. Zeszyty Naukowe Politechniki Rzeszowskiej. Mechanika, 84(284), 25–35.

Smith, C. B., Noruk, J. S., Bendzsak, G. B., North, T. H., Hinrichs, J. F., Heideman, R. J., and Smith, A. O. (2000). Heat and material flow modeling of the friction stir welding process. NIST Special Publication SP, 475–488.

Sonne, M. R., Tutum, C. C., Hattel, J. H., Simar, A., and De Meester, B. (2013). The effect of hardening laws and thermal softening on modeling residual stresses in FSW of aluminum alloy 2024-T3. Journal of Materials Processing Technology, 213(3), 477–486.

Song, Z., Nakata, K., Wu, A., Liao, J., and Zhou, L. (2014). Influence of probe offset distance on interfacial microstructure and mechanical properties of friction stir butt welded joint of Ti6Al4V and A6061 dissimilar alloys. Materials and Design, 57, 269–278.

Sorensen, C. D., and Nelson, T. W. (2007). Friction stir welding of ferrous and nickel alloys. Friction stir welding and processing, 111–121.

SpaceX (2013). Falcon 9 Progress Update (December, 2013) Available from: https://www.spacex.com/news/2013/02/11/falcon–9–progress–update–12: Retrieved on 20th January, 2023.

Su, P., Gerlich, A., North, T.H., Bendzsak, G.J. (2006). Energy utilisation and generation during friction stir spot welding. Science and Technology of Welding and Joining, 11, 163–169.

Sued, M. K., Pons, D., Lavroff, J., and Wong, E. H. (2014). Design features for bobbin friction stir welding tools: Development of a conceptual model linking the underlying physics to the production process. Materials and Design, 54, 632–643.

Suryanarayanan, R., and Sridhar, V. G. (2020). Effect of process parameters in pinless friction stir spot welding of Al 5754-Al 6061 alloys. Metallography, Microstructure, and Analysis, 9, 261–272.

Taban, E., and Kaluc, E. (2007). Comparison between microstructure characteristics and joint performance of 5086–H32 aluminium alloy welded by MIG, TIG and friction stir welding processes. Kovove Materialy, 45(5), 241.

Tan, C. W., Jiang, Z. G., Li, L. Q., Chen, Y. B., and Chen, X. Y. (2013). Microstructural evolution and mechanical properties of dissimilar Al–Cu joints produced by friction stir welding. Materials and Design, 51, 466–473.

Tanaka, T., Hirata, T., Shinomiya, N., and Shirakawa, N. (2015). Analysis of material flow in the sheet forming of friction–stir welds on alloys of mild steel and aluminum. Journal of Materials Processing Technology, 226, 115–124.

Thomas, W. (1991). International Patent Application No. PCT/GB92. GB Patent Application No. 9125978.

Thomas, W. M., Threadgill, P. L., and Nicholas, E. D. (1999). Feasibility of friction stir welding steel. Science and Technology of Welding and Joining, 4(6), 365–372.

Threadgill, P. L., Ahmed, M. M. Z., Martin, J. P., Perrett, J. G., and Wynne, B. P. (2010). The use of bobbin tools for friction stir welding of aluminium alloys. Materials Science Forum, 638, 1179–1184.

Tier, M. D., Rosendo, T. S., Dos Santos, J. F., Huber, N., Mazzaferro, J. A., Mazzaferro, C. P., and Strohaecker, T. R. (2013). The influence of refill FSSW parameters on the microstructure

and shear strength of 5042 aluminium welds. Journal of Materials Processing Technology, 213(6), 997–1005.

Tongne, A., Desrayaud, C., Jahazi, M., and Feulvarch, E. (2017). On material flow in friction stir welded Al alloys. Journal of Materials Processing Technology, 239, 284–296.

Tozaki, Y., Uematsu, Y., and Tokaji, K. (2010). A newly developed tool without probe for friction stir spot welding and its performance. Journal of Materials Processing Technology, 210(6–7), 844–851.

Trimble, D., Monaghan, J. and O'Donnell, G.E. (2012). Force generation during friction stir welding of AA2024-T3. CIRP Annals – Manufacturing Technology, 61(1), 9–12.

Tweedy, B. M., Widener, C. A., Merry, J. D., Brown, J. M., and Burford, D. A. (2008). Factors affecting the properties of swept friction stir spot welds. SAE Technical Paper No. 2008–01–1135.

Uematsu, Y., Tokaji, K., Tozaki, Y., Kurita, T., Murata, S. (2008). Effect of re-filling probe hole on tensile failure and fatigue behaviour of friction stir spot welded joints in Al–Mg–Si alloy. International Journal of Fatigue, 30, 1956–1966.

Upadhyay, P., Hovanski, Y., Jana, S., and Fifield, L. S. (2017). Joining Dissimilar Materials Using Friction Stir Scribe Technique. Journal of Manufacturing Science and Engineering, 139(3), 034501.

Valvi, S. R., Krishnan, A., Das, S., and Narayanan, R. G. (2016). Prediction of microstructural features and forming of friction stir welded sheets using cellular automata finite element (CAFE) approach. International Journal of Material Forming, 9(1), 115–129.

Van Elsen, M., Baelmans, M., Mercelis, P., and Kruth, J. P. (2007). Solutions for modelling moving heat sources in a semi-infinite medium and applications to laser material processing. International Journal of heat and mass transfer, 50(23–24), 4872–4882.

Venkateswaran, P., and Reynolds, A. P. (2012). Factors affecting the properties of Friction Stir Welds between aluminum and magnesium alloys. Materials Science and Engineering: A, 545, 26–37.

Venukumar, S., Yalagi, S., and Muthukumaran, S. (2013). Comparison of microstructure and mechanical properties of conventional and refilled friction stir spot welds in AA 6061-T6 using filler plate. Transactions of Nonferrous Metals Society of China, 23(10), 2833–2842.

Vetrivel Sezhian, M., Giridharan, K., Peter Pushpanathan, D., Chakravarthi, G., Stalin, B., Karthick, A., and Bharani, M. (2021). Microstructural and mechanical behaviors of friction

stir welded dissimilar AA6082-AA7075 joints. Advances in Materials Science and Engineering, 2021, 1–13.

Wan, L., and Huang, Y. (2017). Microstructure and mechanical properties of Al/steel friction stir lap weld. Metals, 7(12), 542.

Wang, X., Morisada, Y., and Fujii, H. (2020). Flat friction stir spot welding of AZ31B magnesium alloy using double side adjustable tools: microstructure and mechanical properties. Science and Technology of Welding and Joining, 25(8), 644–652.

Wang, T., Liu, T., Roosendaal, T., Upadhyay, P. (2022). Reinforcing the exit hole from friction stir welding and processing. Materialia, 26, 101611.

Weinberger, T., Enzinger, N., and Cerjak, H. (2009). Microstructural and mechanical characterisation of friction stir welded 15–5PH steel. Science and Technology of Welding and Joining, 14(3), 210–215.

Wouters, R., and Froyen, L. (1996). Scanning electron microscope fractography in failure analysis of steels. Materials Characterization, 36(4–5), 357–364.

Wu, A., Song, Z., Nakata, K., Liao, J., and Zhou, L. (2015). Interface and properties of the friction stir welded joints of titanium alloy Ti6Al4V with aluminum alloy 6061. Materials and Design, 71, 85–92.

Wu, S. J., Davis, C. L., Shterenlikht, A., and Howard, I. C. (2005). Modeling the ductile-brittle transition behavior in thermomechanically controlled rolled steels. Metallurgical and Materials Transactions A, 36(4), 989–997.

Xiao, L. I. U., Li, L. X., He, F. Y., Jia, Z. H. O. U., Zhu, B. W., and Zhang, L. Q. (2013). Simulation on dynamic recrystallization behavior of AZ31 magnesium alloy using cellular automaton method coupling Laasraoui–Jonas model. Transactions of Nonferrous Metals Society of China, 23(9), 2692–2699.

Xu, S. W., Deng, X., Reynolds, A. P., and Seidel, T. U. (2001). Finite element simulation of material flow in friction stir welding. Science and Technology of Welding and Joining, 6(3), 191–193.

Xue, P., Xiao, B. L., Wang, D., and Ma, Z. Y. (2011a). Achieving high property friction stir welded aluminium/copper lap joint at low heat input. Science and Technology of Welding and Joining, 16(8), 657–661.

Xue, P., Ni, D. R., Wang, D., Xiao, B. L., and Ma, Z. Y. (2011b). Effect of friction stir welding parameters on the microstructure and mechanical properties of the dissimilar Al–Cu joints. Materials science and engineering: A, 528(13–14), 4683–4689.

Yaduwanshi, D. K., Bag, S. and Pal, S. (2014). Effect of preheating in hybrid friction stir welding of aluminum alloy. Journal of Materials Engineering and Performance, 23, 3794–3803.

Yazdi, S. R., Beidokhti, B., and Haddad-Sabzevar, M. (2019). Pinless tool for FSSW of AA 6061-T6 aluminum alloy. Journal of Materials Processing Technology, 267, 44–51.

Yuqing, M., Liming, K., Chunping, H., Fencheng, L., and Qiang, L. (2016). Formation characteristic, microstructure, and mechanical performances of aluminum-based components by friction stir additive manufacturing. The International Journal of Advanced Manufacturing Technology, 83(9–12), 1637–1647.

Zhang, Z., Yang, X., Zhang, J., Zhou, G., Xu, X., and Zou, B. (2011). Effect of welding parameters on microstructure and mechanical properties of friction stir spot welded 5052 aluminum alloy. Materials & Design, 32(8-9), 4461–4470.

Zhang, G.F., Jiao, W.M., Zhang, J.X. (2014). Filling friction stir weld keyhole using pin free tool and T shaped filler bit. Science and Technology of Welding and Joining, 19(2), 98–104.

Zhang, H. F., Zhou, L., Li, G. H., Tang, Y. T., Li, W. L., and Wang, R. (2021). Prediction and validation of temperature distribution and material flow during refill friction stir spot welding of AZ91D magnesium alloy. Science and Technology of Welding and Joining, 26(2), 153–160.

Zhao, Y., Lu, Z., Yan, K., and Huang, L. (2015). Microstructural characterizations and mechanical properties in underwater friction stir welding of aluminum and magnesium dissimilar alloys. Materials and Design, 65, 675–681.

Zhou, L., Liu, D., Nakata, K., Tsumura, T., Fujii, H., Ikeuchi, K., Michishita, Y., Fujiya, Y., Morimoto, M. (2013). New technique of self-refilling friction stir welding to repair keyhole. Science and Technology of Welding and Joining, 17(8), 649–655.

Zhao, Y. H., Lin, S. B., Wu, L., and Qu, F. X. (2005). The influence of pin geometry on bonding and mechanical properties in friction stir weld 2014 Al alloy. Materials Letters, 59(23), 2948–2952.

Zheng, C., Xiao, N., Li, D., and Li, Y. (2008). Microstructure prediction of the austenite recrystallization during multi-pass steel strip hot rolling: A cellular automaton modeling. Computational Materials Science, 44(2), 507–514.

Zhu, X. K., and Chao, Y. J. (2004). Numerical simulation of transient temperature and residual stresses in friction stir welding of 304L stainless steel. Journal of Materials Processing Technology, 146(2), 263–272.

Zimmer, S., Langlois, L., Laye, J., Goussain, J. C., Martin, P., and Bigot, R. (2009). Influence of processing parameters on the tool and workpiece mechanical interaction during friction stir welding. International Journal of Material Forming, 2(1), 299–304.

Publications from this Thesis

Journal Publications:

1. Bhardwaj, N., Narayanan, R. G., and Dixit, U. S. (2023). Experimental and Numerical Investigation on the Effect of Rotational Speed on Exit-Hole Free Friction Stir Spot Welding with Consumable Pin. **International Journal of Material Forming 16** Article 45 (14 pages)
2. Bhardwaj, N., Narayanan, R. G., and Dixit, U. S. (2023). Exit-Hole-Free Friction Stir Spot Welding of Aluminum Alloy Sheets Using a Consumable Pin. **Journal of Materials Engineering and Performance, 32(5),** 2119–2138.
3. Bhardwaj, N., Narayanan, R. G., Dixit, U. S., Petrov, M., and Petrov, P. (2020). An Inverse Approach Towards Determination of Friction in Friction Stir Spot Welding. **Procedia Manufacturing, 47,** 839–846.
4. Bhardwaj N., Ganesh Narayanan R., Dixit U.S. and Hashmi M.S.J. (2019) Recent Developments in Friction Stir Welding and Resulting Industrial Practices, **Advances in Materials and Processing Technologies 5(3),** 461–496.

Conferences:

- Bhardwaj, N., Narayanan, R. G., Dixit, U. S., Petrov, M., and Petrov, P. An inverse approach towards determination of friction in friction stir spot welding. 23rd International ***Conference on Material Forming (ESAFORM 2020).*** BTU, Cottbus, Germany, May 04–06 (2020) (Published as Journal paper #3)
- Bhardwaj N., Ganesh Narayanan R., Dixit U.S. Effect of Lubrication on Energy Requirement and Joint Properties during FSW of AA5052-H32 Aluminium Alloy. *Proceedings of 6th International* ***Conference on Production and Industrial Engineering (CPIE)***, NIT Jalandhar, Punjab, India, p. 38–41, May 02–06 (2019) (Published as book chapter #3)
- Bhardwaj N., Ganesh Narayanan R., Dixit U.S. Refilling of Exit-hole in Friction Stir Spot Welding Using Waste Chips. *Proceedings of* ***7th International and 28th All India Manufacturing Technology, Design and Research (AIMTDR)***, Anna University, Chennai, India, p.133–138, December 14–19 (2018). (Published as book chapter #2)

Book Chapters:

1. Bhardwaj, N., Narayanan, R. G., and Dixit, U. S. (2021). Modeling of Friction Stir Welding Processes. In: Davim, J. P. (ed.) ***Welding Technology,*** Springer Nature, Switzerland.
2. Bhardwaj N., Ganesh Narayanan R., Dixit U.S. (2020) Refilling of Exit-hole in Friction Stir Spot Welding Using Waste Chips. In: Shunmugam, M., Kanthababu, M. (eds.) ***Advances in Additive Manufacturing and Joining: Lecture Notes on Multidisciplinary Industrial Engineering.*** Springer, Singapore
3. Bhardwaj N., Ganesh Narayanan R., Dixit U.S. (2020) Effect of Lubrication on Energy Requirement and Joint Properties during FSW of AA5052-H32 Aluminium Alloy. In: Sharma, V.S. et al. (eds.) ***Manufacturing Engineering: Lecture Notes on Multidisciplinary Industrial Engineering***, Springer, Singapore